Modeling of a folded spring supporting MEMS gyroscope

A Thesis
Submitted to the faculty
of the

Worcester Polytechnic Institute

in partial fulfillment of the requirements for the
Degree of Master of Science
in
Mechanical Engineering

by

_____

Victoria Steward

20 June 2003
Approved:

_____

Prof. Ryszard J. Pryputniewicz, Major Advisor

_____

Prof. Cosme Furlong, Member, Thesis Committee

_____

Prof. Raymond R. Hagglund, Member, Thesis Committee

_____

Prof. Grétar Tryggvason, Member, Thesis Committee

_____

Dimitry Grabbe, Member, Thesis Committee

_____

Howard Last, Member, Thesis Committee

_____

Prof. John M. Sullivan, Jr., Graduate Committee Representative

SUMMARY

Microelectromechanical systems (MEMS) are integrated mechanical and electrical devices that can range from sensors, valves, gears, mirrors, to actuators, and are fabricated on silicon wafers with features micrometers in size. They are built using techniques similar to those used for microelectronics. MEMS devices have potential applications for a range of industries: automotive, aerospace, medical, and many others. Due to this variety of applications, a great deal of work has been done on improving the quality and the functionality of the MEMS components available. However, before more advancements can be made, the behavior of MEMS sensors must be fully understood. Without this basic knowledge of how and why MEMS components and devices react the way they do when they are designed in a specific manner and fabricated using different materials, it is impossible to predict how MEMS systems will behave, and their behavior can only be reliably observed using physical experimentation. Experimentation can be expensive and time consuming since MEMS components are very fragile and even the most robust MEMS device is very vulnerable to external influences which can induce mechanical and structural failures. Therefore, gaining a better understanding of the behavior of MEMS devices is essential.

The purpose of this thesis was to model a folded spring supporting MEMS gyroscope, a type of inertial sensor that measures rates of angular acceleration. This modeling was performed using analytical, computational, and experimental solutions (ACES) methodology. The analytical and computational results were compared with preliminary experimental results. The first step was to develop an analytical model of the

3

behavior of the proof masses, by examining motion of the folded springs that support the proof masses. Then in order to extend the capabilities of the analytical method used to model the folded springs, its components were modeled using computational method. Finally, selected characteristics of parts of the microgyroscope were observed experimentally. More specifically, folded springs supporting proof masses of a MEMS gyroscope were modeled analytically and computationally to determine their deformations due to typical forces generated during functional operation of a microgyroscope. Also, preliminary measurements of parameters characterizing and influencing functional operation of the microgyroscope were made using laser vibrometer method and optoelectronic laser interferometric microscope (OELIM) method. These methods provide very high spatial resolution data with nanometer measurement accuracy that are acquired in full-field-of view, remotely and non-invasively, in near real-time. As such, these methods are particularly suitable for experimental investigations of microgyroscopes, or other MEMS.

Comparison of the analytical and computational results with the preliminary experimental results shows acceptable correlation within the uncertainty limits. This correlation indicates viability of the methodology used in this thesis as a potential tool that may facilitate improvements of the existing microgyroscopes and development of new designs in the future.

ACKNOWLEDGEMENTS

TABLE OF CONTENTS

LIST OF FIGURES

10

11

12

15

17

LIST OF TABLES

21

NOMENCLATURE

a_{max}	maximum acceleration of the proof mass
$a(t)$	sinusoidal in-plane acceleration of the proof mass
b	damping
b	width of sections AB and CD of the Sandia microgyro folded spring
b_{150}	width of the Analog Devices ADXRS150 microgyro spring
b_{BC}	width of section BC of the microgyro folded spring
$c_{1,2}$	torsional coefficients for uniform rectangular bars
f	cyclic frequency
h	thickness of the microgyro folded spring
h_{150}	thickness of the Analog Devices ADXRS150 microgyro spring
$h(x)$	characteristic function
k	spring constant
$k_{y,z}$	shape factor
m	mass
r	radial position
t	time
$\mathbf{v}$	in-plane velocity
$v(t)$	sinusoidal velocity of the proof mass
x	position along the length of section BC of the folded spring
$x(t)$	sinusoidal motion of the proof mass of the Sandia microgyro
$y(t)$	output of the system
z	position along the lengths of sections AB and CD of the folded spring

A	cross sectional area
A_b	cross sectional area of sections AB and CD of the folded spring
A_c	cross sectional area of section BC of the folded spring
A_o	amplitude of the illumination intensity in the object beam
A_r	amplitude of intensity in the reference beam
$A_{x,y,z}$	forces acting at point A of the folded spring
$AB_{x,y,z}$	internal forces acting thru section AB of the folded spring
B	amplitude of oscillation of the proof mass, bias limit
$B_{x,y,z}$	forces acting at point B of the Sandia microgyro folded spring
$BC_{x,y,z}$	internal forces acting thru section BC of the folded spring
BMM	bulk micromachining
$C_{x,y,z}$	forces acting at point C of the folded spring
$CD_{x,y,z}$	internal forces acting thru section CD of the folded spring
$D_{1,2,3,4,5}$	frequency domain signals
E	modulus of elasticity
F_{xmax}	in-plane force, due to the motion of the proof mass acting on the folded spring

$F_{x,y,z}$	arbitrary forces in the three Cartesian directions applied to the folded spring
$F_x(t)$	time varying in-plane force acting on the folded spring
$\mathbf{F}$	force vector
$\mathbf{F}_c$	Coriolis force
F_c	magnitude of the Coriolis force
$\mathbf{F}_i$	external forces
FEM	finite element method
FFT	fast Fourier transform
FRF	frequency response function
G	shear modulus
$\mathbf{H}$	angular momentum
I	moment of inertia
$I_{bx,y}$	moment of inertia for sections AB and CD of the folded spring
$I_{cy,z}$	moment of inertia for section BC of the folded spring
$I_n(x,y)$	irradiance distribution of the nth sequential frame
$I_o(x,y)$	irradiance distribution of the object beam
$I_r(x,y)$	irradiance distribution of the reference beam
I_y	moment of inertia area for motion in the in-plane direction
I_z	moment of inertia for motion in the out-of-plane direction
IC	integrated circuit
$IFFT$	inverse fast Fourier transform
J	polar moment of inertia
J_b	polar moment of inertia for sections AB and CD of the folded spring
J_c	polar moment of inertia for section BC of the folded spring
L	length of a beam
L_{150}	length of the Analog Devices ADXRS150 microgyro spring
L_f	length of the fingers of the electrostatic combdrives of the microgyro
L_{AB}	length of section AB of the folded spring
L_{BC}	length of section BC of the folded spring
L_{CD}	length of section CD of the folded spring
$\mathbf{M}$	internal bending moment
$M_{Ax,y,z}$	moments acting at point A of the folded spring
$M_{ABx,y}$	internal moments acting thru section AB of the folded spring
$M_{Bx,y,z}$	moments acting at point B of the folded spring
$M_{BCy,z}$	internal moments acting thru section BC of the folded spring
$M_{Cx,y,z}$	moments acting at point C of the folded spring
$M_{CDx,y}$	internal moments acting thru section CD of the folded spring
$M(x)$	bending moment acting along a section of the folded spring
$MEMS$	microelectromechanical systems
$\mathbf{N}$	axial load

P_X	precision limit of a system of the entire set of data representing a parameter
PZT	piezoresistive transducer
S_X	precision index of a population
SMM	surface micromachining
T	torque
T	magnitude of a torque
T_{ABz}	internal torque acting thru section *AB* of the folded spring
T_{BCx}	internal torque acting thru section *BC* of the folded spring
T_{CDz}	internal torque acting thru section *CD* of the folded spring
U_i	internal strain energy of a body
U_x	total RSS uncertainty
U_{AB}	strain energy of section *AB* of the folded spring
U_{AL}	strain energy due to axial loading
U_{BC}	strain energy of section *BC* of the folded spring
U_{BM}	strain energy due to bending moments
U_{CD}	strain energy of section *CD* of the folded spring
U_{TM}	strain energy due to torsional moments
U_{TS}	strain energy due to transverse shear loading
V	shear force
W_e	external work
X	an independent parameter
X_i	a dependent parameter
X	mean value of the variable *X*
$\delta_X(\ )$	uncertainty in X
v	poison's ratio
ρ	density
σ	standard deviation of a variable
τ	period of oscillation of the proof mass of the microgyro
ω	angular speed of the oscillating proof mass
ϕ	phase difference between two beams
Δ_{analyt}	analytical deformation
Δ_{comp}	computational deformation
Δ_{expr}	experimental deformation
$\Delta_{dx,y,z}$	deformation of the cantilever beam in all three Cartesian coordinate directions
Δ_k	total displacement of a body in the direction *k*
$\Delta_x(t)$	time dependent in-plane displacement of folded spring
$\Delta_{Bx,y,z}$	total displacement at point *B* of the folded spring in all three Cartesian directions
$\Delta_{Cx,y,z}$	total displacement at point *C* of the folded spring in all three Cartesian directions

$\Delta_{Dx,y,z}$	total displacement at point D of the folded spring in all three Cartesian directions
$\Delta\theta_n$	finite phase difference imposed between sequential frames
Ω	fringe-locus function
$\boldsymbol{\Omega}$	angular velocity
dy/dx	slope of a section of the folded spring
$\partial(\ )/\partial(\ )$	partial derivative

1. OBJECTIVES

The objectives of this thesis were to model folded springs supporting proof masses of a MEMS gyroscope and to develop a preliminary set of parameters characterizing these springs in as-fabricated-state, using the state of the art developments in the field of ACES methodology. The ACES methodology combines analytical, computational, and experimental solutions to obtain results in cases where they will be impossible or, at best, difficult to obtain using any one of the solutions alone.

2. INTRODUCTION

This chapter presents general background information on MEMS technology and devices. Then a discussion of MEMS fabrication processes is provided. Next, inertial sensors are introduced, and then how conventional and MEMS gyroscopes operate is explained.

2.1. MEMS background

Microelectromechanical systems (MEMS) technology is a revolutionary enabling technology (ET), which is based on manufacturing processes that have their roots in photolithographic processing used in microelectronics for fabrication of integrated circuits (ICs) (Pryputniewicz, 1999, 2001). Today, MEMS defines both the methodologies to make the microelectromechanical systems and the systems themselves (Pryputniewicz, et al., 2003). MEMS combine mechanical and electrical components into single devices (Gad-el-Hak, 2002). MEMS fabrication is based on the capability of making controllable mechanical structures that are moveable, and the required electronic components out of silicon and its derivatives using modified IC fabrication techniques. The first MEMS device was made by R. T. Howe in 1982 (Muller, 2000). He demonstrated a technique of how to fabricate microbeams from polycrystalline silicon films; using this technique, a prototype of the first fully integrated MEMS, where both the mechanical and electrical components were fabricated on the same substrate, a

28

chemical vapor sensor, was built (Muller, 2000). This development provided a basis for more research that became the broad field of MEMS.

MEMS components are currently replacing conventionally designed and built devices because of their small size, relatively low cost, and relatively high performance. The small size of the MEMS devices is a plus because it saves space, allowing the "real estate" to be used more efficiently, and this saves money. Individual MEMS components are expensive to fabricate; however, due to the fact that MEMS devices are batch fabricated, where hundreds or thousands are produced at the same time, the cost goes down, making the devices less expensive than conventionally fabricated devices (Pryputniewicz and Furlong, 2002).

Currently there are several different types of MEMS available: accelerometers, gyroscopes, pressure, temperature, and humidity sensors, micromirrors, micro-heat exchangers, microfluidics, micropumps, etc. These MEMS devices are being used for many different applications such as airbag deployment, keyless entry systems, high definition optical displays, scanning electron microscope tips, various medical and biological applications, diode lasers, miniature gas chromatographs, high-frequency fluidic control systems, printing systems, and electronic cooling systems (Gad-el-Hak, 2002; Pryputniewicz and Furlong, 2002; Bryzek, 1996). Figure 2.1 (Madou, 1997) illustrates where MEMS are being used in automobiles: drive train/torque sensors, engine timing/position sensors, antilock brakes/acceleration sensors, engine management systems (EMS)/mass airflow sensors, temperature sensors, transmission sensors, air conditioning/humidity and sun/light sensors, automatic headlight control sensors, airbag

deployment sensors, seat control/load/force sensors, emission control/oxygen sensors, and active suspension/speed and pressure sensors.
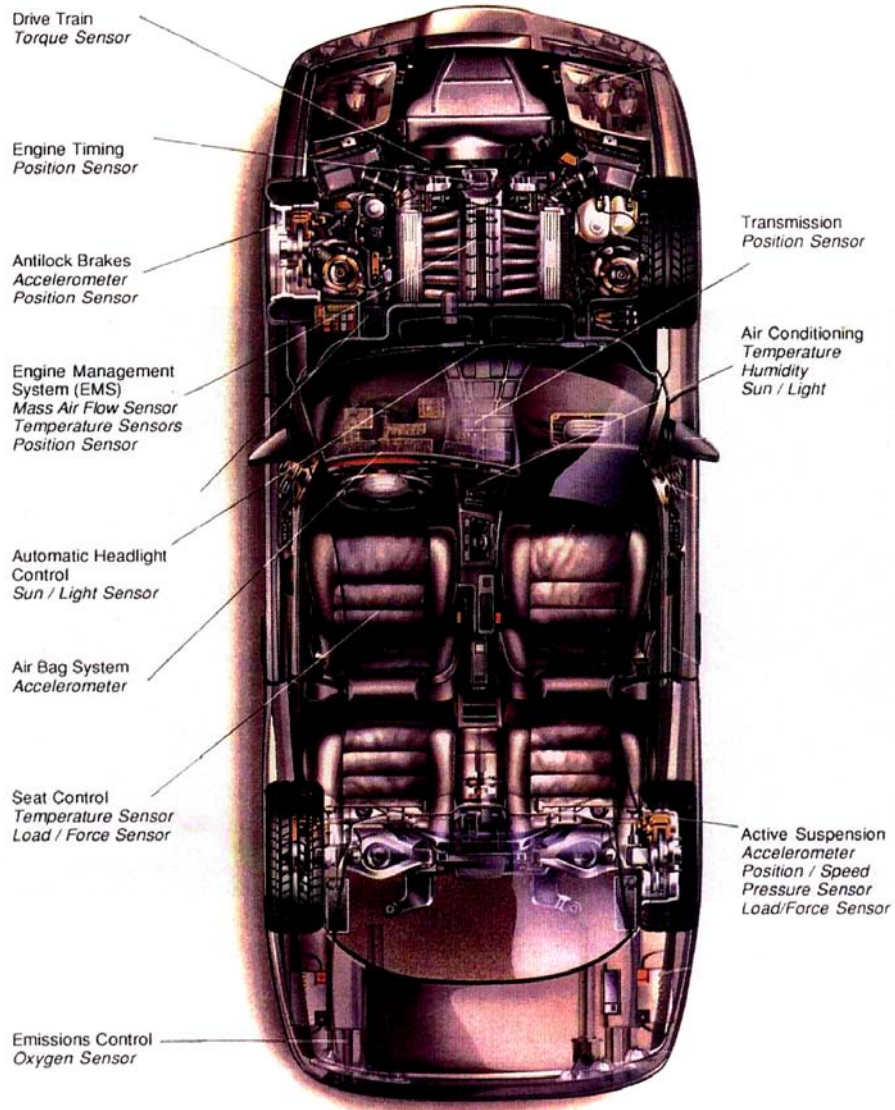
Fig. 2.1. Possible MEMS sensor applications in automobiles (Madou, 1997).

2.2. MEMS fabrication

The earliest methods used to manufacture silicon structures such as MEMS devices made use of lithography and etch technology. Chemical etching removes an unwanted section from the silicon structure. When chemical etching and etch-stopping techniques, such as a masking film, are used together inventively, complex structures can be produced. In 1982 when Howe made his microbeams, he used the now common technique of etching an underlying sacrificial layer. The sacrificial layer has an increased level of phosphorus to enhance the etch rate in hydrofluoric acid (Muller, 2000). Current methods for the fabrication of MEMS devices include: surface micromachining, bulk micromachining, as well as lithography, (Pryputniewicz and Furlong, 2002). Most MEMS devices available currently are produced using either bulk or surface micromachining techniques.

2.2.1. Bulk micromachining

The first appearance of using chemicals to etch a substrate protected otherwise by a mask was in the fifteenth century when acid and wax was used to etch and decorate armor; by the 1600's chemical etching for the decoration of armor and weapons was common practice (Harris, 1976). In 1822 photosensitive masks were introduced as lithography by Niépce and increased the tolerances of the etching to a new level (Madou, 1997). Bulk micromanufacturing, or micromachining, as it is known today, was developed from technology that was first used in the 1960s for microelectronic

applications, but this technology was improved upon and in the 1970s was being

implemented to produce three-dimensional microstructures. Bulk micromachining

(BMM) is used for the production of microsensors and accelerometers; this technique

removes material from a substrate, usually silicon, silicon carbide, gallium arsenide, or

quartz, using a type of etching, either dry or wet, to produce desired three-dimensional

structures (Hsu, 2002), typically for MEMS applications out of silicon. Figure 2.2

illustrates an example of a wet bulk micromachining process.
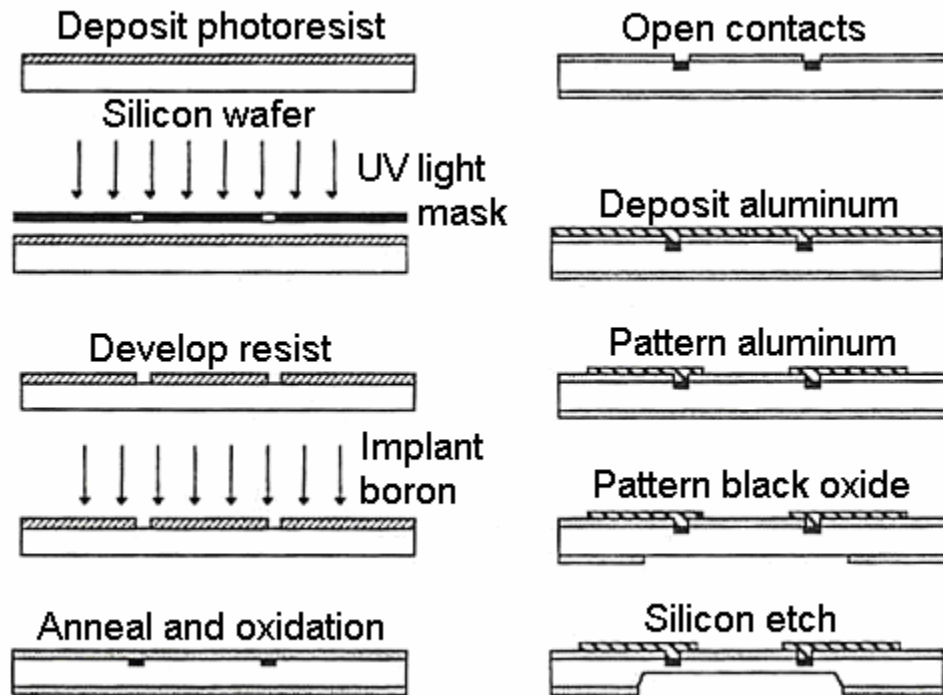
Fig. 2.2. Steps in the bulk micromachining process (Madou, 1997).

Bulk micromachining can also be done using dry etchants; however, wet chemical

etching is traditionally faster, than dry etching processes, having rates of about 1

µm/minute and allows the operator to select specific materials to etch preferentially. Wet

etchants that are used for isotropic etching, where the rate of material removal is the same

in all crystallographic directions, are usually acids: Piranha (4:1, H_2O_2:H_4SO_4), buffered

HF (5:1, NH_4F:conc.HF), and HNA (HF/HNO_3/ CH_3COOH). Anisotropic etchants,

which etch in one crystallographic direction faster than in the other directions, are used

for machining of microcomponents; there are many different types of chemicals that are

used as anisotropic etchants: alkaline aqueous solutions such as KOH, NaOH, LiOH,

CsOH, NH_4OH, quaternary ammonium hydroxides, and alkaline organics like

ethylenediamine, chlorine (trimethyl-2-hydroxyethyl ammonium hydroxide), and

hydrazine with pyrocathechol or pyrazine (Madou, 1997).

2.2.2. Surface micromachining

The first example of surface micromachining for an electromechanical purpose

occurred in 1967 when Nathanson made an underetched metal cantilever beam for a

resonant gate transistor (Nathanson, et al., 1967). By the 1970's plans were being

developed for a metal magnetically actuated microengine; however, there were fatigue

problems with metals, and due to the fatigue problem metals are rarely used as structural

members in micromachining (Madau, 1997). The present state of the micromachining

method was introduced in the 1980's by Howe and Muller (1982) where polysilicon was

introduced as the primary material for the structural layers.

Surface micromachining (SMM) builds structures by patterning thin multiple layers deposited on a substrate (Pryputniewicz and Furlong, 2002). This produces finished product using batch fabrication where no assembly is required. SMM is usually based on low pressure chemical vapor deposition (LPCVD) of the structural, e.g., polysilicon, sacrificial, e.g., silicon dioxide, and photoresistive layers onto the substrate (Hsu, 2002). These layers are then patterned using dry etching to make in-plane features, and wet etching removes the sacrificial layers used to support the structures during deposition (Madou, 1997).

The most advanced of the SMM methodologies available today is the Sandia's *U*ltra-planar *M*EMS *M*ulti-level *T*echnology (SUMMiT™) that allows fabrication of structures out of up to five structural layers, while other methodologies allow fabrication of structures comprising of up to three structural layers (Pryputniewicz, 2002). The film stack used in the SUMMiT™ process is illustrated in Fig. 2.3 (Rogers and Sniegowski, 1998; Sniegowski and Rogers, 1998). Individuals who want to make use of Sandia's micromachining capabilities can utilize the SUMMiT™-V software that allows design of MEMS using a component library, Fig. 2.4 (Pryputniewicz and Furlong, 2003; Pryputniewicz, et al., 2003).

An example from the component library of the SUMMiT[TM]-V software is the anchor hinge; the top view of the hinge, which shows the layers necessary to build up the anchor using the SUMMiT[TM] process, is shown in Fig. 2.5. If a cross section of the hinge anchor were taken along the line A-A shown in Fig. 2.5, the two-dimensional representation of the multi-layer structure of the hinge would be as shown in Fig. 2.6.
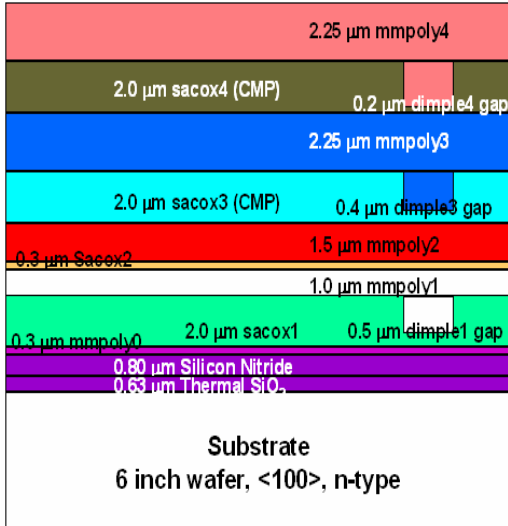
Fig. 2.3. Film stack of the SUMMiT^{TM}
process.
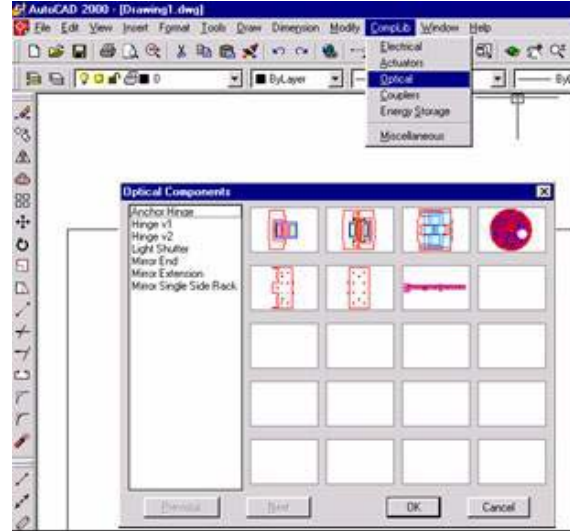
Fig. 2.4. Optical components library of the
SUMMiT^{TM} design tools.
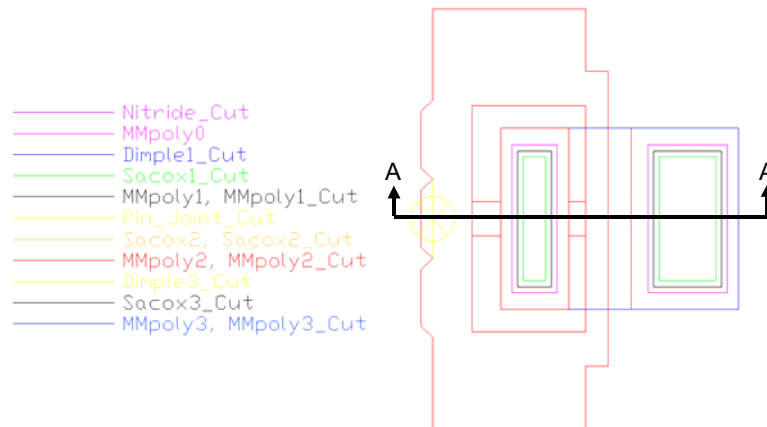
Fig. 2.5. SUMMiT^{TM} representation of the anchor hinge as selected
from the component library (Pryputniewicz and Furlong, 2003).

Fig. 2.6. 2D representation of the cross section of the anchor hinge
along line A-A (Pryputniewicz and Furlong, 2003).

As illustrated in Fig. 2.6, the SMM process produces movable parts such as mechanical

pin joints, springs, gears, cranks, and sliders, along with enclosed cavities, and many

other configurations (Madou, 1997; Pryputniewicz, 2002; Pryputniewicz and Furlong,

2003). These individual components can then be combined to produce complex

mechanical systems.

2.3. Inertial sensors

The largest market for inertial sensors is the automotive industry; inertial sensors

are used in the antilock brakes, traction control, airbag deployment, stability control, and

safety control systems of a car. There are also many applications outside the automotive

world; they include virtual reality, smart toys, industrial motion control, hard drive head

protection systems, image stabilization, GPS receivers, and inertial navigational systems

(Hsu, 2002).

There are two basic inertial MEMS sensors: the MEMS accelerometer that

measures linear acceleration, and the microgyroscope which measures rotational

accelerations (Hanson, et al., 2001). These inertial sensors can measure accelerations

about a single axis or about multiple axes. Examples of a single axis MEMS

accelerometer and gyroscope are illustrated in Figs 2.7 and 2.8, respectively. The

accelerometer in Fig. 2.7 measures forces defined by Newton's second law caused by a

linear acceleration. The tuning fork configuration microgyroscope, illustrated in Fig. 2.8,

measures angular acceleration due to the Coriolis forces acting on the vibrating masses; this will be discussed in more detail in Section 2.3.2.
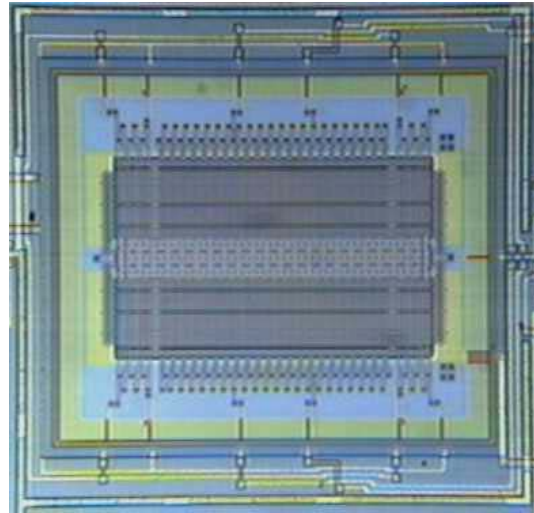
Fig. 2.7. An example of a single axis accelerometer, ADXL190 (Steward and Saggal, 2002).
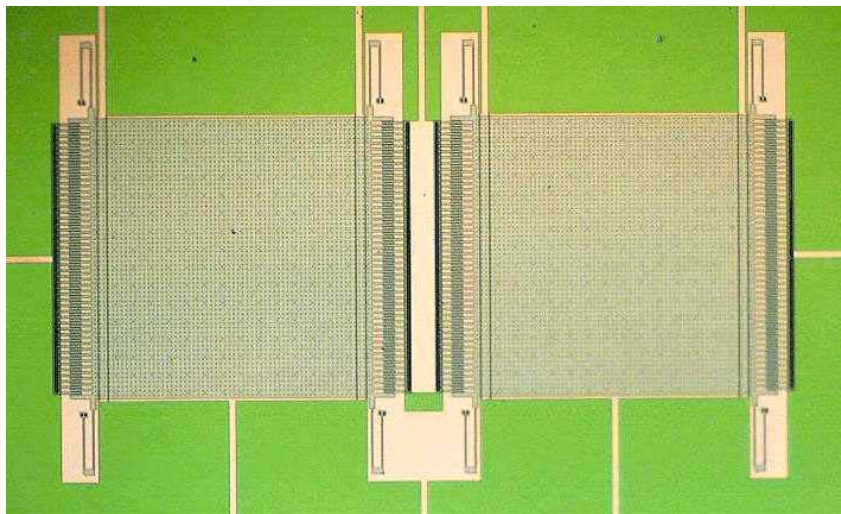
Fig. 2.8. A dual mass tuning fork microgyroscope.

Inertial sensors are made up of a combination of parts: proof masses, elastic springs, dampers, actuators, and a method for measuring displacements of the proof masses. The purpose of the elastic springs is to provide the proof masses with support and to return the masses back to their original positions after linear acceleration, or rotation, has stopped. The dashpot provides the damping for the system; this is usually done one of two ways: thin film and shear damping. Thin film damping is achieved by using a thin gas film between two vibrating plates; through compression and friction, the film disperses the excess energy, thus adding damping to the system (Przekwas, et al., 2001). In other systems that have plates vibrating parallel to one another the film produces shear forces that dissipate energy; this type of damping is known as shear.

There are several methods for determining displacements of the proof masses that are used in inertial sensors. They are: piezoresistive, resonant frequency modulation, capacitive, floating-gate field-effect transistor (FET), strain FET, and tunneling-based. Piezoresistive sensing is used for inertial sensors that make use of single crystals or that are micromachined in bulk quantities. The resonant frequency modulation method of sensing is used mostly for inertial sensors with very high sensitivities. The capacitive sensing method is most commonly used for industrial purposes due to its relative insensitivity to temperature. The floating-gate FET method of sensing is used to measure inertial forces, while the strain FET method measures strains in the packages of the inertial sensors. Both methods have proven difficult to implement in industry. The electron tunneling method is used when displacement must be measured accurately; this method however is still in developmental stages (Bergstrom and Li, 2002).

Principles of operation of conventional gyroscopes are presented in Section 2.3.1, while operation and examples of MEMS gyroscopes are discussed in Section 2.3.2. This thesis focuses on the MEMS vibrating gyroscope shown in Fig. 2.8.

2.3.1. Conventional gyroscopes

In 1852 Jean Bernard León Foucault named a wheel, or rotor, mounted in gimbal rings that allow the wheel to rotate freely in any direction, a gyroscope; almost any rotating mass can be considered as a gyroscope (Cordeiro, 1913). The word gyroscope comes from the Greek words *gyros* and *skopein* that mean "rotation" and "to view," respectively. Conventional spinning gyroscopes function due to Newton's 2nd law which states that angular momentum, **H**, of an object will remain the same unless a torque, **T**, is applied to that object; then, the rate of change of the angular momentum is equal to the magnitude of the torque, which can be expressed as

$$\mathbf{T} = \frac{d\mathbf{H}}{dt} \quad , \tag{2.1}$$

where

$$\mathbf{H} = I\boldsymbol{\omega} \tag{2.2}$$

with I being the moment of inertia of the object and $\boldsymbol{\omega}$ being the angular velocity. The law of gyroscopics states that if the torque is applied perpendicular to the rotating axis of a spinning object the magnitude of the angular velocity cannot change, but the direction of $\boldsymbol{\omega}$ can change. This is illustrated in Fig. 2.9 and can be obtained by defining

$$dH = Hd\theta \quad , \tag{2.3}$$

where $d\theta$ is the angle that the rotating object moves due to the applied torque. Then, substitution of Eq. 2.3 into Eq. 2.1 yields

$$T = \frac{d\mathbf{H}}{dt} = \mathbf{H}\frac{d\theta}{dt} = \mathbf{H} \times \mathbf{\Omega} \quad , \tag{2.4}$$

where $\mathbf{\Omega}$ is the precession rate, or the angular velocity of the wheel perpendicular to the plane defined by the axis of rotation and the direction of the input torque of the rotating object, as shown in Fig. 2.9. In Fig. 2.9 ω is the speed of the rotation about the spin axis, while Ω, the precession rate, is the speed of the rotation perpendicular to the spin axis.
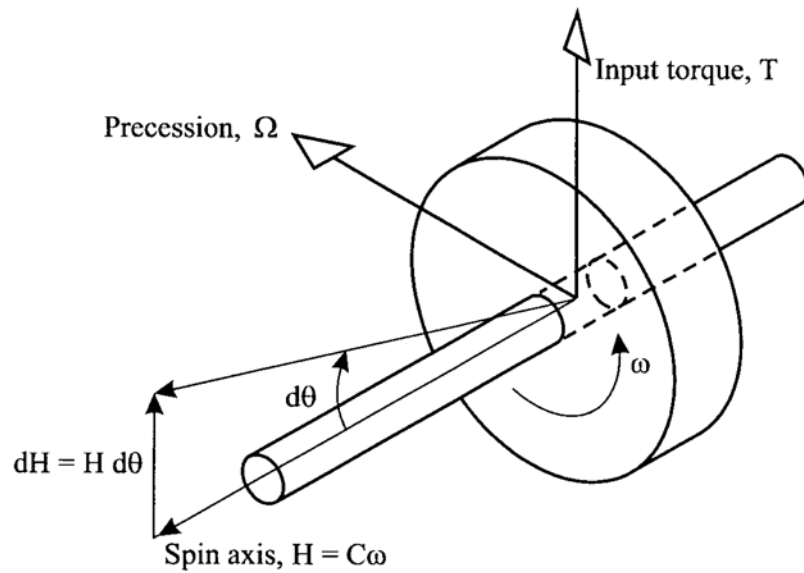
Fig. 2.9. Illustration of the law of gyroscopics (Lawrence, 1998).

In the past, the name of "gyroscope" was reserved only for rotational sensors with spinning wheels, like the toy gyroscope that is illustrated in Fig. 2.10; presently, however, gyroscope refers to any instrument that measures rotation (Lawrence, 1998).

Fig. 2.10. Tedco "original" toy gyroscope (Gyroscopes Online, 2003).

The MEMS gyroscope, also known as microgyroscope, examined in this thesis, is a planar micromachined tuning fork gyroscope. However, before it can be discussed, the macroscale tuning fork gyroscope has to be considered, Fig. 2.11. A tuning fork configuration is a balanced system due to having two tines vibrating in anti-phase. Therefore, at the mount/junction of the two tines, there is no residual motion that could contribute to measurement errors (Lawrence, 1998).
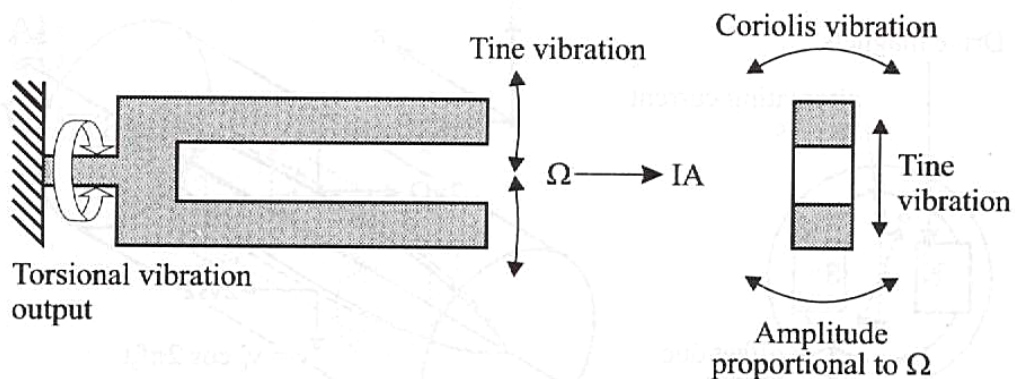
Fig. 2.11. A tuning fork gyroscope (Lawrence, 1998).

A tuning fork gyroscope is governed by the Coriolis acceleration. Coriolis acceleration was defined by Gaspard de Coriolis in 1835 as the acceleration that acts on an object that is rotating about and moving radially toward/away from a fixed point with constant angular $\boldsymbol{\omega}$, and radial, $\mathbf{v}$, velocities, respectively (Lawrence, 1998). Centrifugal acceleration and Coriolis acceleration are defined as

$$\textbf{CentrifugalAcceleration} = -\omega^2 \mathbf{r} \tag{2.5}$$

and

$$\textbf{CoriolisAcceleration} = -2(\mathbf{v} \times \boldsymbol{\Omega}) = 2(\dot{\mathbf{r}} \times \boldsymbol{\Omega}) \quad , \tag{2.6}$$

where $\mathbf{r}$ is the radial position, $\boldsymbol{\omega}$ is the angular velocity, and $\mathbf{v}$ is the linear velocity, the time rate of change of the radial position (Hibbler, 1998). If the tuning fork is rotated about its axis as the tines vibrate in their plane with a sinusoidally varying angular momentum, as shown in Fig. 2.11, the Coriolis acceleration will induce a sinusoidally varying precession about the axis of the tuning fork that will be proportional to the input rate (Lawrence, 1998); this will allow the angular acceleration to be measured.

2.3.2. MEMS gyroscopes

The majority of MEMS gyroscopes have vibrating rather than rotating configurations. Figure 2.12 shows an example of typical suspension configuration for a MEMS tuning fork gyroscope: this microgyro has straight flexural members that act as springs and support the proof masses. The microgyroscope examined for this thesis is shown in Fig. 2.8, instead of the straight flexural members shown in Fig. 2.12, the Sandia

42

microgyro has folded springs; however operation of the two microgyro designs is very

similar. Figure 2.13 illustrates operation of the dual proof mass tuning fork

microgyroscope shown in Fig. 2.12. As illustrated in Fig. 2.13, the two proof masses are

driven in anti-phase by the electrostatic combdrives. Each proof mass is actuated by two

sets of combdrives: one outside and one inside, operating one at a time. The outside

combdrives are at the extreme ends of the dual mass microgyro, i.e., at the extreme left

and right edges of the configuration shown in Figs 2.8, 2.12, and 2.13. The inside

combdrives are between the two proof masses. The combdrives produce electrostatic

forces and therefore can only pull the masses; they cannot push (Pryputniewicz, 2000).

Therefore, an actuation cycle consists of four parts. During part-1, when the actuation

voltage is applied, the outside combdrives pull the proof masses toward themselves while

simultaneously the flexures supporting the proof masses deform storing elastic energy.
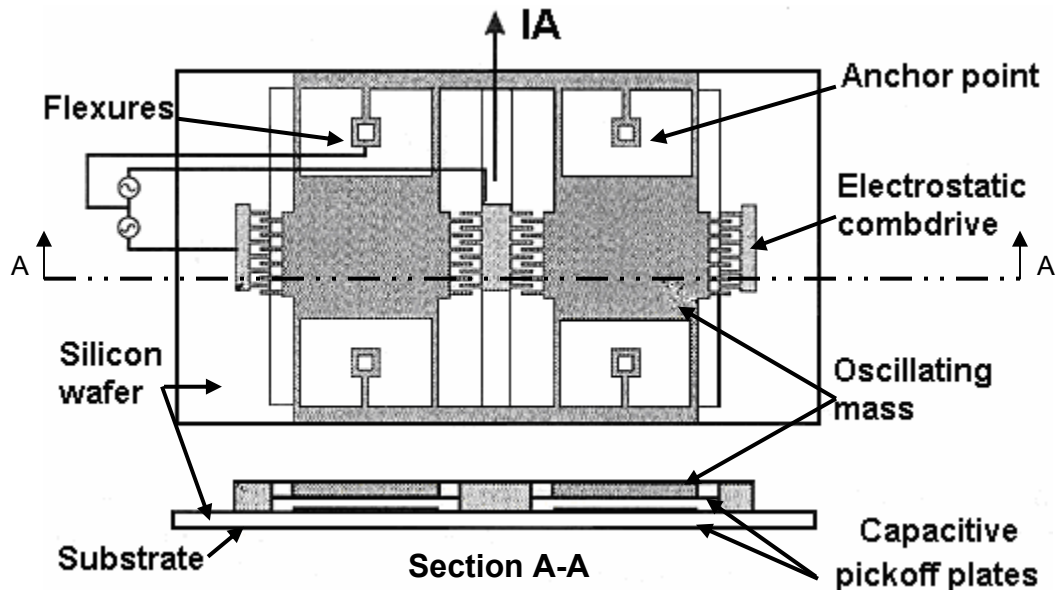
Fig. 2.12. Dual mass micromachined tuning fork microgyro (Lawrence, 1998).
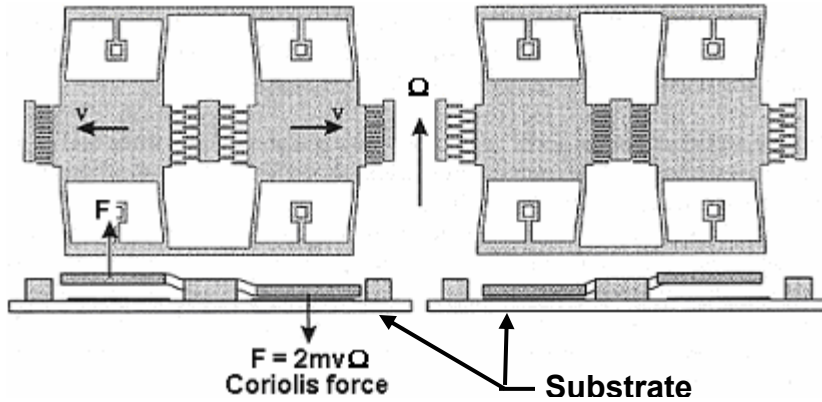
Fig. 2.13. Schemaitic of the operation of a MEMS tuning fork gyro (Lawrence, 1998).

During part-2 of the actuation cycle, when the voltage on the outside combdrives is

reduced, the flexures straighten and bring the proof masses to their original, neutral,

positions. At this point, actuation voltage is applied to the inside combdrives and the

proof masses are pulled toward the inside while the flexures deform away from their

equilibrium positions; this is part-3 of the actuation cycle. During part-4, when the

actuation voltage is reduced again, the flexures return the proof masses to their neutral

positions.

Typically, the 4-part actuation cycle is repeated a few thousand times per second.

This vibration produces the in-plane velocity, $\mathbf{v}$, necessary to define Coriolis acceleration

described by Eq. 2.6. If the vibrating proof masses are subjected to an angular velocity,

$\mathbf{\Omega}$, Fig. 2.13, around the central axis of the two proof masses, then, using Eq. 2.6, the

Coriolis force is defined as

$$\mathbf{F}_c = m \cdot CoriolisAcceleration = 2m(\mathbf{\Omega} \times \mathbf{v}) \quad , \qquad (2.7)$$

where $\mathbf{F}_c$ is the Coriolis force, and m is the mass of each of the vibrating masses. The

Coriolis force will cause one of the proof masses to raise out-of-plane away from the

44

substrate while the other proof mass drop down toward the substrate. The capacitive

plates usually located under each of the proof masses and on the substrate under the proof

masses sense the out-of-plane displacement as a change in voltage, which is then

converted to an angular acceleration.

There are a number of possibilities for other microgyro configurations. As

illustrated in Fig. 2.8, the microgyroscope proof masses are suspended using folded

springs, while the microgyro proof masses illustrated in Fig. 2.12 are supported by

straight flexural members. Another example is the microgyroscope designed by Analog

Devices, which includes additional flexural members/springs that isolate the gyroscope

from sources of in-plane vibration other than the vibration driven by the combdrives

(Analog Devices, 2003a, 2003b). Sections 2.3.2.1 and 2.3.2.2 show some of the details

of the microgyroscopes developed by Analog Devices.

2.3.2.1. ADXRS150

The Analog Devices ADXRS150 is a $\pm$ 150 deg/sec yaw rate gyroscope (Analog

Devices, 2003a). Figure 2.14 shows the overall view of the ADXRS150. A section of

Fig. 2.14, highlighted by a rectangle, contains both proof masses of the microgyro and

this is shown in Fig. 2.15. The section highlighted in Fig. 2.15 emphasizes one of the

proof masses. This proof mass is shown in Fig. 2.16. The section that is highlighted in

Fig. 2.16 is illustrated in Fig. 2.17. The section of the microgyroscope displayed in Fig.

2.17 does not show the folded springs attached to the proof masses with enough detail, therefore the area highlighted is enlarged in Fig. 2.18.
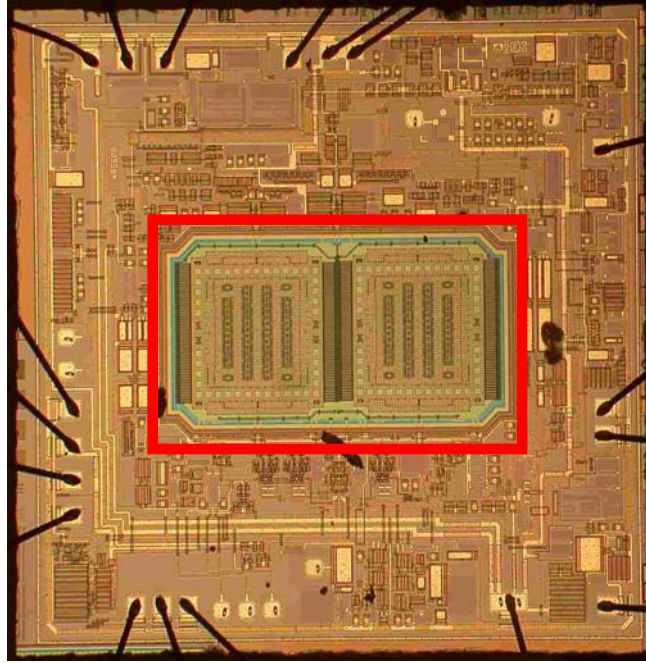
Fig. 2.14. The ADXRS150 gyroscope.
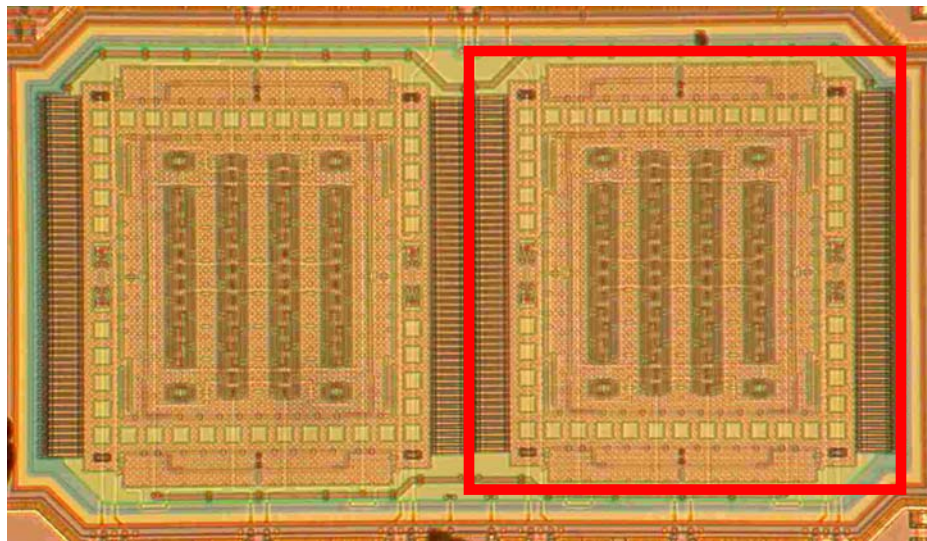
Fig. 2.15. The two proof masses of the ADXRS150 microgyro.
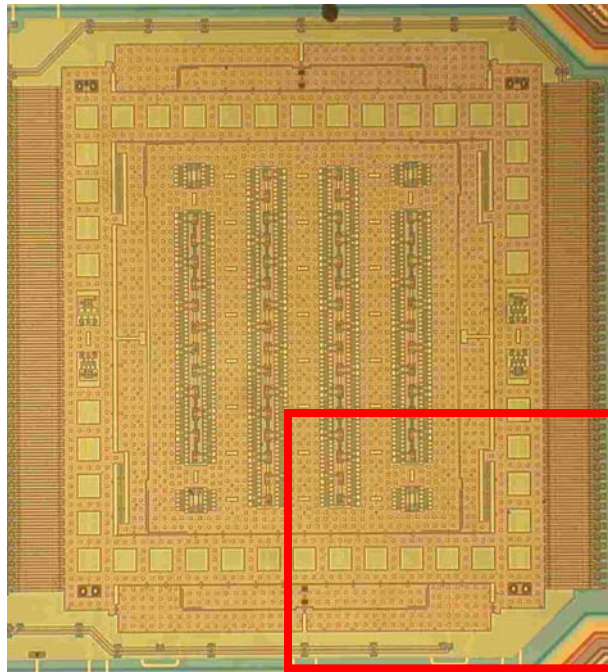
Fig. 2.16. Detail of a proof mass of the ADXRS150.
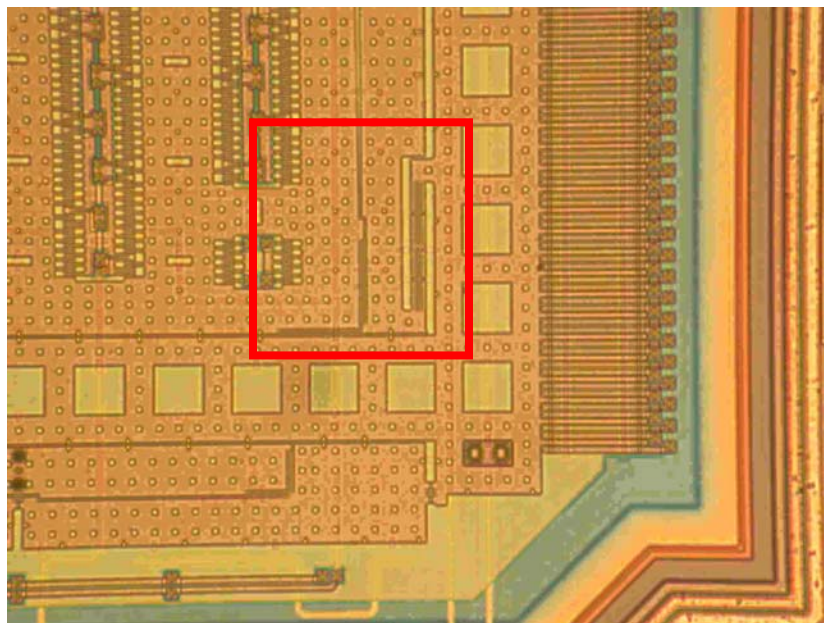
Fig. 2.17. Detail of the lower right corner of a proof mass
of the ADXRS150.
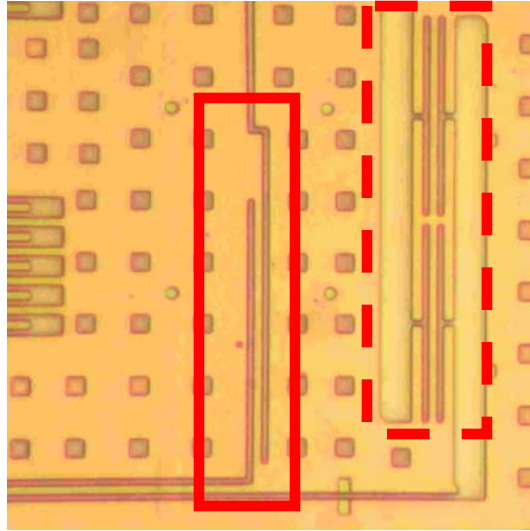
Fig. 2.18. Two spring configurations of the ADXRS150.

Figure 2.18 shows that there are two types of springs in the ADXRS150 gyroscope, and Fig. 2.19 illustrates the spring highlighted by the dashed rectangle while Fig. 2.20 shows the spring highlighted by the solid rectangle.
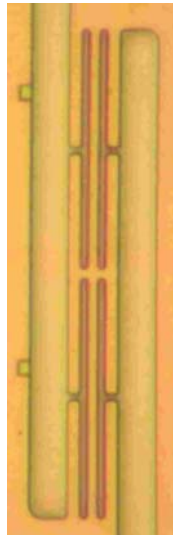
Fig. 2.19. Detail of the isolating spring for the ADXRS150 proof mass.
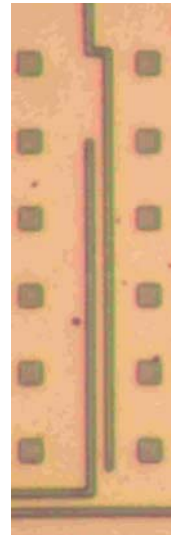
Fig. 2.20. Detail of the flexure for the ADXRS150 proof mass.

The two sets of springs illustrated in Figs 2.19 and 2.20 were designed to perform

separate tasks in the Analog Devices microgyroscope. The spring illustrated in Fig. 2.19

keeps the proof mass from "feeling" external vibrations that could introduce noise to the

vibration controlled by the electrostatic combdrives; the spring in Fig. 2.20 acts like the

flexures described in Section 2.3.2 and returns the proof mass to the neutral position

during the actuation cycle.

2.3.2.2. ADXRS300

The ADXRS300 Analog Devices microgyro is a ± 300 deg/sec yaw rate

gyroscope (Analog Devices, 2003b). The overall view of ADXRS300 is displayed in

Fig. 2.21. The section of Fig. 2.21 highlighted by rectangle is one of the proof masses of

the ADXRS300 microgyro, Fig. 2.22.
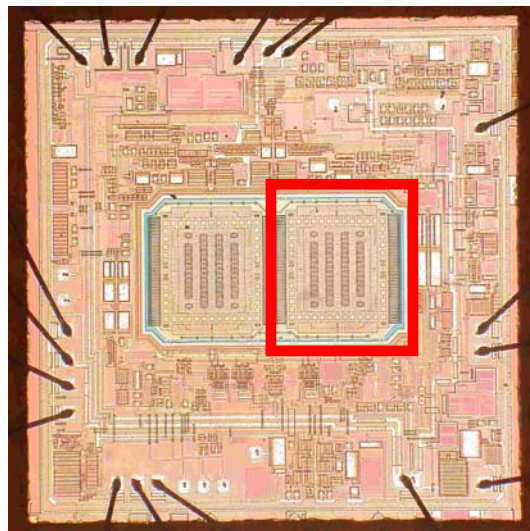
Fig. 2.21. The ADXRS300 gyroscope.
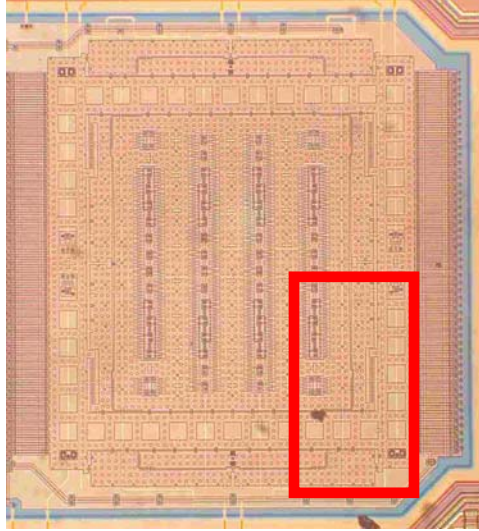
Fig. 2.22. Detail of a proof mass of the ADXRS300.

A section of Fig. 2.22, which is highlighted by a rectangle, is enlarged in Fig. 2.23 to show details of the suspension springs.
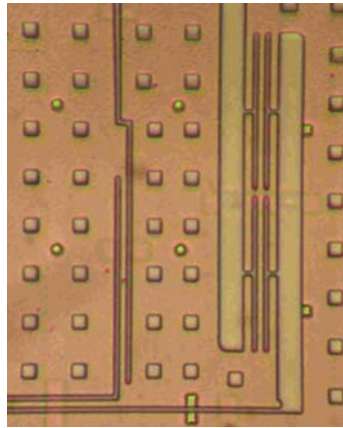
Fig. 2.23. Detail of the two springs
in a proof mass of the ADXRS300.

Figure 2.23 shows that there are the same two types of springs in ADXRS300 as in the ADXRS150. The springs in both of the microgyros have the same dimensions.

The dimensions for the flexural springs in Figs 2.21 and 2.24 are listed in Table 2.1 for

reference purposes only, because the function of these springs is similar to the springs of

the microgyro that is studied in this thesis. Dimensions shown in Table 2.1 were

measured, as a part of this thesis, using an optical microscope with the measurement

resolution characterized by the least count of 0.5 μm.

Table 2.1. Measured dimensions of the flexural spring
for the Analog Devices gyroscopes.

Dimensions of the spring	Value	Units
Length of the spring, L_{150}	60.0	μm
Width of the spring, b_{150}	2.0	μm

3. TEST SAMPLES

The test samples studied in this thesis are MEMS gyroscopes from Sandia

National Laboratories: the 10 kHz dual proof mass tuning fork microgyroscopes.

3.1. Sandia microgyroscope

A representative microgyroscope from Sandia National Laboratories that was

studied in this thesis is shown in Fig. 3.1. This figure shows the actual MEMS gyroscope

as it was observed under a microscope. This microgyroscope has two vibrating proof

masses that are driven by electrostatic combdrives, which are located on each vertical

side, for the orientation shown in Fig. 3.1, of the proof masses, and each proof mass is

supported by four folded springs, one at each corner.
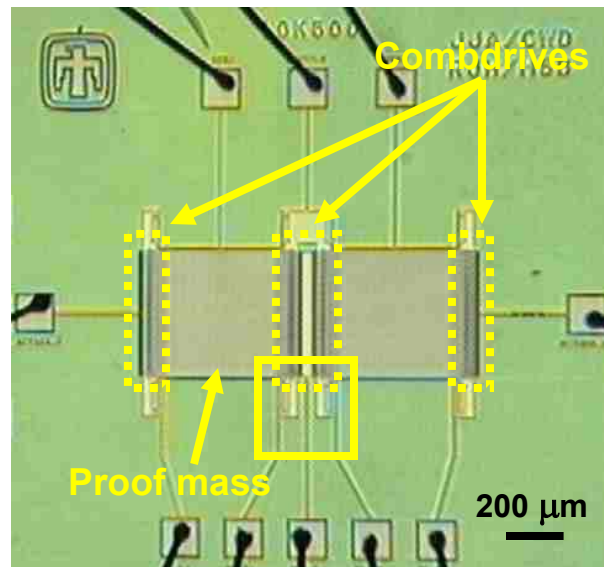
Fig. 3.1. The Sandia dual-mass microgyro.

Figure 3.2 displays a magnified view of the highlighted section shown in Fig. 3.1, and illustrates typical folded springs supporting the proof masses, parts of the combdrives actuating these masses are also shown.
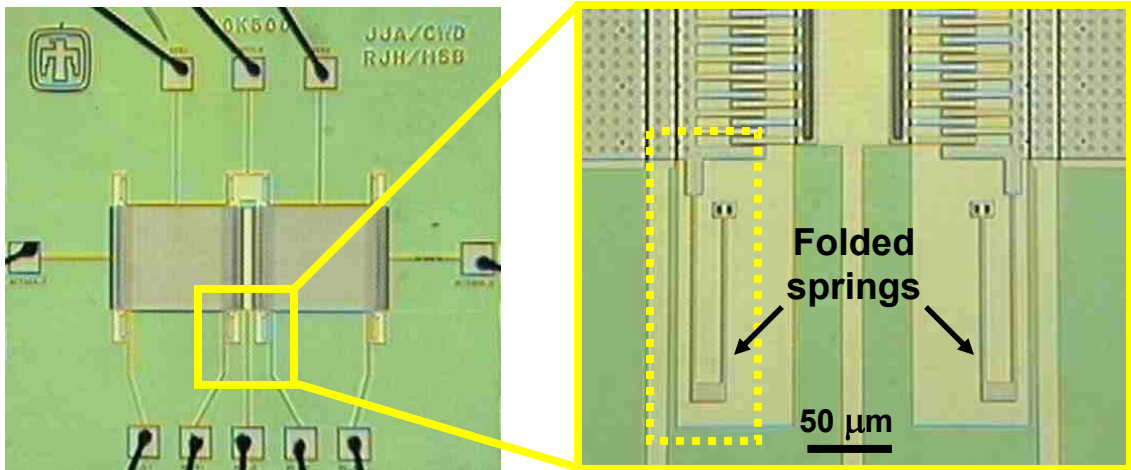
Fig. 3.2. Detail of the section of the Sandia microgyro, highlighted in Fig. 3.1, showing typical folded springs supporting proof masses, parts of the poof masses and combdrives are also shown.

One of the folded springs is highlighted in Fig. 3.2 with a rectangle. The folded spring was observed under a microscope and dimensions were measured, as a part of this thesis, the dimensions are shown in Fig. 3.3 and listed in Table 3.1. In Table 3.1, the thickness of the folded spring is based on specifications characterizing the SUMMiT^{TM}-V process (Sandia, 2003). The lengths of sections *AB* and *CD*, as defined in Fig. 3.3 and Table 3.1, were measured from points *A* and *D*, respectively, to the midpoint of the width of section *BC*. Also the length of section *BC* was measured between the midpoints of the widths of sections *AB* and *CD*. This was done to reduce the error caused by an overlap of the sections at interfaces of sections *AB* and *CD* with section *BC*.

53

As shown in Fig. 3.3, the proof mass attaches to the folded spring via an interface at point *D*. The attachment at point *D* is such that the folded spring and the proof mass are in the same plane. Furthermore, it was assumed, in order to facilitate analytical developments presented in this thesis, that there is no bending of the folded spring at the point of its attachment to the proof mass. That is, the folded spring and the proof ass at point *D* are subjected only to purely translational motion, there is no rotation. Point *A* is where the folded spring is attached to the substrate via a fixed post.
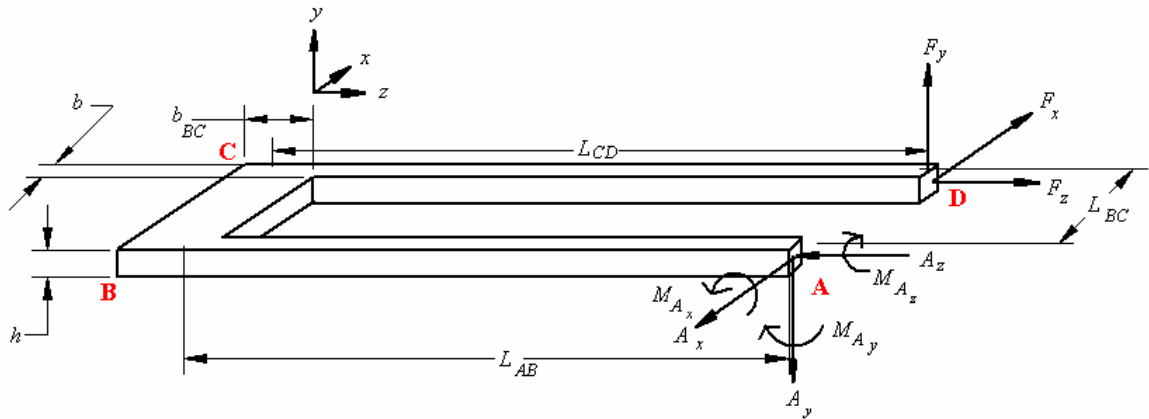
Fig. 3.3. Dimensions of a representative folded spring comprising the suspension of the proof masses in the Sandia microgyroscope.

Table 3.1. Dimensions of the Sandia microgyro.

Dimensions of the folded spring	Value	Units
Length of section *AB*, L_{AB}	111	µm
Length of section *BC*, L_{BC}	17	µm
Length of section *CD*, L_{CD}	98	µm
Width of sections *AB* and *CD*, b	3	µm
Width of section *BC*, b_{BC}	10	µm
Thickness of all of the sections, h	2.5	µm

3.2. Materials

The Sandia microgyro that was studied in this thesis is made from surface
micromachined polysilicon. The properties of this polysilicon are listed in Table 3.2 and
were obtained from descriptions of the SUMMiT[TM]-V process (Pryputniewicz, 2002;
Pryputniewicz and Furlong, 2002; Furlong and Pryputniewicz, 2001; Sandia, 2003).

Table 3.2. Material properties of polysilicon.

Property	Value	Units
Density, ρ	2.33	g/cm^3
Modulus of elasticity, E	160	GPa
Poisson's ratio, μ	0.23	

4. METHODOLOGY

Preliminary characterization of a MEMS gyroscope was done by studying deformations of the suspension that supports the proof masses. The first step was to conduct background research on how MEMS devices, in general, and microgyros, in particular, are built, how meso, or conventional gyroscopes, and microscale gyroscopes function. These background data on the past and current state-of-the-art gyroscope technology cultivated an understanding of how gyroscopes, in general, and more importantly, MEMS gyroscopes, function. This information provided a starting point to begin analysis.

Determining how MEMS gyroscopes function is based on the Analytical, Computational, and Experimental Solutions (ACES) methodology (Pryputniewicz, 1997; Pryputniewicz, et. al., 2001), Fig. 4.1.
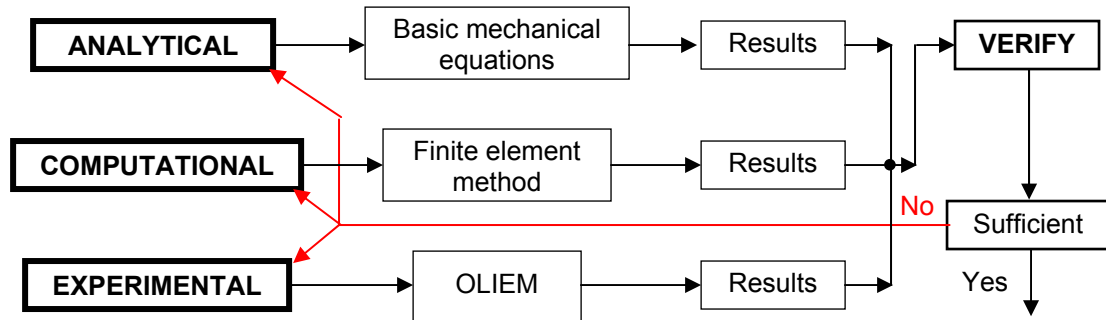
Fig. 4.1. Configuration of the ACES methodology.

As illustrated in Fig. 4.1, the ACES methodology utilized analytical, computational, and experimental methods. The results from one, or two, of these methods are used to

facilitate solutions by the remaining methods. Then computational and experimental

results are compared to determine degree of correlation between them, which is used to

verify, or validate, the process used.

Sections 4.1 to 4.3 describe analytical, computational, and experimental,

respectively, considerations used in this thesis to study the characteristics of

microgyroscopes. In order to accomplish this task, as the first step, the out of plane

displacement of the folded springs that support each of the proof masses, were

determined using a static analysis. This was done analytically by deriving the three-

dimensional equations for the deformations of the folded springs. This derivation was

based on energy methods and Castigliano's second theorem in order to include shear

effects. For the equations that were derived to be useful, forces that are applied to the

folded spring must be known. Thus, all forces acting on the proof mass, that the folded

springs support, must be taken into consideration: i.e., the forces produced by

acceleration of the proof mass by the combdrives and the Coriolis forces produced by the

angular acceleration that the microgyro may be subjected to.

Once the forces that act on the folded springs were determined they were used in

analytical equations to calculate deformations. Then the deformations were also

computed using finite element method (FEM), through the FEM software package

COSMOS/M (2003).

Once the analytical and computational results have been determined, the

experimental analysis began by characterizing deformations of the folded springs, using

the optoelectronic laser interferometric microscope (OELIM) method (Furlong and

Pryputniewicz, 2000, 2002; Pryputniewicz, et al., 2000, 2001; Steward and Saggal, 2002; Steward, et al., 2002, 2003a, 2003b; Steward, 2003). The next step was to observe the out-of-plane behavior of the folded springs under selected excitation frequencies induced by a PZT shaker and measured using the laser vibrometer.

The experimental results were then compared to the analytical and computational results in order to determine validity of the computational modeling and analytical methodology.

4.1. Analytical considerations

The goal of the analytical section of the thesis is to derive an equation for deformations of the folded spring in all three-dimensions along the entire length of the spring. Based on the assumption that the folded spring is a prismatic beam, with the same thickness as the proof mass, deformations of the folded spring were determined using Castigliano's second theorem.

4.1.1. Castigliano's second theorem

Castigliano's second theorem was presented in 1973 (Riley, et al., 1995) and published in 1979 by Alberto Castigliano, an Italian railroad engineer. This theorem defines a way to calculate the slope and displacement at a point in a body with respect to the strain energy stored in it (Hibbler, 2000). Castigliano's second theorem is only

applicable to objects that are made from materials that behave linear elastically and are held at a constant temperature (Riley, et al., 1995). As such, it is applicable to the developments of this thesis, because the folded springs of the microgyros considered satisfy these requirements.

According to Castigliano's theorem, if a body is subjected to external forces, Fig. 4.2, then the external work, $\mathbf{W_e}$, a function of the external loads, is equal to the internal strain energy of the body, $\mathbf{U_i}$, which can be expressed by the following phenomenological equation:

$$\mathbf{U_i} = \mathbf{W_e} = \mathbf{W_e}(\mathbf{F_1}, \mathbf{F_2}, \mathbf{F_3}, \ldots, \mathbf{F_n}) \quad , \tag{4.1}$$

where $\mathbf{F_1}$, $\mathbf{F_2}$, …, $\mathbf{F_n}$ represent the external forces. If one of these forces is increased by an infinitesimal amount, $d\mathbf{F_k}$, the work will also increase by a corresponding infinitesimal amount. Therefore, the strain energy will become

$$\mathbf{U_i} + d\mathbf{U_k} = \mathbf{U_i} + \frac{\partial \mathbf{U_i}}{\partial \mathbf{F_k}} d\mathbf{F_k} \quad . \tag{4.2}$$
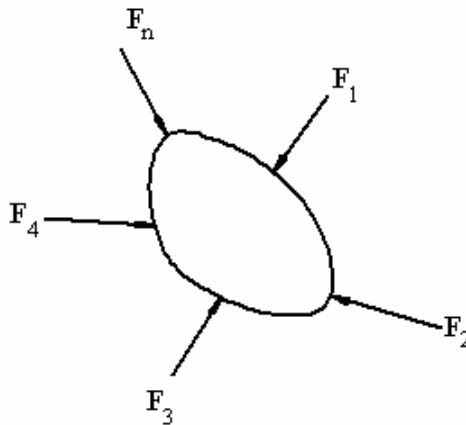
Fig. 4.2. Body subjected to a number of external forces.

However, Eq. 4.2 depends on the order that the forces are applied to the body. In order to make Eq. 4.2 independent of the order that the forces are applied, Δ_k is introduced as the total displacement of the body due to all of the forces $\mathbf{F}_1$, $\mathbf{F}_2$, …, $\mathbf{F}_n$ in the direction of $\mathbf{F}_k$, and the infinitesimal increase in the strain energy is defined as

$$d\mathbf{U}_k = d\mathbf{F}_k \Delta_k \qquad , \tag{4.3}$$

due to the change in forces. Now, substituting the definition of $d\mathbf{U}_k$ from Eq. 4.3 into Eq. 4.2, it can be written that (Hibbler, 2000)

$$d\mathbf{F}_k \Delta_k = \frac{\partial \mathbf{U}_i}{\partial \mathbf{F}_k} d\mathbf{F}_k \qquad , \tag{4.4}$$

where

$$\Delta_k = \frac{\partial \mathbf{U}_i}{\partial \mathbf{F}_k} \qquad . \tag{4.5}$$

4.1.2. Internal strain energies

Equation 4.5 will be used to solve for the displacements of the folded springs that support the proof masses of the microgyroscopes; however, in order to use Eq. 4.5, the internal strain energies have to be defined for a spring. The internal strain energy of a spring is calculated as the sum of the individual strain energies, i.e.,

$$\mathbf{U}_i = \mathbf{U}_{AL} + \mathbf{U}_{BM} + \mathbf{U}_{TS} + \mathbf{U}_{TM} \qquad , \tag{4.6}$$

where $\mathbf{U}_{AL}$, $\mathbf{U}_{BM}$, $\mathbf{U}_{TS}$, and $\mathbf{U}_{TM}$ are as defined in Eq. 4.7 to 4.10, respectively.

The strain energy component defined by the axial loading acting through the length of the beam L, $\mathbf{U}_{AL}$, is calculated as

$$\mathbf{U}_{AL} = \int_0^L \frac{\mathbf{N}^2}{2AE} dx \quad , \tag{4.7}$$

where $\mathbf{N}$ is the axial load, A is the cross sectional area, E is the modulus of elasticity, and L is the length of the beam.

The strain energy component defined by the bending moment over L, $\mathbf{U}_{BM}$, is calculated as

$$\mathbf{U}_{BM} = \int_0^L \frac{\mathbf{M}^2}{2EI} dx \quad , \tag{4.8}$$

where $\mathbf{M}$ is the internal bending moment.

The transverse shear loading component of the strain energy along L, $\mathbf{U}_{TS}$, is defined as

$$\mathbf{U}_{TS} = \int_0^L \frac{k_{y,z} \cdot \mathbf{V}^2}{2GA} dx \quad , \tag{4.9}$$

where $k_{y,z}$ is the shape factor, which is defined for multiple cross sections in Table 4.1, $\mathbf{V}$ is the shear force, and G is the shear modulus.

Table 4.1. Shape factor values when y and z are the centroidal principle axes of the cross section (Cook and Young, 1985).

Cross section type	k_y	k_z
Rectangle	1.20	1.20
Solid circle	1.11	1.11
Thin-walled cylinder	2.00	2.00
I-section, web parallel to z-axis	1.20	1.00
Closed thin-walled section	1.00	1.00

The final component of the strain energy is due to the torsional moment acting

through the length of the beam L, $\mathbf{U}_{TM}$, and it is calculated as

$$\mathbf{U}_{TM} = \int_0^L \frac{\mathbf{T}^2}{2GJ} dx \quad , \tag{4.10}$$

where $\mathbf{T}$ is the torque acting through the length of the beam, while J is the polar moment

of inertia of the cross sectional area of the spring and is calculated (Riley, et al., 1995) as

$$J = \int_A x^2 dA + \int_A y^2 dA \quad . \tag{4.11}$$

4.1.3. Energy analysis of the single fold spring

For the folded spring that is illustrated in Fig. 4.3, application of Castigliano's

theorem has to be modified since the folded spring can be divided into three beams, or

sections that will be called *AB*, *BC*, and *CD*, as labeled in Fig. 4.3. Therefore, the

equation for the internal strain energy of the folded spring will be a sum of the strain

energies of all three sections, i.e.,

$$\mathbf{U}_i = \mathbf{U}_{AB} + \mathbf{U}_{BC} + \mathbf{U}_{CD} \quad , \tag{4.12}$$

where the strain energies of the individual sections are defined as

$$\mathbf{U}_{AB} = \mathbf{U}_{ALAB} + \mathbf{U}_{BMAB} + \mathbf{U}_{TSAB} + \mathbf{U}_{TMAB} \quad , \tag{4.13}$$

$$\mathbf{U}_{BC} = \mathbf{U}_{ALBC} + \mathbf{U}_{BMBC} + \mathbf{U}_{TSBC} + \mathbf{U}_{TMBC} \quad , \tag{4.14}$$

and

$$\mathbf{U}_{CD} = \mathbf{U}_{ALCD} + \mathbf{U}_{BMCD} + \mathbf{U}_{TSCD} + \mathbf{U}_{TMCD} \quad , \tag{4.15}$$

respectively.

4.1.3.1. Reaction forces and moments

In order to calculate the internal strain energies, and then the displacements using Eq. 4.5, the reaction forces and moments of the folded spring at point A, Fig. 4.3, have to be determined, based on which the forces, moments, and torques acting on each of the three sections: AB, BC, and CD, can be derived.
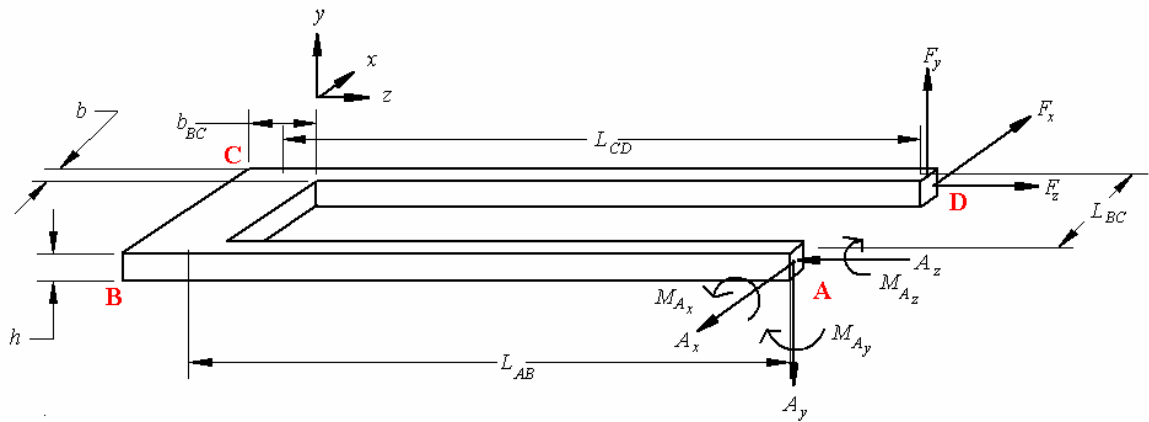
Fig. 4.3. Free body diagram for the folded spring.

Based on Fig. 4.3 and on the free body diagram of section AB of the folded spring, Fig. 4.4, Cartesian components of the reaction force at A can be defined as

$$A_x = F_x \quad , \tag{4.16}$$

$$A_y = F_y \quad , \tag{4.17}$$

and

$$A_z = F_z \quad , \tag{4.18}$$

while components of the reaction moment can be shown to be

$$M_{Ax} = F_y\left(L_{AB} - L_{CD}\right) \quad , \tag{4.19}$$

$$M_{Ay} = F_x\left(L_{CD} - L_{AB}\right) - F_z L_{BC} \quad , \tag{4.20}$$

and

$$M_{Az} = F_y L_{BC} \quad . \tag{4.21}$$
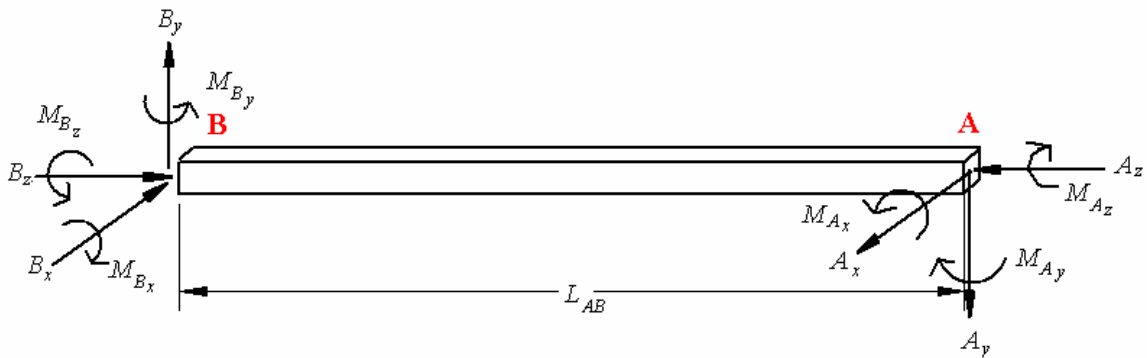
Fig. 4.4. Free body diagram of section AB.

Using the reaction forces and moments at point A, as defined by Eqs 4.16 to 4.21, the

forces and moments at point B for section AB, Fig. 4.4, were derived to be

$$B_x = A_x = F_x \quad , \tag{4.22}$$

$$B_y = A_y = F_y \quad , \tag{4.23}$$

$$B_z = A_z = F_z \quad , \tag{4.24}$$

$$M_{Bx} = -F_y L_{CD} \quad , \tag{4.25}$$

$$M_{By} = F_x L_{CD} - F_z L_{BC} \quad , \tag{4.26}$$

and

$$M_{Bz} = F_y L_{BC} \quad . \tag{4.27}$$

Also using Fig. 4.3 and the free body diagram of section *CD* of the folded spring, Fig. 4.5, Cartesian components of the reaction force at *C* can be defined as

$$C_x = F_x \quad , \tag{4.28}$$

$$C_y = F_y \quad , \tag{4.29}$$

and

$$C_z = F_z \quad , \tag{4.30}$$

while components of the reaction moment can be shown to be

$$M_{Cx} = F_y L_{CD} \quad , \tag{4.31}$$

$$M_{Cy} = F_x L_{CD} \quad , \tag{4.32}$$

and

$$M_{Cz} = 0 \quad . \tag{4.33}$$
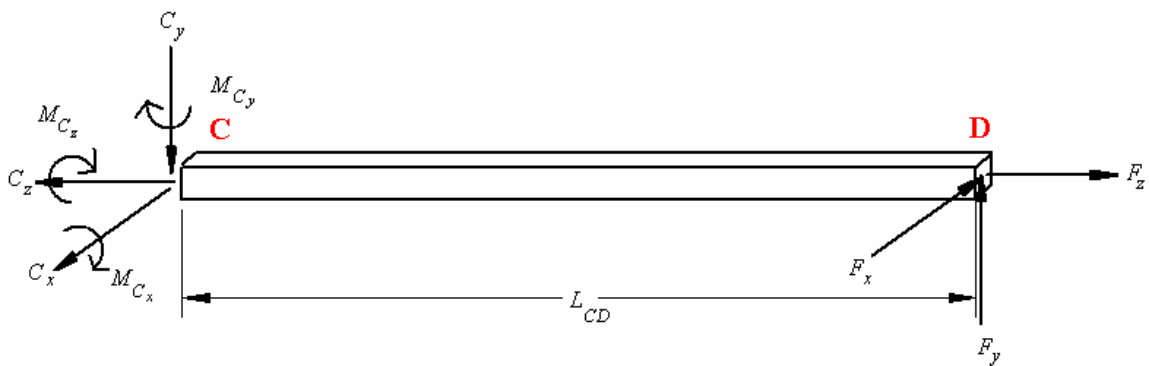
Fig. 4.5. Free body diagram of section *CD*.

4.1.3.2. Deformations at point *D* while considering only the cantilever *CD* of the folded spring

Before proceeding with the derivation of an equation for deformations at point *D* while considering the entire folded spring, derivation of an equation for deformations at the point of force application on the folded spring represented only by the cantilever section *CD* will be made. For this derivation, the cantilever will be fixed at point *C* and loaded at point *D*, Fig. 4.6.
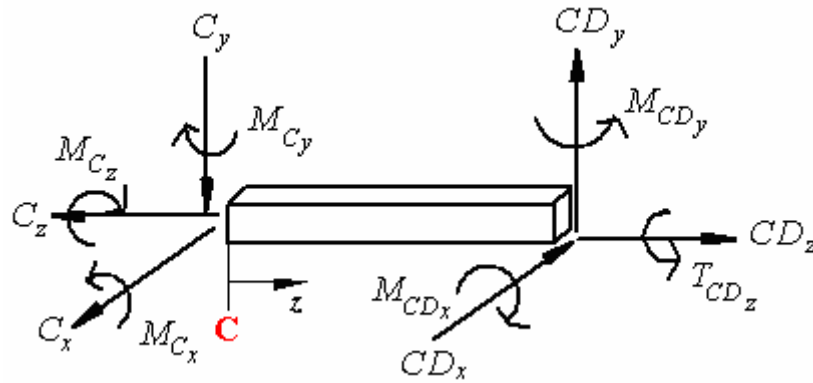
Fig. 4.6. Free body diagram for a part of section *CD*.

Based on the free body diagram shown in Fig. 4.6, the shear forces acting on section *CD* are

$$CD_x = C_x = F_x \quad , \tag{4.34}$$

$$CD_y = C_y = F_y \quad , \tag{4.35}$$

$$CD_z = C_z = F_z \quad , \tag{4.36}$$

and the reaction moments are

$$M_{CDx}(z) = F_y(z - L_{CD}) \quad , \tag{4.37}$$

$$M_{CDy}(z) = F_x(L_{CD} - z) \quad , \tag{4.38}$$

$$T_{CDz}(z) = 0 \quad . \tag{4.39}$$

Therefore, using Eqs 4.15, and 4.7 to 4.10, an equation for the internal strain energy of section CD, can be derived to be

$$U_{CD} = \int_0^{L_{CD}} \frac{CD_z^{\,2}}{2EA_b} dz + \int_0^{L_{CD}} \frac{M_{CDx}^{\,2}}{2EI_{bx\,or\,by}} dz + \int_0^{L_{CD}} \frac{M_{CDy}^{\,2}}{2EI_{bx\,or\,by}} dz +$$
$$\int_0^{L_{CD}} \frac{k_{y,z} CD_x^{\,2}}{2GA_b} dz + \int_0^{L_{CD}} \frac{k_{y,z} CD_y^{\,2}}{2GA_b} dz + \int_0^{L_{CD}} \frac{T_{CDz}^{\,2}}{2GJ_b} dz \tag{4.40}$$

where for a rectangular cross section, $k_{y,z}$ is equal to 6/5, and A_b is the cross sectional area of sections AB and CD, i.e.,

$$A_b = bh \quad , \tag{4.41}$$

I_{bx} the moment of inertia for sections AB and CD in the out-of-plane direction of motion,

$$I_{bx} = \frac{bh^3}{12} \quad , \tag{4.42}$$

I_{by} is the moment of the inertia for sections AB and CD in the in-plane direction of motion,

$$I_{by} = \frac{hb^3}{12} \quad , \tag{4.43}$$

and J_b is the polar moment of inertia for sections AB and CD. For the case of a rectangular cross section, the polar moment of inertia is defined by (Beer and Johnston, 1992) as

$$J_b = c_1 bh^3 \quad , \tag{4.44}$$

where b is the width of the beam, h is the thickness, and c_1 is the torsional coefficient for

a rectangular beam that is defined in Table 4.2 based on the ratio of the width to

thickness.

Table 4.2. Torsional coefficients for uniform
rectangular bars (Beer and Johnston, 1992).

b/h	c_1	b/h	c_1
1.0	0.208	3.0	0.267
1.2	0.219	4.0	0.282
1.5	0.231	5.0	0.291
2.0	0.246	10.0	0.312
2.5	0.258	∞	0.333

Equation 4.40 has six terms instead of four found in Eq. 4.13 because in Eq. 4.13 the

vectors of the forces, moments, and torques are used, while in Eq. 4.40 the individual

components are included. Equations 4.40 and 4.34 to 4.39 can be substituted into Eq. 4.5

to obtain the x-component of deformation at point D, at the end of section CD, to be

$$
\Delta_{dx} = \frac{\partial U_{CD}}{\partial F_x} = \int_0^{L_{CD}} \frac{CD_z}{A_b E}\left(\frac{\partial CD_z}{\partial F_x}\right) dz + \int_0^{L_{CD}} \frac{M_{CDx}}{I_{bx} E}\left(\frac{\partial M_{CDx}}{\partial F_x}\right) dz +
$$

$$
\int_0^{L_{CD}} \frac{M_{CDy}}{I_{bx} E}\left(\frac{\partial M_{CDy}}{\partial F_x}\right) dz + \int_0^{L_{CD}} \frac{6}{5}\cdot\frac{CD_x}{A_b G}\left(\frac{\partial CD_x}{\partial F_x}\right) dz + \qquad , \qquad (4.45)
$$

$$
\int_0^{L_{CD}} \frac{6}{5}\cdot\frac{CD_y}{A_b G}\left(\frac{\partial CD_y}{\partial F_x}\right) dz + \int_0^{L_{CD}} \frac{T_{CDz}}{J_b G}\left(\frac{\partial T_{CDz}}{\partial F_x}\right) dz
$$

Equation 4.45 can be simplified to

$$
\Delta_{dx} = \frac{F_x L_{CD}}{3EI_{by}} + \frac{6F_x L_{CD}}{5GA_b} \qquad . \qquad (4.46)
$$

Finally, using the forces, moments, and torques defined by Eqs 4.34 to 4.39, equations defining y-component and z-component of deformation at point D can be derived by substituting Eq. 4.40 into Eq. 4.5 and solving to obtain

$$\Delta_{dy} = \frac{\partial U_{CD}}{\partial F_y} = \frac{F_y L_{CD}^3}{3EI_{bx}} + \frac{6F_y L_{CD}}{5GA_b} \quad , \tag{4.47}$$

and

$$\Delta_{dz} = \frac{\partial U_{CD}}{\partial F_z} = \frac{F_z L_{CD}}{EA_b} \quad . \tag{4.48}$$

Results obtained from Eqs 4.46 to 4.48, modeling deformations at the point D, on the cantilever section CD representing the folded spring, will be compared with the computational results for the same representation of the folded spring.

4.1.3.3. Deformations at point B

The next step was to derive the deformation of the entire folded spring. This was done by taking the reaction forces and moments derived for the section AB and deriving the shear and moment equations for the section AB using a free body diagram of a part of the section of an arbitrary length along the z-axis, Fig. 4.7. Based on the free body diagram of Fig. 4.7, the shear forces acting on section AB are

$$AB_x = A_x = F_x \quad , \tag{4.49}$$

$$AB_y = A_y = F_y \quad , \tag{4.50}$$

$$AB_z = A_z = F_z \quad , \tag{4.51}$$

and the reaction moments are

$$M_{ABx}(z) = F_y(L_{AB} - L_{CD} - z) \quad , \tag{4.52}$$

$$M_{ABy}(z) = F_x(L_{CD} - L_{AB} + z) - F_z L_{BC} \quad , \tag{4.53}$$

$$T_{ABz}(z) = F_y L_{BC} \quad . \tag{4.54}$$
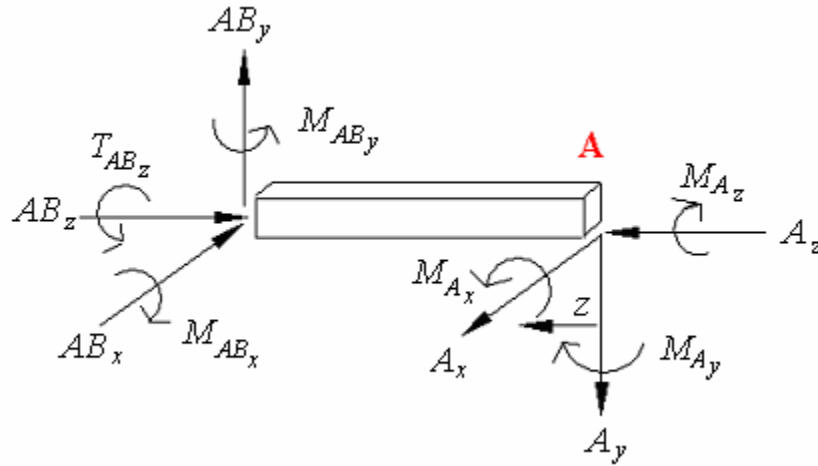
Fig. 4.7. Free body diagram for the cut of section AB.

Using the forces, moments, and torques that are described by Eqs 4.49 to 4.54 an equation for the internal strain energy of section AB can be written, based on Eqs 4.13 and 4.7 to 4.10, to be

$$
\begin{aligned}
U_{AB} = & \int_0^{LAB} \frac{AB_z^2}{2EA_b}dz + \int_0^{LAB} \frac{M_{ABz}^2}{2EI_{bx\,or\,by}}dz + \int_0^{LAB} \frac{M_{ABy}^2}{2EI_{bx\,or\,by}}dz + \\
& \int_0^{LAB} \frac{k_{y,z}AB_x^2}{2GA_b}dz + \int_0^{LAB} \frac{k_{y,z}AB_y^2}{2GA_b}dz + \int_0^{LAB} \frac{T_{ABz}^2}{2GJ_b}dz
\end{aligned}
\tag{4.55}
$$

The *x*-component of deformation at point *B* of section *AB*, Δ_{Bx}, can be determined by substituting Eq. 4.55 into Eq. 4.5, i.e.,

$$
\begin{aligned}
\Delta_{Bx} = \frac{\partial U_{AB}}{\partial F_x} = &\int_0^{L_{AB}} \frac{AB_z}{EA_b}\left(\frac{\partial AB_z}{\partial F_x}\right)dz + \int_0^{L_{AB}} \frac{M_{ABz}}{EI_{by}}\left(\frac{\partial M_{ABz}}{\partial F_x}\right)dz + \\
&\int_0^{L_{AB}} \frac{M_{ABy}}{EI_{by}}\left(\frac{\partial M_{ABy}}{\partial F_x}\right)dz + \int_0^{L_{AB}} \frac{6}{5}\cdot\frac{AB_x}{GA_b}\left(\frac{\partial AB_x}{\partial F_x}\right)dz + \\
&\int_0^{L_{AB}} \frac{6}{5}\cdot\frac{AB_y}{GA_b}\left(\frac{\partial AB_y}{\partial F_x}\right)dz + \int_0^{L_{AB}} \frac{T_{ABz}}{GJ_b}\left(\frac{\partial T_{ABz}}{\partial F_x}\right)dz
\end{aligned}
\quad . \qquad (4.56)
$$

Equation 4.56 can be simplified to

$$
\begin{aligned}
\Delta_{Bx} = &\frac{F_x}{2EI_{by}}\left(L_{AB}^3 - 3L_{AB}^2 L_{CD} + 3L_{AB}L_{CD}^2\right) + \frac{6F_x L_{AB}}{5GA_b} + \\
&\frac{F_z L_{BC}}{2EI_{by}}\left(L_{AB}^2 - 2L_{AB}L_{CD}\right)
\end{aligned}
\quad . \qquad (4.57)
$$

The forces, moments, and torques, Eqs 4. 49 to 4.54, the equation that defines the internal strain energies for Section *AB*, Eq. 4.55, and the definition of Castigliano's theorem, Eq. 4.5, that were used to derive the equation for displacement in the *x*-direction are also used to derive the relationships describing deformations in the *y*-direction and *z*-direction, i.e.,

$$
\begin{aligned}
\Delta_{By} = \frac{\partial U_{AB}}{\partial F_y} = &\frac{F_y}{3EI_{bx}}\left(L_{AB}^3 - 3L_{AB}^2 L_{CD} + 3L_{AB}L_{CD}^2\right) + \frac{6F_y L_{AB}}{5GA_b} + \\
&\frac{F_y L_{BC}^2 L_{AB}}{GJ_b}
\end{aligned}
\qquad (4.58)
$$

and

$$
\Delta_{Bz} = \frac{\partial U_{AB}}{\partial F_z} = \frac{F_z L_{AB}}{EA_b} + \frac{F_x L_{BC}}{2EI_{by}}\left(L_{AB}^2 - 2L_f L_{AB}\right) + \frac{F_z L_{BC}^2 L_{AB}}{EI_{by}} \quad , \qquad (4.59)
$$

respectively.

4.1.3.4. Deformations at point *C*

Based on the deformations at point *B*, deformations at point *C* of Section *BC* can be derived. As for the displacement at point *B*, the shear and moment equations for section *BC* are derived using a free body diagram at a point of the section of an arbitrary length along the *x*-axis, Fig. 4.8. Based on the free body diagram, displayed in Fig. 4.8, the shear forces acting on section *BC* are

$$BC_x = B_x = F_x \quad , \tag{4.60}$$

$$BC_y = B_y = F_y \quad , \tag{4.61}$$

$$BC_z = B_z = F_z \quad , \tag{4.62}$$

and the reaction moments are

$$T_{BCx}(x) = -F_y L_{CD} \quad , \tag{4.63}$$

$$M_{BCy}(x) = F_x L_{CD} + F_z (x - L_{BC}) \quad , \tag{4.64}$$

$$M_{BCz}(x) = F_y (L_{BC} - x) \quad . \tag{4.65}$$

Using Eqs 4.60 to 4.65, a relationship for the internal strain energy of section *BC*, based on Eqs 4.14 and 4.7 to 4.10 can be derived to be

$$
\begin{aligned}
U_{BC} = & \int_0^{L_{BC}} \frac{BC_x^2}{2EA_c} dx + \int_0^{L_{BC}} \frac{M_{BCy}^2}{2EI_{cy\,or\,cz}} dx + \int_0^{L_{BC}} \frac{M_{BCz}^2}{2EI_{cy\,or\,cz}} dx + \\
& \int_0^{L_{BC}} \frac{6}{5} \cdot \frac{BC_y^2}{2GA_c} dx + \int_0^{L_{BC}} \frac{6}{5} \cdot \frac{BC_z^2}{2GA_c} dx + \int_0^{L_{BC}} \frac{T_{BCx}^2}{2GJ_c} dx
\end{aligned}
\quad , \tag{4.66}
$$

where A_c is the cross sectional area of section BC, i.e.,

$$A_c = b_{BC} h \quad . \tag{4.67}$$
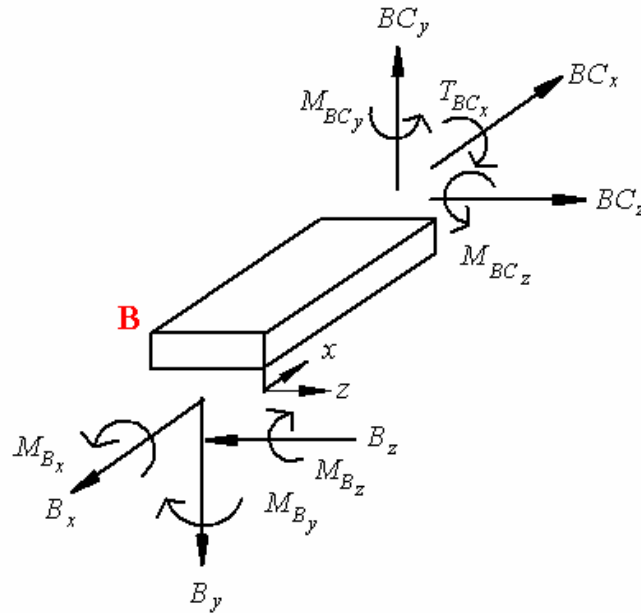
Fig. 4.8. Free body diagram for a part of section BC.

I_{cy} is the moment of inertia for section BC in the in-plane direction of motion

$$I_{cy} = \frac{h b_{BC}^{3}}{12} \quad , \tag{4.68}$$

I_{cz} is the moment of inertia for section BC in the out-of-plane direction of motion

$$I_{cz} = \frac{b_{BC} h^{3}}{12} \quad , \tag{4.69}$$

and J_c is the polar moment of inertia for sections BC, which is calculated as

$$J_c = c_1 b_{BC} h^{3} \quad , \tag{4.70}$$

where c_1 is defined in Table 4.2. Now, Eq. 4.66 and Eqs 4.60 to 4.65 will be used in Eq. 4.5 to obtain the displacements at the end of section BC, point C, first in the x-direction, i.e.,

$$
\begin{aligned}
\Delta_{Cx} = \Delta_{Bx} + \frac{\partial U_{BC}}{\partial F_x} = \Delta_{Bx} + \int_0^{L_{BC}} \frac{BC_x}{EA_c}\left(\frac{\partial BC_x}{\partial F_x}\right)dx + \\
\int_0^{L_{BC}} \frac{M_{BCy}}{EI_{cy}}\left(\frac{\partial M_{BCy}}{\partial F_x}\right)dx + \int_0^{L_{BC}} \frac{M_{BCz}}{EI_{cy}}\left(\frac{\partial M_{BCz}}{\partial F_x}\right)dx + \\
\int_0^{L_{BC}} \frac{6}{5}\cdot\frac{BC_y}{GA_c}\left(\frac{\partial BC_y}{\partial F_x}\right)dx + \int_0^{L_{BC}} \frac{6}{5}\cdot\frac{BC_z}{GA_c}\left(\frac{\partial BC_z}{\partial F_x}\right)dx + \\
\int_0^{L_{BC}} \frac{T_{BCx}}{GJ_c}\left(\frac{\partial T_{BCx}}{\partial F_x}\right)dx
\end{aligned} \tag{4.71}
$$

Equation 4.71 can be simplified to

$$
\begin{aligned}
\Delta_{Cx} = \frac{F_x}{2EI_{by}}\left(L_{AB}{}^3 - 3L_{AB}{}^2 L_{CD} + 3L_{AB}L_{CD}{}^2\right) + \frac{6F_x L_{AB}}{5GA_b} + \\
\frac{F_z L_{BC}}{2EI_{by}}\left(L_{AB}{}^2 - 2L_{AB}L_{CD}\right) + \frac{F_x L_{BC}}{A_c E} + \frac{F_x L_{BC}L_{CD}{}^2}{EI_{cy}} - \frac{F_z L_{BC}{}^2 L_{CD}}{2EI_{cy}}
\end{aligned} \tag{4.72}
$$

Again, using the forces, moments, and torques defined by Eqs 4.60 to 4.65, equations defining y-component and z-component of deformation at point C can be derived by substituting Eq. 4.66 into Eq. 4.5 and solving to obtain

$$
\begin{aligned}
\Delta_{Cy} = \Delta_{By} + \frac{\partial U_{BC}}{\partial F_y} = \frac{F_y}{3EI_{bx}}\left(L_{AB}{}^3 - 3L_{AB}{}^2 L_{CD} + 3L_{AB}L_{CD}{}^2\right) + \\
\frac{6F_y L_{AB}}{5GA_b} + \frac{F_y L_{BC}{}^2 L_{AB}}{GJ_b} + \frac{F_y L_{BC}{}^3}{3EI_{cz}} + \frac{6F_y L_{BC}}{5GA_c} + \\
\frac{F_y L_{CD}{}^2 L_{BC}}{GJ_c}
\end{aligned} \tag{4.73}
$$

and

$$\Delta_{Cz} = \Delta_{Bz} + \frac{\partial U_{BC}}{\partial F_z} = \frac{F_z L_{AB}}{EA_b} + \frac{F_x L_{BC}}{2EI_{by}}\left(L_{AB}{}^2 - 2L_{AB}L_{CD}\right) +$$

$$\frac{F_z L_{BC}{}^2 L_{AB}}{EI_{by}} - \frac{F_x L_{CD}L_{AB}{}^2}{2EI_{cy}} + \frac{F_z L_{BC}{}^3}{3EI_{cy}} + \quad . \tag{4.74}$$

$$\frac{6F_z L_{BC}}{5GA_c}$$

4.1.3.5. Deformations at point *D* while considering the entire folded spring

Deformations at point *D* of Section *CD* can be determined following procedures used to determine displacements at points *B* and *C*. However this was already done in Section 4.1.3.2. In order to obtain the deformation in the *x*-direction at point *D* for the entire folded spring, the deformation at point *D* for the cantilever beam, Eq. 4.46, was added to the deformation at point *C*, Eq. 4.72, i.e.,

$$\Delta_{Dx} = \Delta_{Cx} + \Delta_{dx} , \tag{4.75}$$

Equation 4.75 can be simplified to

$$\Delta_{Dx} = \frac{F_x}{2EI_{by}}\left(L_{AB}{}^3 - 3L_{AB}{}^2 L_{CD} + 3L_{AB}L_{CD}{}^2\right) + \frac{6F_x L_{AB}}{5GA_b} +$$

$$\frac{F_z L_{BC}}{2EI_{by}}\left(L_{AB}{}^2 - 2L_{AB}L_{CD}\right) + \frac{F_x L_{BC}}{A_c E} + \frac{F_x L_{BC}L_{CD}{}^2}{EI_{cy}} - \quad . \tag{4.76}$$

$$\frac{F_z L_{BC}{}^2 L_{CD}}{2EI_{cy}} + \frac{F_x L_{CD}{}^3}{3EI_{by}} + \frac{6F_x L_{CD}}{5GA_b}$$

The procedure used to derive Eq. 4.76 was followed in order to obtain deformations at point *D* in the *y* and *z* directions, i.e.,

$$\Delta_{Dy} = \Delta_{Cy} + \Delta_{dy} = \frac{F_y}{3EI_{bx}}\left(L_{AB}^{3} - 3L_{AB}^{2}L_{CD} + 3L_{AB}L_{CD}^{2}\right) +$$

$$\frac{6F_y L_{AB}}{5GA_b} + \frac{F_y L_{BC}^{2} L_{AB}}{GJ_b} + \frac{F_y L_{BC}^{3}}{3EI_{cz}} + \frac{6F_y L_{BC}}{5GA_c} + , \qquad (4.77)$$

$$\frac{F_y L_{CD}^{2} L_{BC}}{GJ_c} + \frac{F_y L_{CD}^{3}}{3EI_{bz}} + \frac{6F_y L_{CD}}{5GA_b}$$

and

$$\Delta_{Dz} = \Delta_{Cz} + \Delta_{dz} = \frac{F_z L_{AB}}{EA_b} + \frac{F_x L_{BC}}{2EI_{by}}\left(L_{AB}^{2} - 2L_{CD}L_{AB}\right) +$$

$$\frac{F_z L_{BC}^{2} L_{AB}}{EI_{by}} - \frac{F_x L_{CD} L_{BC}^{2}}{2EI_{cy}} + \frac{F_z L_{BC}^{3}}{3EI_{cy}} + . \qquad (4.78)$$

$$\frac{6F_z L_{BC}}{5GA_c} + \frac{F_z L_{CD}}{EA_b}$$

Comparing Eqs 4.76 to 4.78 with Eqs 4.46 to 4.48 is should be noted that complexity of equations increases when deformations at point D are determined while considering the entire folded spring, rather than its representation as a cantilever. Detailed determination of deformations of the folded spring of the microgyro, based on Eqs 4.76 to 4.78, is included in Appendix A.

4.1.4. Determination of forces acting on the folded spring

Forces used in equations for deformations, which were derived in Section 4.1.3, must be determined. Because of the nature of the functional operation of the microgyroscopes studied in this thesis, the forces acting in the x, i.e., in-plane, and y, i.e., out-of-plane, directions were calculated, while the force in the z-direction was assumed to

be zero. The force that acts on the folded springs in the x-direction is due to the vibration of the proof masses. Therefore, in order to calculate this force, Newton's second law was applied, i.e.,

$$F_{spring} = \frac{ma(t)}{4} \quad , \tag{4.79}$$

where for the case of the microgyroscope, m is the total mass of the proof mass, and $a(t)$ is the time dependent acceleration that is acting on the proof mass. In order to obtain the force that acts on each of the four folded springs that support a single proof mass, it was assumed that each spring evenly shares the force; therefore, the total force is divided by four in order to obtain the force for a single spring.

The acceleration acting on the proof masses was obtained by evaluating double time derivative of the equation of sinusoidal motion of the proof masses, i.e.,

$$x(t) = B \sin(\omega t) \quad , \tag{4.80}$$

$$v(t) = \frac{d}{dt} x(t) = B \omega \cos(\omega t) \quad , \tag{4.81}$$

$$a(t) = \frac{d}{dt} v(t) = \frac{d^2}{dt^2} x(t) = -B \omega^2 \sin(\omega t) \quad , \tag{4.82}$$

where x, v, and a, are the instantaneous position, speed, and acceleration, respectively, of the proof mass, B is the amplitude of the oscillation, ω is the angular speed of oscillation, and t is time. For the motion of the proof mass it is assumed that the maximum amplitude of the displacement of the proof mass is defined as

$$B = \frac{L_f}{2} - 3 \quad , \tag{4.83}$$

where L_f is the length of the combdrive fingers. Three micrometers less than half of the

finger length are used because if the proof mass moved half the finger length, the fingers

might stick and the microgyro would fail. The angular speed of the motion of the proof

mass was calculated as

$$\omega = 2\pi f \quad , \tag{4.84}$$

where f is the cyclic frequency of the vibration of the proof mass.

Based on Eq. 4.82, the maximum acceleration will be obtained when $sin(\omega t)$ will

be equal to one; therefore the maximum acceleration "felt" by the proof mass of the

gyroscope will be

$$a_{max} = B\,\omega^2 \quad . \tag{4.85}$$

By substituting 4.85 into 4.79, the maximum force acting on the proof mass is calculated

to be

$$F_{max} = \frac{mB\omega^2}{4} = \frac{m\left(\dfrac{L_f}{2} - 3\right)\omega^2}{4} \quad , \tag{4.86}$$

and then applied to the folded spring in order to determine in-plane deformation in the x-

direction.

The force that acts on the folded springs in the y-direction is the Coriolis force,

Eq. 2.7. Based on literature addressing MEMS gyroscopes, angular velocities that

microgyroscopes are subjected to can range from 0 rad/sec to $\pm 6\pi$ rad/sec, or 0°/s to

± 1080°/s (Analog Devices, 2003a, 2003b; Fujita, et al., 1997; Geiger, et al., 1998;

Hedenstierna, et al., 2001; Kuisma, et al., 1997). However, most of the angular rates are

lower, on the order of 100°/s, and this is the angular acceleration that was applied to Eq.

2.7. The average in-plane velocity, in Eq. 2.7, is defined as

$$v = \frac{4B}{\tau} \quad , \tag{4.87}$$

where τ is the period of the vibration of the proof mass. Only a quarter of the period is

used in this case because the proof mass moves, traversing the amplitude defined by Eq.

4.83, four times during a single cycle. Therefore, the distance B is traveled ever quarter

of the period. The period is calculated as the reciprocal of the cyclic frequency, i.e.,

$$\tau = \frac{1}{f} \quad . \tag{4.88}$$

The values necessary to solve for the maximum in-plane acceleration, the in-plane

velocity, the in-plane force acting on the folded springs, and the Coriolis force acting on

the folded springs are listed in Table 4.3. A detailed determination of the forces that are

applied to the folded spring from Sandia is included in Appendix B.

Table 4.3. Values necessary to calculate the forces acting on the folded spring.

Description and symbol	Value
Calculated total mass of the proof mass, m	1.25502 nkg
Measured length of the comb drive fingers, L_f	40.0 µm
Operational frequency of the proof mass, f	10.0 kHz
Angular rate, ω	1.7533 rad/sec

4.1.5. Uncertainty analysis

An uncertainty analysis was done on the displacements that were derived in Section 4.1.3 for the folded springs that support the proof masses of the Sandia microgyro. This was done to determine by how much the deformation of the folded spring could vary due to assumptions and approximations that were used in the analytical calculations. That is, the uncertainty analysis gives basis for determination of how good the analytical results are (Pryputniewicz, 1993).

The uncertainty analysis that was conducted in this thesis was performed based on the root-sum-square (RSS) approach (Pryputniewicz, 1993), which assumes a Gaussian distribution in the values of the uncertainty for the variables that are considered.

For multiple measurements of a single parameter, X, the total RSS uncertainty, δ_X, is defined as

$$\delta_X = \left(B^2 + P_X{}^2\right)^{1/2} \quad , \tag{4.89}$$

where B is the bias limit and P_X is the precision of the entire set of data for the parameter X.

However, for the case of a result that is calculated from many individual variables, a *general uncertainty analysis* must be done using the RSS approach. For this case, each independent parameter, X_i, will have (Coleman and Steele, 1989) associated with it

$$B = 0 \quad . \tag{4.90}$$

Therefore, based on Eq. 4.90, Eq. 4.89 reduces to

$$\delta_{X_i} = P_{X_i} \quad . \tag{4.91}$$

Using Eq. 4.91, general uncertainty analysis begins by writing a phenomenological equation expressing the dependent parameter, uncertainty of which is to be determined, in terms of its independent parameters $X_1, X_2,\ldots, X_n$ (Pryputniewicz, 1993), i.e.,

$$X = X(X_1, X_2,\ldots, X_n) \quad . \tag{4.92}$$

Based on Eq. 4.92, the uncertainty δ_X can be calculated, using, e.g., the RSS approach, to be

$$\delta_X = \left[\left(\frac{\partial X}{\partial X_1} \delta_{X_1} \right)^2 + \left(\frac{\partial X}{\partial X_2} \delta_{X_2} \right)^2 + \ldots + \left(\frac{\partial X}{\partial X_n} \delta_{X_n} \right)^2 \right]^{\frac{1}{2}} \quad , \tag{4.93}$$

where the δ_{Xi} parameters represent uncertainties of the individual independent parameters, X_i.

Using Eqs 4.92 and 4.93, the uncertainty analyses were performed for the deformations at point D of the folded spring. For example, using the explicit definition of the x-component of deformation at point D, given by Eq. 4.76, the corresponding phenomenological equation is written as

$$\Delta_{Dx} = \Delta_{Dx}(F_x, F_z, L_{AB}, L_{BC}, L_{CD}, A_b, A_c, I_{by}, I_{cy}, E, G) \quad . \tag{4.94}$$

The next step is to write the phenomenological equations for each of the variables in Eq. 4.94 that themselves are functions of their own independent parameters. This is,

$$F_x = F_x(m, a) \quad , \tag{4.95}$$

where

$$m = m(V_{proof}, \rho) \quad , \tag{4.96}$$

81

and

$$a = a(B, \omega) \quad . \tag{4.97}$$

In Eqs 4.96 and 4.97, we have

$$V_{proof} = V_{proof}(A_{proof}, h) \quad , \tag{4.98}$$

$$B = B(L_f) \quad , \tag{4.99}$$

and

$$\omega = \omega(f) \quad . \tag{4.100}$$

Also in Eq. 4.94, we have

$$A_b = A_b(b, h) \quad , \tag{4.101}$$

$$A_c = A_c(b_{BC}, h) \quad , \tag{4.102}$$

$$I_{by} = I_{by}(b, h) \quad , \tag{4.103}$$

$$I_{cy} = I_{cy}(b_{BC}, h) \quad , \tag{4.104}$$

and

$$G = G(E, \mu) \quad . \tag{4.105}$$

Using Eq 4.93, uncertainties in parameters defined by Eqs 4.94 to 4.105 can be determined. Once these uncertainties are known, they can be used to determine the overall uncertainty (Pryputniewicz, 1993) in the x-component of deformation at point D, i.e.,

$$\delta\Delta_{\mathrm{Dx}} = \left[\left(\frac{\partial\Delta_{\mathrm{Dx}}}{\partial F_x} \delta F_x \right)^2 + \left(\frac{\partial\Delta_{\mathrm{Dx}}}{\partial F_z} \delta F_z \right)^2 + \left(\frac{\partial\Delta_{\mathrm{Dx}}}{\partial L_{AB}} \delta L_{AB} \right)^2 + \right.$$

$$\left(\frac{\partial\Delta_{\mathrm{Dx}}}{\partial L_{BC}} \delta L_{BC} \right)^2 + \left(\frac{\partial\Delta_{\mathrm{Dx}}}{\partial L_{CD}} \delta L_{CD} \right)^2 + \left(\frac{\partial\Delta_{\mathrm{Dx}}}{\partial A_b} \delta A_b \right)^2 +$$

$$\left(\frac{\partial\Delta_{\mathrm{Dx}}}{\partial A_c} \delta A_c \right)^2 + \left(\frac{\partial\Delta_{\mathrm{Dx}}}{\partial I_{by}} \delta I_{by} \right)^2 + \left(\frac{\partial\Delta_{\mathrm{Dx}}}{\partial I_{cy}} \delta I_{cy} \right)^2 + \qquad (4.106)$$

$$\left. \left(\frac{\partial\Delta_{\mathrm{Dx}}}{\partial E} \delta E \right)^2 + \left(\frac{\partial\Delta_{\mathrm{Dx}}}{\partial G} \delta G \right)^2 \right]^{1/2}$$

The procedure used to derive Eq. 4.106 was followed to obtain overall uncertainties in the *y*-component and *z*-component of deformations at point *D*. The phenomenological relationships, based on Eqs 4.77 and 4.78 are

$$\Delta_{\mathrm{Dy}} = \Delta_{\mathrm{Dy}}\left(F_y, L_{AB}, L_{BC}, L_{CD}, A_b, A_c, I_{bx}, I_{cz}, J_b, J_c, E, G \right) \quad , \qquad (4.107)$$

$$\Delta_{\mathrm{Dz}} = \Delta_{\mathrm{Dz}}\left(F_x, F_z, L_{AB}, L_{BC}, L_{CD}, A_b, A_c, I_{by}, I_{cy}, E, G \right) \quad , \qquad (4.108)$$

respectively. Based on Eqs 4.107 and 4.108, the overall uncertainties in the *y*-direction and *z*-direction are

$$\delta\Delta_{\mathrm{Dy}} = \left[\left(\frac{\partial\Delta_{\mathrm{Dy}}}{\partial F_y} \delta F_y \right)^2 + \left(\frac{\partial\Delta_{\mathrm{Dy}}}{\partial L_{AB}} \delta L_{AB} \right)^2 + \left(\frac{\partial\Delta_{\mathrm{Dy}}}{\partial L_{BC}} \delta L_{BC} \right)^2 + \right.$$

$$\left(\frac{\partial\Delta_{\mathrm{Dy}}}{\partial L_{CD}} \delta L_{CD} \right)^2 + \left(\frac{\partial\Delta_{\mathrm{Dy}}}{\partial A_b} \delta A_b \right)^2 + \left(\frac{\partial\Delta_{\mathrm{Dy}}}{\partial A_c} \delta A_c \right)^2 +$$

$$\left(\frac{\partial\Delta_{\mathrm{Dy}}}{\partial I_{by}} \delta I_{bx} \right)^2 + \left(\frac{\partial\Delta_{\mathrm{Dy}}}{\partial I_{cy}} \delta I_{cz} \right)^2 + \left(\frac{\partial\Delta_{\mathrm{Dy}}}{\partial J_b} \delta J_b \right)^2 + \qquad (4.109)$$

$$\left. \left(\frac{\partial\Delta_{\mathrm{Dy}}}{\partial J_b} \delta J_b \right)^2 + \left(\frac{\partial\Delta_{\mathrm{Dy}}}{\partial E} \delta E \right)^2 + \left(\frac{\partial\Delta_{\mathrm{Dy}}}{\partial G} \delta G \right)^2 \right]^{1/2}$$

and

$$\delta\Delta_{\text{Dz}} = \left[\left(\frac{\partial\Delta_{\text{Dz}}}{\partial F_x} \delta F_x \right)^2 + \left(\frac{\partial\Delta_{\text{Dz}}}{\partial F_z} \delta F_z \right)^2 + \left(\frac{\partial\Delta_{\text{Dz}}}{\partial L_{AB}} \delta L_{AB} \right)^2 + \right.$$

$$\left(\frac{\partial\Delta_{\text{Dz}}}{\partial L_{BC}} \delta L_{BC} \right)^2 + \left(\frac{\partial\Delta_{\text{Dz}}}{\partial L_{CD}} \delta L_{CD} \right)^2 + \left(\frac{\partial\Delta_{\text{Dz}}}{\partial A_b} \delta A_b \right)^2 +$$

$$\left(\frac{\partial\Delta_{\text{Dz}}}{\partial A_c} \delta A_c \right)^2 + \left(\frac{\partial\Delta_{\text{Dz}}}{\partial I_{by}} \delta I_{by} \right)^2 + \left(\frac{\partial\Delta_{\text{Dz}}}{\partial I_{cy}} \delta I_{cy} \right)^2 +$$

$$\left. \left(\frac{\partial\Delta_{\text{Dz}}}{\partial E} \delta E \right)^2 + \left(\frac{\partial\Delta_{\text{Dz}}}{\partial G} \delta G \right)^2 \right]^{\frac{1}{2}} \qquad , \qquad (4.110)$$

respectively. Values of uncertainties for the individual variables that were used to obtain

the overall uncertainties in the three components of deformations at point D of the folded

spring are listed in Table 4.4.

Table 4.4. Values and initial uncertainties of parameters
characterizing the folded spring.

Variable	Units	Value	Uncertainty
F_x	N	0	0
L_{AB}	μm	111	0.5
L_{BC}	μm	17	0.5
L_{CD}	μm	98	0.5
b	μm	3	0.5
b_{BC}	μm	10	0.5
h	μm	2.5	0.5
L_f	μm	40	0.5
f	kHz	10	0.5
ω	rad/sec	1.745	0.0005
E	GPa	160	5
ρ	g/cm^3	2.330	0.005
μ		0.23	0.005

The uncertainties for the measured dimensions were initially taken to be the resolution of the microscope used, the uncertainty for the thickness was taken to be 0.5 μm as a "safety factor," uncertainties in the material properties were taken from the tolerances set by Sandia (2003), all other uncertainties were taken as half of the least significant digit of the value (Pryputniewicz, 1993). Detailed determination of the uncertainties is included in Appendix C.

4.2. Computational considerations

The purpose of the computational considerations was to determine displacements, at the point where the forces were applied, using the finite element method (FEM). The procedure was to first draw the folded spring in a CAD package, e.g., SolidWorks (2001) software, illustrated in Fig. 4.9. Once the model was complete it was imported into the FEM software used, COSMOS/M (2003), for this thesis. Using COSMOS/M software, material properties of the folded spring, resultant forces from the proof mass acting on the face at point D, and boundary conditions, that the folded spring was fixed over the face at point A, the model was meshed using 2 different types of elements: 1) linear tetrahedral solid elements which have four corner nodes and six edges and 2) parabolic tetrahedral elements which have four corner nodes, six edges, and six mid-side nodes, Fig. 4.10.

When the FEM model was completed, a convergence analysis was performed starting with the minimum allowable number of solid elements and ending when changes

between deformations corresponding to the two most recent dicretizations were below

0.1%. Results of the convergence analyses are discussed in Section 5.2.

Fig. 4.9. SolidWorks representation of the folded spring used in the Sandia microgyro.
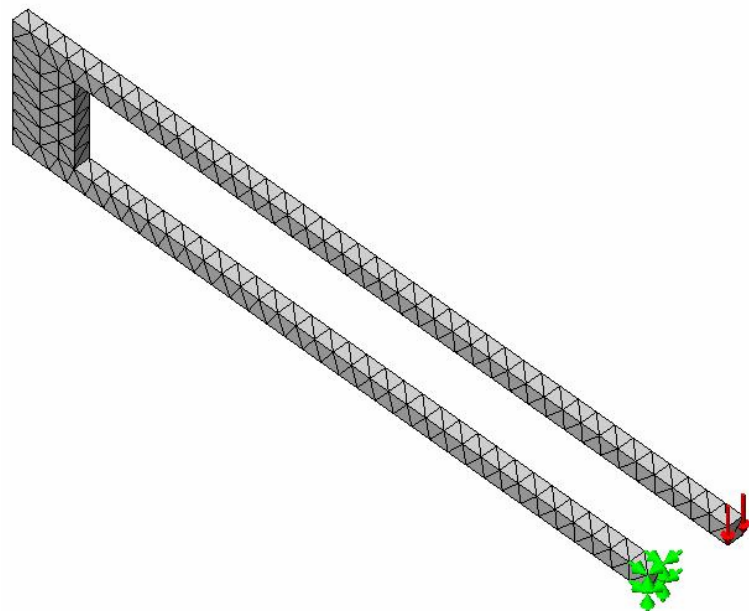
Fig. 4.10. Solid parabolic tetrahedral element mesh of the folded spring.

4.3. Experimental considerations

The purpose of the experimental study of the folded spring was to test how well the analytical and computational models compare to what happens in the real world. This was done by using a laser vibrometer to measure displacements of the proof mass as the microgyroscope is shaken out-of-plane by a PZT shaker. The displacements measured by the vibrometer were then compared to displacements calculated analytically. After this was completed, shapes of the microgyros were characterized using optoelectronic laser interferometeric microscope (OELIM) methodology. The laser vibrometer method is described in Section 4.3.1 while the OELIM methodology is presented in Section 4.3.2.

4.3.1. Laser vibrometer method

Displacements were measured using laser vibrometer setup (Polytech, 2001), Fig. 4.11. The way the laser vibrometer was used was that a signal generator sends a sinusoidal voltage to the piezoelectric transducer (PZT) shaker driver, the driver sends a signal to the PZT, and the PZT shakes the microgyroscope die which is attached to a mirror, which is itself mounted on the PZT, Fig. 4.12. The vibrometer laser was then focused on the object to be measured, either the proof mass or the mirror; the decoder would then compare the signal from the object to the reference beam, and obtain a voltage that corresponds to a displacement by the conversion factor of 50 nm/Volt. The signal from the decoder was then entered into a signal analyzer where the frequency and

the time-domain responses were analyzed to obtain the displacement response of the

microgyroscope. A schematic diagram of the vibrometer setup is illustrated in Fig. 4.13.

The frequency response obtained from the vibrometer when the mirror is observed is the

response of the mirror, the adhesive that attaches the mirror to the PZT, which for this

case was super glue, the PZT shaker, the PZT driver, and the signal that is produced by

the signal analyzer. The signal obtained from the proof mass is the frequency response of

the proof mass of the microgyro, the substrate of the die that the microgyro is located on,

the adhesive that was used to attach the die to the mirror, and the response of all of the

components that are viewed by the signal obtained from the mirror.
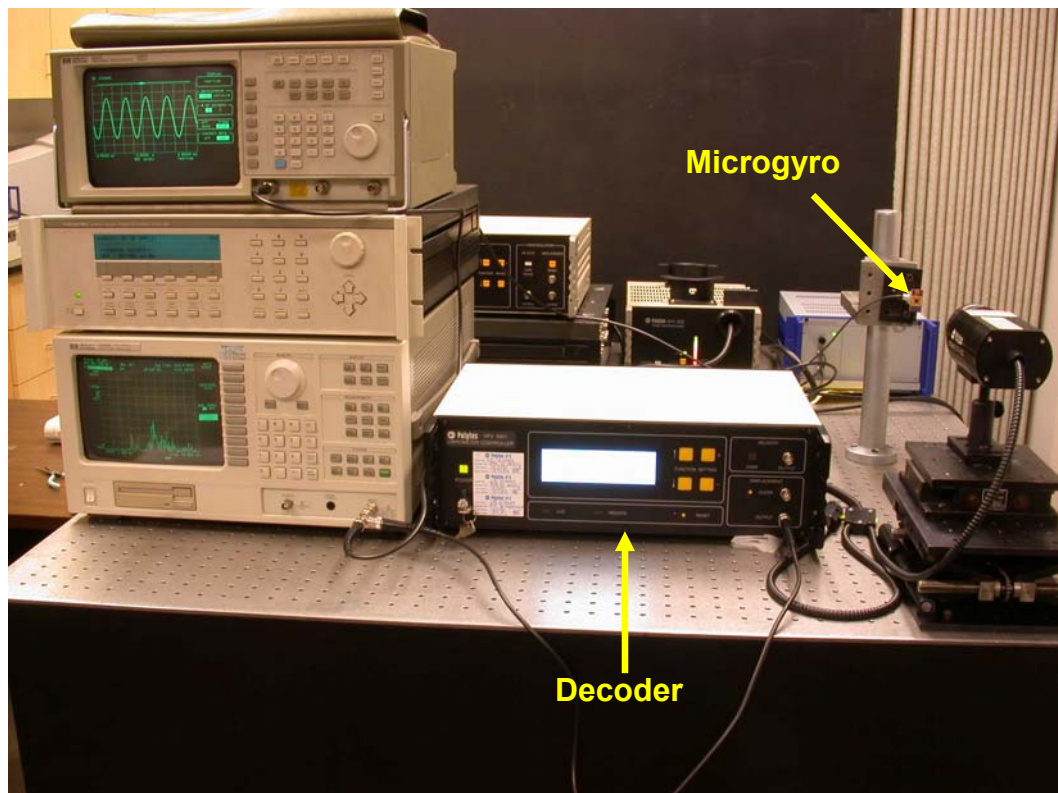
Fig. 4.11. Laser vibrometer setup.
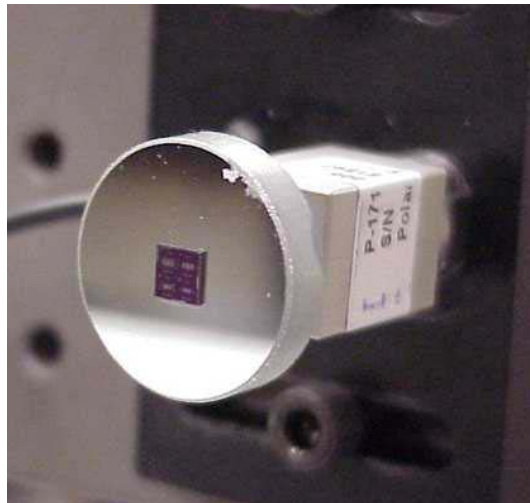
Fig. 4.12. Close-up of the mounted microgyro
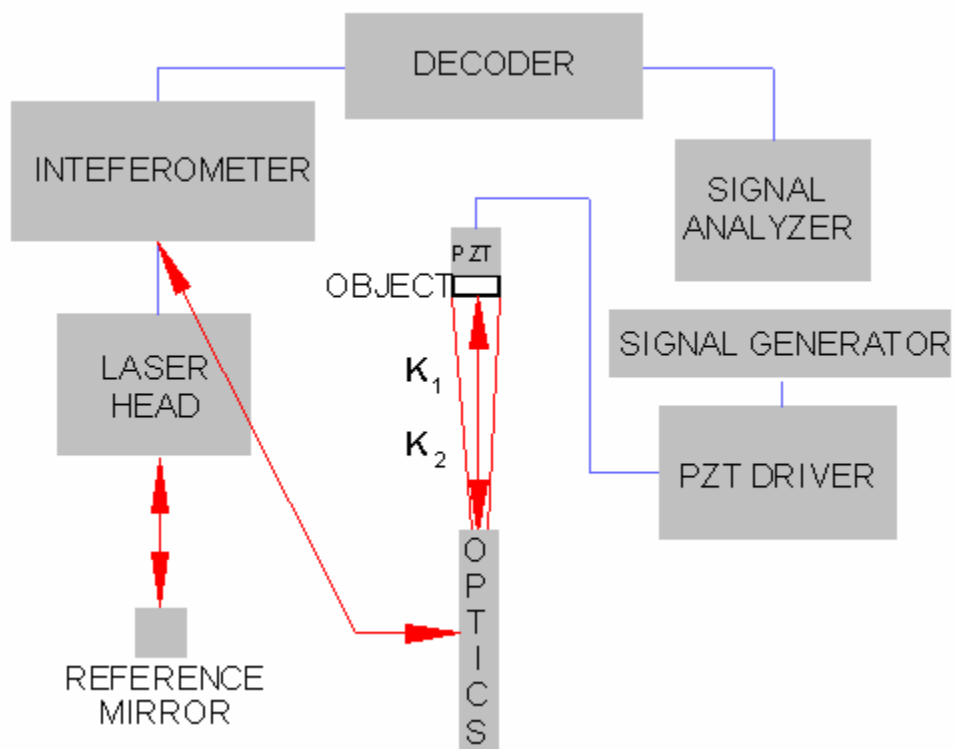
Fig. 4.13. Schematic diagram of the laser vibrometer setup.

A check of how the system works was done first by obtaining the frequency

response function (FRF) of the substrate/proof mass in order to check whether the

substrate/proof mass cleanly transmitts the input signal from the PZT and mirror, or if it

changes the signal.

The system illustrated in Fig. 4.14 will be used to explain how the FRF can be

calculated.
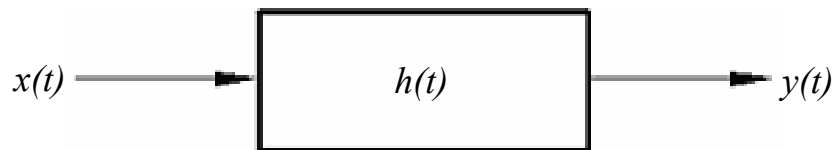
Fig. 4.14. Block diagram of a system in the time-domain.

In Fig. 4.14 *x(t)* is the input to the system, *h(t)* is the characteristic function of what

happens in the system in the time-domain, and *y(t)* is the outuput of the system. For the

time-domain, the relationship between the input, characteristic function, and output is

described by a convolution integral

$$y(t) = \int_{-\infty}^{\infty} h(\tau)x(t-\tau)d\tau \quad , \tag{4.111}$$

where τ is the integration variable. Convolution is defined as an integral which expresses

the amount of overlap of one function as it is shifted over another function (Weisstein,

1999; Jeffrey, 2002). For many applications it is easier to deal with the frequency

response of a system rather than the time-domain. The block diagram for the frequency

domain for the system is illustrated in Fig. 4.15.
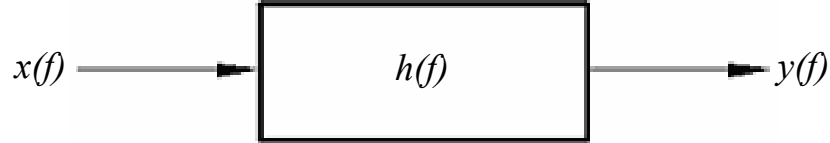
Fig. 4.15. The block diagram for a system in the frequency-domain.

When a function is changed from the time domain to the frequency domain it is transfomed using the following equation:

$$y(f) = \int_{-\infty}^{\infty} y(t)e^{-2j\pi ft}dt \quad .$$

(4.112)

Based on Eq. 4.112, Eq. 4.111 can be re-written as

$$\int_{-\infty}^{\infty} y(t)e^{-2j\pi ft}dt = \int_{-\infty}^{\infty}\left[\int_{-\infty}^{\infty} h(\tau)x(t-\tau)d\tau\right]e^{-2j\pi ft}dt \quad ,$$

(4.113)

or

$$\int_{-\infty}^{\infty} y(t)e^{-2j\pi ft}dt = \int_{-\infty}^{\infty} h(\tau)\left[\int_{-\infty}^{\infty} x(t-\tau)e^{-2j\pi ft}dt\right]d\tau \quad .$$

(4.114)

If a temporary function, $\sigma = t - \tau$, is introduced into Eq. 4.114 it changes to

$$\int_{-\infty}^{\infty} y(t)e^{-2j\pi ft}dt = \int_{-\infty}^{\infty} h(\tau)\left[e^{-2j\pi f\tau}\int_{-\infty}^{\infty} x(\sigma)e^{-2j\pi f\sigma}d\sigma\right]d\tau \quad ,$$

(4.115)

$$y(f) = x(f)\int_{-\infty}^{\infty} h(\tau)\cdot e^{-2j\pi f\tau}d\tau \quad .$$

(4.116)

Based on the definition of the conversion from the time domain to the frequency domain, Eq. 4.116 can be simplified to the form (Furlong, 1993)

$$y(f) = x(f)\cdot h(f) \quad .$$

(4.117)

91

Equation 4.117 proves that if two functions are convolved in the time domain they are multiplied by the frequency domain (Brigham, 1988). The experimental setup that was illustrated in Figs 4.11 to 4.13 can be also modeled as a mass-spring-damper system, since each electrical or mechanical part of the total experimental system can be modeled, based on the force-voltage analogy as a mass/inductance, spring/inverse of the capacitor, and damper/resistor system, (Ogata, 1978) Fig. 4.16. Another way of illustrating the system is using a block diagram similar to that in Fig. 4.17.
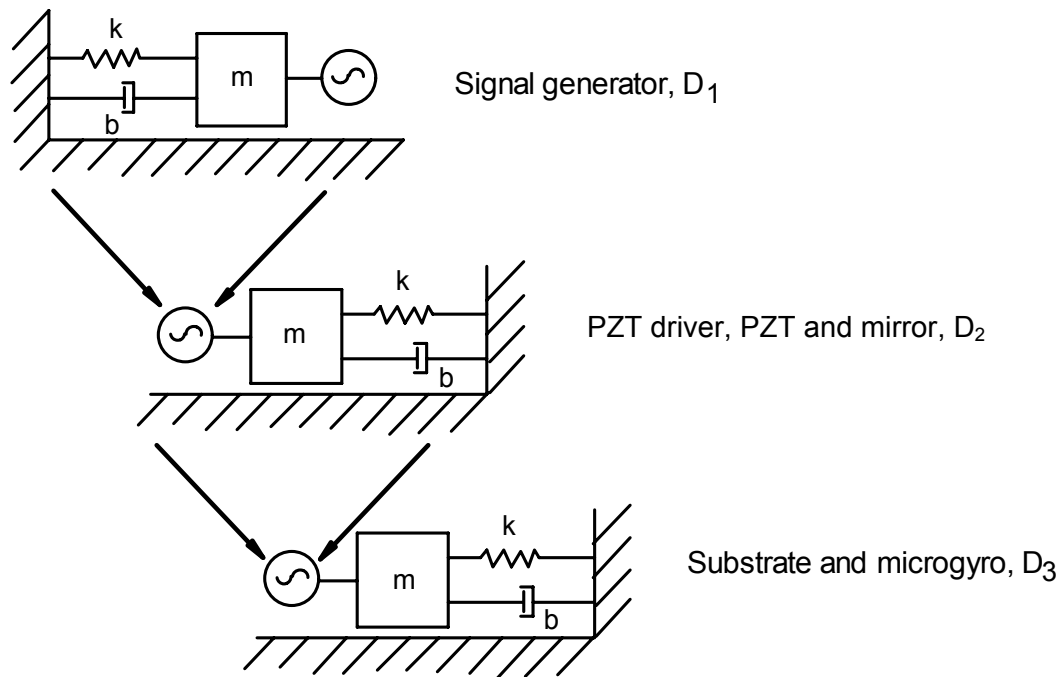
Fig. 4.16. Schematic diagram of the experimental system, where *m* is the mass, *k* is the spring, *b* is the damper.
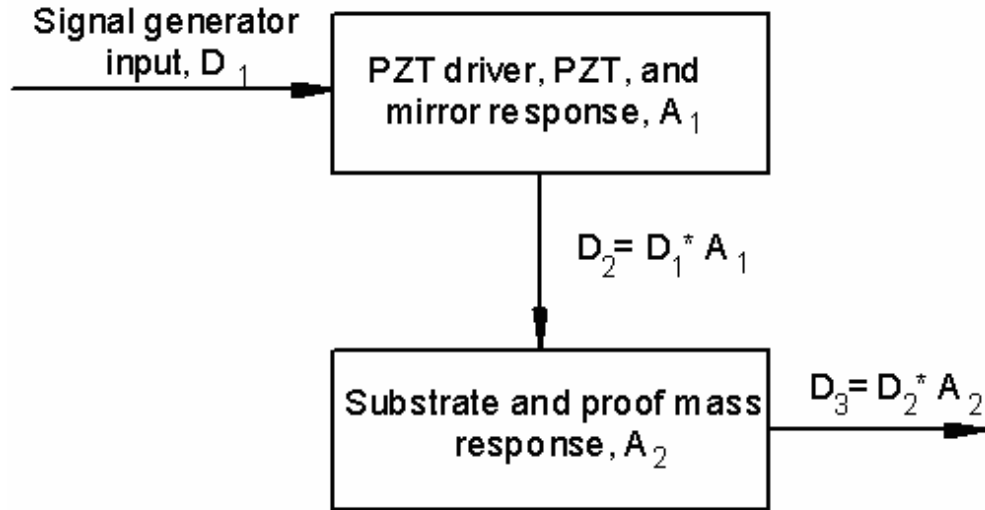
Fig. 4.17. Block diagram for the experimental system.

As shown in Figs 4.16 and 4.17, the frequency response from the signal generator and

cable, D_1, acts as a driver for the PZT driver, PZT, and mirror, for which the FRF is A_1,

and the product of D_1 and A_1 produces D_2; then D_2 acts as the driver for the

substrate/proof mass, for which the FRF is A_2, and the product of the D_2 and A_2 produces

the output, D_3. In order to obtain the FRF of just the substrate/proof mass it is necessary

to remove the extra components: the mirror, PZT, PZT driver, and signal from the signal

generator. This is done by de-convolving the three frequency responses from one

another. This is achieved by solving the equation for D_3, which is defined in Fig. 4.17, to

determine A_2, i.e.,

$$A_2 = \frac{D_3}{D_2} \quad . \tag{4.118}$$

Once this deconvolved signal is obtained the inverse fast Fourier transform (IFFT) of the

signal is taken in order to obtain the response of the substrate/proof mass in the time

domain. In order to obtain the amplitude of displacement that the proof mass experiences due to the excitation, both the mirror and the substrate/proof mass have to be observed in the time-domain. The difference between the two responses provides the displacement of the substrate/proof mass.

4.3.2. OELIM methodology

Optoelectronic laser interferometric microscope (OELIM) methodology is the state-of-the-art methodology for studies of MEMS in full field of view. The OELIM is based on the optoelectronic holography (OEH) method that is described in Section 4.3.2.1.

4.3.2.1. Opto-electronic holography

Advances in the phase step hologram interferometry, speckle metrology, and computer technology allowed development of a system for direct electronic recording of holograms and transmission of holographic interferograms by television systems for real-time display of fringes (Pryputniewicz, 1985; Furlong, 1999; Brown and Pryputniewicz, 2000; Pryputniewicz, et. al, 2000). This opto-electronic holography (OEH) system, in addition to other electronic and optical components, consists of a modified speckle interferometer, which produces speckles large enough to be resolved by a TV camera (Pryputniewicz, et. al, 2001). The output of the TV camera is fed to a system that

computes and stores the magnitude and phase, relative to the reference beam, of each picture element in the image of the illuminated object.

Any of the usual phenomena that generate characteristic fringes in hologram interferometry will do so in this process also, and the characteristic fringe functions will be impressed on the magnitudes of the values stored.

4.3.2.1.1. Fundamentals of OEH

There are a number of experimental methods used to study displacements and deformation of objects. These methods are primarily based on the use of mechanical probes, strain gauges, and accelerometers and, in general, are invasive because they may affect response of the component to the load. In 1965, however, the method of hologram interferometry was invented (Powell and Stetson, 1965) and provided means by which holograms of objects could be readily recorded. Quantitative interpretation of interference fringes has traditionally been tedious and prone to considerable inaccuracy. This has led to the use of heterodyne and phase step methods to read out the interferometric fringes produced during reconstruction of holograms of vibrating objects. Although these methods (Ineichen and Mastner, 1980; Stetson, 1970, 1982; Hariharan and Oreb, 1986; and Pryputniewicz, 1988) allowed high accuracy, 1/1000 and 1/100 of one fringe, respectively, in measurements of local phase differences, they still required physical recording of a permanent hologram in some type of photosensitive medium, which requires lengthy processing. Therefore, these methods, which require lengthy

processing, do not qualify for fully automated hologram analysis. To overcome this

drawback, an automated method for processing of vibration fringes has been developed

(Stetson and Brohinsky, 1988). In this method, measurements of irradiances produced by

mutual interference of the object and reference fields are made electronically by a

detector array. Processing of this interferometric information and display of the

computational results are carried out concomitantly with measurements of irradiation.

Because this method does not depend on recording of holograms in a conventional media,

but rather relies on electronic acquisition, processing, and display of optical interference

information, it is called OEH, also referred to as Electronic Holography, or TV

Holography (Pryputniewicz, 1990).

The OEH method allows automated processing of fringes of statically and

dynamically loaded objects (Stetson and Brohinsky, 1988; Pryputniewicz and Stetson,

1989). In this method, measurements of irradiances produced by mutual interference of

the object and the reference fields are made electronically by a CCD camera, Fig. 4.18.

In the following sections, application of OEH to static measurements is described.

4.3.2.1.2. Electronic processing of holograms

The OEH system is capable of performing either static or dynamic measurements.

In the discussion that follows, static measurements are implemented by the double-

exposure method. The double-exposure method was utilized in this project to perform

96

measurements on the MEMS gyroscope. More specifically, "static" double-exposure

method was used to study shape and static deformations of the microgyroscopes.
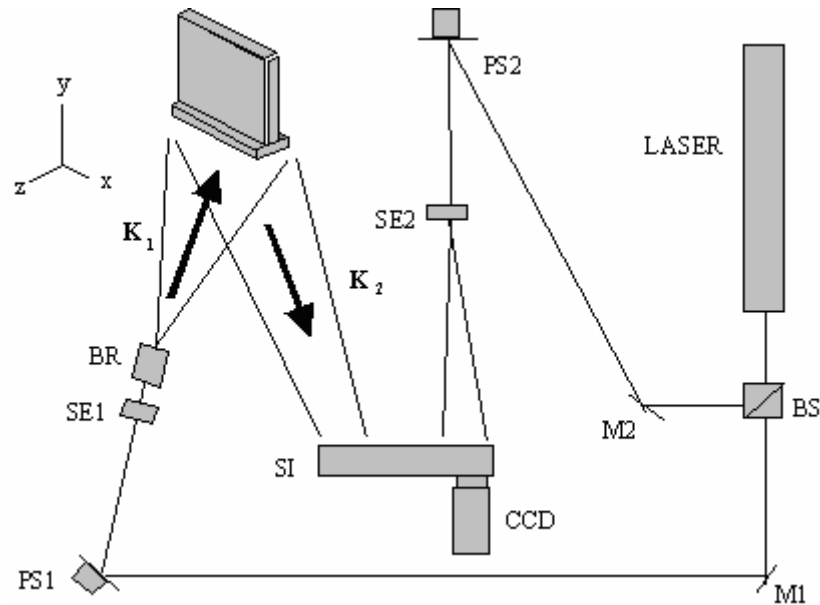
Fig. 4.18. The OEH system: BS is the beam splitter, M1 and M2 are the mirrors, PS1 and PS2 are the phase steppers, SE1 and SE2 are the spatial filter beam expander assemblies, BR is the object beam rotator, SI is the speckle interferometer, CCD is the camera, and K_1 and K_2 are the directions of illumination and observation vectors, respectively.

4.3.2.1.2.1. Double-exposure method

Static measurements are characterized by recording "single-exposure" holograms

of an object at different states of stress (Pryputniewicz, et. al, 2001). As a result of

interference between a set of two "single-exposure" holograms, fringes form, if there are

any optical path differences between the corresponding points on the object as recorded

in the two holograms.

In OEH, this process is carried out by recording sequential frames of images of the object corresponding to the two states of stress (Pryputniewicz, 1983). Typically, four (or more) sequential frames are recorded, with a finite phase step - imposed on the reference beam - between each frame, for every single-exposure image of the object. In the following discussion, in order to simplify derivation of equations describing the OEH process for static measurements, the object will be initially unstressed; results would be the same if the object was stressed initially but mathematics would be much more complicated (Pryputniewicz, et. al, 2001).

The image of an unstressed (i.e., unloaded) object can be described by the irradiance distribution for the *n-th* sequential frame, $I_n(x, y)$, the irradiance at the detector array of a CCD camera in the OEH system setup, as

$$I_n(x,y) = I_o(x,y) + I_r(x,y) + 2A_o(x,y)A_r(x,y)\cos[\Delta\phi(x,y) + \Delta\theta_n] \quad , \qquad (4.119)$$

while the corresponding image of the stressed (i.e., loaded) object can be described by the irradiance distribution, $I_n{'}(x, y)$, as

$$I_n{'}(x,y) = I_o{'}(x,y) + I_r{'}(x,y) + \\ 2A_o{'}(x,y)A_r{'}(x,y)\cos[\Delta\phi(x,y) + \Omega(x,y) + \Delta\theta_n] \qquad . \qquad (4.120)$$

In Eqs 4.119 and 4.120, x and y identify coordinates of the detectors in the array, I_o and I_r are irradiances of the object and reference beams, respectively, $\Delta\phi$ is the phase difference between these beams, $\Delta\theta_n$ is the finite phase step imposed on the reference beam between sequential frames recording individual images, and Ω is the fringe-locus function, constant values of which define fringe loci on the surface of the object.

Since I and I' are measured at known coordinates x and y, Eqs 4.119 and 4.120 contain four unknowns, i.e., irradiances (which are squares of the amplitudes) of the two fields, the phase difference between these fields, and the fringe-locus function. The goal of the analysis is to determine Ω because it is related directly to displacements and deformations of the object.

In OEH, $\Delta\phi$ is eliminated by recording sequentially four image frames with an introduction of a 90° phase step between each frame. That is, $\Delta\theta_n$, appearing in Eqs 4.119 and 4.120 takes on the values of 0°, 90°, 180°, and 270°. This process can be represented by two sets of four simultaneous equations corresponding to Eqs 4.119 and 4.120, respectively, i.e.,

$$I_1 = I_o + I_r + 2A_o A_r \cos(\Delta\phi + 0°) \quad , \tag{4.121}$$

$$I_2 = I_o + I_r + 2A_o A_r \cos(\Delta\phi + 90°) \quad , \tag{4.122}$$

$$I_3 = I_o + I_r + 2A_o A_r \cos(\Delta\phi + 180°) \quad , \tag{4.123}$$

$$I_4 = I_o + I_r + 2A_o A_r \cos(\Delta\phi + 270°) \quad , \tag{4.124}$$

and

$$I_1' = I_o' + I_r + 2A_o' A_r \cos(\Delta\phi + \Omega + 0°) \quad , \tag{4.125}$$

$$I_2' = I_o' + I_r + 2A_o' A_r \cos(\Delta\phi + \Omega + 90°) \quad , \tag{4.126}$$

$$I_3' = I_o' + I_r + 2A_o' A_r \cos(\Delta\phi + \Omega + 180°) \quad , \tag{4.127}$$

$$I_4' = I_o' + I_r + 2A_o' A_r \cos(\Delta\phi + \Omega + 270°) \quad , \tag{4.128}$$

where the arguments (x, y) were omitted for simplification. Evaluation of Eqs 4.121 to 4.128 yields

$$I_1 = I_o + I_r + 2A_o A_r \cos \Delta\phi \quad , \tag{4.129}$$

$$I_2 = I_o + I_r + 2A_o A_r \sin \Delta\phi \quad , \tag{4.130}$$

$$I_3 = I_o + I_r - 2A_o A_r \cos \Delta\phi \quad , \tag{4.131}$$

$$I_4 = I_o + I_r - 2A_o A_r \sin \Delta\phi \quad , \tag{4.132}$$

and

$$I_1' = I_o' + I_r + 2A_o' A_r \cos(\Delta\phi + \Omega) \quad , \tag{4.133}$$

$$I_2' = I_o' + I_r + 2A_o' A_r \sin(\Delta\phi + \Omega) \quad , \tag{4.134}$$

$$I_3' = I_o' + I_r - 2A_o' A_r \cos(\Delta\phi + \Omega) \quad , \tag{4.135}$$

$$I_4' = I_o' + I_r - 2A_o' A_r \sin(\Delta\phi + \Omega) \quad . \tag{4.136}$$

It should be noted that systems of equations similar to Eqs 4.129 to 4.132 and Eqs 4.133 to 4.136 could be obtained using any value of the phase step, however, use of the 90° phase step results in the simplest computations.

Subtracting Eqs 4.129 and 4.131 as well as Eqs 4.130 and 4.132 we obtain, for the unstressed object, the following set of two equations:

$$(I_1 - I_3) = 4A_o A_r \cos \Delta\phi \quad , \tag{4.137}$$

and

$$(I_2 - I_4) = 4A_o A_r \sin \Delta\phi \quad . \tag{4.138}$$

Following the above procedure and subtracting Eqs 4.133 and 4.135 as well as 4.134 and 4.136, a set of two equations is obtained for the stressed object, i.e.,

$$\left(I_1' - I_3'\right) = 4A_o' A_r \cos(\Delta\phi + \Omega) \quad , \tag{4.139}$$

and

$$\left(I_2{}' - I_4{}'\right) = 4A_o{}' A_r \sin(\Delta\phi + \Omega) \quad . \tag{4.140}$$

Addition of Eqs 4.137 and 4.139 yields

$$\left(I_1 - I_3\right) + \left(I_1{}' - I_3{}'\right) = 4A_o A_r \cos\Delta\phi + 4A_o{}' A_r \cos(\Delta\phi + \Omega) \quad . \tag{4.141}$$

Because object displacements and deformations are small, it can be assumed that

$A_o' \approx A_o$. Therefore, Eq. 4.141 becomes

$$\left(I_1 - I_3\right) + \left(I_1{}' - I_3{}'\right) = 4A_o A_r \left[\cos\Delta\phi + \cos(\Delta\phi + \Omega)\right] \quad . \tag{4.142}$$

Recognizing that $\cos(\Delta\phi + \Omega) = \cos\Delta\phi\cos\Omega - \sin\Delta\phi\sin\Omega$, Eq. 4.142 can be written as

$$D_1 = \left(I_1 - I_3\right) + \left(I_1{}' - I_3{}'\right) = 4A_o A_r \left[(1 + \cos\Omega)\cos\Delta\phi - \sin\Delta\phi\sin\Omega\right] \quad . \tag{4.143}$$

In a similar way, addition of Eqs 4.138 and 4.140 simplifies to

$$D_2 = \left(I_2 - I_4\right) + \left(I_2{}' - I_4{}'\right) = 4A_o A_r \left[(1 + \cos\Omega)\sin\Delta\phi + \cos\Delta\phi\sin\Omega\right] \quad . \tag{4.144}$$

Finally, addition of the squares of Eqs 4.133 and 4.144 yields

$$D_1{}^2 + D_2{}^2 = \{4A_o A_r \left[(1 + \cos\Omega)\cos\Delta\phi - \sin\Delta\phi\sin\Omega\right]\}^2 + \\ \{4A_o A_r \left[(1 + \cos\Omega)\sin\Delta\phi + \cos\Delta\phi\sin\Omega\right]\}^2 \tag{4.145}$$

which reduces to

$$D_1{}^2 + D_2{}^2 = 16A_o{}^2 A_r{}^2 \left[(1 + \cos\Omega)^2 + \sin^2\Omega\right] \quad , \tag{4.146}$$

wherefrom

$$D_1{}^2 + D_2{}^2 = 32A_o{}^2 A_r{}^2 (1 + \cos\Omega) \quad . \tag{4.147}$$

Furthermore, recognizing that $(1 + \cos\Omega) = 2\cos^2\left(\dfrac{\Omega}{2}\right)$, Eq 4.147 can be reduced to

$$\sqrt{\left(D_1^{\,2} + D_2^{\,2}\right)} = 8 A_o A_r \cos\left(\frac{\Omega}{2}\right) \quad , \tag{4.148}$$

which represents the static viewing image displayed by the OEH. In Eq. 4.148, Ω is the fringe-locus function corresponding to the static displacements and/or deformations of the object. The fringe-locus function can be determined by processing the sequential OEH images as described below.

In order to obtain data from the OEH images, we will again employ Eqs 4.127 to 4.136 and follow the procedure used to derive Eq. 4.147. The result of this procedure is

$$D_3 = \left(I_1 - I_3\right) - \left(I_1' - I_3'\right) = 4 A_o A_r \left[(1 - \cos\Omega)\cos\Delta\phi + \sin\Delta\phi\sin\Omega\right] \quad , \tag{4.149}$$

$$D_4 = \left(I_2 - I_4\right) - \left(I_2' - I_4'\right) = 4 A_o A_r \left[(1 - \cos\Omega)\sin\Delta\phi - \cos\Delta\phi\sin\Omega\right] \quad , \tag{4.150}$$

Equations 4.149 and 4.150 lead to

$$D_3^{\,2} + D_4^{\,2} = 32 A_o^{\,2} A_r^{\,2}(1 - \cos\Omega) \quad . \tag{4.151}$$

Subtracting Eq 4.151 from Eq 4.147 we obtain

$$D = \left(D_1^{\,2} + D_2^{\,2}\right) - \left(D_3^{\,2} + D_4^{\,2}\right) = 32 A_o^{\,2} A_r^{\,2}(1 + \cos\Omega) - 32 A_o^{\,2} A_r^{\,2}(1 - \cos\Omega)$$

or

$$D = 64 A_o^2 A_r^2 \cos\Omega \quad . \tag{4.152}$$

Starting with Eqs 4.137 to 4.140, we can also determine (Pryputniewicz, 1983)

$$N_1 = \left(I_1 - I_3\right) + \left(I_2' - I_4'\right) = 4 A_o A_r \left[(1 + \sin\Omega)\cos\Delta\phi + \sin\Delta\phi\cos\Omega\right] \quad , \tag{4.153}$$

$$N_2 = \left(I_2 - I_4\right) + \left(I_1' - I_3'\right) = 4A_o A_r\left[(1 + \sin\Omega)\sin\Delta\phi - \cos\Delta\phi\cos\Omega\right] \quad, \quad (4.154)$$

$$N_3 = \left(I_1 - I_3\right) + \left(I_2' - I_4'\right) = 4A_o A_r\left[(1 - \sin\Omega)\cos\Delta\phi - \sin\Delta\phi\cos\Omega\right] \quad, \quad (4.155)$$

$$N_4 = \left(I_2 - I_4\right) + \left(I_1' - I_3'\right) = 4A_o A_r\left[(1 - \sin\Omega)\sin\Delta\phi + \cos\Delta\phi\cos\Omega\right] \quad, \quad (4.156)$$

$$N_1{}^2 + N_2{}^2 = 32A_o{}^2 A_r{}^2(1 + \sin\Omega) \quad, \quad (4.157)$$

$$N_3{}^2 + N_4{}^2 = 32A_o{}^2 A_r{}^2(1 - \sin\Omega) \quad, \quad (4.158)$$

and

$$N = \left(N_1{}^2 + N_2{}^2\right) - \left(N_3{}^2 + N_4{}^2\right) = 64A_o{}^2 A_r{}^2 \sin\Omega \quad . \quad (4.159)$$

Finally, dividing Eq. 4.159 by Eq. 4.152, we obtain

$$\frac{N}{D} = \frac{64A_o{}^2 A_r{}^2 \sin\Omega}{64A_o{}^2 A_r{}^2 \cos\Omega} \quad, \quad (4.160)$$

from which it follows that

$$\Omega = \tan^{-1}\left(\frac{N}{D}\right) \quad . \quad (4.161)$$

It should be noted that Ω, computed from Eq. 4.161, is a spatial function that depends on coordinates x and y. Therefore, its values are determined for every coordinate pair (x, y) in the object space. Once the values of Ω are determined, they can be used to compute object displacements as discussed in Section 4.3.2.1.2.2.

4.3.2.1.2.2. Determination of displacements based on the fringe-locus function

As described in Section 4.3.2.1.2.1, images recorded by the CCD are processed by the image-processing computer (IP) to determine the fringe-locus function, Ω, constant values of which define fringe loci on the surface of object under investigation. The values of Ω relate to the system geometry and the unknown vector **L,** defining deformations, via the relationship (Pryputniewicz, 1995a; Furlong and Pryputniewicz, 2000)

$$\Omega = \left(\mathbf{K}_2 - \mathbf{K}_1\right) \bullet \mathbf{L} = \mathbf{K} \bullet \mathbf{L} \quad , \tag{4.162}$$

where **K** is the sensitivity vector defined in terms of vectors $\mathbf{K}_1$ and $\mathbf{K}_2$ identifying directions of illumination and observation, respectively, in the OEH system, Fig. 4.19.

Quantitative determination of structural deformations due to the applied loads can be obtained, by solving a system of equations similar to Eq. 4.162, to yield (Pryputniewicz, 1995a)

$$\mathbf{L} = \left[\widetilde{\mathbf{K}}^{\mathrm{T}}\widetilde{\mathbf{K}}\right]^{-1}\left(\widetilde{\mathbf{K}}^{\mathrm{T}}\Omega\right) \quad , \tag{4.163}$$

where $\widetilde{\mathbf{K}}^{\mathrm{T}}$ represents the transpose of the matrix of the sensitivity vectors **K**. Equation 4.163 indicates that deformations determined from interferograms are functions of **K** and Ω, which have spatial, i.e., (*x,y,z*), distributions over the field of interest on the object being investigated. Equation 4.163 can be represented by a phenomenological equation (Pryputniewicz, 1993)

$$\mathbf{L} = \mathbf{L}\left(\mathbf{K},\Omega\right) \quad , \tag{4.164}$$

based on which the RSS-type uncertainty in **L**, i.e., $\delta\mathbf{L}$, can be determined to be

$$\delta\mathbf{L} = \left[\left(\frac{\partial\mathbf{L}}{\partial\mathbf{K}}\delta\mathbf{K}\right)^2 + \left(\frac{\partial\mathbf{L}}{\partial\Omega}\delta\Omega\right)^2\right]^{1/2} \quad , \tag{4.165}$$

where $\partial\mathbf{L}/\partial\mathbf{K}$ and $\partial\mathbf{L}/\partial\Omega$ represent partial derivatives of $\mathbf{L}$ with respect to $\mathbf{K}$ and Ω, respectively, while $\delta\mathbf{K}$ and $\delta\Omega$ represent the uncertainties in $\mathbf{K}$ and Ω, respectively. It should be remembered that $\mathbf{K}$, $\mathbf{L}$, and Ω are functions of spatial coordinates (x,y,z), i.e., $\mathbf{K} = \mathbf{K}(x,y,z)$, $\mathbf{L} = \mathbf{L}(x,y,z)$, and $\Omega = \Omega(x,y,z)$, respectively, when performing partial differentiations.
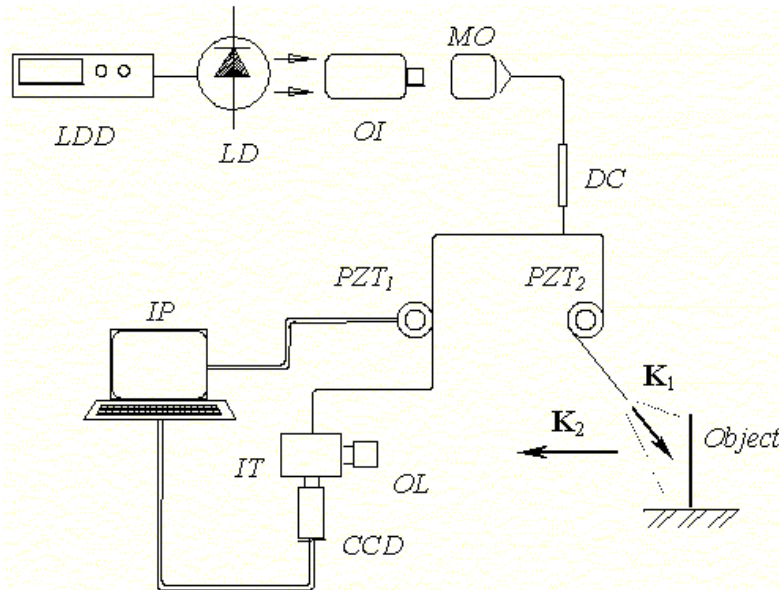
Fig. 4.19. Single-illumination and single-observation geometry of a fiber optic based OEH system: *LDD* is the laser diode driver, *LD* is the laser diode, *OI* is the optical isolator, *MO* is the microscope objective, DC is the fiber optic directional coupler, *PZT$_1$* andand *PZT$_2$* are the piezoelectric fiber optic modulators, *IP* is the image-processing computer, *IT* is the interferometer, *OL* is the objective lens, *CCD* is the camera, while $\mathbf{K}_1$ and $\mathbf{K}_2$ are the directions of illumination and observation, respectively.

After evaluating, Eq. 4.165 indicates that $\delta\mathbf{L}$ is proportional to the product of the local value of $\mathbf{L}$ with the RSS value of the ratios of the uncertainties in $\mathbf{K}$ and Ω to their corresponding local values, i.e.,

$$\delta\mathbf{L} \propto \mathbf{L}\left[\left(\frac{\delta\mathbf{K}}{\mathbf{K}}\right)^2 + \left(\frac{\delta\Omega}{\Omega}\right)^2\right]^{1/2} \quad . \tag{4.166}$$

For typical geometries of the OEH systems used in recording of interferograms, the values of $\delta\mathbf{K}/\mathbf{K}$ are less than 0.01. However, for small deformations, the typical values of $\delta\Omega/\Omega$ are about one order of magnitude greater than the values for $\delta\mathbf{K}/\mathbf{K}$. Therefore, the accuracy with which the fringe orders are determined influences the accuracy in the overall determination of deformations (Pryputniewicz, 1981). To minimize this influence, a number of algorithms for determination of Ω were developed. Some of these algorithms require multiple recordings of each of the two states, in the case of double-exposure method, of the object being investigated with introduction of a discrete phase step between the recordings (Furlong, 1999; Pryputniewicz, 1995b; Furlong and Pryputniewicz, 2000).

4.3.2.2. OELIM methodology

Deformations of microgyroscopes were determined, in this thesis, using optoelectronic laser interferometric microscope (OELIM) methodology, which is based on the OEH method (Section 4.3.2.1), but specifically implemented for the study of MEMS (Brown and Pryputniewicz, 2000). In OELIM, a beam of collimated coherent

light is brought into the system and is directed into a spatial filter (SF) assembly

consisting of a microscope objective and a pinhole filter, Fig. 4.20. The resulting,

expanded, light field is then collimated by lens L1, and redirected by the directional beam

splitter (DBS) through the long distance microscope objective lens (MO) to illuminate the

microgyroscope (Pryputniewicz, et al., 2000). In the OELIM configuration shown in Fig.

4.20, the proximal beam splitter (PBS) is placed close to the MEMS. The reflected light

is transmitted back through MO, DBS, and the relay lens to the CCD camera. The CCD

camera captures images of the microgyroscope to measure its shape, or as it deforms

during functional operation. The images are then analyzed and shape or deformation

fields are determined.
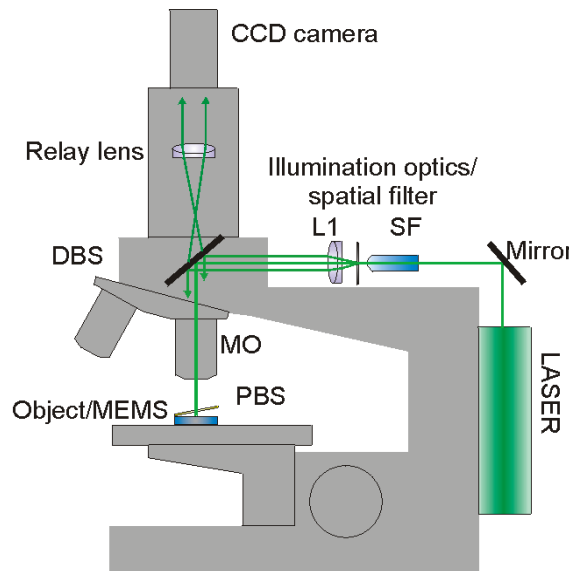
Fig. 4.20. Microscope based optical configuration of the OELIM
system: SF is the spatial filter/beam expander, L1 is the
illumination optics, DBS is the directional beam splitter, MO is the
microscope objective, PBS is the proximal beam splitter, CCD is
the host computer controlled image acquisition camera
(Pryputniewicz, et al., 2000).

4.3.2.3. OELIM system and procedure

The optical and electronic configurations of the OELIM system are shown in Figs 4.20 and 4.21, respectively. In the OELIM system, the laser output is divided into two beams by means of a beam splitter. One of these beams is directed via a piezoelectrically driven mirror and is shaped by the spatial filter beam expander assembly to illuminate the object uniformly; this mirror can be driven at the same frequency as the object excitation to provide bias vibration, when studying MEMS during their functional operation. The other beam, also spatially filtered and expanded, is directed toward the reference input of the speckle interferometer by another piezoelectrically driven mirror that introduces 90° phase steps between consecutive frames. The speckle interferometer combines the object beam with the reference beam and directs them collinearly toward the detector array of the CCD camera (Steward and Saggal, 2002; Steward, et al., 2002).
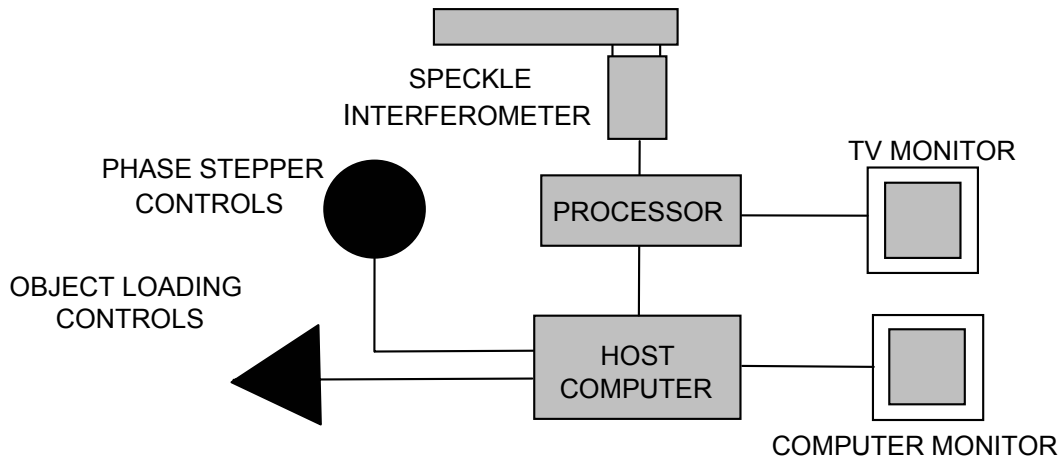
Fig. 4.21. Electronic configuration of the OELIM system.

In the OELIM system, the CCD camera detects the interference pattern and sends it to the pipeline processor, Fig. 4.21. In the processor, the sequential frames are analyzed. All computations, relating to image analysis, are done in a pipeline processor, which operates under control of a host computer. The host computer also controls excitation of the object, coordinates it with the bias vibration imposed on the object, and keeps track of the 90° phase stepping between the frames.

By operating on each input image and its three predecessors, the pipeline processor produces a hologram, and this hologram may be viewed concomitantly on the TV monitor. The resulting electronic holograms are then processed by the host computer to determine spatial distribution of the displacement/deformation vectors that can be viewed directly on the computer monitor. The microscope setup that was used to measure the shape of the microgyro is illustrated in Figs 4.22 and 4.23.

Fig. 4.22. OELIM microscope setup.

Fig. 4.23. Close-up of the microscope setup.

5. RESULTS AND DISCUSSION

This thesis makes use of the ACES methodology to determine deformations of MEMS gyroscopes. Therefore, the results were obtained using the analytical, computational, and experimental solutions methodology that was described in Chapter 4. These results are presented in this chapter beginning with the analytical displacement calculations for a folded spring, which are complemented by the computational FEM analyses done in COSMOS/M, and then followed by the preliminary experimental results. When presenting analytical, computational, and experimental results, selected comparisons between these results were made to determine degrees of correlation, subject to the uncertainty limits.

5.1. Analytical results

Because of inherent differences that usually are found between analytical and computational results of the same object, due to assumptions and approximations used while developing models, two different cases, addressing modeling of the folded spring, were considered in this thesis. The first case, addressing model of the folded spring represented only by a cantilever section *CD*, was used to establish degree of correlation between the analytical and computational results on a relatively simple structure such as a cantilever. Clearly, of this case, when the analytical model and computational model are properly developed and solved, differences between the corresponding results should be "zero."

In the second case, addressing the entire folded spring, assumptions and approximations used to develop the analytical model may not be the same as those used in the commercial FEM code used for the computational solutions. Therefore, finite differences may be obtained when comparing results of analytical and computational solutions for deformations of the folded spring. Analytical results presented in this section comprise of deformations at point D of the cantilever beam alone, at point D considering the entire folded spring, and the uncertainty analysis of these deformations, discussed in Sections 5.1.1 and 5.1.2, respectively.

5.1.1. Analytically determined deformations at point D

Analytical results were obtained by applying the force in the x, i.e., in-plane direction, Eq. 4.86, and the Coriolis force, Eq. 2.7, to the folded spring. The force in the x, or the in-plane direction, is due to the oscillatory motion of the proof mass. Therefore, the force calculated for the in-plane displacement is time varying, i.e., $F_x(t)$, leading to time varying displacement $\Delta_x(t)$. In order to obtain the $F_x(t)$, the displacement of the proof mass had to be calculated first, using Eq. 4.80, the motion of the proof mass over five periods of oscillation is illustrated in Fig. 5.1.

After the displacements were calculated the time derivative of Eq. 4.80 was taken to obtain the speed of the proof mass expressed by Eq. 4.81, with the results displayed in Fig. 5.2. In order to determine the force applied to the folded springs that support the proof masses of the microgyro, acceleration the proof mass was calculated based on Eq.

111

4.82, Fig. 5.3.
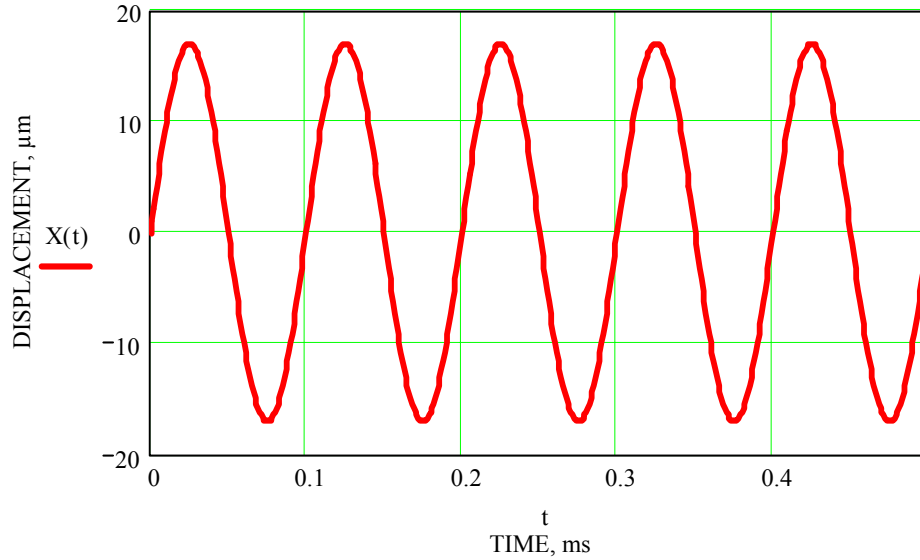
Fig. 5.1. Sinusoidal displacements, as a function of time, for the proof mass of the microgyro resonating at 10 kHz.
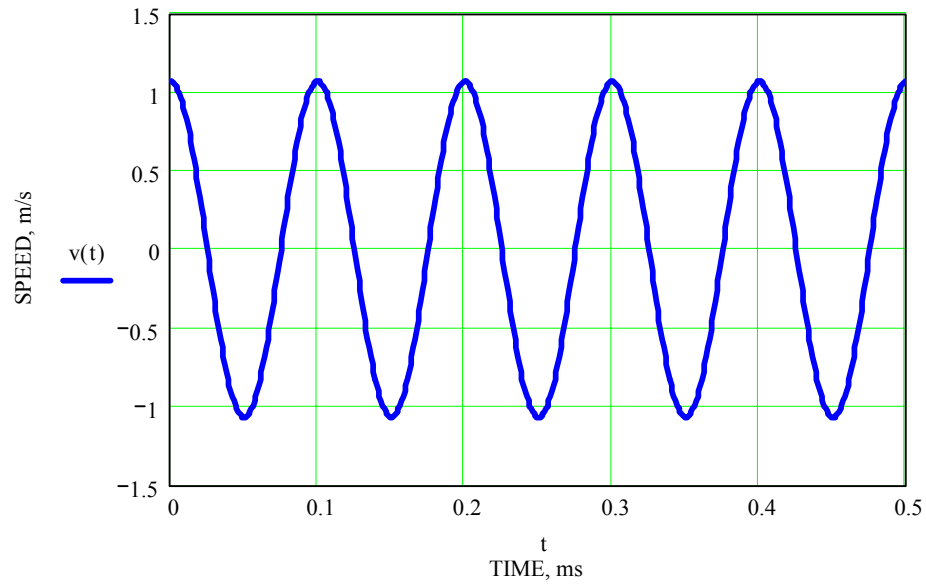
Fig. 5.2. Speed, as a function of time, for the proof mass of the microgyro resonating at 10 kHz.
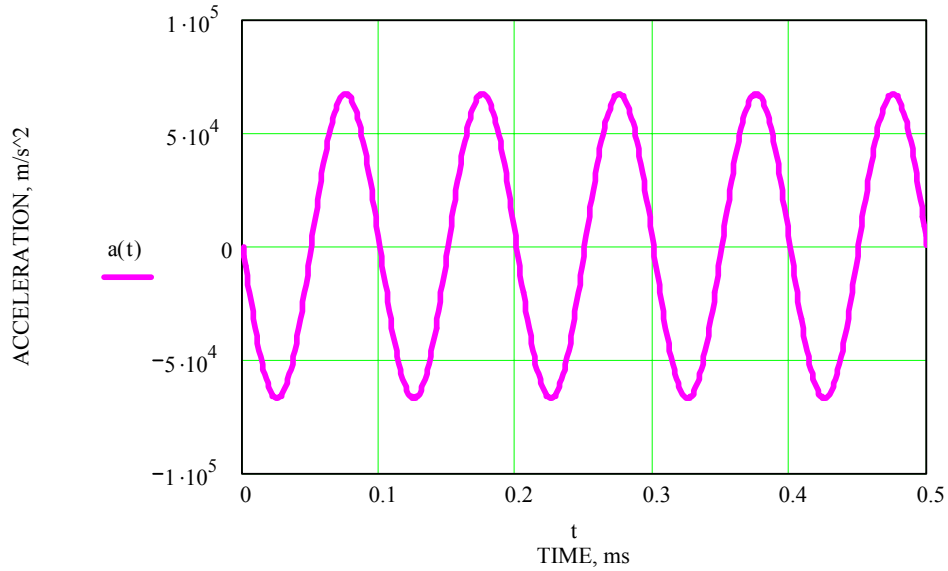
Fig. 5.3. Acceleration, as a function of time, for the proof mass of the microgyro resonanting at 10 kHz.

For many applications, the acceleration of an object is represented in g's, i.e., multiples of gravitational acceleration. Figure 5.4 illustrates acceleration of the proof mass of the microgyro in g's.

Using accelerations illustated in Figs 5.3 and 5.4, the time dependent in-plane force acting on the individual folded springs was calculated, using Eq. 4.79, and is illustrated in Fig. 5.5. The time dependent in-plane force, $F_x(t)$, was used to determine the x-component and z-component of the displacement defined by Eqs 4.76 and 4.78, respectively, with the results displayed in Figs 5.6 and 5.7, respectively. The magnitude of the x-component of these displacements varies from -21 μm to +21 μm, while the magnitude of the z-component of the displacements ranges from -2.4 μm to +2.4 μm.

113
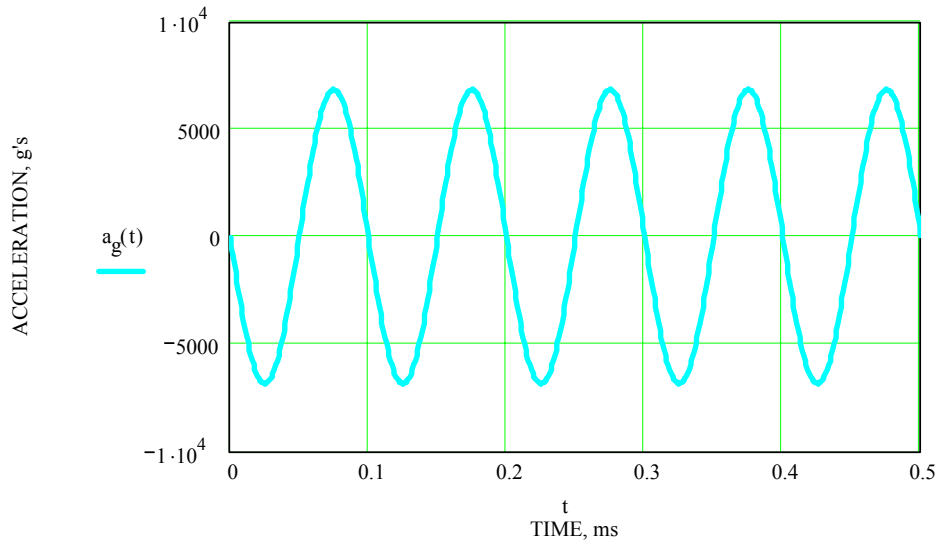
Fig. 5.4. Acceleration in g's, as a function of time, for the proof mass of the microgyro resonanting at 10 kHz.
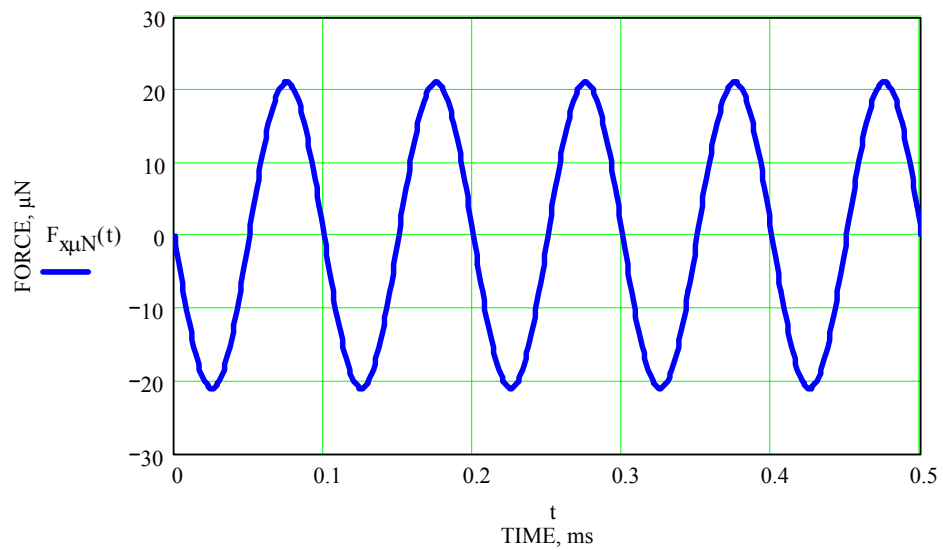
Fig. 5.5. Time dependent in-plane force acting on the folded spring of the microgyro.
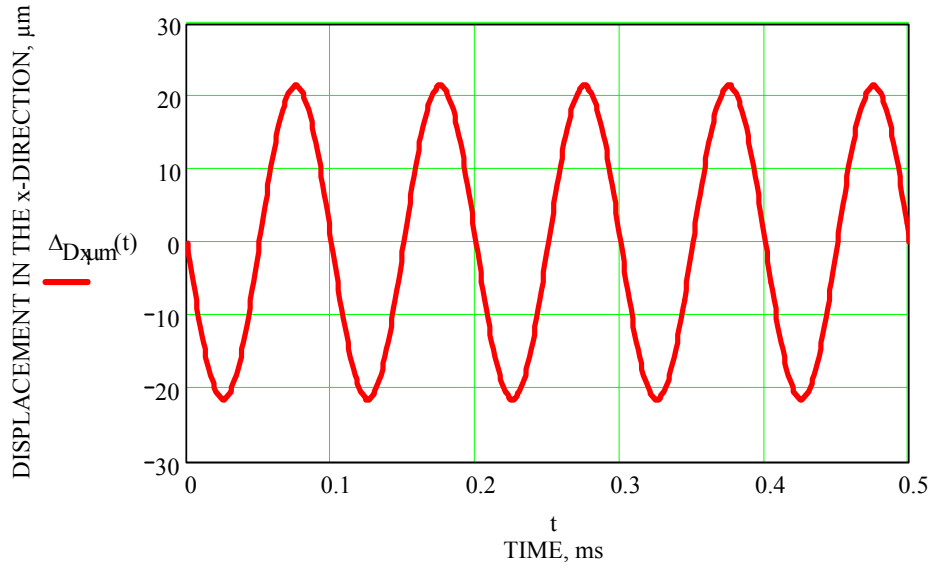
Fig. 5.6. Time dependent *x*-component of displacement at point *D*, of the folded spring at the proof mass, of the microgyroscope resonanting at 10 kHz.
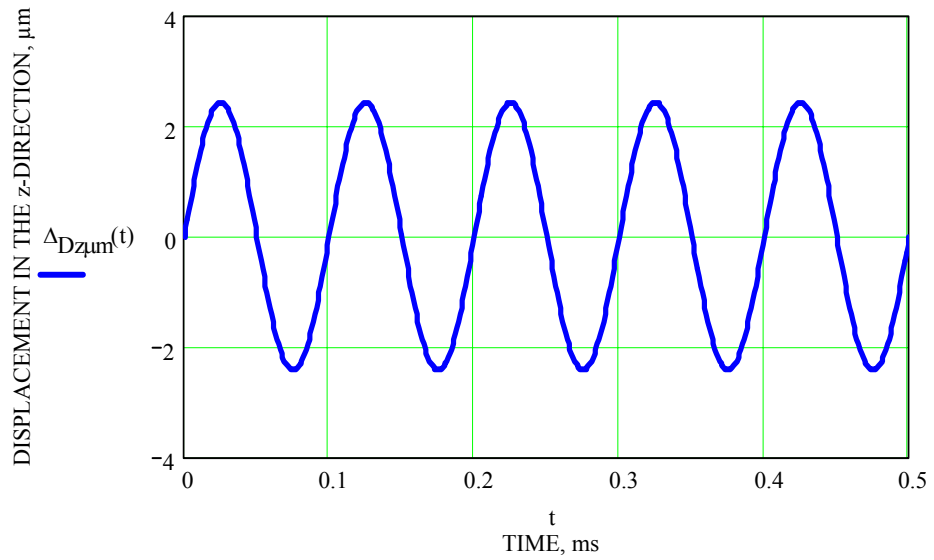
Fig. 5.7. Time dependent *z*-component of displacement, at point *D* on the folded spring at the proof mass, of the microgyroscope resonanting at 10 kHz.

Based on the results shown in Fig. 5.5 and the results obtained using Eq. 2.7, forces used in the analytical and computational determinations of the deformations at point D on the folded spring are as listed in Table 5.1, where the force in the z-direction was assumed to be zero, for this application.

Table 5.1. Forces applied to the analytical equations.

Force	Value
x-direction, F_x	21.075 μN
y-direction, F_y	0.744747 nN
z-direction, F_z	0.0

The displacements at the point of force application, point D, for the cantilever beam representing the folded spring, derived in Section 4.1.3.2, were determined using the forces listed in Table 5.1 and Eqs 4.46 to 4.48 with results summarized in Table 5.2. Displacements at point D while considering the entire folded spring were determined using the forces listed in Table 5.1 and Eqs 4.76 to 4.78 with results summarized in Table 5.3

Table 5.2. Displacements at point D based on the analytical considerations of the cantilever beam.

Direction	Value
x-displacement, Δ_{dx}	10.6719 μm
y-displacement, Δ_{dy}	0.5434 nm
z-displacement, Δ_{dz}	0 μm

Table 5.3. Displacements at point *D* based on the analytical
considerations of the entire folded spring.

Direction	Value
x-displacement, Δ_{Dx}	21.4583 μm
y-displacement, Δ_{Dy}	1.1314 nm
z-displacement, Δ_{Dz}	-2.4268 μm

Based on Eqs 4.76 to 4.78, in Table 5.3 there is displacement in the *z*-direction, for the

folded spring, even without force acting directly in the *z*-direction, because of bending

effects in Section *BC*, due to the force in the *x*-direction. However, based on Eqs 4.46 to

4.48, there is no deformation in the *z*-direction because the cantilever does not produce

any twisting; therefore, there is no deformation in the *z*-direction. The values shown in

Tables 5.2 and 5.3 will be used for comparisons with the computational results.

5.1.2. Uncertainty analysis of the analytically determined deformations at point *D*

In order to determine how good the analytical results obtained in Section 5.1.1

are, an uncertainty analysis was performed. This analysis was performed for all three

Cartesian components of the deformations at point *D*, based on Eqs 4.76 to 4.78, Section

4.1.5. Initial evaluation of the overall uncertainties in Δ_{Dx}, Δ_{Dy}, and Δ_{Dz} was based on the

values of the independent parameters and their uncertainties as listed in Table 4.4.

Results for this first case of determination of uncertainties in deformations at point *D* are

summarized in Table 5.4 and indicate that percent overall uncertainties for all three

deformations were above 55%. The percent overall uncertainties are based on the

analytically determined deformations at point D listed in Table 5.3. The largest

individual contributors to the overall uncertainty were due to the uncertainty in the

thickness for the deformations in the out-of-plane direction and due to the uncertainty in

width of Sections *AB* and *CD* for the deformations in the in-plane directions.

Table 5.4. Summary of overall uncertainties in the deformations at
point *D*, for the first case.

Calculated uncertainty		Percent uncertainty	Largest contributor
$\delta\Delta_{Dx}$	12.51 μm	58.29%	δb
$\delta\Delta_{Dy}$	0.72 nm	61.60%	δh
$\delta\Delta_{Dz}$	1.42 μm	58.49%	δb

Since the overall uncertainties in the first case were too high they had to be

reduced. This reduction can only be achieved by optimizing uncertainties in the

independent parameters without any changes in the nominal values of these parameters

(Pryputniewicz, 1993). For example, to reduce the overall uncertainty in Δ_{Dy}, the

uncertainty in the thickness, which was established to be the largest contributor to $\delta\Delta_{Dy}$,

was reduced to 0.125 μm representing 5% of the nominal value, i.e., current industry

practice for the tolerance in fabricating the thickness. In order to reduce the overall

uncertainties in Δ_{Dx} and Δ_{Dz}, the uncertainty in the width, *b*, was also decreased, to 0.25

μm. This was done because this uncertainty may be assumed to be half of the least

significant digit, (i.e., the least count) in the resolution that is equal to 0.5 μm. Realizing

that width and length are measured using the same microscope, uncertainties in all width

and length dimensions were assumed to be equal to 0.25 μm, as summarized in Table 5.5.

The values of Table 5.5 were used to determine overall uncertainties in deformations at point D, for the second case, Table 5.6.

Table 5.5. Values and uncertainties used during determination of overall uncertainties in deformations at point D, for the second case.

Variable	Units	Value	Uncertainty
L_{AB}	μm	111	0.25
L_{BC}	μm	17	0.25
L_{CD}	μm	98	0.25
b	μm	3	0.25
b_{BC}	μm	10	0.25
h	μm	2.5	$(0.05h) = 0.125$
L_f	μm	40	0.25

Table 5.6. Overall uncertainties in the deformations at point D, for the second case.

Calculated uncertainty		Percent uncertainty	Largest contributor
$\delta\Delta_{Dx}$	5.98 μm	27.85%	δb
$\delta\Delta_{Dy}$	0.21 nm	17.67%	δh
$\delta\Delta_{Dz}$	0.68 μm	27.94%	δb

Using the values of uncertainties of the second case Table 5.5 reduced $\delta\Delta_{Dy}$ to about 18% with δh contributing most to the overall uncertainty, while $\delta\Delta_{Dx}$ and $\delta\Delta_{Dz}$ were reduced to about 28% with δb contributing the most to the corresponding values in the overall uncertainties, Table 5.6. These changes were expected since for the out-of-plane deformations, the largest contributor to the overall uncertainty is the thickness: due to the fact that thickness is cubed in the equations for moment of inertia. Therefore, a change of the uncertainty in thickness should produce a large change in the overall uncertainty. The

119

same is true for the in-plane deformations in the x and z directions: the width is cubed in the moment of inertia; therefore, a reduction of the uncertainty in width produced a large change in the overall uncertainty. Examination of the results summarized in Table 5.6 indicates that all overall uncertainties reduced substantially when compared with the results summarized in Table 5.4. Specifically $\delta\Delta_{Dy}$ reduced from about 62% to about 18%.

The uncertainties of the second case were still large; therefore, to reduce the uncertainties even more, the uncertainty in the thickness was reduced to 1% of the total thickness, i.e., to 0.025 μm. This was done since 1% of the total thickness is the tolerance in thickness that is becoming a practice in fabrication processes for MEMS. Using this value for the uncertainty in thickness, the overall uncertainties for a third case were determined, Table 5.7. The reduction in the uncertainty of the thickness reduced the uncertainty for the deformation in the y-direction to about 10%. The largest contributors to the overall uncertainties were the width for all three Cartesian directions, x, y, and z. Therefore, in order to reduce the overall uncertainties in the deformations at point D the uncertainties in width and length will have to be reduced again, subject to ability to obtain them using fabrication processes available for making MEMS.

Table 5.7. Overall uncertainties in the deformations at point D, for the third case.

Calculated uncertainty		Percent uncertainty	Largest contributor
$\delta\Delta_{Dx}$	5.98 μm	26.96%	δb
$\delta\Delta_{Dy}$	0.12 nm	10.12%	δb
$\delta\Delta_{Dz}$	0.68 μm	27.07%	δb

5.2. Computational results

The first set of computational results obtained in COSMOS/M that will be discussed are those for the deformations of just the cantilever section *CD* representing the folded spring. The results in the *x*-direction will be presented first. Before the deformations were computed, convergence analyses were performed to establish proper meshing, i.e., discretization, of the cantilever. This was done using both linear and parabolic tetrahedral elements. For the linear tetrahedral elements it took about 20,000 elements to properly discretize the cantilever to reach convergence, meaning that the difference between the two most recent discretizations was less than 0.1%; however for the parabolic tetrahedral elements it only took about 7,000 elements.

Results of the convergence analyses for the force acting in the *x*-direction are summarized in Table 5.8 and illustrated in Fig. 5.8 for linear tetrahedral elements and in Table 5.9 and Fig. 5.9 for parbolic tetrahedral elements. Using the COSMOS/M model of the cantilever comprising of 20,000 linear tetrahedral solid elements, deformation field due to the force acting in the *x*-direction was determined, indicating maximum deformation of 10.66 μm at the point of force application, and using 6,664 parabolic tetrahedral solid elements, the deformation field was determined, Fig. 5.10, indicating a maximum deformation of 10.66 μm at point *D*.

The results obtained computationally in COSMOS/M for the deformations in the *y*, i.e., the out-of-plane direction, for the cantilever using linear and parabolic tetrahedral solid elements will now be reviewed. Again, convergence indicates that the folded spring, subjected to a force in the *y*-direction, requires about 20,000 elements to properly

discretize it for the linear elements, Table 5.10 and Fig. 5.11, while only about 7,000

elements for the parabolic elements, Table 5.11 and Fig. 5.12.

Table 5.8. Convergence of the maximum values of the
deformation component in the *x*-direction for the cantilever using
linear tetrahedral elements.

Number of elements	Displacement, μm
188	1.2439
252	2.0705
353	2.988
768	5.2284
1,433	6.0965
6,664	8.3394
13,997	10.66
23,317	10.661
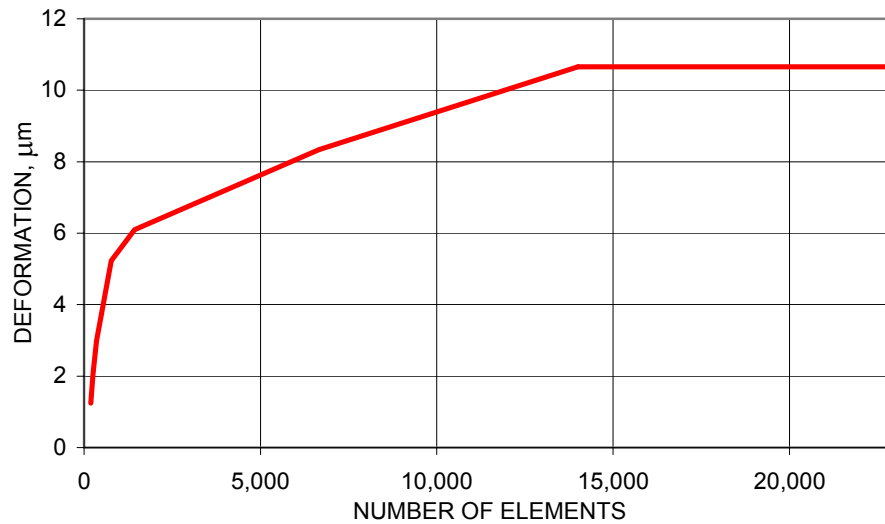
Fig. 5.8. Convergence of the maximum deformations in the *x*-direction, due to
the force in the *x*-direction, for the cantilever using linear tetrahedral elements.

Table 5.9. Convergence of the maximum values of the deformation component in the *x*-direction for the cantilever using parabolic tetrahedral elements.

Number of elements	Deformation, μm
188	10.627
353	10.649
768	10.651
1,786	10.655
4,494	10.659
6,664	10.659
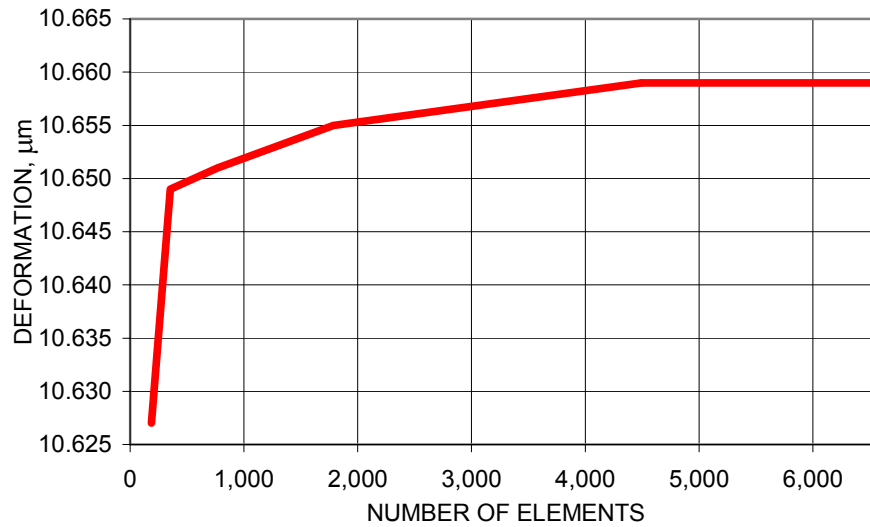
Fig. 5.9. Convergence of the maximum deformations in the *x*-direction, due to the force in the *x*-direction, for the cantilever using parabolic tetrahedral elements.

Using the COSMOS/M model of the cantilever beam comprising of 20,000 linear tetrahedral solid elements, deformation field due to the force acting in the *y*-direction was determined, indicating maximum deformation of 0.54 nm at the point of force application, and using 6,664 parabolic tetrahedral solid elements, the deformation field was determined, Fig. 5.13, indicating a maximum deformation of 0.54 nm at point *D*.
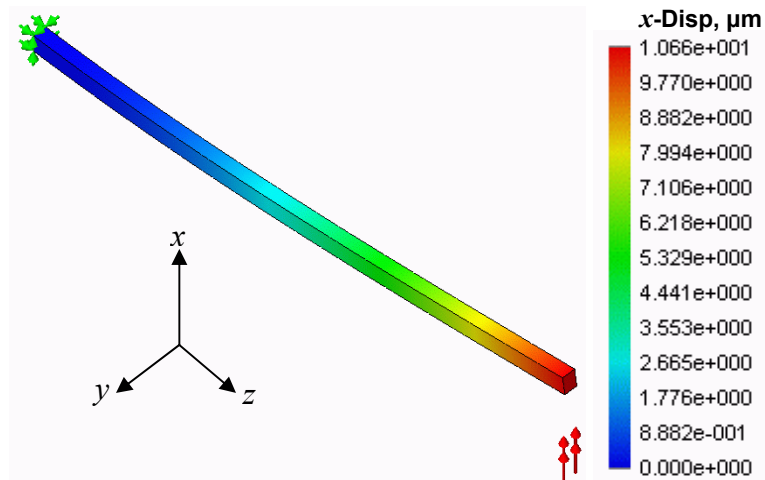
Fig. 5.10. COSMOS/M determined deformation field in the *x*-direction
due to the force in the *x*-direction, for the cantilever using 6,664 parabolic
tetrahedral solid elements.

Table 5.10. Convergence of the maximum values of the deformation component
in the *y*-direction for the cantilever using linear tetrahedral elements.

Number of elements	Deformation, nm
188	0.0557
252	0.085428
353	0.13442
1,433	0.23037
6,664	0.39804
13,997	0.54278
23,317	0.54278

Results from the convergence analyses will be compared with the analytical

deformations that are summarized in Table 5.2. The convergence results illustrate that

the parabolic tetrahedral solid elements converge faster than the linear tetrahedral

elements, because of this the convergence analyses for the entire folded spring were done

using only the parabolic tetrahedral solid elements.
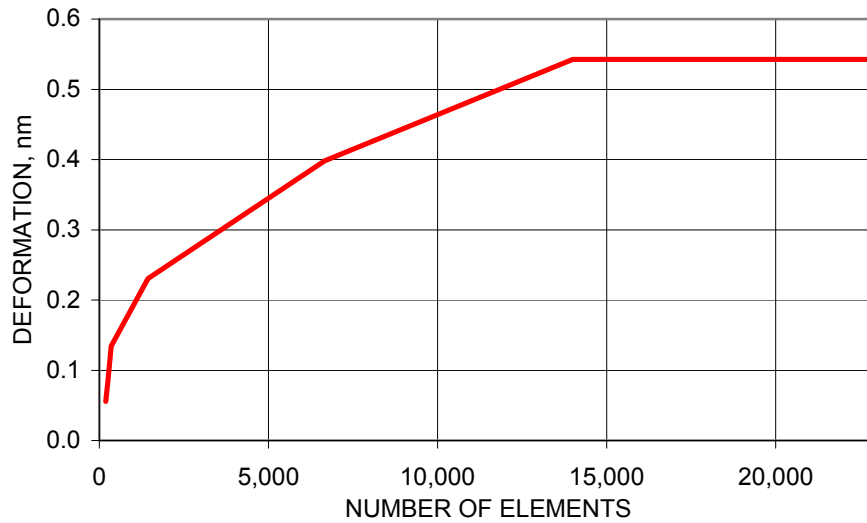
Fig. 5.11. Convergence of the maximum deformations in the *y*-direction, due to the force in the *y*-direction, for the cantilever using linear tetrahedral elements.

Table 5.11. Convergence of the maximum values of the deformation component in the *y*-direction for the cantilever using parabolic tetrahedral elements.

Number of elements	Deformation, nm
188	0.54113
353	0.5418
768	0.54228
1,786	0.5426
4,494	0.54266
6,664	0.54271

Results of convergence analysis of deformations for the entire folded spring due to the force acting in the *x*-direction are summarized in Table 5.12 and displayed in Fig. 5.14. These results indicate that, as the number of elements representing the folded spring increases, the maximum value of the deformation in the direction of the applied force also increases at a decreasing rate, reaching 19.58 μm when 17,000 parabolic

125

tetrahedral solid elements are used. Using the COSMOS/M model of the folded spring comprising of 17,000 parabolic tetrahedral solid elements, deformation field due to the force acting in the x-direction was determined, Fig. 5.15, indicating maximum deformation of 19.58 μm at the point of force application.

The results obtained computationally in COSMOS/M for the deformation in the y, out-of-plane, direction will now be discussed. Again, convergence indicates that the entire folded spring, subjected to a force in the y-direction, requires about 17,000 elements to properly discretize it, Table 5.13 and Fig. 5.16.

COSMOS/M determined deformation field of the spring, defined about 17,000 elements and loaded by a force acting in the y-direction is displayed in Fig. 5.17 indicating that the maximum deformation of 0.001098 μm is at the point of force application.
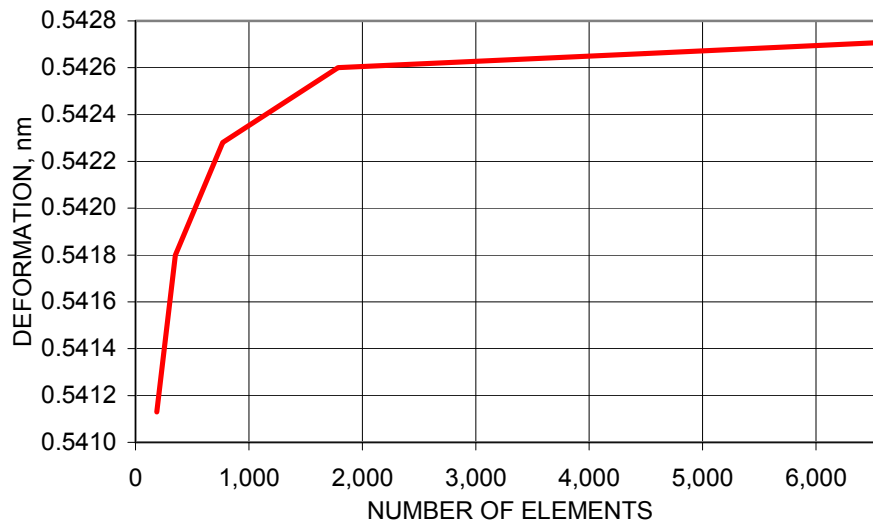
Fig. 5.12. Convergence of the maximum deformations in the y-direction, due to the force in the y-direction, for the cantilever using parabolic tetrahedral elements.
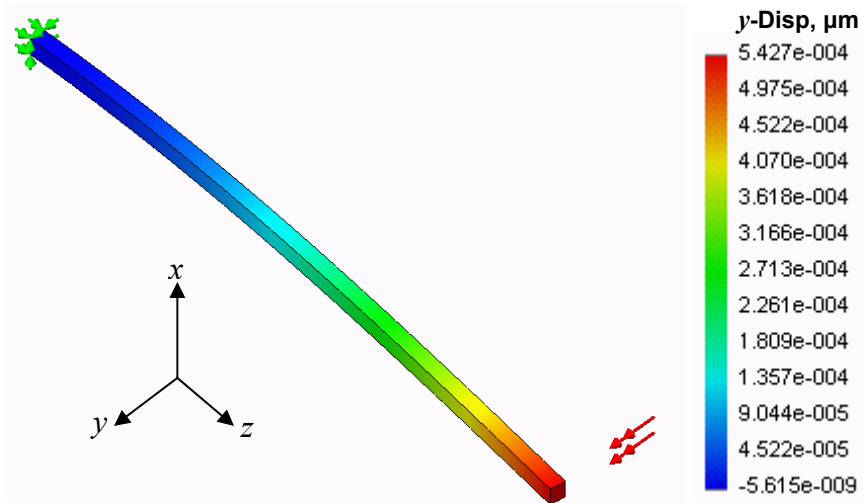
Fig. 5.13. COSMOS/M determined deformation field in the *y*-direction
due to the force in the *y*-direction, for the cantilever using 6,664 parabolic
tetrahedral solid elements.

Table 5.12. Convergence of the maximum values of the deformation
component in the *x*-direction for the entire folded spring of the microgyro,
using parabolic tetrahedral elements.

Number of elements	Deformation, μm
346	19.394
569	19.456
812	19.475
1,263	19.495
1,952	19.520
5,245	19.545
11,501	19.569
17,285	19.582

Now the results obtained computationally in COSMOS/M for the deformation in

the *z*-direction, due to the force in the *x*-direction, will be presented. Results of

convergence analysis for this case are summarized in Table 5.14 and displayed in Fig.

5.18. These results indicate that about 17,000 elements adequately discretize the folded

spring. Deformation field for this case is shown in Fig. 5.19 displaying the maximum value of -2.282 μm.
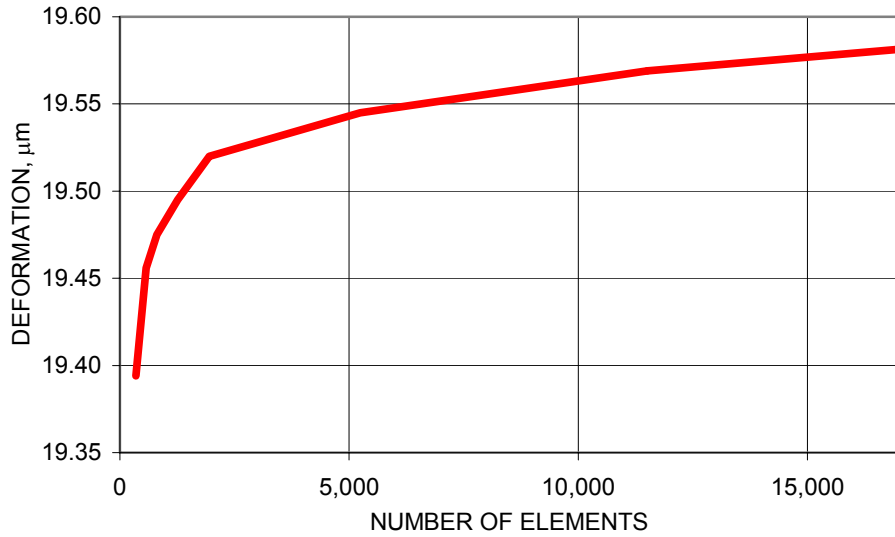
Fig. 5.14. Convergence of the maximum deformations in the *x*-direction, due to the force in the *x*-direction, for the entire folded spring of the microgyro.
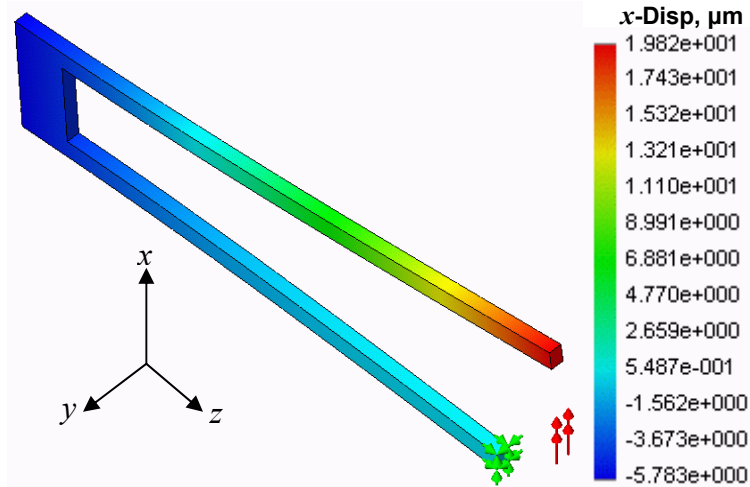
Fig. 5.15. COSMOS/M determined deformation field in the *x*-direction due to the force in the *x*-direction for the entire folded spring using 17,285 parabolic tetrahedral solid elements.

128

Table 5.13. Convergence of the maximum values of deformation component in the *y*-direction for the entire folded spring of the microgyro, using parabolic tetrahedral elements.

Number of elements	Deformation, nm
346	1.0767
512	1.0806
1,086	1.0858
1,263	1.0874
1,746	1.0892
1,952	1.0900
3,056	1.0940
5,245	1.0947
11,501	1.0967
17,285	1.0981
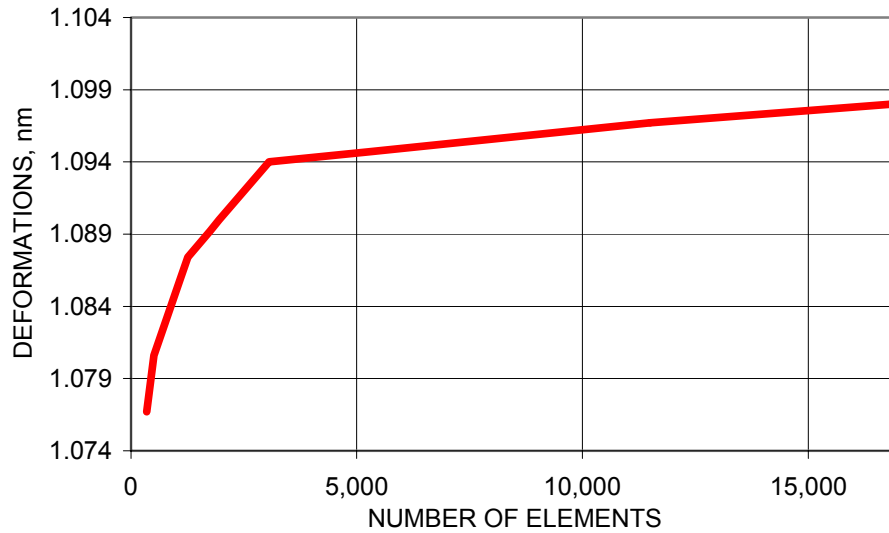
Fig. 5.16. Convergence of the maximum deformations in the *y*-direction, due to the force in the *y*-direction, for the entire folded spring of the microgyro.

The convergence analyses for the entire folded spring, done with parabolic tetrahedral solid elements for all three Cartesian coordinate directions, took about 17,000 elements. This increase in the number of elements needed to properly discretize the model of the entire folded spring, when compared to the 6,664 elements necessary to

discretize the cantilever, makes sense, since the model increased in complexity when sections *AB* and *BC* were added to the cantilever, section *CD*. Therefore the number of elements necessary to discretize the FEM model had to increase to account for the additional complexity.
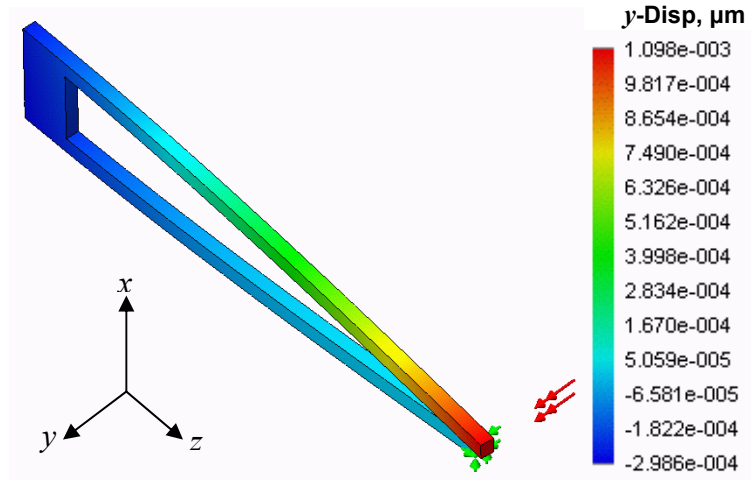
Fig. 5.17. COSMOS/M determined deformation field in the *y*-direction due to the force in the *y*-direction for the entire folded spring using 17,285 prabolic tetrahedral elements.

Table 5.14. Convergence of the maximum values of deformation component in the *z*-direction for the entire folded spring of the microgyro, using parabolic tetrahedral elements.

| Number of elements	Deformation, μm
346	-2.2570
569	-2.2708
812	-2.2723
1,263	-2.2740
1,952	-2.2760
3,056	-2.2775
5,245	-2.2786
11,501	-2.2808
17,285	-2.2815
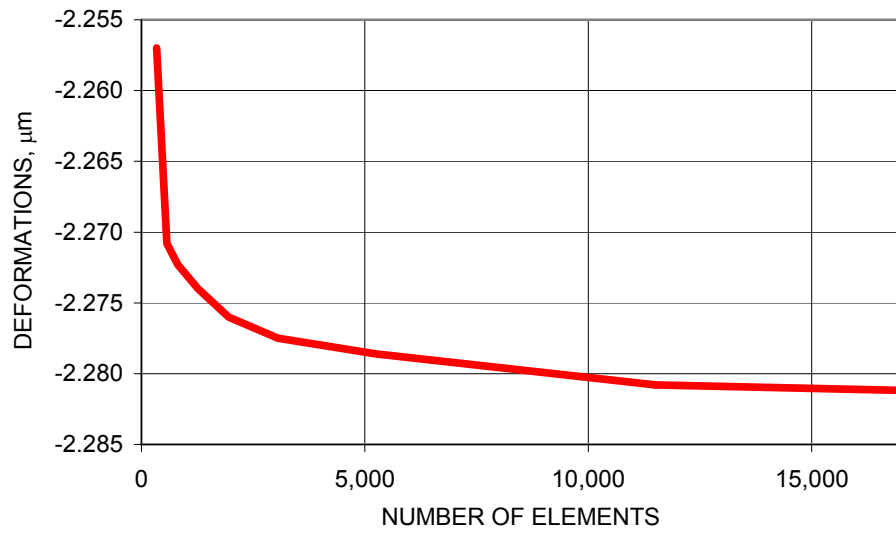
Fig. 5.18. Convergence of the maximum deformations in the *z*-direction, due to the force in the *x*-direction, for the entire folded spring of the microgyro.
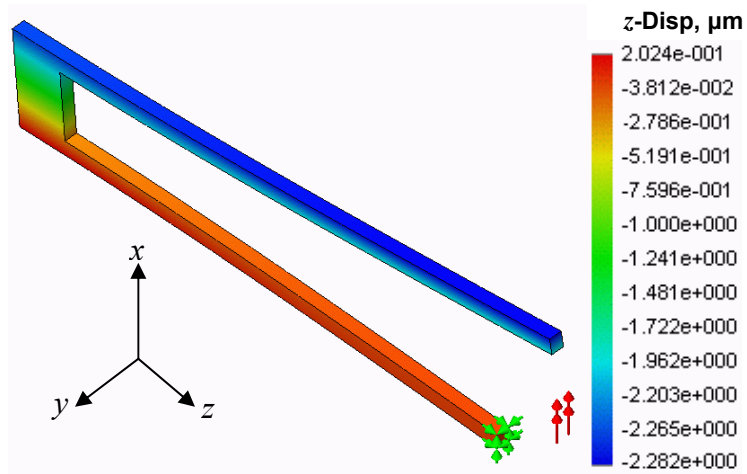
Fig. 5.19. COSMOS/M determined deformation field in the *z*-direction due to the force in the *x*-direction for the entire folded spring using 17,285 parabolic tetrahedral elements.

5.3. Comparison of the analytical and computational results

A comparison of the deformation values found analytically and computationally for the spring was done using percent difference calculated according to the following equation:

$$PercentDifference = \frac{\Delta_{comp} - \Delta_{analyt}}{\Delta_{analyt}} \cdot 100\% \quad , \tag{5.1}$$

where Δ_{comp} is the deformation obtained computationally, and Δ_{analyt} is the deformation obtained from the analytical considerations. The percentage difference based on Eq. 5.1 provides a convenient way of indicating whether computational results are under representing or over representing the analytical results, because of the sign of the results obtained. That is, a negative percent difference indicates that the computational result under represents the corresponding analytical result and a positive percent difference indicates over representation of the analytical result.

The computationally determined *x*-component of displacement for the cantilever representation of the folded spring, based on the linear and parabolic tetrahedral solid elements, will now be compared to the analytically calculated displacement in the *x*-direction using the values of Tables 5.2, 5.8, and 5.9, and applying these values to Eq. 5.1. Results of the comparison are summarized in Tables 5.15 and 5.16 and illustrated in Figs 5.20 and 5.21.

Based on Tables 5.15 and 5.16 and Figs 5.20 and 5.21, at convergence the percent differences between the analytical and computational displacements for the linear and

parabolic tetrahedral solid elements reached about -0.1%, using 23,317 linear and 6,664 parabolic elements, respectively.

Table 5.15. COSMOS/M percent differences for cantilever deformations in the *x*-direction using linear tetrahedral solid elements.

Number of elements	Deformation, μm	Percent difference, %
188	1.2439	-757.935
252	2.0705	-415.424
353	2.988	-257.157
768	5.2284	-104.113
1,433	6.0965	-75.049
6,664	8.3394	-27.969
10,761	9.1918	-16.102
13,997	10.66	-0.111
23,317	10.661	-0.102

Fig. 5.20. Percent differences between COSMOS/M and analytically determined *x*-components of deformation for the cantilever due to the force in the *x*-direction, using linear tetrahedral solid elements.

133

Table 5.16. COSMOS/M percent differences for cantilever deformations in
the *x*-direction using parabolic tetrahedral solid elements.

Number of elements	Deformation, μm	Percent difference, %
188	10.627	-0.422
353	10.649	-0.215
768	10.651	-0.196
1,786	10.655	-0.158
4,494	10.659	-0.121
6,664	10.659	-0.121

The computationally determined *y*-component of displacement for the cantilever,

based on the linear and parabolic tetrahedral solid elements, will now be compared to the

analytically calculated displacement in the *y*-direction using the values of Tables 5.2,

5.10, and 5.11, and applying these values to Eq. 5.1. Results of the comparison are

summarized in Tables 5.17 and 5.18 and illustrated in Figs 5.22 and 5.23.

Fig. 5.21. Percent differences between COSMOS/M and analytically determined
x-components of deformation for the cantilever due to the force in the *x*-direction,
using parabolic tetrahedral solid elements.

134

Table 5.17. COSMOS/M percent differences for cantilever deformations in
the *y*-direction using linear tetrahedral solid elements.

Number of elements	Deformations, nm	Percent difference, %
188	0.0557	-875.619
252	0.085428	-536.115
353	0.13442	-304.270
1,433	0.23037	-135.890
6,664	0.39804	-36.524
10,761	0.45019	-20.709
13,997	0.54278	-0.118
23,317	0.54278	-0.118
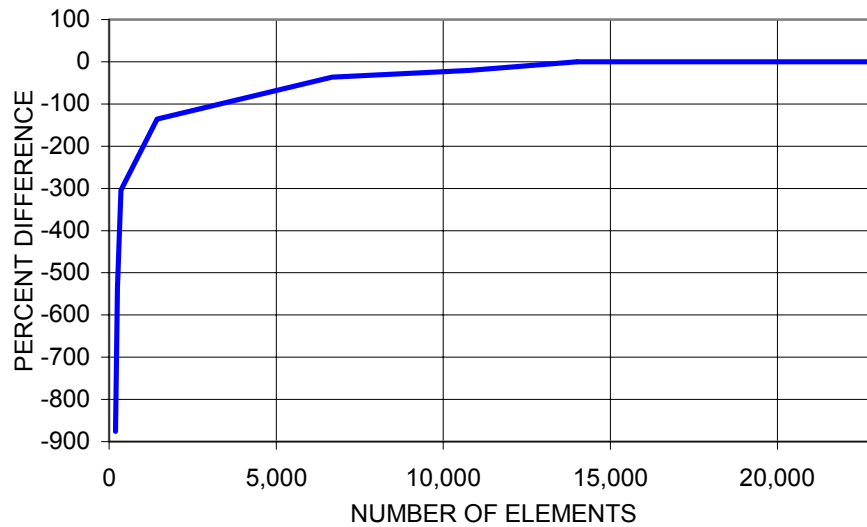
Fig. 5.22. Percent differences between COSMOS/M and analytically determined
y-components of deformation for the cantilever due to the force in the *y*-direction,
using linear tetrahedral solid elements.

Based on Tables 5.17 and 5.18 and Figs 5.22 and 5.23, at convergence the percent

difference between the analytical and computational displacements for 23,317 linear and

6,664 parabolic tetrahedral solid elements reached about -0.1%, respectively. Since it

took the linear elements about 3.5 times more elements to converge than it took the

135

parabolic elements to properly discretize, the parabolic elements reach convergence faster than the linear elements.

Table 5.18. COSMOS/M percent differences for cantilever deformations in the *y*-direction using parabolic tetrahedral solid elements.

Number of elements	Deformations, nm	Percent difference, %
188	0.54113	-0.423
353	0.5418	-0.299
768	0.54228	-0.210
1,786	0.5426	-0.151
4,494	0.54266	-0.140
6,664	0.54271	-0.131
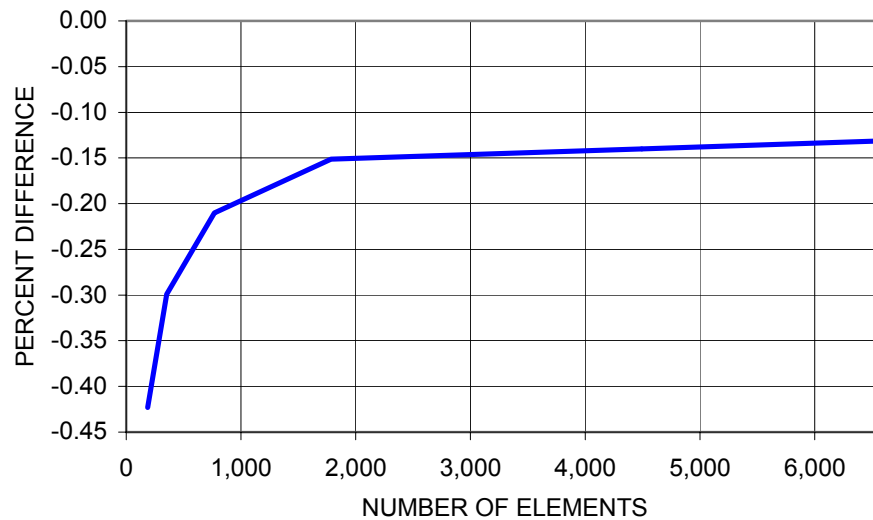
Fig. 5.23. Percent differences between COSMOS/M and analytically determined *y*-components of deformation for the cantilever due to the force in the *y*-direction, using parabolic tetrahedral solid elements.

Results shown in Tables 5.17 and 5.18 and Figs 5.22 and 5.23 show that, at convergence, percent differences between the computational results based on the linear and parabolic tetrahedral solid elements and the analytical results are about -0.1%.

Therefore, results shown in Tables 5.15 to 5.18 and Figs 5.20 to 5.23 indicate that, both, linear and parabolic tetrahedral solid element discretization of the folded spring is appropriate for this application. However, since the parabolic elements require fewer elements, only 6,664 elements compared to 23,317 linear elements, the parabolic elements are more desirable. These results also indicate that Castigliano's second theorem and energy methods are a valid way to model deformations of the cantilever, and therefore the entire folded spring.

The computationally determined x-component of deformation for the entire folded spring will now be compared to the analytically calculated deformation in the x-direction using the values of Tables 5.3 and 5.12 and applying these values to Eq. 5.1. Results of the comparison are summarized in Table 5.19 and Fig. 5.24. Based on Table 5.19 and Fig. 5.24, at convergence, which occurs with 17,285 parabolic tetrahedral solid elements, the percent difference maximum deformations of the entire folded spring, determined analytically and computationally using parabolic tetrahedral elements, reached about -8.7%.

Convergence for the deformations in the y-direction, Fig. 5.16, will now be compared to the analytically calculated deformations in the y-direction using Eq. 5.1. The percent differences calculated using Eq. 5.1, based on the values in Tables 5.3 and 5.13 are shown in Table 5.20 and Fig. 5.25. Based on the information in Table 5.20 and

Fig. 5.25, at convergence, using 17,285 parabolic tetrahedral solid elements, the percent

difference between the analytical and computational displacements in the *y*-direction

reached -2.9%.

Table 5.19. Percent differences between maximum deformations of the entire folded spring based on the analytical and COSMOS/M results for the *x*-component of deformation.

Number of elements	Deformation, μm	Percent difference, %
346	19.394	-9.62
569	19.456	-9.33
812	19.475	-9.24
1,263	19.495	-9.15
1,952	19.520	-9.03
5,245	19.545	-8.92
11,501	19.569	-8.80
17,285	19.582	-8.74
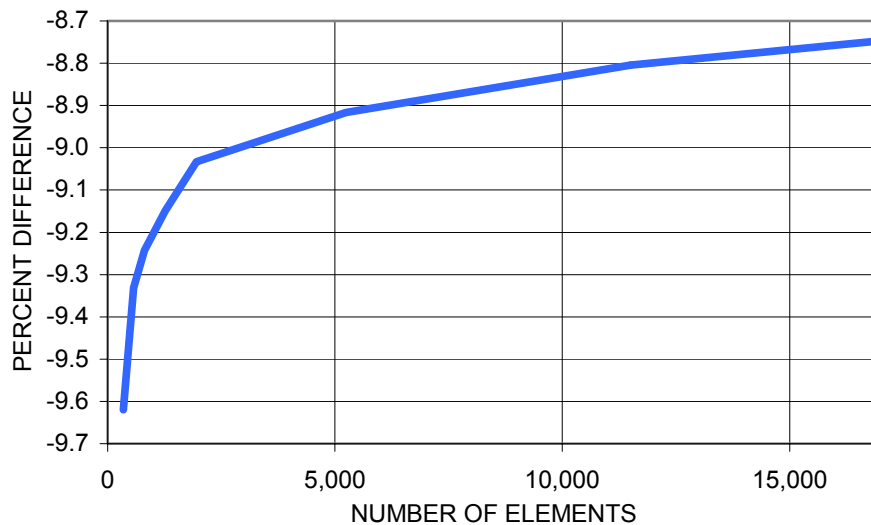
Fig. 5.24. Percent differences between COSMOS/M and analytically determined *x*-components of deformation for the entire folded spring due to the force in the *x*-direction, using parabolic tetrahedral solid elements.

Table 5.20. Percent differences between maximum deformations of the entire folded spring based on the analytical and COSMOS/M results for the *y*-component of deformation.

Number of elements	Displacement, nm	Percent difference, %
346	1.0767	-4.83
512	1.0806	-4.49
1,086	1.0858	-4.03
1,263	1.0874	-3.89
1,746	1.0892	-3.73
1,952	1.0900	-3.66
3,056	1.0940	-3.31
5,245	1.0947	-3.24
11,501	1.0967	-3.07
17,285	1.0981	-2.94
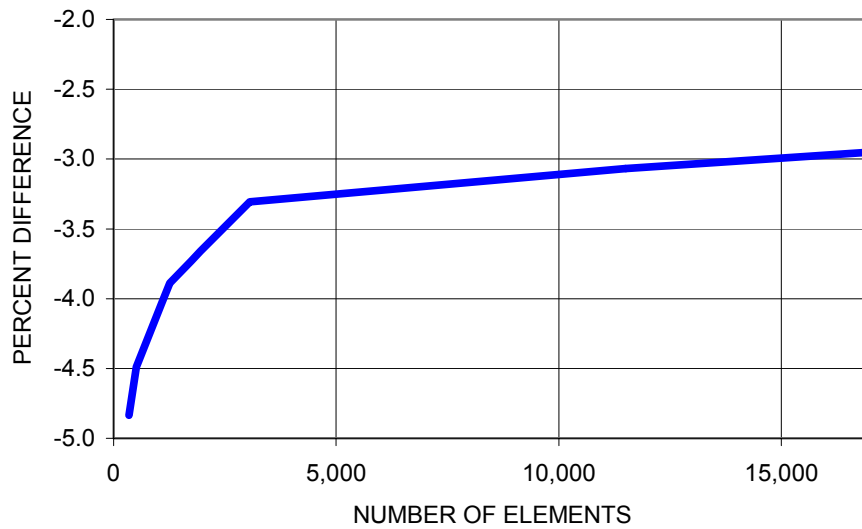
Fig. 5.25. Percent differences between COSMOS/M and analytically determined *y*-components of deformation for the entire folded spring due to the force in the *y*-direction, using parabolic tetrahedral solid elements.

Convergence for the deformations in the *z*-direction, Fig. 5.18, will now be compared to the analytically calculated displacements in the *z*-direction using Eq. 5.1.

The percent difference calculated using the values in Tables 5.2 and 5.14 are shown in Table 5.21 and Fig. 5.26. Based on Table 5.21 and Fig. 5.26, at convergence, using 17,285 parabolic tetrahedral solid elements, the percent difference between the analytical and computational displacements in the z-direction reached -6%.

Table 5.21. Percent differences between maximum deformations of the entire folded spring based on the analytical and COSMOS/M results for the z-component of deformation.

Number of elements	Displacement, µm	Percent difference, %
346	-2.2570	-7.00
569	-2.2708	-6.43
812	-2.2723	-6.37
1,263	-2.2740	-6.30
1,952	-2.2760	-6.21
3,056	-2.2775	-6.15
5,245	-2.2786	-6.11
11,501	-2.2808	-6.02
17,285	-2.2815	-6.00

The percent differences between the analytical and computational methodology range from -2.9% to -8.7% for the deformations in the y and x-directions, respectively. The differences between the two methods could stem from numerous assumptions that were made during the derivation of the equations for the deformations of the folded spring; however, since the percent differences between the analytical and computational results for the cantilever were around 0.1% in both the x and y-directions, the error between the two methods must have been introduced when modeling the interfaces between the coupler, section BC, and sections AB and CD.
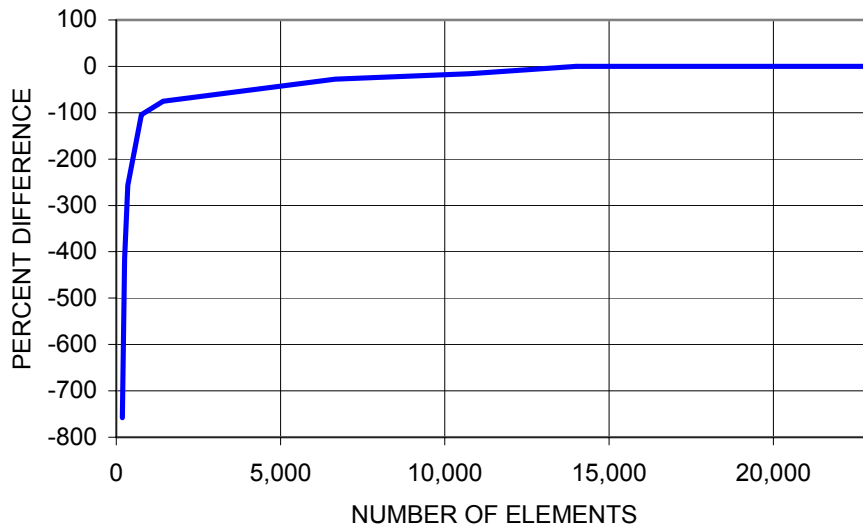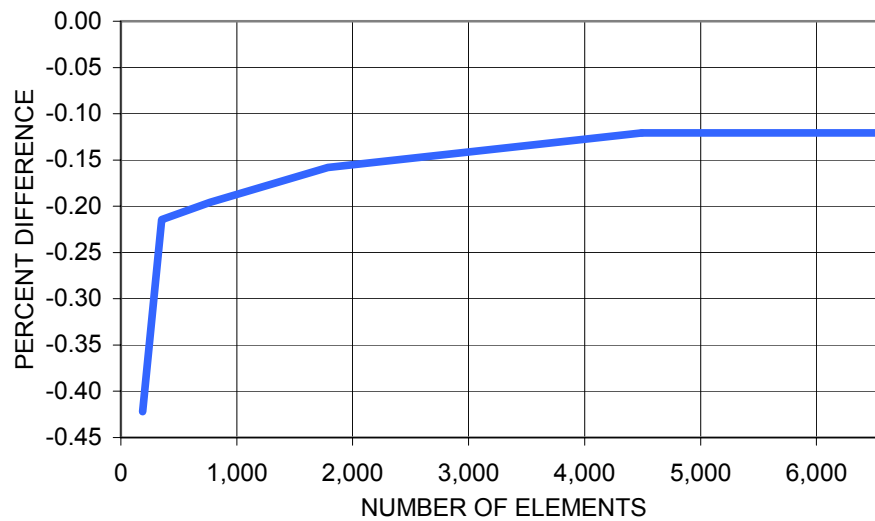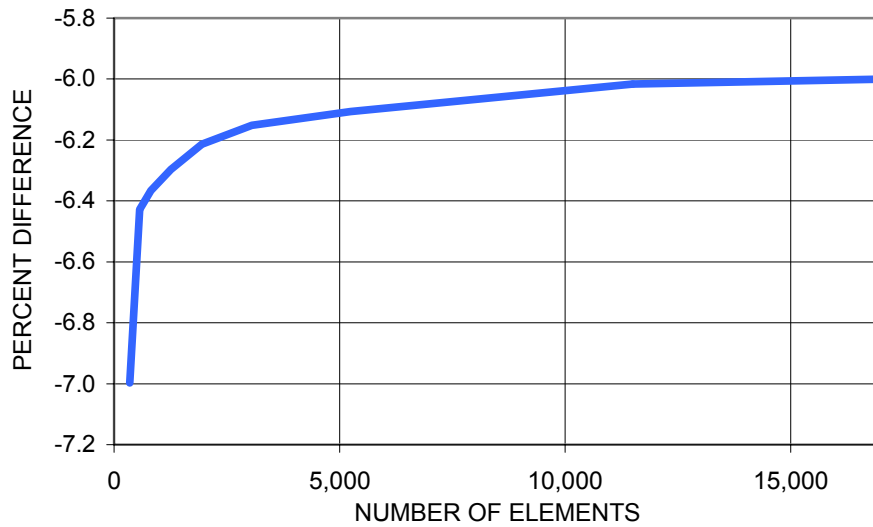
Fig. 5.26. Percent differences between COSMOS/M and analytically determined z-components of deformation for the entire folded spring due to the force in the x-direction, using parabolic tetrahedral solid elements.

Another reason that could have caused the differences between the analytically and computationally calculated deformations is that the equations derived using Castigliano's second theorem did not include interactions between the forces and deformations in all directions. For example: the equation for the displacement in the x-direction, does not include any factor due to the force in the y-direction; however when a force in the y-direction was applied in COSMOS/M, there was a deformation, on the order of 0.1 nm, that occurred in both the x and the z-directions. Conversely, when a force in the x-direction was applied to the folded spring in COSMOS/M, there was a small component of deformation that occurred in the y-direction. A way to improve the correlation between the analytical and computational results would be to determine a

141

procedure to include these interactions between the deformations in the x, y, and z-directions.

5.4. Experimental results

The main purpose for obtaining experimental results was to validate the analytical and computational results and/or to facilitate their interpretation. The experimental results for the deformation of the folded springs were obtained using the vibrometer method, described in Section 4.3.1, and the results for the shape of the microgyroscopes: proof masses and folded springs, obtained using the OELIM methodology, described in Section 4.3.2, are presented in Sections 5.4.1 and 5.4.2, respectively.

5.4.1. Vibrometer results

The fist step of the vibrometer experiment was to determine at which frequencies the microgyroscope would be excited: peak-to-peak signal amplitude of 25 mV was produced by the signal generator for all the measurements. This was done by first exciting the system with a randomly swept signal for the frequency range, including 10 kHz, which is the operational frequency of the microgyro design considered in this thesis, as described in Section 3. Knowing this, the frequency range was subdivided into four divisions and four linear sweeps of the frequencies in the ranges corresponding to these divisions were applied to the system, Table 5.22. Using information from the vibrometer,

an average of fifty data samples was taken by the signal analyzer and used to obtain the

mean peak frequency for each of the frequency ranges, Table 5.22. An average was

taken of the four peaks in each of the four subdivisions, to obtain the frequency that

would be used to excite the system, in Table 5.22. As described in Section 4.3.1, the

system was excited using each of the four frequencies, listed in Table 5.22.

Table 5.22. Frequency sampling.

Linear sweep frequency ranges	Mean peak kHz	Average frequency kHz
1-5 kHz	3.816	3.752
	3.496	
	4.328	
	3.24	
5-10 kHz	6.824	7.528
	9.768	
	6.888	
	6.696	
10-15 kHz	10.728	11.432
	14.504	
	10.472	
	10.152	
15-17 kHz	15.784	15.848
	16.296	
	15.464	
	15.848	

For the first of the frequencies, the signals coming from the mirror and the

substrate/proof mass were recorded in the signal analyzer, and these two frequency

responses were de-convolved to obtain the FRF of the substrate/proof mass, Fig. 5.27. If

the IFFT of the FRF of the substrate/proof mass produced a flat curve with an amplitude

approximately one, then it would imply that the substrate/proof mass transmits the signal

from the PZT without modifying it. However, according to Fig. 5.27, the FRF is a

random function of magnitude greater than one, which means that the signal measured on

the substrate/proof mass has been altered by its transmission "path" from the PZT.
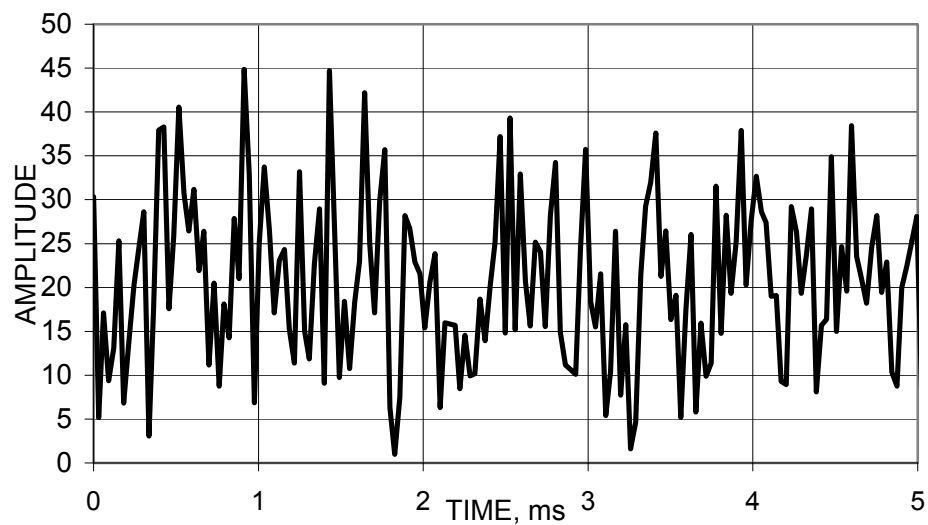
Fig. 5.27. Deconvolved frequency response for the proof mass at the input
frequency of 3.752 kHz.

The next step was to obtain the time-domain responses of the mirror and the

substrate/proof mass, Fig. 5.28, based on which deformations of the substrate/proof mass

can be determined. The signal from the mirror was then subtracted from the signal from

the proof mass in order to obtain the net motion of the substrate/proof mass. This

difference is illustrated in Fig. 5.29.
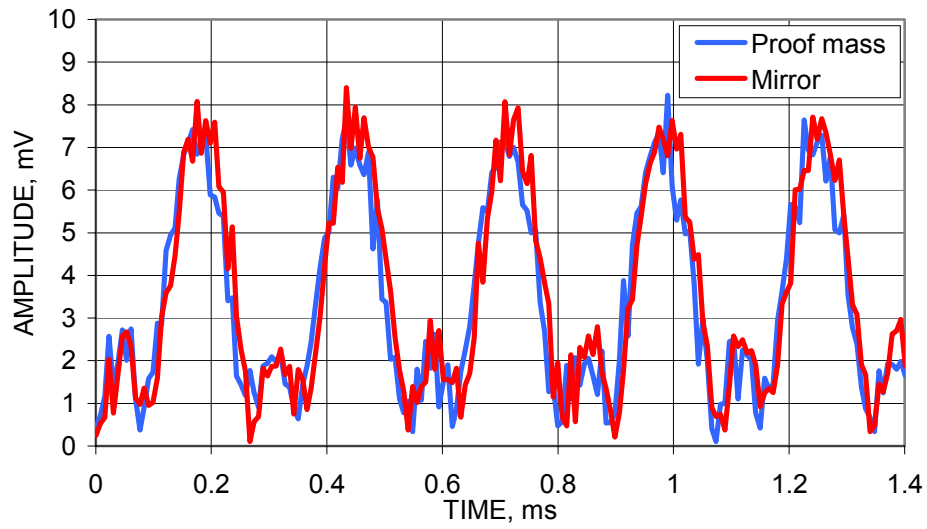
Fig. 5.28. Comparison of the proof mass and mirror time responses for the input signal at 3.752 kHz.
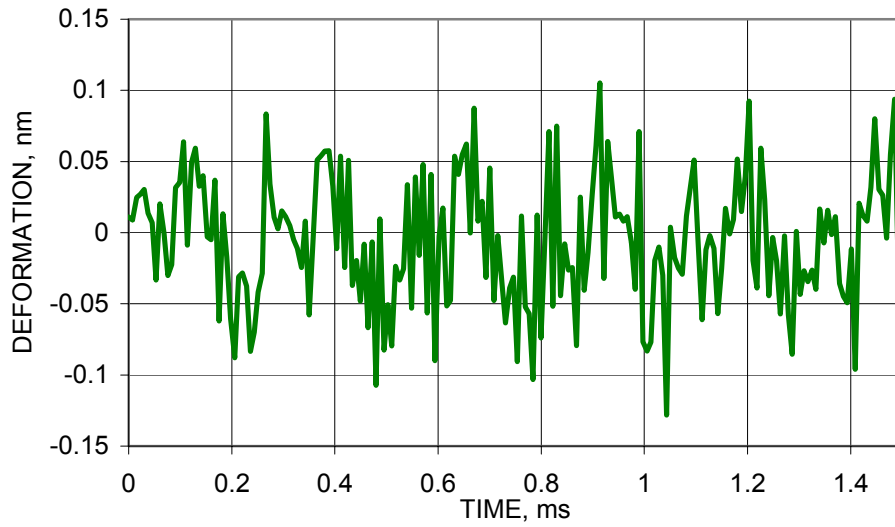
Fig. 5.29. Difference between the substrate/proof mass and mirror responses for the input signal at 3.752 kHz.

Using the data of Fig. 5.29, an average was taken of the absolute values for all of the data points in the difference between the proof mass and mirror responses; this value was then used as the amplitude of the oscillation of the substrate/and proof mass in Section 5.4.1.1. This average value was calculated to be 0.0347 nm.
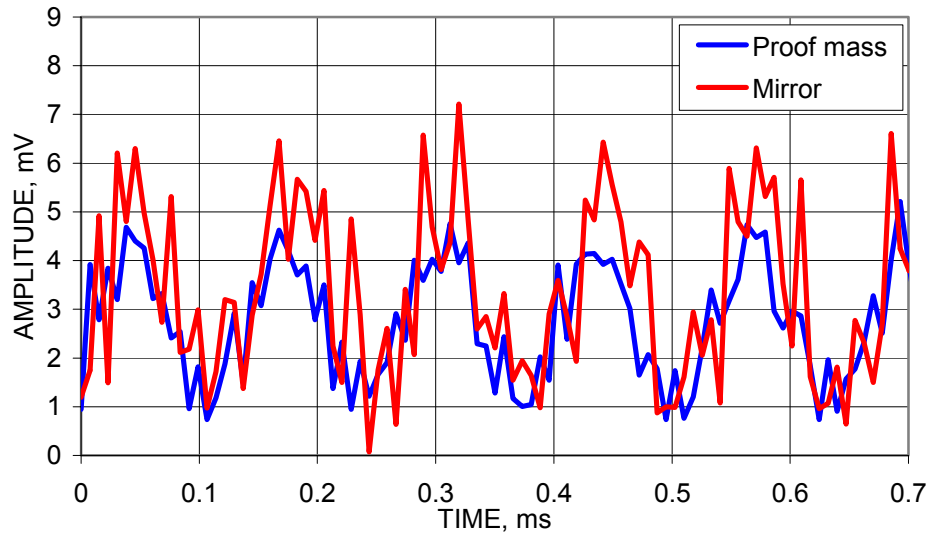
Fig. 5.30. Comparison of the proof mass and mirror time responses for the input signal at 7.528 kHz.

The time-domain responses off of the mirror and the substrate/proof mass for the second excitation frequency of 7.528 kHz are shown in Fig. 5.30. Using the two curves of Fig. 5.30, the signal from the mirror was subtracted from the signal from the proof mass in order to obtain the net motion of the substrate/proof mass. This difference is illustrated in Fig. 5.31. Using the data illustrated in Fig. 5.31, an average was taken of the absolute values for all of the data points in the difference between the proof mass and mirror responses; this value was then used as the amplitude of the oscillation of the

substrate/and proof mass in Section 5.4.1.1. This average value, from Fig. 5.31, was

calculated to be 0.0563 nm.
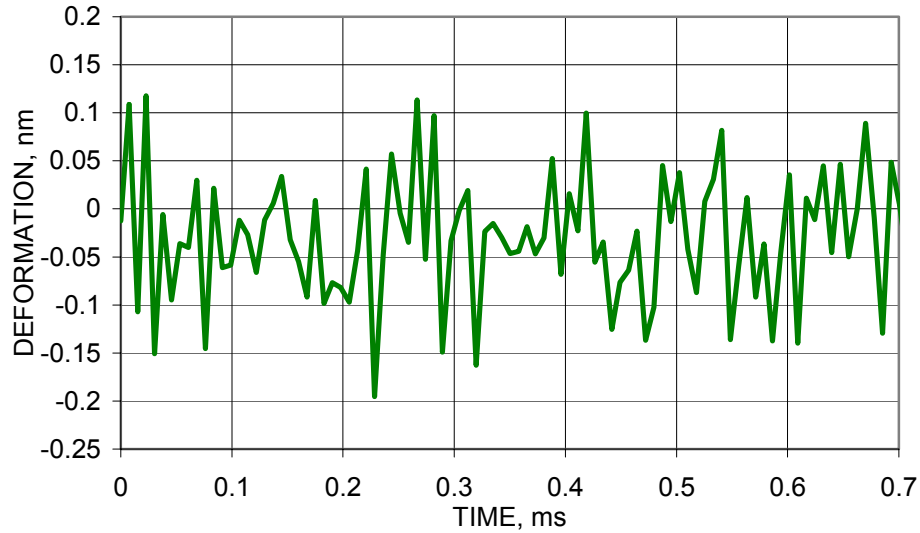
Fig. 5.31. Difference between the substrate/proof mass and mirror responses
for the input signal at 7.528 kHz.

The time-domain responses off of the mirror and the substrate/proof mass for the

third excitation frequency of 11.432 kHz are shown in Fig. 5.32. Using the two curves of

Fig. 5.32, the signal from the mirror was subtracted from the signal from the proof mass

in order to obtain the net motion of the substrate/proof mass. The difference is illustrated

in Fig. 5.33. Using the data illustrated in Fig. 5.33, an average was taken of the absolute

values for all of the data points in the difference between the proof mass and mirror

responses; this value was then used as the amplitude of the oscillation of the substrate/and

proof mass in Section 5.4.1.1. This average value was calculated to be 0.1007 nm.

147
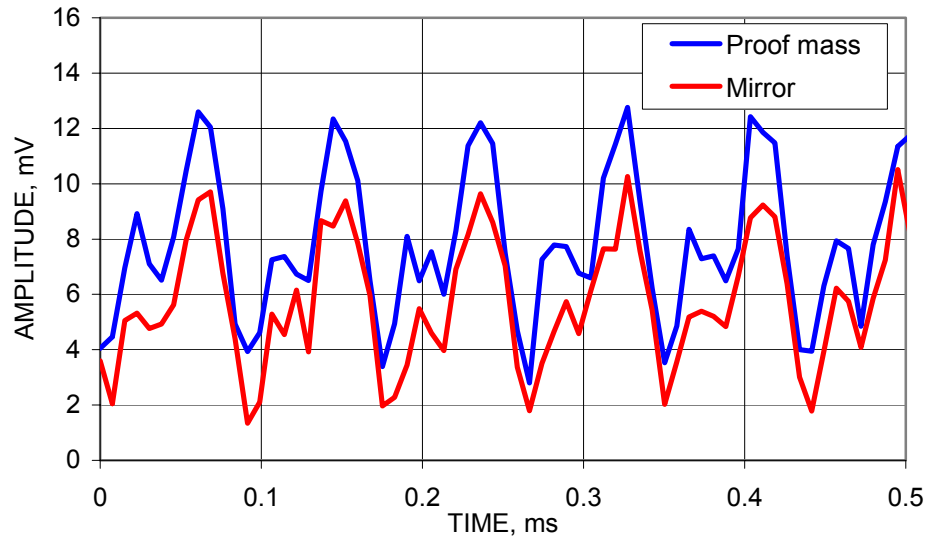
Fig. 5.32. Comparison of the proof mass and mirror time responses for the input signal the 11.432 kHz.
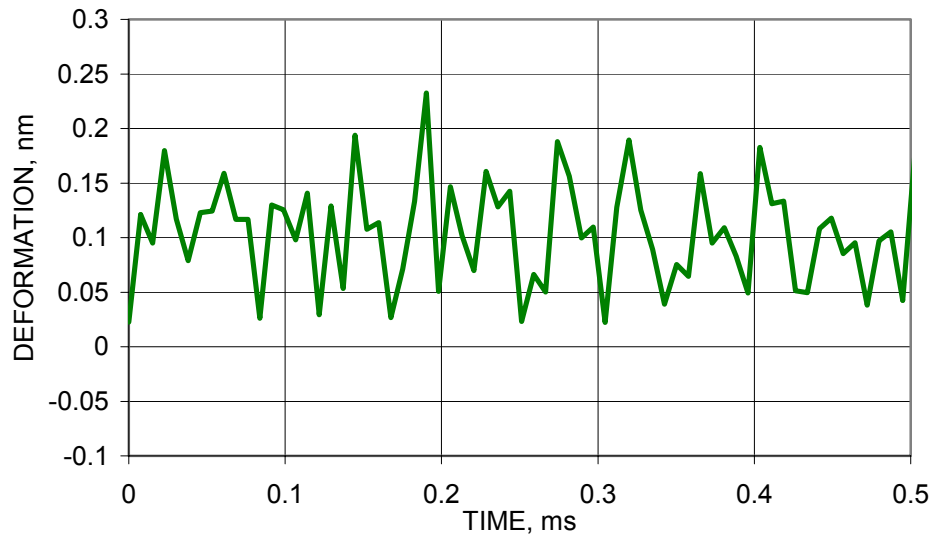
Fig. 5.33. Difference between the substrate/proof mass and mirror responses for the input signal at 11.432 kHz.

148
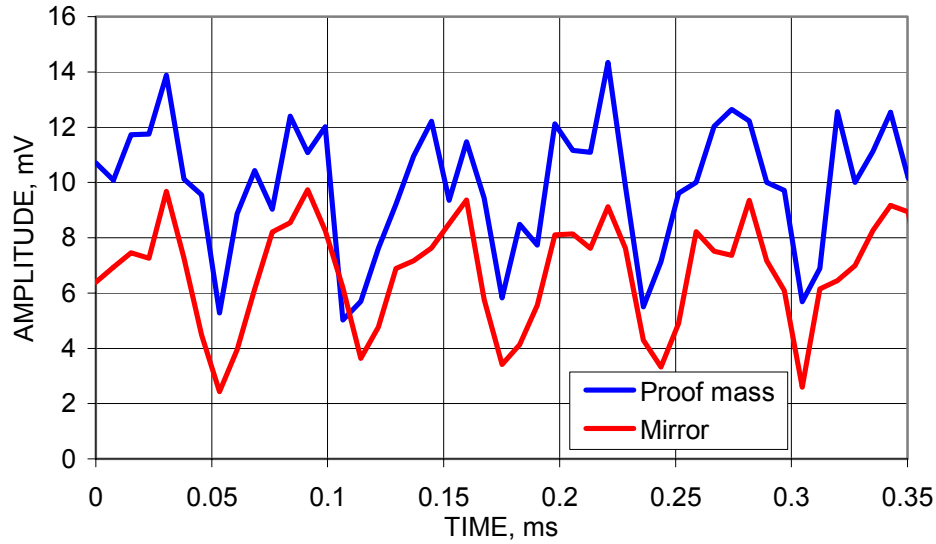
Fig. 5.34. Comparison of the proof mass and mirror time responses for the input signal at 15.848 kHz.

The time-domain responses off of the mirror and the substrate/proof mass for the fourth excitation frequency of 15.848 kHz are shown in Fig. 5.34. Subtracting the "mirror" curve from the "proof mass" curve, net motion of the substrate/proof mass is determined, Fig. 5.35.

Using the data illustrated in Fig. 5.35, an average was taken of the absolute values for all of the data points in the difference between the proof mass and mirror responses; this value was then used as the amplitude of the oscillation of the substrate/and proof mass in Section 5.4.1.1. This average value, from Fig. 5.35, was calculated to be 0.1738 nm.
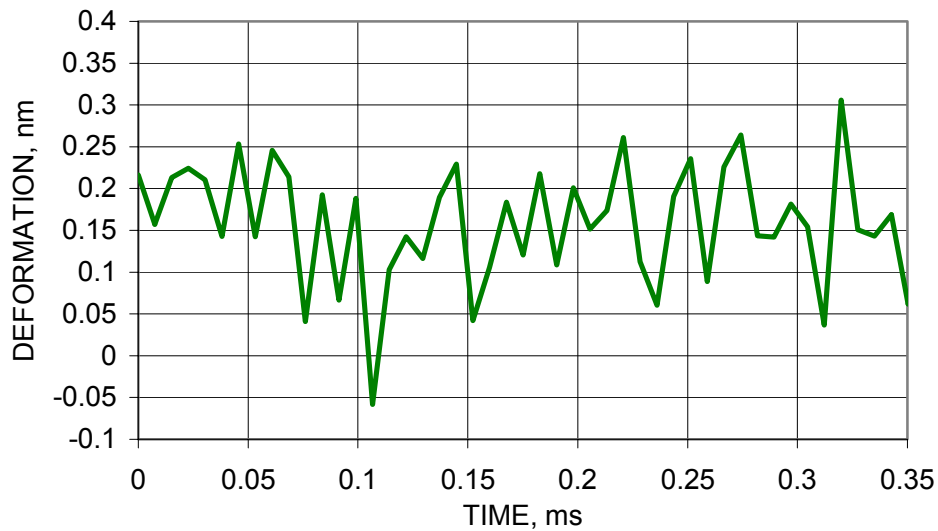
Fig. 5.35. Difference between the substrate/proof mass and mirror responses
for the input signal at 15.848 kHz.

5.4.1.1. Comparison of the laser vibrometer and analytical results

In order to compare the information gathered from the laser vibrometer, described

in Section 5.4.1, to deformations calculated analytically, the deformations had to be

calculated using Eq. 4.77, the equation for the deformation in the *y*-direction. From the

results shown in the Section 5.4.1, the motion of the substrate/proof mass is not a simple

sinusoidal motion, Fig. 5.28. However for comparison, the motion was assumed to be a

sinusoidal, with the amplitude based on the average of the absolute value of the

difference in the time-domain responses of the mirror and the substrate/proof mass; these

values were then applied to Eqs 4.79 thru 4.86, and the force was calculated. This force

was then applied to Eq. 4.77, and the deformation in the *y*-direction was calculated. The

experimental data used in the calculations of the forces and deformations, and results of

these calculations are presented in Table 5.23. Once the analytically calculated

deformations were obtained, they were compared to the experimental maximum

deformation using a relationship similar to Eq. 5.1, i.e.,

$$PercentDifference = \frac{\Delta_{exper} - \Delta_{analyt}}{\Delta_{exper}} \cdot 100\% \quad ,$$
(5.2)

where Δ_{exper} is the experimentally obtained amplitude of the deformation, and Δ_{analyt} is the

deformation obtained from Eq. 4.77. This comparison is also shown in Table 5.23. The

results shown in Table 5.23 indicate that there is a difference between the analytically

calculated deformations and those found using the vibrometer of -10.5%. This difference

is in good agreement with the uncertainty shown in Table 5.7.

Table 5.23. Representative comparison of experimental
and analytical deformations.

Excitation frequency, kHz	7.528
Amplitude, nm	0.0563
Calculated force, nN	0.0396
Analytical displacement, nm	0.0623
Percent difference, %	*-10.52*

5.4.2. OELIM results

Because of to the difference between the analytical results and experimental

displacements found using the laser vibrometer, it was necessary to determine the actual

shape of the microgyro is. This is important because the spring was modeled analytically

and computationally as a flat structure that is parallel to the substrate and at the same

level as the proof mass. If this is not the case, then there may be errors between the analytical, computational, and experimental results.

5.4.2.1. Dual proof mass results

The entire microgyroscope was observed first, and interferograms of both of the proof masses were recorded, Fig. 5.36. These interferograms were then analyzed to determine the shape of the proof masses and the corresponding mechanisms supporting them. Figure 5.37 shows a two-dimensional representation of the shape, i.e., deformations of the proof masses and the folded springs supporting them, indicating maximum deformations on the order of 0.58 μm, at room temperature. The contours of the two proof masses are also illustrated as three-dimensional wireframe and color representations, Figs 5.38 and 5.39, respectively.
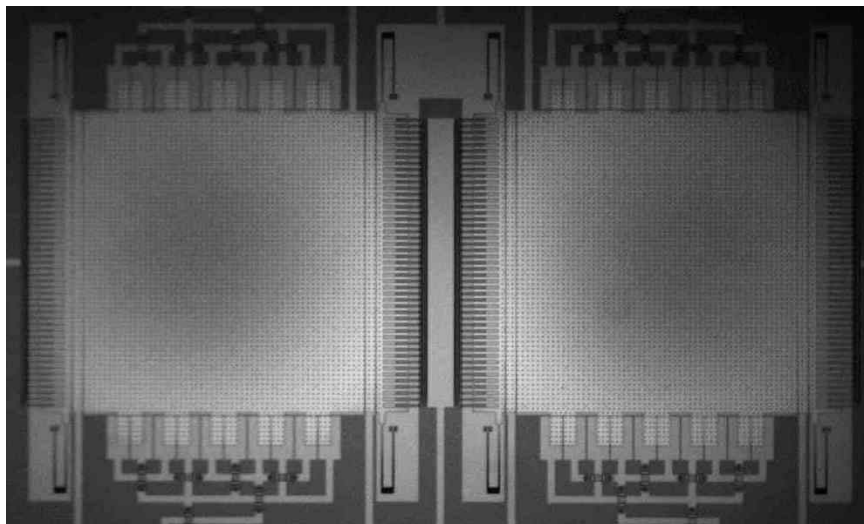
Fig. 5.36. Representative OELIM interferogram of the microgyro at room temperature.

Results displayed in Figs 5.36 to 5.39 give good representation of deformation fields. Frequently, however, while characterizing microgyroscopes, detailed trace-like information about deformations along a specific line, across the microgyroscope, is needed. This information can be easily extracted from the OELIM data. For example, deformations along the horizontal line H-H, shown in Fig. 5.39, are displayed in Fig. 5.40. This trace indicates that the displayed deformations of the proof masses themselves are on the order of 0.1 μm, or about 100 nm. These deformations, although very small on the absolute scale, have significant influence on functional performance of microgyroscopes (Hanson, et al., 2001).
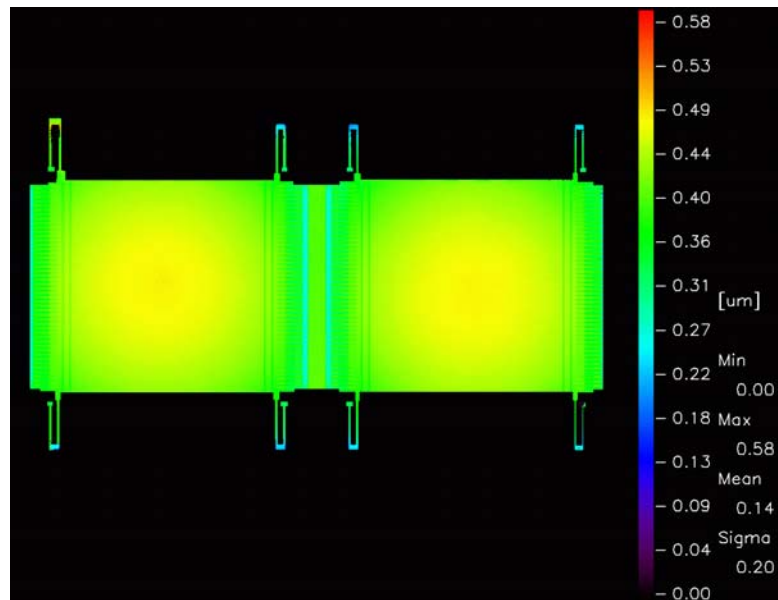
Fig. 5.37. Two-dimensional color representation of the shape of the microgyroscope.
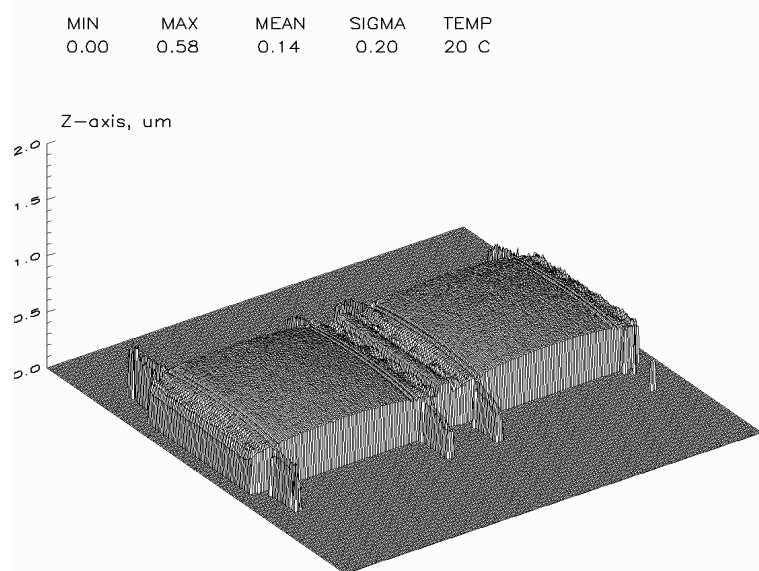
Fig. 5.38. Three-dimensional wireframe representation of the shape of the microgyroscope.
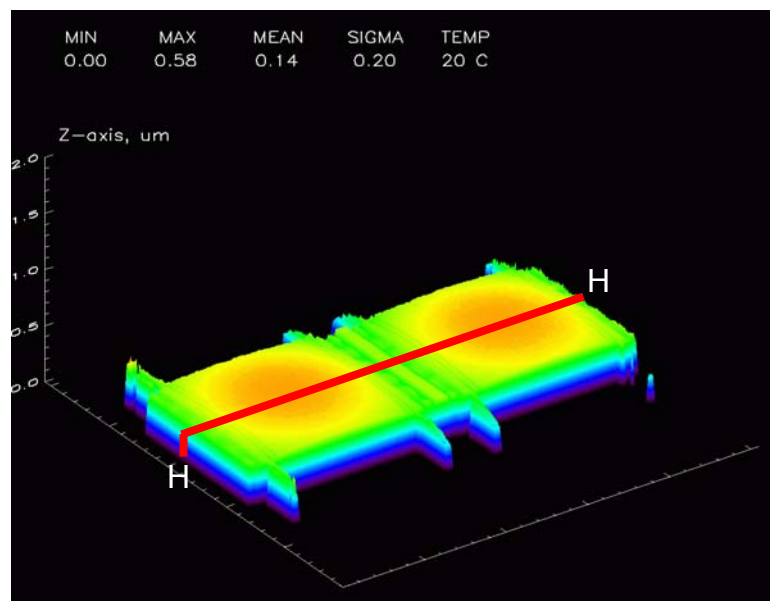
Fig. 5.39. Three-dimensional color representation of the shape of the microgyroscope.
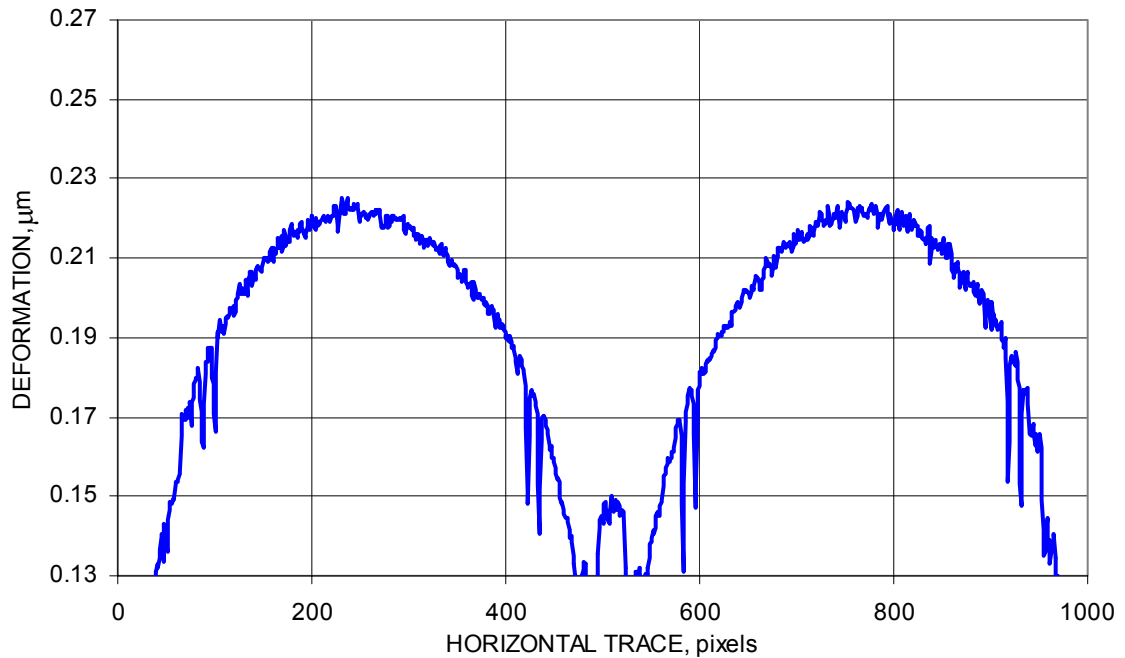
Fig. 5.40. Deformations along line H-H, shown in Fig. 5.39, across both proof masses of the microgyroscope.

Another area of interest for this thesis is that of the deformations of the folded spring. So, if there is a difference between the proof mass elevation and that of the folded spring it may lead to differences between the analytical and experimental results. In addition, a source of possible differences may be due to mismatch between elevations of teeth in the combdrives used to actuate the proof masses during functional operation of the microgyroscopes (Hanson, et al., 2001).

Preliminary results showing mismatch between teeth of a combdrive corresponding to the left proof mass of a microgyroscope are presented in Section 5.4.2.2, while those for representative folded springs are presented in Section 5.4.2.3.

155

5.4.2.2. Results for the left proof mass of the microgyroscope

In order to examine the way the springs interact with the proof masses, the microscope was focused at higher magnification than that used to obtain results presented in Section 5.4.2.1. Because the field of view of the camera used decreases as magnification increases; one proof mass was recorded at a time. In fact, to obtain detailed information on the deformations of the proof masses and the folded springs, three sets of interferograms were taken for each of the proof masses: the proof mass itself, the upper part of the proof mass and the two top springs, and then the lower part of the proof mass and the two bottom springs.

The left proof mass was observed first, and the interferograms of the proof mass itself were recorded, Fig. 5.41. The interferograms were analyzed to obtain the shape of the left proof mass. Figure 5.42 shows a two-dimensional color representation of the deformations of the left proof mass. The deformations of the left proof mass are also illustrated as three-dimensional wireframe and color representations, Figs 5.43 and 5.44, respectively. The results shown in Figs 5.41 to 5.44 indicate that deformations of the left proof mass are approximately 0.1 μm, or 100 nm. However this does not show the area of interest, the folded spring, very well, so the upper part of the left proof mass was observed next, and the corresponding interferograms were recorded, Fig. 5.45.

Fig. 5.41. Representative OELIM interferogram
of the left proof mass of the microgyro.

Fig. 5.42. Two-dimensional color representation of
deformations of the left proof mass.

Fig. 5.43. Three-dimensional wireframe representation
of deformations of the left proof mass.
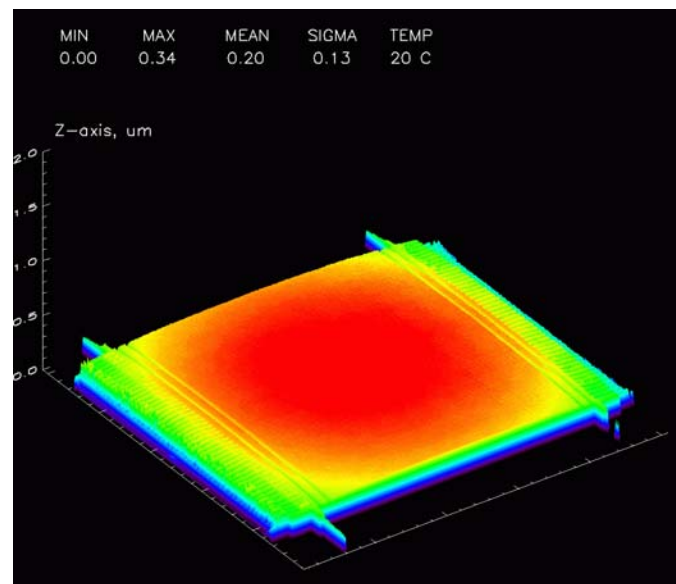
Fig. 5.44. Three-dimensional color representation of
deformations of the left proof mass.

These interferograms were analyzed to obtain the shape of the upper part of the

left proof mass and the two top folded springs. Figure 5.46 shows the two-dimensional

color representation of the deformations of the upper part of the left proof mass, it looks

like there are missing teeth in the combdrives; however, this is a result of "resolution"

while analyzing the images. The deformations are also illustrated as three-dimensional

wireframe and color representations of the upper part of the left proof mass, Figs 5.47

and 5.48, respectively. The results shown in Figs 5.45 to 5.48 indicate that the upper part

of the left proof mass are approximately 0.1 μm or 100 nm, as presented earlier in this

section. However, deformations of the folded springs themselves are about 0.15 μm or

150 nm from the points on the substrate to the parts where they are attached to the proof
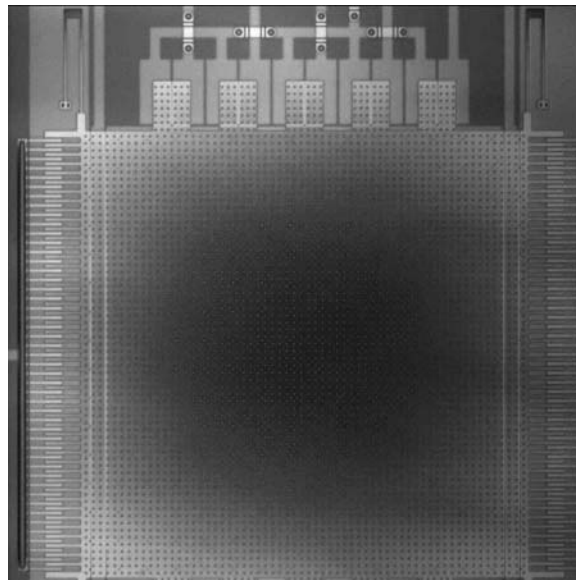
mass.

Fig. 5.45. Representative OELIM interferogram of the
upper part of the left proof mass of the microgyro.
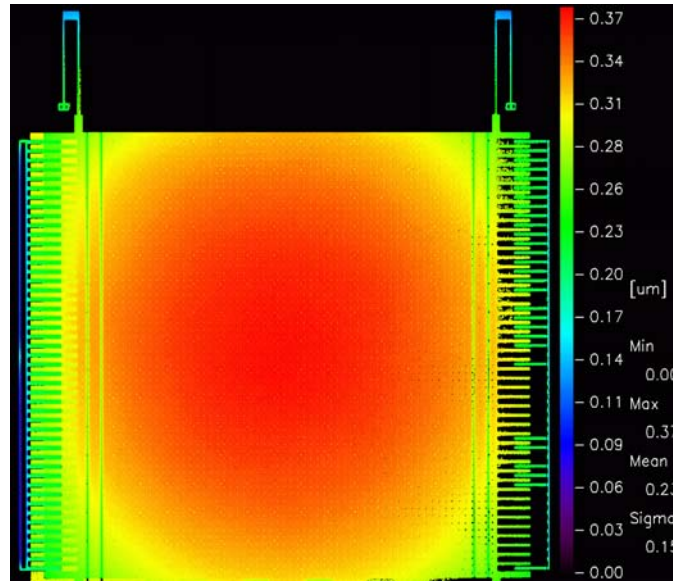
Fig. 5.46. Two-dimensional color representation of deformations of the upper part of the left proof mass.

Fig. 5.47. Three-dimensional wireframe representation of deformations of the upper part of the left proof mass.
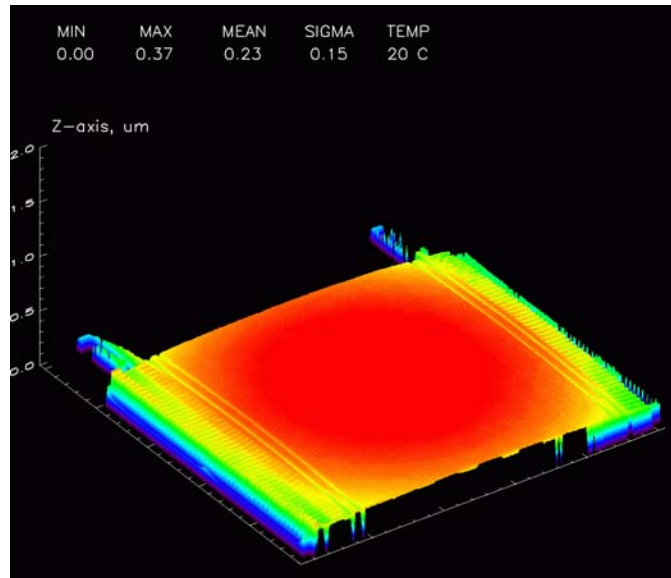
Fig. 5.48. Three-dimensional color representation of
deformations of the upper part of the left proof mass.

To obtain similar information about deformation of the folded springs at the

bottom of the left proof mass, OELIM interferograms of the lower part of the left proof

mass were recorded, Fig. 5.49. The interferograms were analyzed to obtain deformations

of the lower part of the left proof mass and the two bottom folded springs. Figure 5.50

shows the two-dimensional color representation of deformations of the bottom part of the

left proof mass. The deformations are also illustrated as three-dimensional wireframe

and color representations of the bottom part of the left proof mass, Figs 5.51 and 5.52,

respectively.

To obtain detailed information on local deformations of the left proof mass,

deformations were determined along the vertical line V-V, Fig. 5.52. It should be noted

that the line V-V starts at the bottom of a lower left spring, traverses the length of the

161

spring and combdrive, and ends at the top of the combdrive. Deformations measured

along the line V-V are displayed in Fig. 5.53.
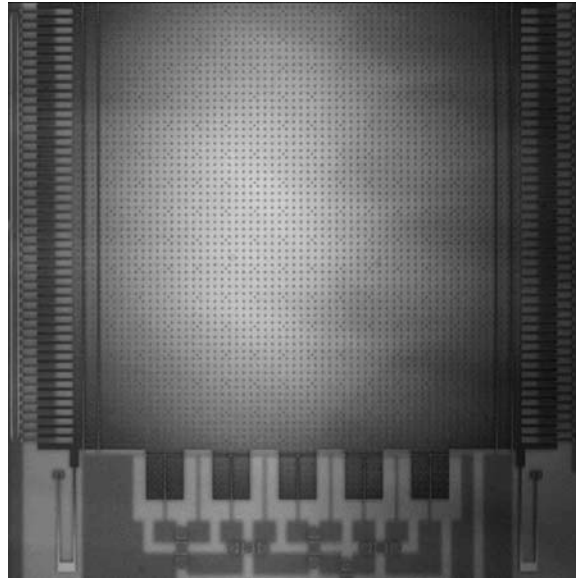
Fig. 5.49. Representative OELIM interferogram of the
lower part of the left proof mass of the microgyro.
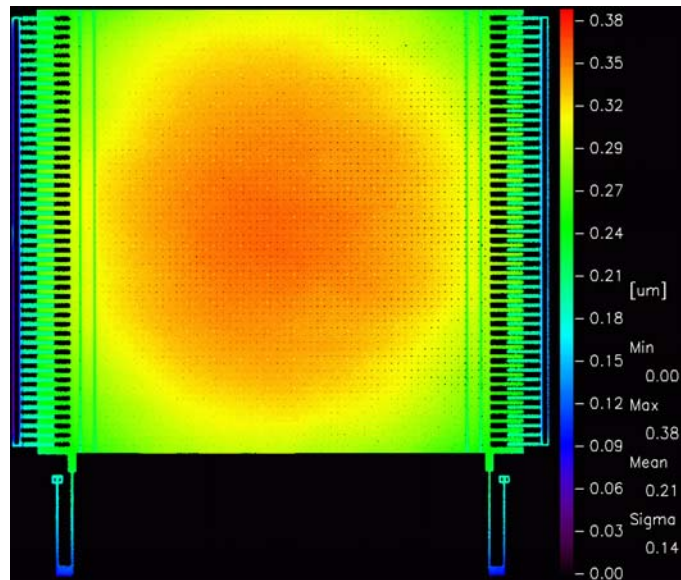
Fig. 5.50. Two-dimensional color representation of
deformations of the lower part of the left proof mass.

Fig. 5.51. Three-dimensional wireframe representation of
deformations of the lower part of the left proof mass.
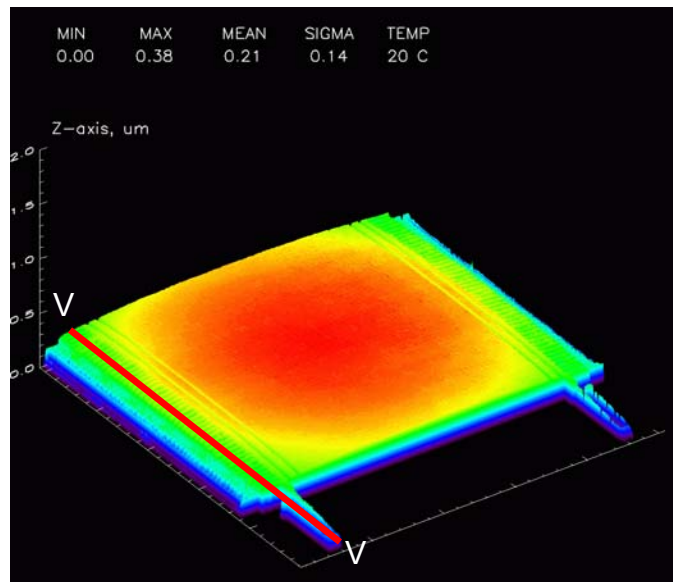
Fig. 5.52. Three-dimensional color representation of
deformations of the lower part of the left proof mass.
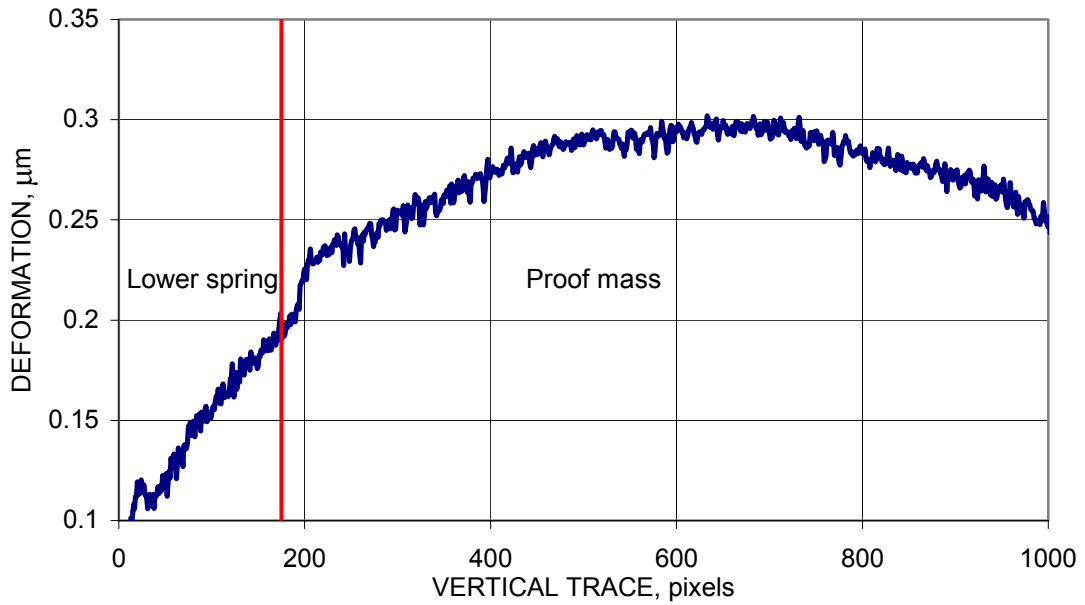
Fig. 5.53. Deformations along line V-V, shown in Fig. 5.52, of the left proof mass of the microgyro.

Based on the information shown in Fig. 5.53, deformations of the proof mass and the folded spring amount to about 0.2 μm. This trace clearly shows that the folded spring is not flat and its ends are at different elevations. Also using trace information, mismatch was determined for one of the combdrives. This, and other combdrives, consists of two sets of fingers: one set is fixed to the substrate and the other is an integral part of the proof mass. Deformations of the fixed set of the teeth and the movable, i.e., attached to the proof mass, set of teeth of a combdrive are displayed in Fig. 5.54.

Figure 5.54 shows that there is a mismatch in elevation between the two sets of teeth in the combdrive that ranges from about 0.05 μm to 0.11 μm. This means that the combdrive is not perfectly aligned. This misalignment produces electrostatic forces that do not meet the design specifications, and this causes the microgyro to not function as

164

designed. Interferograms were also obtained for the right proof mass, however since they show the same type of information that results in similar mismatch, they were placed in Appendix D, Section D.1.
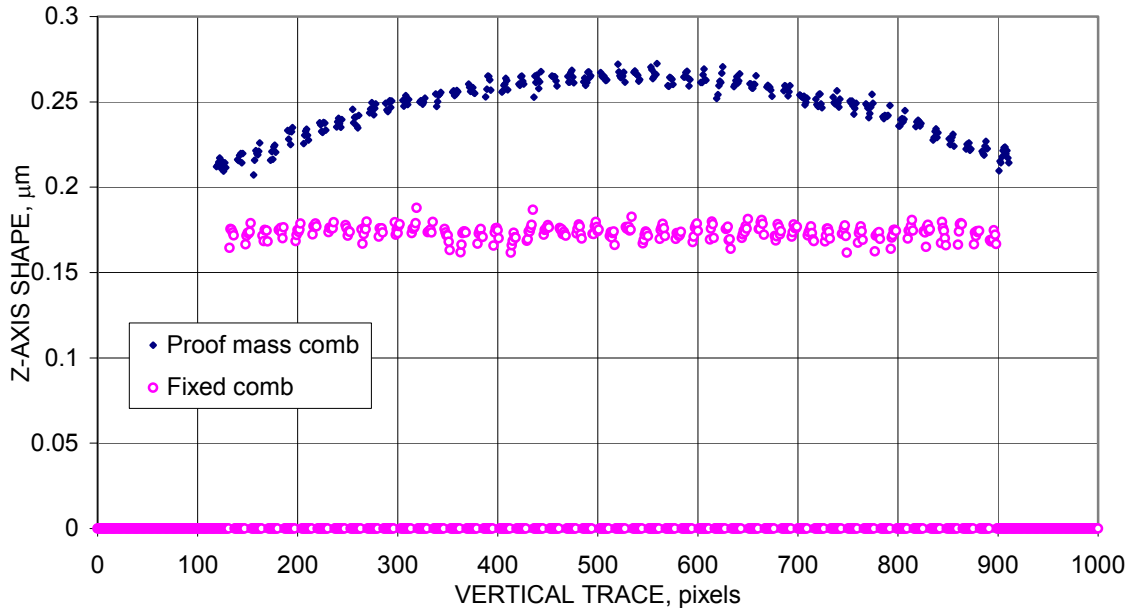
Fig. 5.54. Deformations of the fixed and moveable sets of teeth of the combdrive of the left proof mass.

5.4.2.3. Individual folded spring results

Although the interferograms of Section 5.4.2.3 provided information on the folded springs, more detailed representation of their deformations is needed. Therefore, the folded springs were observed at a higher magnification so that their deformations can be determined in detail. Figure 5.55 identifies the folded springs and indicates the order in which they were examined. Based on Fig. 5.55, springs 1 to 4 support the left proof

165

mass, while springs 5 to 8 support the right proof mass. Spring 1, at the upper right corner of the left proof mass, was observed first, and the interferograms were recorded, Fig. 5.56. These interferograms were analyzed to obtain the shape of Spring 1 of the microgyro. Figure 5.57 shows the two-dimensional color representation of deformations of the Spring 1. The deformations of Spring 1 are also illustrated as three-dimensional wireframe and color representations, Figs 5.58 and 5.59, respectively.
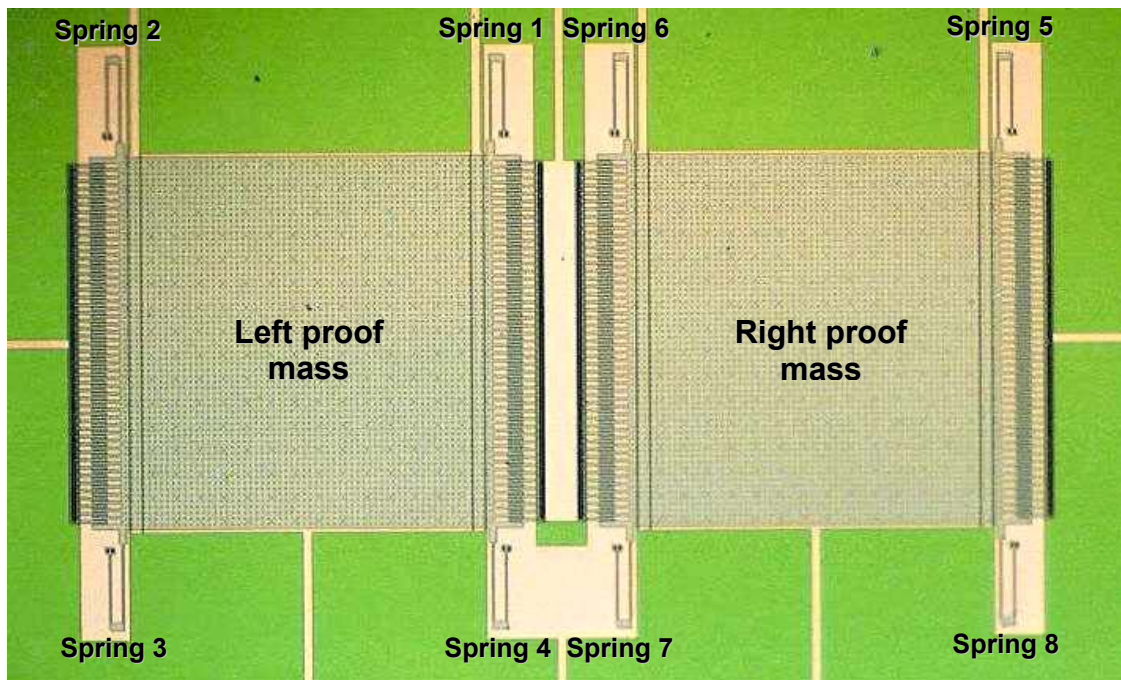
Fig. 5.55. Folded springs of the microgyro.

Results shown in Figs 5.56 to 5.59 indicate deformations of approximately 0.14 μm. These deformations are large when compared with the overall thickness of the folded spring equal to 2.5 μm. Using the results of Figs 5.56 to 5.59, two traces were obtained along the lengths of the folded springs, indicated by lines AB and CD that run

along the lengths of the two arms of the folded spring, as shown in Fig. 5.59. The

deformations found along the traces are displayed in Fig. 5.60.
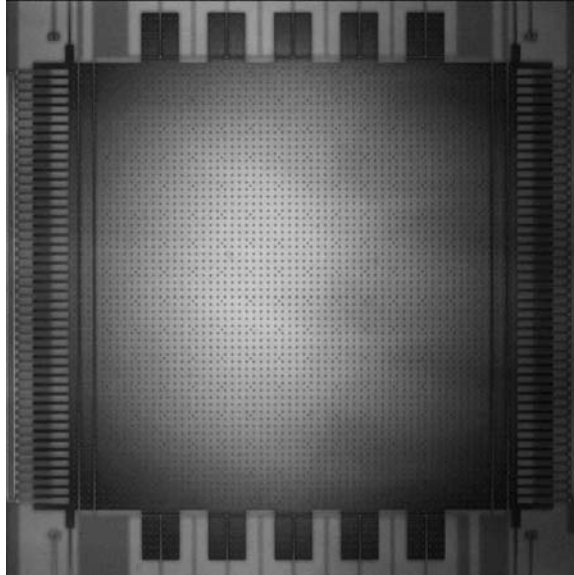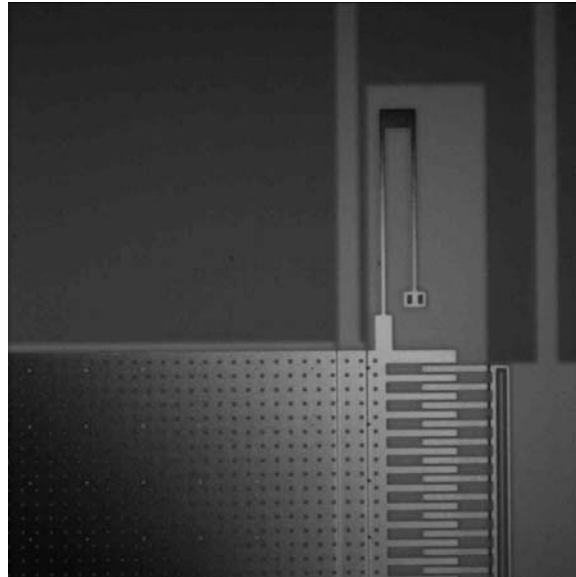

Fig. 5.56. Representative OELIM interferogram
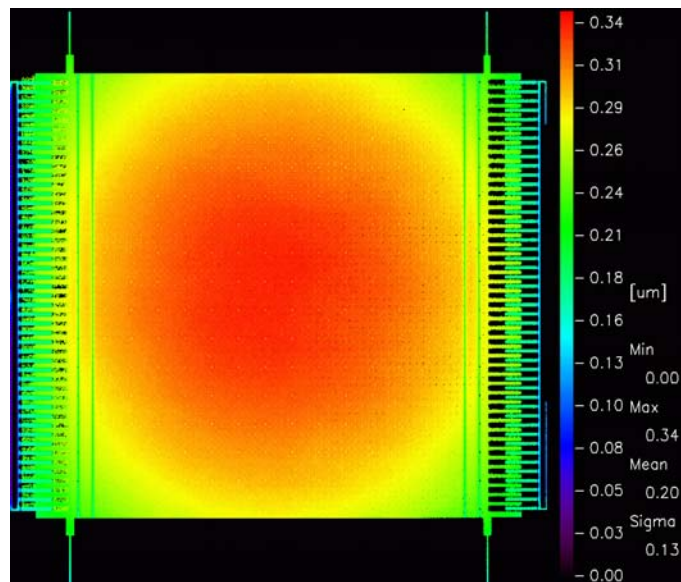of Spring 1 of the microgyro.
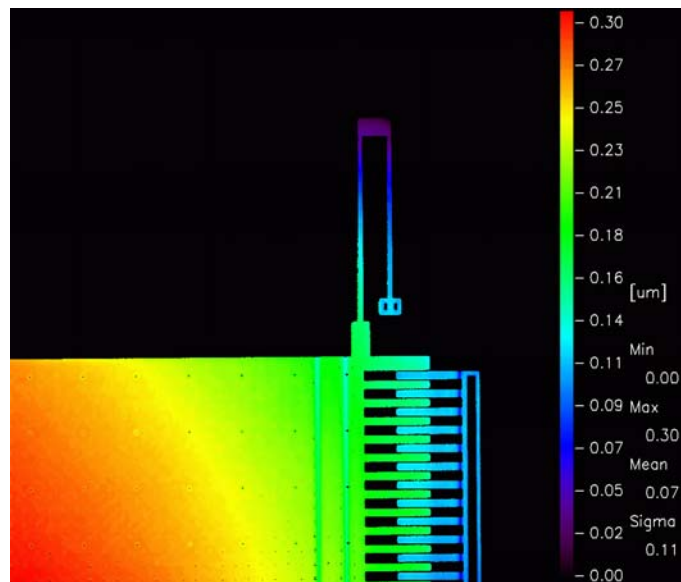
Fig. 5.57. Two-dimensional color representation of
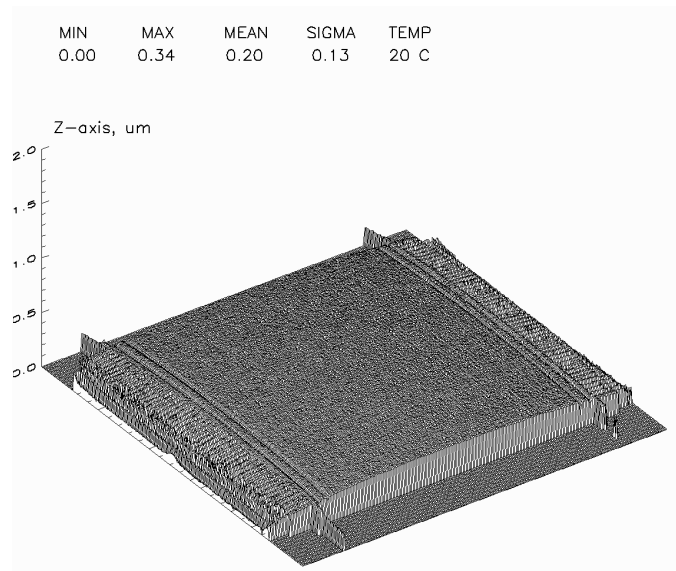deformations of Spring 1 of the microgyro.
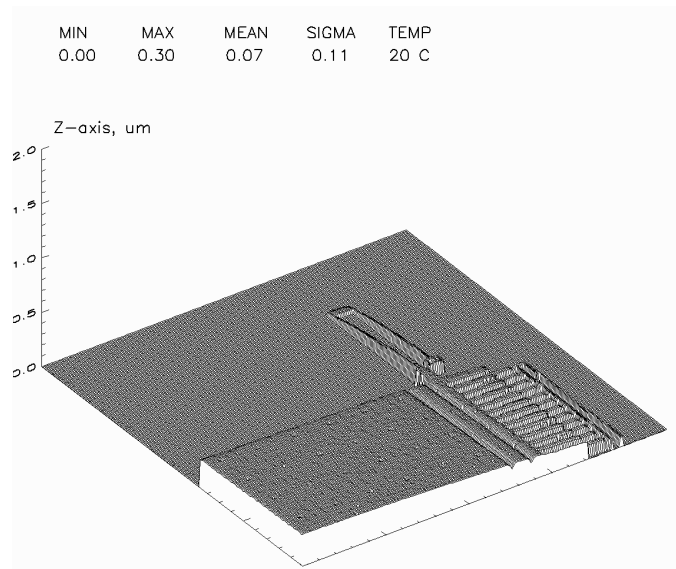
Fig. 5.58. Three-dimensional wireframe representation of deformations of Spring 1 of the microgyro.
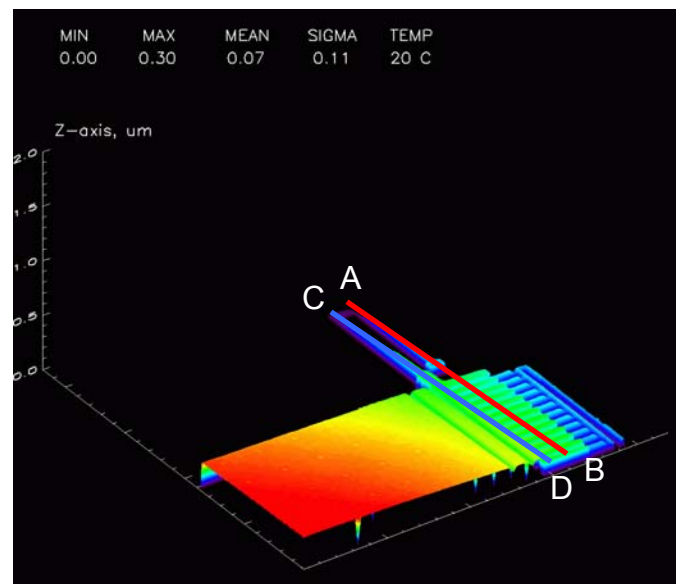
Fig. 5.59. Three-dimensional color representation of deformations of Spring 1 of the microgyro.
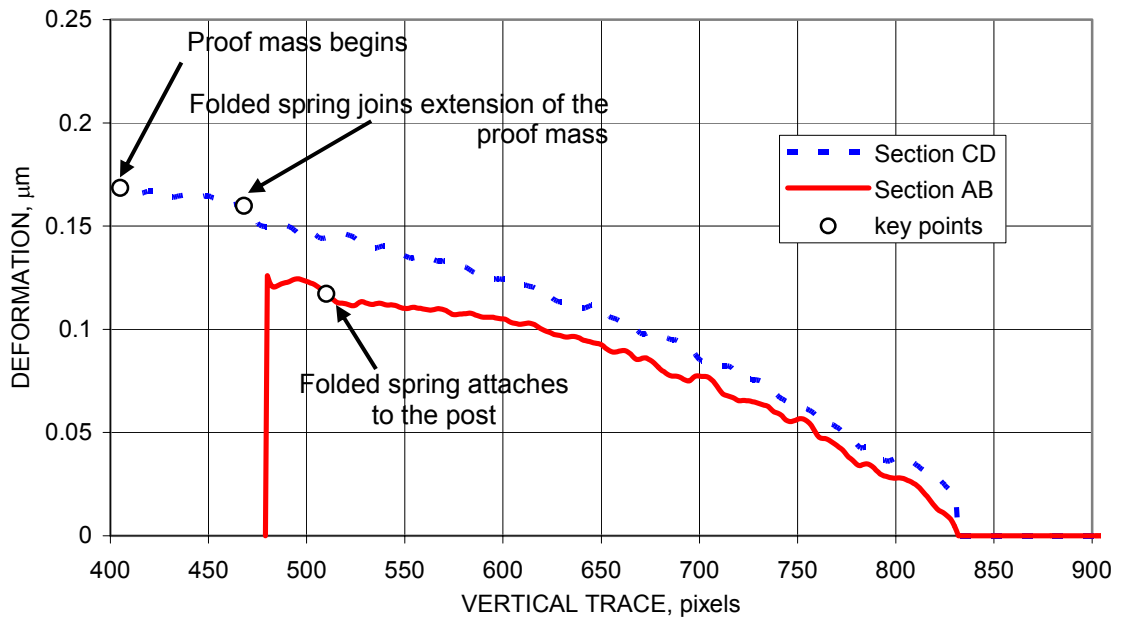
Fig. 5.60. Deformations along both arms of Spring 1.

In Fig. 5.60, key points indicate where the folded spring attaches to the post in Section *AB*, and where it joins the proof mass in Section *CD*. These data show that Section *AB* of the spring deforms approximately 0.126 μm or 126 nm, while section *CD* of the spring deforms approximately 0.15 μm or 150 nm with respect to the point where it joins the proof mass. Because of the magnitude of deformations of Spring 1, it is important to examine all of the springs that support the left proof mass.

The second spring, Spring 2, at the upper left corner of the left proof mass was observed next, and the interferograms were recorded, Fig. 5.61. These interferograms were then analyzed to obtain the shape of Spring 2 of the microgyro. Figure 5.62 shows the two-dimensional color representation of deformations of the Spring 2. These deformations are also illustrated as three-dimensional wireframe and color

169

representations, Figs 5.63 and 5.64, respectively. The results displayed in Figs 5.61 to

5.64 show that deformations of Spring 2 are approximately 0.15 μm or 150 nm.
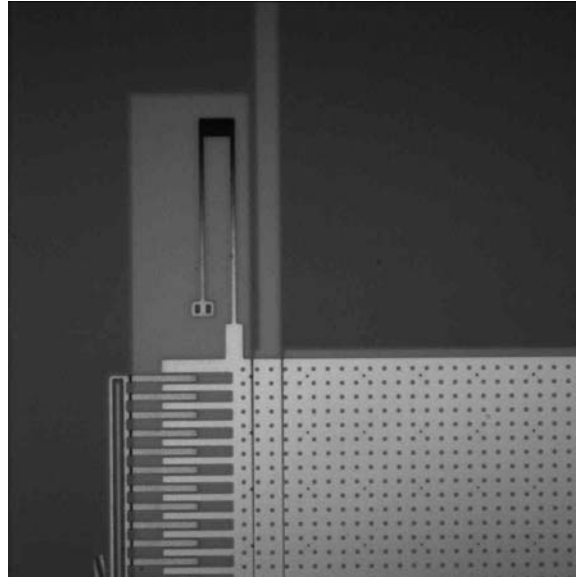
Fig. 5.61. Representative OELIM interferogram
of Spring 2 of the microgyro.
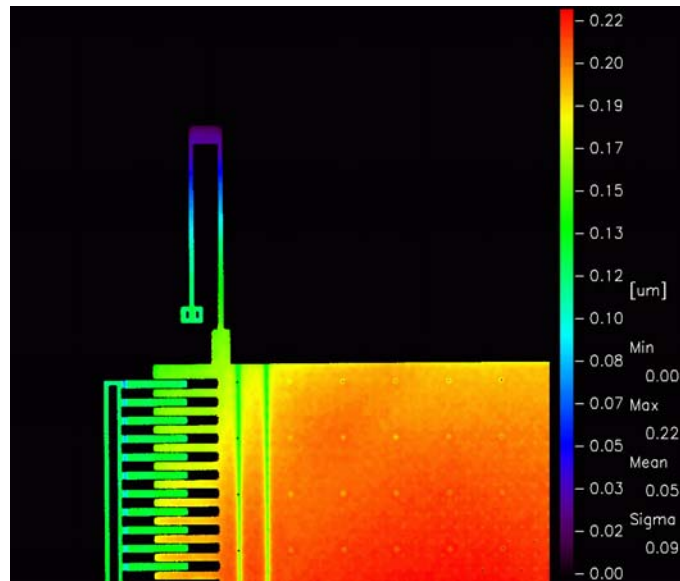
Fig. 5.62. Two-dimensional color representation of
deformations of Spring 2 of the microgyro.
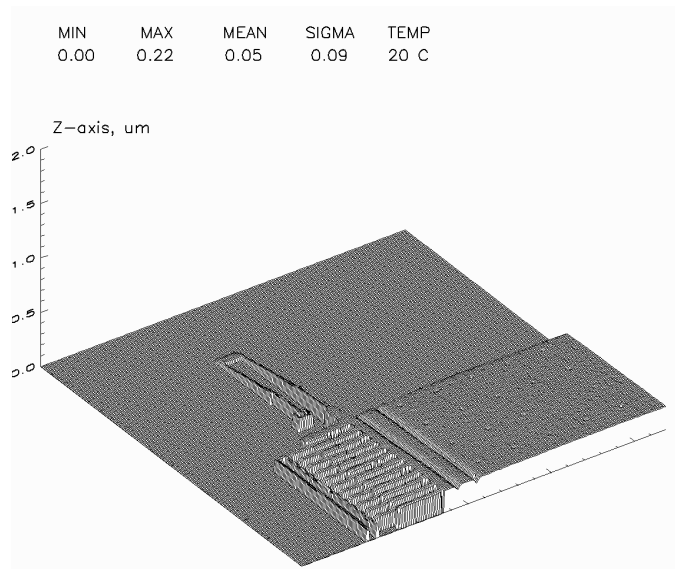
Fig. 5.63. Three-dimensional wireframe representation
of deformations of Spring 2 of the microgyro.
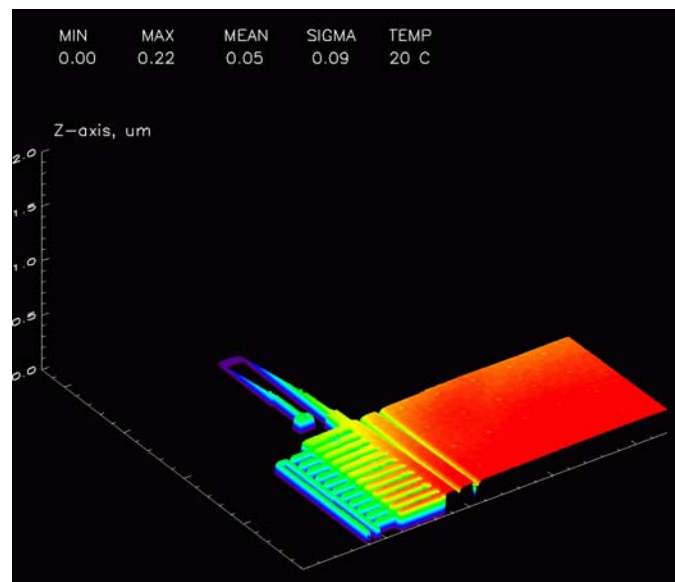
Fig. 5.64. Three-dimensional color representation of
deformations of Spring 2 of the microgyro.

171

The third spring, Spring 3, at the lower left corner of the left proof mass was

observed next, and the interferograms were recorded, Fig. 5.65. These interferograms

were analyzed to obtain the shape of Spring 3 of the microgyro. Figure 5.66 shows the

two-dimensional color representation of deformations of the Spring 3. These

deformations are also illustrated as three-dimensional wireframe and color

representations, Figs 5.67 and 5.68, respectively. The results displayed in Figs 5.65 to

5.68 show that deformations of Spring 3 are approximately 0.19 μm or 190 nm. Figure

5.68 also shows that there is some twisting in the folded spring; this factor is not included

in either analytical or computational models of the folded spring, at this time.
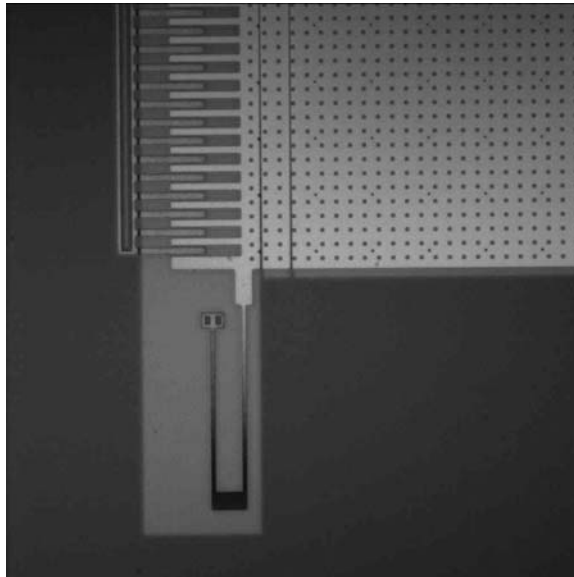
Fig. 5.65. RepresentativeOLIEM interferogram of
Spring 3 of the microgyro.

172
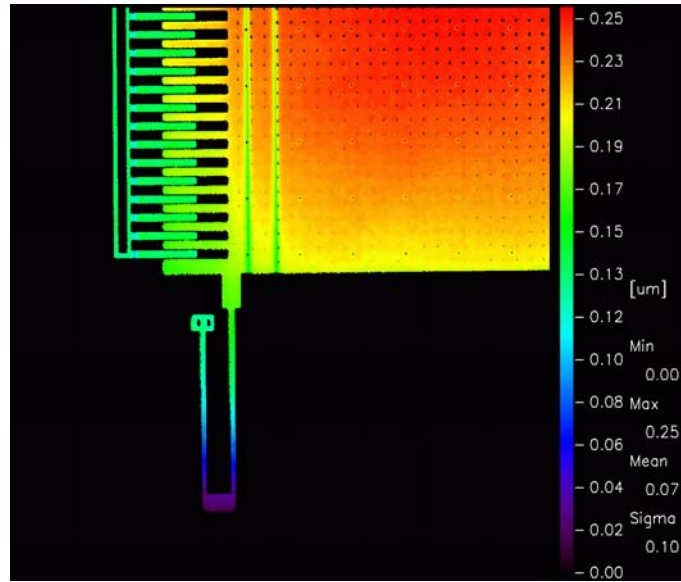
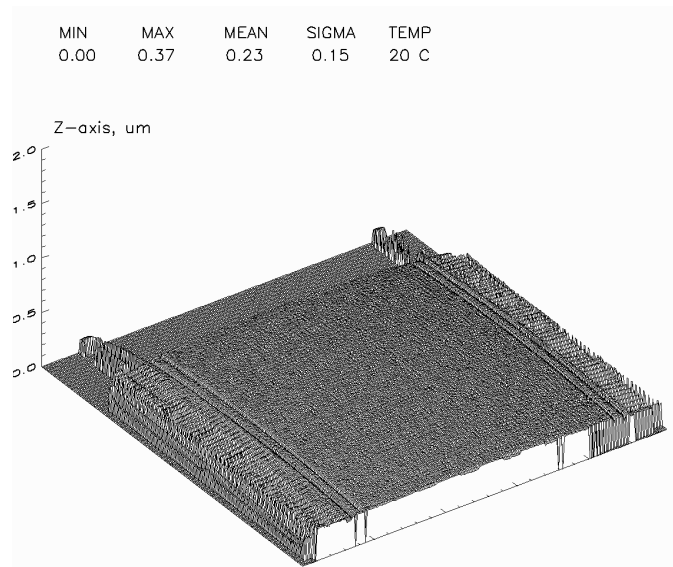Fig. 5.66. Two-dimensional color representation of deformations of Spring 3 of the microgyro.
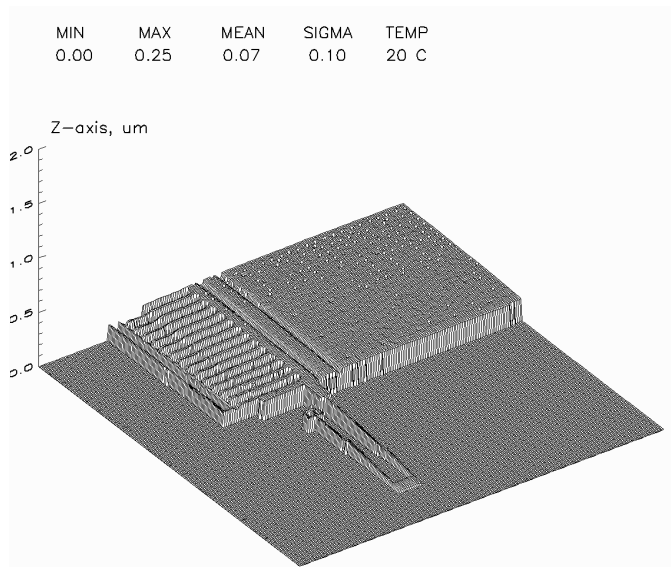
Fig. 5.67. Three-dimensional wireframe representation of deformations of Spring 3 of the microgyro.
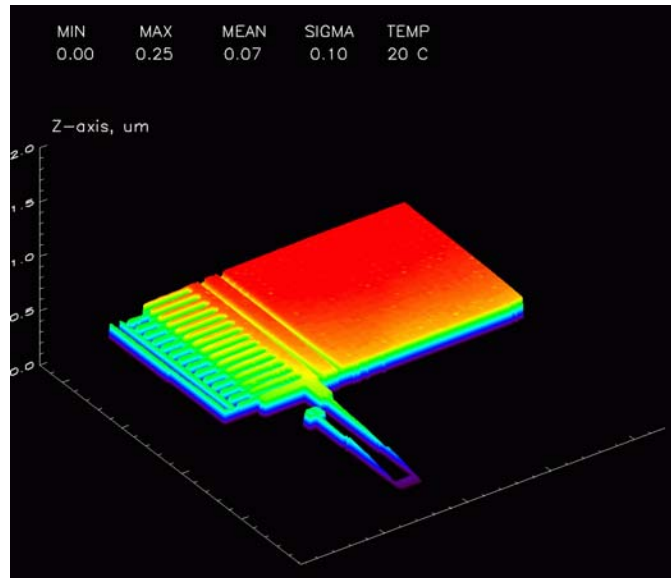
Fig. 5.68. Three-dimensional color representation of
deformations of Spring 3 of the microgyro.

Finally, the fourth spring, Spring 4, at the lower right corner of the left proof

mass was observed, and the interferograms of the spring were recorded, Fig. 5.69. These

interferograms were analyzed to obtain shape of Spring 4 of the microgyro. Figure 5.70

shows the two-dimensional color representation of deformations of the Spring 4. These

deformations are also illustrated as three-dimensional wireframe and color

representations, Figs 5.71 and 5.72, respectively. Using the data displayed in Fig. 5.72,

two traces were obtained along the lengths of the folded springs, indicated by lines AB

and CD that run along the lengths of the two arms of the folded spring. The deformations

found along the traces are illustrated in Fig. 5.73.
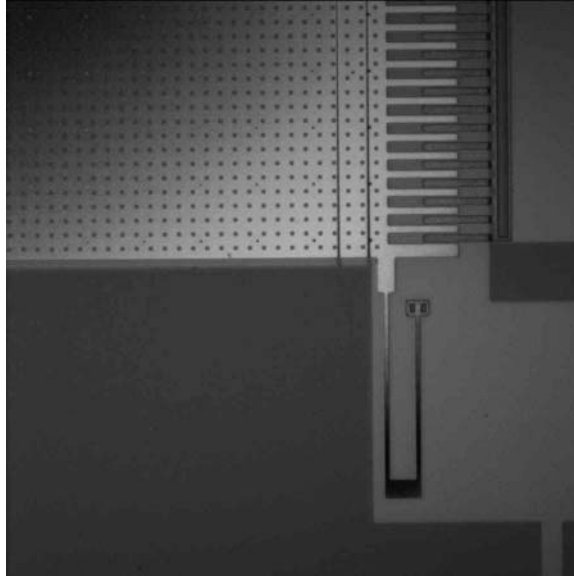
Fig. 5.69. Representative OLIEM interferogram
of Spring 4 of the microgyro.
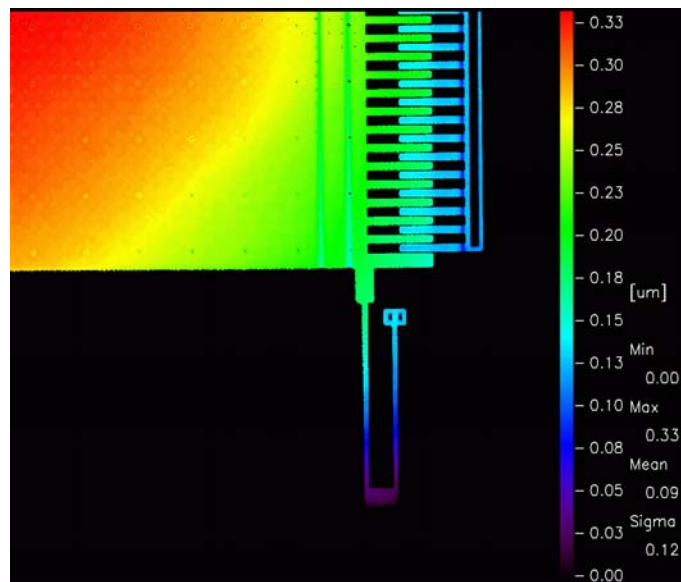
Fig. 5.70. Two-dimensional color representation of
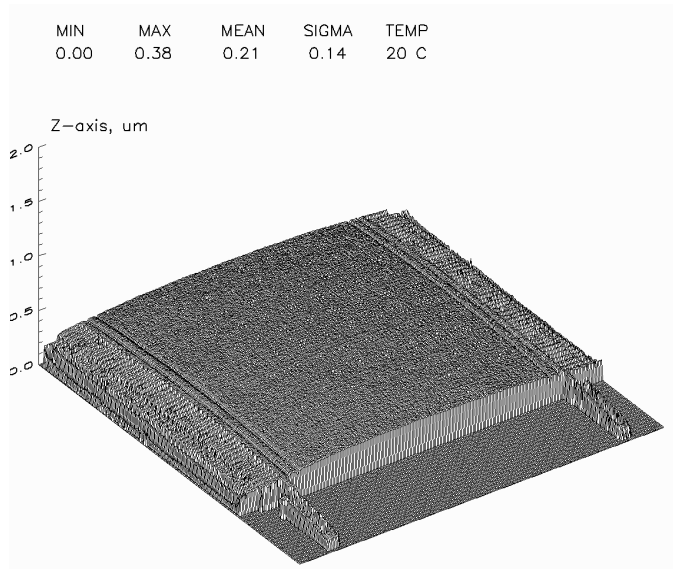deformations of Spring 4 of the microgyro.
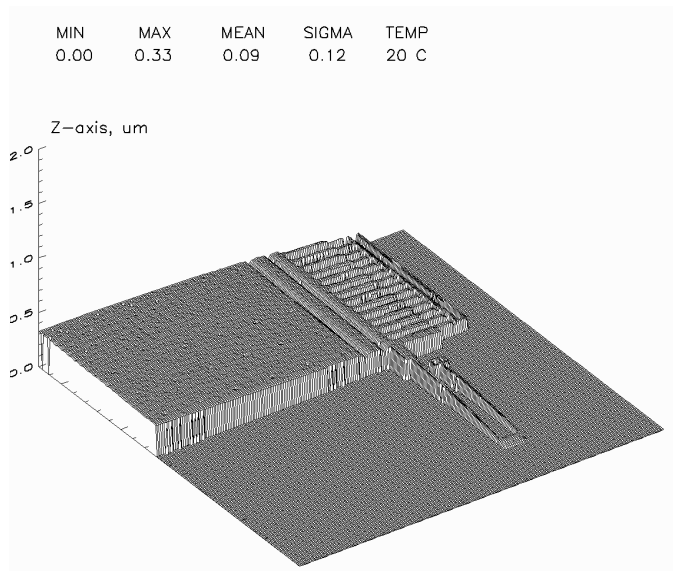
Fig. 5.71. Three-dimensional wireframe representation
of deformations of Spring 4 of the microgyro.
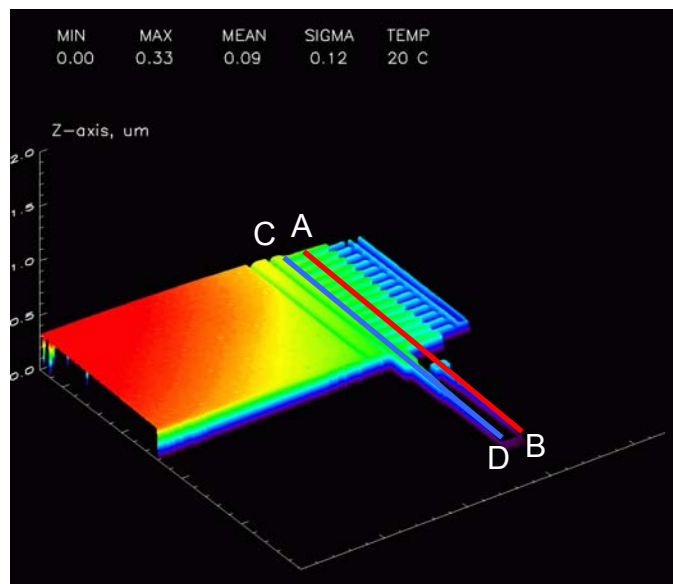
Fig. 5.72. Three-dimensional color representation of
deformations of Spring 4 of the microgyro.
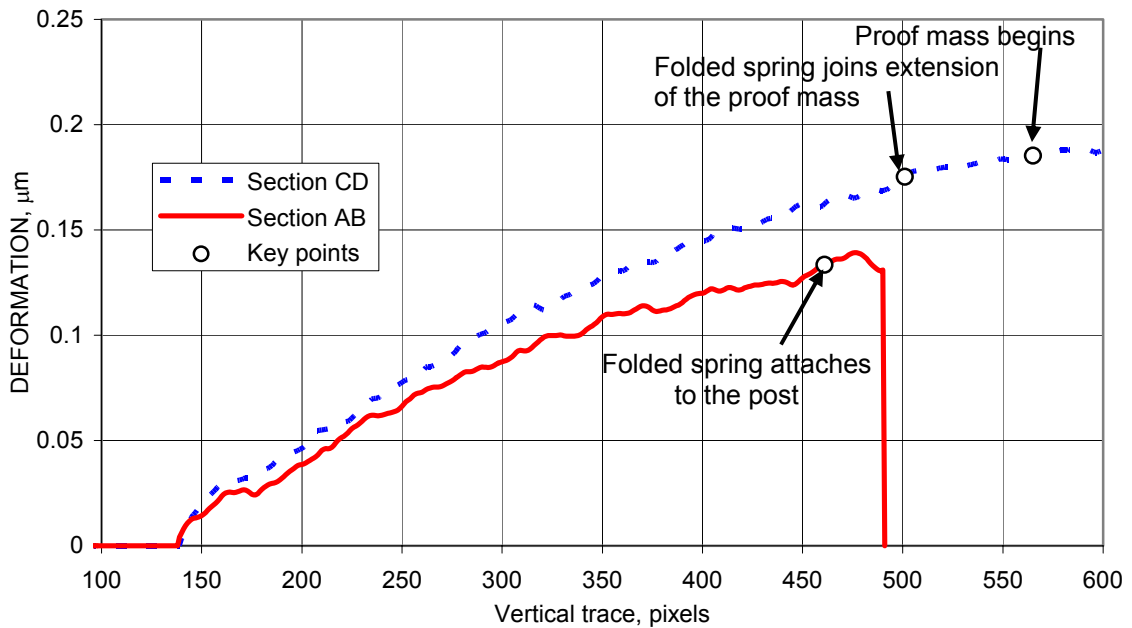
Fig. 5.73. Deformations along both arms of Spring 4.

In Fig. 5.73, key points indicate where the folded spring attaches to the post in Section *AB*, and where it joins the proof mass in Section *CD*. The results of Fig. 5.73 show that Section *AB* of the spring deforms approximately 0.133 μm or 133 nm. Section *CD* of the spring deforms approximately 0.175 μm or 175 nm. Just as in Fig. 5.68 for Spring 3, Fig. 5.72 shows that there is some twisting in Spring 4. This twisting is due to the fact that the connection of the folded spring to the proof mass does not occur in the same plane; therefore, moments are introduced to the folded spring at the interface and these induce twisting.

Interferograms were also obtained for Springs 5 to 8 supporting the right proof mass. However, since these interferograms show the same type of information as those

shown in Figs 5.56 to 5.73, and indicate deformations of the folded spring of up to 200 nm, they are included in Section D.2.

Based on the information in this section, and Sections 5.4.2.1 and 5.4.2.2, it is clear that the folded springs, and even the proof masses of the microgyroscope are not entirely flat and all in the same plane. Due to these deformations, operational functionality of the microgyro may be altered. In some cases, the folded springs themselves are twisted as a result of fabrication processes. These deformations of various components of the microgyroscope could be contributing to the difference between the experimental and analytical results presented in this thesis.

To better understand the influence that residual deformations of various components of the microgyroscopes have on their functional operation, more detailed study of these deformations should be conducted in the future. This study could also include effects that parameters characterizing various steps in the fabrication process have on the performance of the microgyroscopes (Hanson, et al., 2001).

6. CONCLUSIONS AND RECOMMENDATIONS

In this thesis, fundamentals of operation of conventional and MEMS gyroscopes were discussed. A surface micromachined tuning fork MEMS gyroscope from Sandia National Laboratories was examined. The Sandia microgyro has a dual proof mass configuration in which each proof mass is supported by folded springs at every one of its four corners. Deformations of folded springs of the microgyro were modeled using analytical and computational methods. In addition, preliminary measurements of parameters characterizing and influencing functional operation of the microgyroscope were made using laser vibrometer method and optoelectronic laser microscope (OELIM) method. These methods provide very high spatial resolution data with nanometer measurement accuracy that are acquired in full-field-of-view, remotely and noninvasively, in near real-time. As such, these methods are particularly suitable for experimental investigations of microgyroscopes, or other MEMS.

The analytical deformation equations were derived for all three Cartesian coordinate directions using Castigliano's second theorem and the strain energies of prismatic beams for two cases: 1) a cantilever representation of the folded spring and 2) the entire folded spring. The 3D representation of the geometry considered was developed in SolidWorks and then modeled in COSMOS/M following convergence analyses. The analytical and computational results for the deformations of the cantilever compared within 0.1%, indicating good correlation between the analytical and computational solutions used, while percent differences for deformations for the entire folded spring ranged from -2.9% for the deformation in the y-direction to -8.7% for the

179

deformation in the *x*-direction. The differences between the results obtained using analytical and computational models for the folded spring was most probably introduced in modeling the interfaces between section *BC* and sections *AB* and *CD*.

Experimental deformations were obtained using the laser vibrometer. When the deconvolved frequency response of the substrate/proof mass was converted to the time domain and the maximum deformation amplitude was compared to analytically calculated deformations, the differences between the analytical and experimental results were on the order of 10% and are in agreement with the uncertainty limits. One cause of these differences maybe related to the fact that the microgyroscopes, studied in this thesis are not perfectly planar structures, as the theory assumes. For this reason, the shapes of the microgyroscope and the folded springs were measured using the OELIM methodology. Quantitative interpretation of the OELIM interferograms of the microgyroscopes indicated that deformations of the microgyroscope can be as much as 200 nm, which is 8% of the thickness of 2.5 μm of the proof masses and the corresponding folded springs. The deformations indicate that the folded springs and proof masses they support are not in the same plane. Therefore, during operation, the microgyros may be subjected to loads that are not anticipated during design and corresponding analyses, which assume the microgyros to be planar structures. Consideration of the effects that the experimentally determined non-planarity of the microgyros may on their functional operation should be made as a follow up of this thesis.

This thesis only began development of a methodology for modeling the microgyroscope. The next step would be to incorporate into the analytical model the fact that the folded springs and proof mass are not located in the same plane. This requires addition of moments at the interface between the folded spring and the proof mass, at point *D*. The interfaces between section *BC* and sections *AB* and *CD* should also be re-evaluated. As these changes are implemented into the analytical and computational models, the laser vibrometer experiments should be conducted in order to determine which error: the non-planarity of the folded springs and proof mass, or the modeling of the interfaces, contribute most to the differences between the analytical and the experimental results.

Another step would be to analytically and/or computationally determine the influence that residual deformations of various components of the microgyroscope have on its operational performance. The experiments should also be performed to evaluate designs of the microgyroscopes different than the design considered in this thesis to ensure that the differences observed are not due to the characteristics of a specific design. Once these additional experiments are completed, and causes of the differences between the analytical, computational, and experimental results are understood, the methodology used in this thesis might become useful to model behavior of the suspension of the proof masses. At that stage of its development, this methodology may facilitate improvement of existing designs and development of new designs of gyroscopes.

7. REFERENCES

Analog Devices, 2003a, "± 150°/s single chip yaw rate gyro with signal conditioning, ADXRS150," Analog Devices, Inc., Norwood, MA. Found online: www.analogdevices.com, January 2003.

Analog Devices, 2003b, "± 300°/s single chip yaw rate gyro with signal conditioning, ADXRS300," Analog Devices, Inc., Norwood, MA. Found online: www.analogdevices.com, January 2003.

F. P. Beer and E. R. Johnston, Jr., 1992, *Mechanics of materials*, 2nd ed., McGraw-Hill, New York, p. 164.

P. L. Bergstrom and G. G. Li, 2002, "Inertial sensors," Ch. 24 in *The MEMS handbook*, M. Gad-el-Hak, ed., CRC Press, Boca Raton, FL, 33431, pp. 1-30.

E. O. Brigham, 1988, *The fast Fourier transform and its applications*, Prentice-Hall, Englewood Cliffs, NJ.

G. C. Brown and R. J. Pryputniewicz, 2000, "New test methodology for static and dynamic shape measurements of microelectromechanical systems," *Opt. Eng.*, 39:127-136.

J. Bryzek, 1996, "Impact of MEMS technology on society," *Sensors and Actuators*, Elsevier Science S.A., pp.1-9. Found Online: www.sciencedirect.com, 21 May 2001.

R. B. Cook and W. C. Young, 1985, *Advanced mechanics of materials*, Macmillian, New York, pp. 227-231 and 243-247.

F. J. B. Cordeiro, 1913, *The gyroscope*, Spon & Chamberlain, New York.

H. W. Coleman and W. G. Steele, Jr., 1989, *Experimentation and uncertainty anlysis for engineers*, Wily, New York, pp. 26-47.

COSMOS/M, 2003, *Advanced finite element analysis*, Structural Research & Analysis Corporation, Los Angeles, CA.

T. Fujita, T. Mizuno, R. Kenny, K. Maenaka, and M. Maeda, 1997, "Two-dimensional micromachined gyroscope," *Transducers '97, 1997 Internat. Conf. on Solid-State Sensors and Actuators*, Chicago, pp. 887-890. Found online: www.ieeexplore.ieee.org/Xplore/DynWel.jsp, March 2003.

C. Furlong, 1993, "Deconvolution of two signals," *ME 559 laboratory report 8*, Worcester Polytechnic Institute, Worcester, MA.

C. Furlong, 1999, *Hybrid, experimental and computational, approach for the efficient study and optimization of mechanical and electro-mechanical components*, Ph.D. Dissertation, Worcester Polytechnic Institute, Worcester, MA.

C. Furlong and R. J. Pryputniewicz, 2000, "Absolute shape measurements using high-resolution optoelectronic holography methods," *Opt. Eng.*, 39:216-223.

C. Furlong and R. J. Pryputniewicz, 2001, "Measurements and modeling of a nanoindentation process for MEMS," *Proc. Internat. Symp. On MEMS: Mechanics and Measurements*, Portland, OR, pp.28-33.

C. Furlong and R. J. Pryputniewicz, 2002, "Characterization of shape and deformation of MEMS by quantitative optoelectronic metrology techniques," *Proc. SPIE,* 4778:1-10.

M. Gad-el-Hak, 2002, "Introduction," Ch.1 in *The MEMS handbook*, M. Gad-el-Hak, ed., CRC Press, Boca Raton, FL, pp. 1-4.

W. Geiger, B. Folkmer, J. Merz, H. Sandmaier, and W. Lang, 1998, "A new silicon rate gyroscope," *Proc. Eleventh Annual Internat. Workshop on Micro Electro Mechanical Systems*, Heidelberg, Germany, pp. 615-620. Found online: www.ieeexplore.ieee.org/Xplore/DynWel.jsp, March 2003.

Gyroscopes Online, 2003, "The Tedco 'original' toy gyroscope," Gyroscope.com. Found Online: www.gyroscopes.co.uk, 1 December 2002.

D. S. Hanson, T. F. Marinis, C. Furlong, and R. J. Pryputniewicz, 2001, "Advances in optimization of MEMS inertial sensor packaging," *Proc. Internat. Congress on Experimental and Applied Mechanics in Emerging Technologies*, Portland, OR, pp. 821-825.

P. Hariharan and B. F. Oreb, 1986, "Stroboscopic holographic interferometry: application of digital techniques," *Opt. Commun.,* 59:83.

T. W. Harris, 1976, *Chemical milling*, Claredon Press, Oxford.

N. Hedenstierna, S. Habibi, S. M. Nilsen, and T. Kvisterøy, 2001, "Bulk micromachined angular rate sensor based on the 'butterfly'-gyro structure," *Proc. 14th IEEE Internat. Conf. on Micro Electro Mechanical Systems*, Berkley, CA, pp. 178-181. Found online: www.ieeexplore.ieee.org/Xplore/DynWel.jsp, March 2003.

R. C. Hibbler, 1998, *Engineering mechanics: dynamics*, 8th ed., Prentice-Hall, Upper Saddle River, NJ, pp. 292-295, 358.

R. C. Hibbler, 2000, *Mechanics of materials*, 4th ed., Prentice-Hall, Upper Saddle River, NJ, pp. 762-763 and 768-770.

R. T. Howe and R. S. Muller, 1982, "Polycrystalline silicon micromechanical beams," *Proc. Spring Meeting of the Electrochemical Society*, Montreal, Canada, pp. 184-185.

T. R. Hsu, 2002, *MEMS & microsystems: design and manufacture*, McGraw-Hill, New York.

B. Ineichen and J. Mastner, 1980, "Vibration analysis by stroboscopic two-reference-beam heterodyne holographic interferometry," *Optics Applied to Metrology*, SPIE-210:207-212.

A. Jeffrey, 2002, *Advanced engineering mathematics*, Hardcourt/Academic Press, Burlington, MA, p. 401.

H. Kuisma, T. Ryhänen, J. Lahdenperä, E. Punkka, S. Ruotsalainen, T. Sillanpää, and H. Seppä, 1997, "A bulk micromachined silicon angular rate sensor," *Transducers '97*, *1997 Internat. Conf. on Solid-State Sensors and Actuators*, Chicago, pp. 875-878. Found online: www.ieeexplore.ieee.org/Xplore/DynWel.jsp, March 2003.

A. Lawrence, 1998, *Modern inertial technology: navigation, guidance, and control*, F. F. Ling, ed., 2nd ed., Mechanical Engineering Series, Springer, New York.

M. S. Machate, 2003 (in preparation), *Joule heat effects on reliability of RF MEMS switches*, MS Thesis, Worcester Polytechnic Institute, Worcester, MA.

M. Madou, 1997, *Fundamentals of microfabrication*, CRC Press, Boca Raton, FL.

R. S. Muller, 2000, "MEMS: quo vadis in century XXI?" *Microelectronic Engineering*, Elsevier Science B.V., pp. 47-54. Found Online: www.elsevier.nl/locate/mee, 21 May 2001.

H. C. Nathanson, W. E. Newell, R. A. Wickstron, and J. R. Davis, 1967, "The resonant gate transistor," *IEEE Trans. Electron Devices*, ED-14, pp. 117-133.

K. Ogata, 1978, *System dynamics*, Prentice-Hall, Englewood Cliffs, NJ, p. 127.

Polytech PI, 2001, *Laser Doppler vibrometer: fiber-optic vibrometer*, Polytech GmbH, Karlsruhe, Germany. Found Online: http://www.polytec.de/polytec-com/l_vib/feat_spec_fiber_optic_vib.html, 15 March 2003.

R. L. Powell and K. A. Stetson, 1965, "Interferometric analysis by wave-front reconstruction," *J. Opt. Soc. Am.*, 55:1593-1598.

D. R. Pryputniewicz, 1997, *ACES approach to the development of microcomponents*, MS Thesis, Worcester Polytechnic Institute, Worcester, MA.

D. R. Pryputniewicz, C. Furlong, and R. J. Pryputniewicz, 2001, "ACES approach to the study of material properties of MEMS," *Proc. Internat. Symp. On MEMS: Mechanics of Measurements*, Portland, OR, pp. 80-83.

E. J. Pryputniewicz, 2000, *ACES approach to the study of electrostatically driven microengines*, MS Thesis, Worcester Polytechnic Institute, Worcester, MA.

R. J. Pryputniewicz, 1981, "High precision hologrammetry," *Internat. Arch. Photogramm.*, 24:377-386.

R. J. Pryputniewicz, 1983, *Holographic numerical analysis*, Worcester Polytechnic Institute, Worcester, MA.

R. J. Pryputniewicz, 1985, "Time-average holography in vibration analysis," *Opt. Engrg.*, 24:843-848.

R. J. Pryputniewicz, 1988, "Vibration studies using heterodyne hologram interferometry," *Industrial Laser Interferometry II,* SPIE-955:154-161.

R. J. Pryputniewicz, 1990, "Automated systems for quantitative analysis of holograms," *Holography*, SPIE-IS8:215-246.

R. J. Pryputniewicz, 1993, *Engineering experimentation*, Worcester Polytechnic Institute, Worcester, MA.

R. J. Pryputniewicz, 1995a, "Quantitative determination of displacements and strains from holograms," Ch. 3 in *Holographic interferometry*, Vol. 68 of Springer Series in Sciences, Springer-Verlag, Berlin, pp. 33-72.

R. J. Pryputniewicz, 1995b, "Hologram interferometry from silver halide to silicon and … beyond," *Proc. SPIE*, 2545:405-427.

R. J. Pryputniewicz, 1999, "Integrated approach to teaching of design, analysis, and characterization of micromechatronics," *Paper No. IMECE2000/DE-13*, Am. Soc. Mech. Eng., New York.

R. J. Pryputniewicz, 2001, "MEMS design education by case studies," *Paper No. IMECE2001/DE-23292*, Am. Soc. Mech. Eng., New York.

R. J. Pryputniewicz, 2002, *MEMS SUMMiT^{TM} technology*, Worcester Polytechnic Institute, Worcester, MA.

R. J. Pryputniewicz, J. J. Allen, C. W. Dyck, and G. C. Brown, 2000, "Experimental method for measurements of dynamic characteristics of microgyroscopes," *Proc. Internat. Symp. on Microscale Systems*, Orlando, FL, pp. 84-87.

R. J. Pryputniewicz, J. J. Allen, C. W. Dyck, and G. C. Brown, 2001, "Dynamic characterization of MEMS microgyros," *Proc. 28th Annual Symp. & Exhibition of IMAPS-NE*, Boxboro, MA, pp. 218-224.

R. J. Pryputniewicz, R. P. Champagne, J. P. Angelosanto, G. C. Brown, C. Furlong, and E. J. Pryputniewicz, 2000, "Multivariable MEMS polysilicon sensor: analysis and measurements," *Proc. Internat. Symp. on Microscale Systems*, Orlando, FL, pp. 76-79.

R. J. Pryputniewicz and C. Furlong, 2002, *MEMS and nanotechnology*, Worcester Polytechnic Institute, Worcester, MA.

R. J. Pryputniewicz and C. Furlong, 2003, "Novel electronic methodology for testing MOEMS," *Proc. Internat. Symp. on MOEMS and Miniaturized Systems III*, SPIE-4983:11-25.

R. J. Pryputniewicz, E. Shepherd, J. J. Allen, and C. Furlong, 2003, "University-National Laboratory Alliance for MEMS education," *Proc. 4th Internat. Symp. on MEMS and nanotechnology (ISMAN)*, Charlotte, NC, pp. 364-371.

R. J. Pryputniewicz, C. Furlong, G. C. Brown, and E. J. Pryputniewicz, 2001, "Optical methodology for static and dynamic measurements of nanodisplacements," *Proc. Internat. Congress on Experimental and Applied Mechanics for Emerging Technologies*, Portland, OR, pp. 826-831.

R. J. Pryputniewicz, C. Furlong, G. C. Brown, E. J. Pryputniewicz, and M. E. Seta, 2001, "Optoelectronic method for studies of MEMS," *Proc. Internat Congress on Experimental and Applied Mechanics for Emerging Technologies*, Portland, OR, pp. 817-820.

R. J. Pryputniewicz and K. A. Stetson, 1989, "Measurement of vibration patterns using electro-optic holography," *Proc. SPIE,* 1162:456-467.

A. J. Przekwas, M. Turowski, M. Furmanczyk, A. Heike, and R. J. Pryputniewicz, 2001, "Multiphysics design and simulation environment for microelectromechanical systems," *Proc. Internat. Symp. on MEMS: Mechanics and Measurements,*" Portland, OR, pp. 84-89.

W. F. Riley, L. D. Sturges, and D. H. Morris, 1995, *Statics and mechanics of materials, an integrated approach*, Wiley, New York, pp. 370-491, 514-519, and 537-540.

M. S. Rogers and J. J. Sniegowski, 1998, "5-level polysilicon surface micromachined technology: application to complex mechanical systems," *Proc. Solid State and Actuator Workshop*, Hilton Head, SC.

Sandia National Laboratories, 2003, *Sandia's Ultra-planar MEMS Multi-level Technology-V*, Albuquerque, NM.

J. J. Sniegowski and M. S. Rogers, 1998, "Manufacturing microsystems-on-a-chip with a 5-level surface micromachining technology," *Proc. 2ⁿᵈ Internat. Conf. on Engineering Design and Automation,* Maui, HI.

SolidWorks, 2001*, Solid modeling*, Solid Works Corporation, Concord, MA.

K. A. Stetson, 1970, "Effects of beam modulation on fringe loci and localization in time-average hologram interferometry," *J. Opt. Soc. Am.*, 60:1378-1384.

K. A. Stetson, 1982, "Method of vibration measurements in heterodyne interferometry," *Opt. Lett.,* 7:233-234.

K. A. Stetson and W. R. Brohinsky, 1988, "Electro-optic holography and its application to hologram interferometry", *Proc. SPIE*, 746:44-51.

V. Steward, 2003, "Dynamics of MEMS gyroscopes," *Proc. Student Symp. on Mechanics and Packaging (SSMP)*, Worcester, MA, pp. 56-57.

V. Steward, D. G. Grabbe, C. Furlong, and R. J. Pryputniewicz, 2003a, "Characterization of MEMS gyroscopes," *Proc. 30th Annual Symp. and Exhibition of IMAPS-NE*, Boxboro, MA, pp. 222-229.

V. Steward, D. G. Grabbe, and R. J. Pryputniewicz, 2003b (in press), "MEMS sensor systems: consideration of a microgyroscope," *Proc. 4ᵗʰ Internat. Symp. on MEMS and Nanotechnology (ISMAN)*, Charlotte, NC, pp. 35-48.

V. Steward and P. J. Saggal, 2002, *Dynamics of MEMS accelerometers*, MQP Report No. RJP-0120, Worcester Polytechnic Institute, Worcester, MA.

V. Steward, P. J. Saggal, C. Furlong, and R. J. Pryputniewicz, 2002, "Study of dynamics of a MEMS accelerometer," *Proc. 29ᵗʰ Annual Symp. and Exhibition of IMAPS-NE*, Boxboro, MA, pp. 108-113.

E. W. Weisstein, 1999, "Convolution," CRC Press. Found Online: http://mathworld.wolfram.com/Convolution.html, 26 May 2003.

APPENDIX A. ANALYTICAL DETERMINATION OF DEFORMATIONS OF FOLDED SPRINGS OF THE SANDIA MICROGYRO

In order to derive equations for deformations of the folded springs at point D where the force is applied, a methodology based on energy methods and Castigliano's second theorem was used. In order to begin, internal energy of the folded spring had to be determined. The internal energies need to take into account strain energies due to the axial loading, bending moments, transverse shear forces, and torsional moments. Equations A.1 to A.4 define the four strain energy components. The strain energy due to axial loading is defined as

$$U_{AL} = \int_0^L \frac{N^2}{2AE} dx \quad , \tag{A.1}$$

where N is the axial load, A is the cross sectional area, E is the modulus of elasticity of the material, and L is the length of the beam. The strain energy due to the moment is

$$U_{BM} = \int_0^L \frac{M^2}{2EI} dx \quad , \tag{A.2}$$

where M is the internal moment and I is the moment of inertia of the beam. The strain energy due to the transverse shear loading is given by

$$U_{TS} = \int_0^L \frac{f_s V^2}{2GA} dx \quad , \tag{A.3}$$

where V is the shear force acting in the beam, f_s is the shape factor which for a rectangular cross section is equal to 6/5, and G is the shear modulus of the material. The strain energy due to the torque is calculated using

$$U_{TM} = \int_0^L \frac{T^2}{2GJ} dx \quad , \tag{A.4}$$

where T is the torque acting on the beam and J is the polar moment of inertia of the beam. The internal energy is calculated as a sum of individual strain energies, i.e.,

$$U_i = U_{AL} + U_{BM} + U_{TS} + U_{TM} \quad . \tag{A.5}$$

To facilitate derivation of the governing equations, the folded spring was divided into three beams: AB, BC, and CD. Therefore, Eq. A.5 becomes a sum of the strain energies of all three sections, i.e.,

$$U_i = U_{AB} + U_{BC} + U_{CD} \quad , \tag{A.6}$$

where each of the section energies is calculated using

$$U_{AB} = U_{ALab} + U_{BMab} + U_{TSab} + U_{TMab} \quad , \tag{A.7}$$

$$U_{BC} = U_{ALbc} + U_{BMbc} + U_{TSbc} + U_{TMbc} \quad , \tag{A.8}$$

and

$$U_{CD} = U_{ALcd} + U_{BMcd} + U_{TScd} + U_{TMcd} \quad , \tag{A.9}$$

respectively.

In order to calculate the internal energies, equations defining the forces, moments, and torques acting on each of the sections of the beam, and the forces, moments, and torques acting through each of the three sections were derived.

A.1. Reaction forces and moments of the folded spring

The first step in the derivation of an equation for determination of deformations of the folded spring was to calculate the reaction forces and moments occurring at the fixed end, i.e., at point A, Fig. A.1.

189
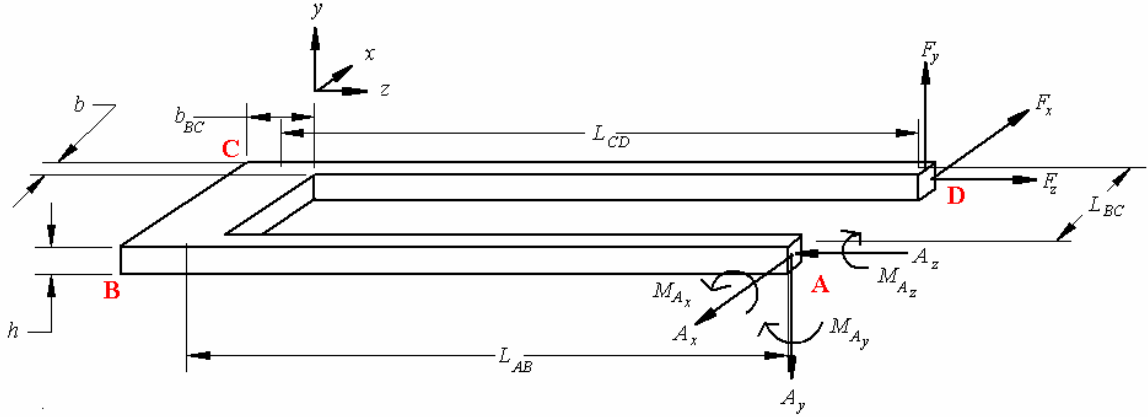
Fig. A.1. Free body diagram of the folded spring.

Using the free body diagram in Fig. A.1, the equations for static equilibrium can be written for the forces and moments acting at point A. Equations A.10 to A.15 define the Cartesian components of the reaction force acting at point A, i.e.,

$$\sum F_x = 0 = F_x - A_x \quad , \tag{A.10}$$

$$A_x = F_x \quad , \tag{A.11}$$

$$\sum F_y = 0 = F_y - A_y \quad , \tag{A.12}$$

$$A_y = F_y \quad , \tag{A.13}$$

and

$$\sum F_z = 0 = F_z - A_z \quad , \tag{A.14}$$

$$A_z = F_z \quad , \tag{A.15}$$

while the components of the reaction moment can be shown to be

$$\sum M_{xA} = 0 = F_y \left(L_{CD} - L_{AB} \right) + F_z 0 - M_{Ax} \quad , \tag{A.16}$$

$$M_{Ax} = F_y \left(L_{AB} - L_{CD} \right) \quad , \tag{A.17}$$

190

$$\sum M_{yA} = 0 = F_x(L_{CD} - L_{AB}) + F_z L_{BC} - M_{Ay} \quad , \tag{A.18}$$

$$M_{Ay} = F_x(L_{CD} - L_{AB}) - F_z L_{BC} \quad , \tag{A.19}$$

and

$$\sum M_{zA} = 0 = F_y L_{BC} + F_x 0 - M_{Az} \quad , \tag{A.20}$$

$$M_{Az} = F_y L_{BC} \quad . \tag{A.21}$$

Equations A.10 to A.21 will be used to calculated forces acting on each of the sections of the folded spring, i.e., the sections *AB*, *BC*, and *CD*.

A.2. Deformations at point *B*

In order to derive the equation for deformation at point *B,* the forces, moments, and torques acting along and through section *AB* had to be determined, as discussed in Sections A.2.1 to A.2.3.

A.2.1. Reaction forces and moments of section *AB*

Reaction forces at point *B* were derived using the free body diagram of Fig. A.2.
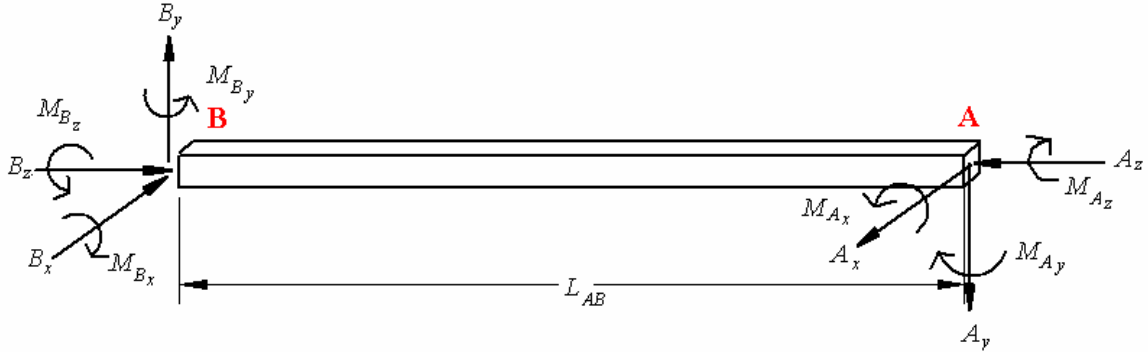
Fig. A.2. Free body diagram of section *AB*.

Using the free body diagram of Fig. A.2, equations for static equilibrium, in

Cartesian coordinates, can be written for the forces and moments acting at point *B* to be

$$\sum F_x = 0 = B_x - A_x \quad , \tag{A.22}$$

$$B_x = A_x = F_x \quad , \tag{A.23}$$

$$\sum F_y = 0 = B_y - A_y \quad , \tag{A.24}$$

$$B_y = A_y = F_y \quad , \tag{A.25}$$

$$\sum F_z = 0 = B_z - A_z \quad , \tag{A.26}$$

$$B_z = A_z = F_z \quad , \tag{A.27}$$

$$\sum M_{xB} = 0 = M_{Bx} + A_y L_{AB} + A_z 0 - M_{Ax} \quad , \tag{A.28}$$

$$M_{Bx} = M_{Ax} - A_y L_{AB} = F_y (L_{AB} - L_{CD}) - F_y L_{AB} = -F_y L_{CD} \quad , \tag{A.29}$$

$$\sum M_{yB} = 0 = M_{By} + A_x L_{AB} + A_z 0 - M_{Ay} \quad , \tag{A.30}$$

$$M_{By} = M_{Ay} + A_x L_{AB} = F_x(L_{CD} - L_{AB}) - F_z L_{BC} + F_x L_{AB} \quad , \tag{A.31}$$

$$M_{By} = F_x L_{CD} - F_z L_{BC} \quad , \tag{A.32}$$

and

$$\sum M_{zB} = 0 = M_{Bz} + A_y 0 + A_x 0 - M_{Az} \quad , \tag{A.33}$$

$$M_{Bz} = M_{Az} = F_y L_{BC} \quad . \tag{A.34}$$

Now that the reaction forces for section *AB* were derived, the internal forces, moments, and torques that are acting through section *AB* can be derived, as shown in Section A.2.2.

A.2.2. Internal forces and moments of section *AB*

The forces, moments, and torques acting through section *AB* were derived using the free body diagram for the cut at an arbitrary position *z* within the section *AB*, Fig. A.3. Based on the free body diagram of Fig. A.3, the shear forces acting through section the *AB* are

$$\sum F_x = 0 = AB_x - A_x \quad , \tag{A.35}$$

$$AB_x = A_x = F_x \quad , \tag{A.36}$$

$$\sum F_y = 0 = AB_y - A_y \quad , \tag{A.37}$$

$$AB_y = A_y = F_y \quad , \tag{A.38}$$

$$\sum F_z = 0 = AB_z - A_z \quad , \tag{A.39}$$

$$AB_z = A_z = F_z \quad , \tag{A.40}$$

and the moments acting thru the section *AB* are

193

$$\sum M_{xAB} = 0 = M_{ABx} + A_y z + A_z 0 - M_{Ax} \quad , \tag{A.41}$$

$$M_{ABx} = M_{Ax} - A_y z = F_y (L_{AB} - L_{CD}) - F_y z \quad , \tag{A.42}$$

$$\sum M_{yAB} = 0 = M_{ABy} - A_x z + A_z 0 - M_{Ay} \quad , \tag{A.43}$$

$$M_{ABy} = M_{Ay} - A_x z = F_x (L_{CD} - L_{AB}) - F_y L_{BC} + F_x z \quad , \tag{A.44}$$

$$\sum M_{zAB} = 0 = T_{ABy} - B_y z + B_x 0 - M_{Az} \quad , \tag{A.45}$$

$$T_{ABz} = M_{Az} = F_y L_{BC} \quad . \tag{A.46}$$
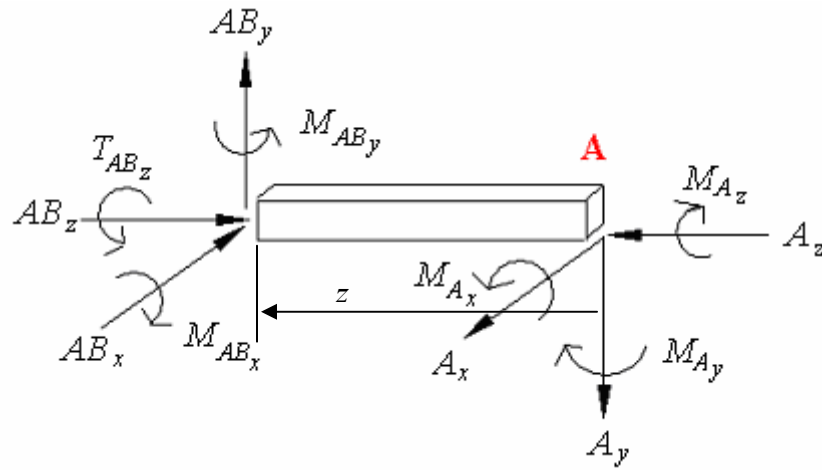
Fig. A.3. Free body diagram of the cut of section *AB*.

A.2.3. Derivation of the deformations at point *B*

Using the forces, moments, and torques, defined by, Eqs A.35 to A.46, the
equations for the internal energy for section *AB* in terms of the individual components of
the strain energy can be written as

$$U_{AB} = AxialLoadingSE + BendingMomentsSE + TransverseShearSE + \\ TorsionalMomentSE \tag{A.47}$$

Substituting Eqs A.1 to A.4 and Eqs A.35 to A.46 into Eq. A.47 we obtain

$$
U_{AB} = \int_0^{L_{AB}} \frac{AB_z{}^2}{2A_bE}\,dz + \int_0^{L_{AB}} \frac{M_{ABx}{}^2}{2EI_{by}}\,dz + \int_0^{L_{AB}} \frac{M_{ABy}{}^2}{2EI_{by}}\,dz +
$$
$$
\int_0^{L_{AB}} \frac{\tfrac{6}{5}AB_x{}^2}{2GA_b}\,dz + \int_0^{L_{AB}} \frac{\tfrac{6}{5}AB_y{}^2}{2GA_b}\,dz + \int_0^{L_{AB}} \frac{T_{ABz}{}^2}{2GJ_b}\,dz \quad . \tag{A.48}
$$

In order to determine, e.g., the *x*-component of displacement at point *B* on the beam, partial derivative of the internal energy of section *AB* has to be taken with respect to the force, F_x, acting in the direction of the desired displacement, i.e.,

$$
\frac{\partial}{\partial F_x} U_{AB} = \Delta_{Bx} \quad , \tag{A.49}
$$

Therefore, Eq. A.49 yields

$$
\Delta_{Bx} = \int_0^{L_{AB}} \frac{AB_z}{A_bE}\left(\frac{\partial}{\partial F_x}AB_z\right)dz + \int_0^{L_{AB}} \frac{M_{ABx}}{EI_{by}}\left(\frac{\partial}{\partial F_x}M_{ABx}\right)dz +
$$
$$
\int_0^{L_{AB}} \frac{M_{ABy}}{EI_{by}}\left(\frac{\partial}{\partial F_x}M_{ABy}\right)dz + \int_0^{L_{AB}} \frac{6AB_x}{5GA_b}\left(\frac{\partial}{\partial F_x}AB_x\right)dz + \quad , \tag{A.50}
$$
$$
\int_0^{L_{AB}} \frac{6AB_y}{5GA_b}\left(\frac{\partial}{\partial F_x}AB_y\right)dz + \int_0^{L_{AB}} \frac{T_{ABz}}{GJ_b}\left(\frac{\partial}{\partial F_x}T_{ABz}\right)dz
$$

After the derivatives are taken, Eq. A.31 becomes

$$
\Delta_{Bx} = \int_0^{L_{AB}} \frac{AB_z}{A_bE}(0)dz + \int_0^{L_{AB}} \frac{M_{ABx}}{EI_{by}}(0)dz +
$$
$$
\int_0^{L_{AB}} \frac{F_x(L_{CD}-L_{AB}+z)-F_zL_{BC}}{EI_{by}}(L_{CD}-L_{AB}+z)dz + \quad , \tag{A.51}
$$
$$
\int_0^{L_{AB}} \frac{6F_x}{5GA_b}(1)dz + \int_0^{L_{AB}} \frac{6F_y}{5GA_b}(0)dz + \int_0^{L_{AB}} \frac{F_yL_{BC}}{GJ_b}(0)dz
$$

which simplifies to

$$\Delta_{Bx} = \int_0^{L_{AB}} \frac{F_x \left(L_{CD} - L_{AB} + z\right)^2 - F_z L_{BC}\left(L_{CD} - L_{AB} + z\right)}{EI_{by}} dz +$$
$$\int_0^{L_{AB}} \frac{6F_x}{5GA_b}(1)dz$$

(A.52)

Once the integral is taken, Eq. A.52 simplifies to the equation for the *x*-component of deformation at point *B*, i.e.,

$$\Delta_{Bx} = \frac{F_x}{3EI_{by}}\left(L_{AB}{}^3 - 3L_{AB}{}^2 L_{CD} + 3L_{AB}L_{CD}{}^2\right) + \frac{6F_x L_{AB}}{5GA_b} +$$
$$\frac{F_z L_{BC}}{2EI_{by}}\left(L_{AB}{}^2 - 2L_{AB}L_{CD}\right)$$

(A.53)

To find the displacement in the *y*-direction at point *B*, partial derivative of the internal energy of section *AB* was taken with respect to F_y yielding

$$\frac{\partial}{\partial F_y} U_{AB} = \Delta_{By} \quad , $$

(A.54)

which becomes

$$\Delta_{By} = \int_0^{L_{AB}} \frac{AB_z}{A_b E}\left(\frac{\partial}{\partial F_y} AB_z\right)dz + \int_0^{L_{AB}} \frac{M_{ABx}}{EI_{bx}}\left(\frac{\partial}{\partial F_y} M_{ABx}\right)dz +$$
$$\int_0^{L_{AB}} \frac{M_{ABy}}{EI_{bx}}\left(\frac{\partial}{\partial F_y} M_{ABy}\right)dz + \int_0^{L_{AB}} \frac{6AB_x}{5GA_b}\left(\frac{\partial}{\partial F_y} AB_x\right)dz +$$
$$\int_0^{L_{AB}} \frac{6AB_y}{5GA_b}\left(\frac{\partial}{\partial F_y} AB_y\right)dz + \int_0^{L_{AB}} \frac{T_{ABz}}{GJ_b}\left(\frac{\partial}{\partial F_y} T_{ABz}\right)dz$$

(A.55)

After the derivatives are taken, Eq A.55 takes the form

$$\Delta_{By} = \int_0^{L_{AB}} \frac{AB_z}{A_b E}(0)dz + \int_0^{L_{AB}} \frac{F_y\left(L_{AB} - L_{CD} - z\right)}{EI_{bx}}\left(L_{AB} - L_{CD} - z\right)dz +$$
$$\int_0^{L_{AB}} \frac{M_{ABy}}{EI_{bx}}(0)dz + \int_0^{L_{AB}} \frac{6F_x}{5GA_b}(0)dz +$$
$$\int_0^{L_{AB}} \frac{6F_y}{5GA_b}(1)dz + \int_0^{L_{AB}} \frac{F_y L_{BC}}{GJ_b}\left(L_{BC}\right)dz$$

(A.56)

which simplifies to

$$\Delta_{By} = \int_0^{L_{AB}} \frac{F_y(L_{AB}-L_{CD}-z)^2}{EI_{bx}}dz + \int_0^{L_{AB}} \frac{6F_y}{5GA_b}dz + \int_0^{L_{AB}} \frac{F_yL_{BC}^2}{GJ_b}dz \quad . \tag{A.57}$$

After Eq. A.57 is integrated, the *y*-component of deformation at point *B* can be expressed as

$$\Delta_{By} = \frac{F_y}{3EI_{bx}}\left(L_{AB}^3 - 3L_{AB}^2L_{CD} + 3L_{AB}L_{CD}^2\right) + \frac{6F_yL_{AB}}{5GA_b} + \frac{F_yL_{BC}^2L_{AB}}{GJ_b} \quad . \tag{A.58}$$

The displacement in the *z*-direction at point *B* was found by taking the partial derivative of the internal energy of section *AB* with respect to F_z, i.e.,

$$\frac{\partial}{\partial F_z}U_{AB} = \Delta_{Bz} \quad , \tag{A.59}$$

which can be represented as

$$\begin{aligned}\Delta_{Bz} = &\int_0^{L_{AB}} \frac{AB_z}{A_bE}\left(\frac{\partial}{\partial F_z}AB_z\right)dz + \int_0^{L_{AB}} \frac{M_{ABx}}{EI_{by}}\left(\frac{\partial}{\partial F_z}M_{ABx}\right)dz + \\ &\int_0^{L_{AB}} \frac{M_{ABy}}{EI_{by}}\left(\frac{\partial}{\partial F_z}M_{ABy}\right)dz + \int_0^{L_{AB}} \frac{6AB_x}{5GA_b}\left(\frac{\partial}{\partial F_z}AB_x\right)dz + \\ &\int_0^{L_{AB}} \frac{6AB_y}{5GA_b}\left(\frac{\partial}{\partial F_z}AB_y\right)dz + \int_0^{L_{AB}} \frac{T_{ABz}}{GJ_b}\left(\frac{\partial}{\partial F_z}T_{ABz}\right)dz\end{aligned} \quad . \tag{A.60}$$

After the derivatives are taken, Eq A.60 becomes

$$\begin{aligned}\Delta_{Bz} = &\int_0^{L_{AB}} \frac{F_z}{A_bE}(1)dz + \int_0^{L_{AB}} \frac{M_{ABx}}{EI_{by}}(0)dz + \\ &\int_0^{L_{AB}} \frac{F_x(L_{CD}-L_{AB}+z)-F_zL_{BC}}{EI_{by}}(-L_{BC})dz + \int_0^{L_{AB}} \frac{F_yL_{BC}}{GJ_b}(0)dz\end{aligned} \quad , \tag{A.61}$$

which simplifies to

$$\Delta_{Bz} = \int_0^{L_{AB}} \frac{F_z}{A_b E} dz + \int_0^{L_{AB}} \frac{-F_x L_{BC}(L_{CD} - L_{AB} + z) + F_z L_{BC}^2}{EI_{by}} dz \quad , \tag{A.62}$$

and after integration, the *z*-component of deformation at point *B* becomes

$$\Delta_{Bz} = \frac{F_z L_{AB}}{A_b E} + \frac{F_x L_{BC}(L_{AB}^2 - 2L_{CD}L_{AB})}{2EI_{by}} + \frac{F_z L_{BC}^2 L_{AB}}{EI_{by}} \quad . \tag{A.63}$$

A.3. Deformations at point *C*

Equation for deformations at point *C* were derived next. In order to do this, the forces, moments and torques acting along and through section *BC* had to be determined, as presented in Section A.3.1.

A.3.1. Reaction forces and moments of section *BC*

Reaction forces at point *C* were determined using the free body diagram of Fig. A.4. Using the free body diagram of Fig. A.4, equations for static equilibrium, in Cartesian coordinates, can be written for the forces and moments acting at point *C* as

$$\sum F_x = 0 = C_x - B_x \quad , \tag{A.64}$$

$$C_x = B_x = F_x \quad , \tag{A.65}$$

$$\sum F_y = 0 = C_y - B_y \quad , \tag{A.66}$$

$$C_y = B_y = F_y \quad , \tag{A.67}$$

$$\sum F_z = 0 = C_z - B_z \quad , \tag{A.68}$$

$$C_z = B_z = F_z \quad , \tag{A.69}$$

$$\sum M_{xB} = 0 = -M_{Bx} + C_y 0 + C_z 0 - M_{Cx} \quad , \tag{A.70}$$

$$M_{Cx} = M_{Bx} = -F_y L_{CD} \quad , \tag{A.71}$$

$$\sum M_{yB} = 0 = -M_{By} + C_x 0 + C_z L_{BC} - M_{Cy} \quad , \tag{A.72}$$

$$M_{Cy} = M_{By} + C_z L_{BC} = F_x L_{CD} - F_z L_{BC} + F_z L_{BC} = F_x L_{CD} \quad , \tag{A.73}$$

and

$$\sum M_{zB} = 0 = -M_{Cz} + C_x 0 + C_y L_{BC} - M_{Bz} \quad , \tag{A.74}$$

$$M_{Cz} = M_{Bz} + C_y L_{BC} = F_y L_{BC} - F_y L_{BC} = 0 \quad . \tag{A.75}$$
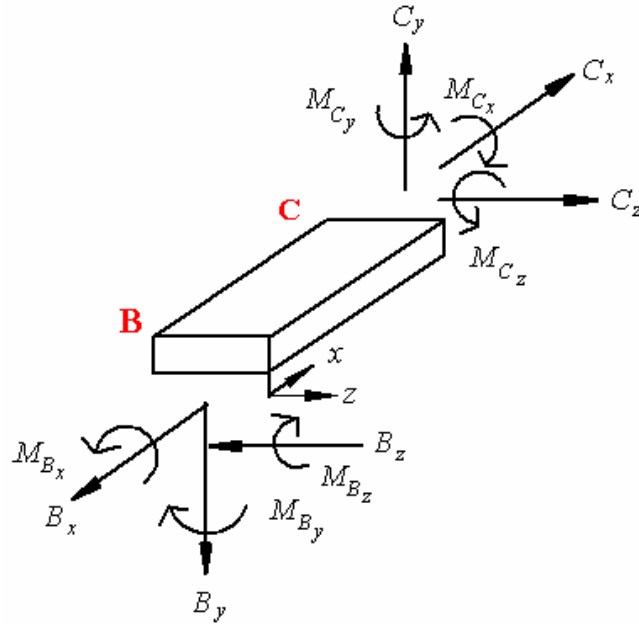
Fig. A.4. Free body diagram of section *BC*.

A.3.2. Internal forces and moment of section *BC*

The forces, moments, and torques acting through section *BC* were derived using the free body diagram for a part of section *BC* of arbitrary length in the *x*-direction, Fig. A.5.
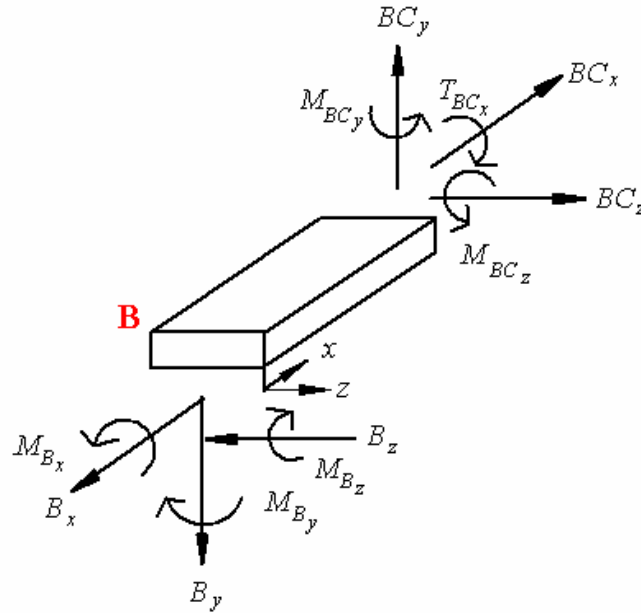
Fig. A.5. Free body diagram for a part of section *BC*.

Based on the free body diagram of Fig. A.5, the shear forces acting through the section *BC* are determined to be

$$\Sigma F_x = 0 = BC_x - B_x \quad , \tag{A.76}$$

$$BC_x = B_x = F_x \quad , \tag{A.77}$$

$$\Sigma F_y = 0 = BC_y - B_y \quad , \tag{A.78}$$

$$BC_y = B_y = F_y \quad , \tag{A.79}$$

$$\sum F_z = 0 = BC_z - B_z \quad , \tag{A.80}$$

$$BC_z = B_z = F_z \quad , \tag{A.81}$$

and the moments acting thru section *BC* are

$$\sum M_{xBC} = 0 = T_{BCx} + B_y 0 + B_z 0 - M_{Bx} \quad , \tag{A.82}$$

$$T_{BCx} = M_{Bx} = -F_y L_{CD} \quad , \tag{A.83}$$

$$\sum M_{yBC} = 0 = M_{BCy} + B_x 0 + B_z x - M_{By} \quad , \tag{A.84}$$

$$M_{BCy} = M_{By} + B_z x = F_x L_{CD} - F_z L_{BC} + F_z x = F_x L_{CD} + F_z (x - L_{BC}) \quad , \tag{A.85}$$

and

$$\sum M_{zBC} = 0 = M_{BCz} + B_y x + B_x 0 - M_{Bz} \quad , \tag{A.86}$$

$$M_{BCz} = M_{Bz} + B_y x = F_y L_{BC} - F_y x = F_y (L_{BC} - x) \quad . \tag{A.87}$$

A.3.3. Derivation of the deformations at point *C*

Using the forces, moments, and torques defined by, Eqs A.76 to A.87, equations defining deformations at point *C* will be derived. To do this partial derivative of the internal energy of section *AC*, not just that of the coupler section *BC*, has to be taken with respect to the force, F_x, acting in the direction, *x*, of the desired displacement. This means that the partial derivative of the internal energy of section *BC* has to be added to the deformation already determined at point *B*, i.e.,

$$\frac{\partial}{\partial F_x} U_{AC} = \frac{\partial}{\partial F_x} (U_{AB} + U_{BC}) = \Delta_{Bx} + \frac{\partial}{\partial F_x} U_{BC} = \Delta_{Cx} \quad . \tag{A.88}$$

Therefore, based on Eq. A.88,

201

$$\Delta_{Cx} = \Delta_{Bx} + \int_0^{L_{BC}} \frac{BC_x}{A_cE}\left(\frac{\partial}{\partial F_x}BC_x\right)dx + \int_0^{L_{BC}} \frac{M_{BCy}}{EI_{cy}}\left(\frac{\partial}{\partial F_x}M_{BCy}\right)dx +$$
$$\int_0^{L_{BC}} \frac{M_{BCz}}{EI_{cy}}\left(\frac{\partial}{\partial F_x}M_{BCz}\right)dx + \int_0^{L_{BC}} \frac{6BC_y}{5GA_c}\left(\frac{\partial}{\partial F_x}BC_y\right)dx +$$
$$\int_0^{L_{BC}} \frac{6BC_z}{5GA_c}\left(\frac{\partial}{\partial F_x}BC_z\right)dx + \int_0^{L_{BC}} \frac{T_{BCx}}{GJ_c}\left(\frac{\partial}{\partial F_x}T_{BCx}\right)dx \qquad . \qquad \text{(A.89)}$$

After the derivatives are taken, Eq A.89 becomes

$$\Delta_{Cx} = \Delta_{Bx} + \int_0^{L_{BC}} \frac{F_x}{A_cE}(1)dx + \int_0^{L_{BC}} \frac{F_xL_{CD} + F_z(x-L_{BC})}{EI_{cy}}(L_{CD})dx +$$
$$\int_0^{L_{BC}} \frac{M_{BCz}}{EI_{cy}}(0)dx + \int_0^{L_{BC}} \frac{6F_y}{5GA_c}(0)dx + \int_0^{L_{BC}} \frac{6F_z}{5GA_c}(0)dx + \int_0^{L_{BC}} \frac{T_{ABx}}{GJ_c}(0)dx \qquad , \qquad \text{(A.90)}$$

which simplifies to

$$\Delta_{Cx} = \Delta_{Bx} + \int_0^{L_{BC}} \frac{F_x}{A_cE}dx + \int_0^{L_{BC}} \frac{F_xL_{CD}^2 + F_zL_{CD}(x-L_{BC})}{EI_{cy}}dx \qquad . \qquad \text{(A.91)}$$

Integrating Eq. A.91, the *x*-component of deformation at point *C* can be written as

$$\Delta_{Cx} = \Delta_{Bx} + \frac{F_xL_{BC}}{A_cE} + \frac{F_xL_{CD}^2L_{BC}}{EI_{cy}} - \frac{F_zL_{CD}L_{BC}^2}{2EI_{cy}} \qquad . \qquad \text{(A.92)}$$

Equation A.92 simplifies to

$$\Delta_{Cx} = \frac{F_x}{3EI_{by}}\left(L_{AB}^3 - 3L_{AB}^2L_{CD} + 3L_{AB}L_{CD}^2\right) + \frac{6F_xL_{AB}}{5GA_b} +$$
$$\frac{F_zL_{BC}}{2EI_{by}}\left(L_{AB}^2 - 2L_{AB}L_{CD}\right) + \frac{F_xL_{BC}}{A_cE} + \frac{F_xL_{CD}^2L_{BC}}{EI_{cy}} - \frac{F_zL_{CD}L_{BC}^2}{2EI_{cy}} \qquad . \qquad \text{(A.93)}$$

Displacement in the *y*-direction at point *C* is derived by taking partial derivative of the internal energy of section *AC* with respect to F_y, i.e.,

$$\frac{\partial}{\partial F_y}U_{AC} = \frac{\partial}{\partial F_y}(U_{AB} + U_{BC}) = \Delta_{By} + \frac{\partial}{\partial F_y}U_{BC} = \Delta_{Cy} \qquad , \qquad \text{(A.94)}$$

which yields

$$\Delta_{Cy} = \Delta_{By} + \int_0^{L_{BC}} \frac{BC_x}{A_c E}\left(\frac{\partial}{\partial F_y} BC_x\right) dx + \int_0^{L_{BC}} \frac{M_{BCy}}{EI_{cz}}\left(\frac{\partial}{\partial F_y} M_{BCy}\right) dx +$$
$$\int_0^{L_{BC}} \frac{M_{BCz}}{EI_{cz}}\left(\frac{\partial}{\partial F_y} M_{BCz}\right) dx + \int_0^{L_{BC}} \frac{6BC_y}{5GA_c}\left(\frac{\partial}{\partial F_y} BC_y\right) dx + \qquad , \qquad (A.95)$$
$$\int_0^{L_{BC}} \frac{6BC_z}{5GA_c}\left(\frac{\partial}{\partial F_y} BC_z\right) dx + \int_0^{L_{BC}} \frac{T_{BCx}}{GJ_c}\left(\frac{\partial}{\partial F_y} T_{BCx}\right) dx$$

After the derivatives are taken, Eq A.95 becomes

$$\Delta_{Cy} = \Delta_{By} + \int_0^{L_{BC}} \frac{BC_x}{A_c E}(0)dx + \int_0^{L_{BC}} \frac{M_{BCy}}{EI_{cz}}(0)dx +$$
$$\int_0^{L_{BC}} \frac{F_y(L_{BC}-x)}{EI_{cz}}(L_{BC}-x)dx + \int_0^{L_{BC}} \frac{6F_y}{5GA_c}(1)dx + \int_0^{L_{BC}} \frac{6F_z}{5GA_c}(0)dx + \quad , \qquad (A.96)$$
$$\int_0^{L_{BC}} \frac{-F_y L_{CD}}{GJ_c}(-L_{CD})dx$$

which simplifies to

$$\Delta_{Cy} = \Delta_{By} + \int_0^{L_{BC}} \frac{F_y(L_{BC}-x)^2}{EI_{cz}}dx + \int_0^{L_{BC}} \frac{6F_y}{5GA_c}dx + \int_0^{L_{BC}} \frac{F_y L_{CD}^2}{GJ_c}dx \qquad . \qquad (A.97)$$

After integration, Eq. A.97 becomes

$$\Delta_{Cy} = \Delta_{By} + \frac{F_y L_{BC}^3}{EI_{cz}} + \frac{6F_y L_{BC}}{5GA_c} + \frac{F_y L_{BC}^2 L_{BC}}{GJ_c} \qquad , \qquad (A.98)$$

and simplifies to the following equation for the *y*-component of deformation at point *C*:

$$\Delta_{Cy} = \frac{F_y}{3EI_{bx}}\left(L_{AB}^3 - 3L_{AB}^2 L_{CD} + 3L_{AB}L_{CD}^2\right) + \frac{6F_y L_{AB}}{5GA_b} +$$
$$\frac{F_y L_{BC}^2 L_{AB}}{GJ_b} + \frac{F_y L_{BC}^3}{EI_{cz}} + \frac{6F_y L_{BC}}{5GA_c} + \frac{F_y L_{BC}^2 L_{BC}}{GJ_c} \qquad . \qquad (A.99)$$

Displacement in the *z*-direction at point *C* is derived by taking partial derivative of the internal energy of section *AC* with respect to F_z, which can be expressed as

$$\frac{\partial}{\partial F_z} U_{AC} = \frac{\partial}{\partial F_z}(U_{AB} + U_{BC}) = \Delta_{Bz} + \frac{\partial}{\partial F_z} U_{BC} = \Delta_{Cz} \qquad (A.100)$$

203

and represented by

$$\Delta_{Cz} = \Delta_{Bz} + \int_0^{L_{BC}} \frac{BC_x}{A_c E}\left(\frac{\partial}{\partial F_z}BC_x\right)dx + \int_0^{L_{BC}} \frac{M_{BCy}}{EI_{cy}}\left(\frac{\partial}{\partial F_z}M_{BCy}\right)dx +$$
$$\int_0^{L_{BC}} \frac{M_{BCz}}{EI_{cy}}\left(\frac{\partial}{\partial F_z}M_{BCz}\right)dx + \int_0^{L_{BC}} \frac{6BC_y}{5GA_c}\left(\frac{\partial}{\partial F_z}BC_y\right)dx +$$
$$\int_0^{L_{BC}} \frac{6BC_z}{5GA_c}\left(\frac{\partial}{\partial F_z}BC_z\right)dx + \int_0^{L_{BC}} \frac{T_{BCx}}{GJ_c}\left(\frac{\partial}{\partial F_z}T_{BCx}\right)dx \qquad . \qquad \text{(A.101)}$$

After the derivatives are taken, Eq A.101 becomes

$$\Delta_{Cz} = \Delta_{Bz} + \int_0^{L_{BC}} \frac{BC_x}{A_c E}(0)dx + \int_0^{L_{BC}} \frac{F_x L_{CD} + F_z(x - L_{BC})}{EI_{cy}}(x - L_{BC})dx +$$
$$\int_0^{L_{BC}} \frac{M_{BCz}}{EI_{cy}}(0)dx + \int_0^{L_{BC}} \frac{6F_y}{5GA_c}(0)dx + \int_0^{L_{BC}} \frac{6F_z}{5GA_c}(0)dx + \int_0^{L_{BC}} \frac{T_{BCx}}{GJ_c}(0)dx \qquad , \qquad \text{(A.102)}$$

which simplifies to

$$\Delta_{Cz} = \Delta_{Bz} + \int_0^{L_{BC}} \frac{F_x L_{CD}(x - L_{BC}) + F_z(x - L_{BC})^2}{EI_{cy}}dx + \int_0^{L_{BC}} \frac{6F_z}{5GA_c}dx \qquad . \qquad \text{(A.103)}$$

After integration, Eq. A.103 becomes

$$\Delta_{Cz} = \Delta_{Bz} - \frac{F_x L_{CD} L_{BC}^2}{2EI_{cy}} + \frac{F_z L_{BC}^3}{3EI_{cy}} + \frac{6F_z L_{BC}}{5GA_c} \qquad , \qquad \text{(A.104)}$$

and simplifies to the equation for the z-component of deformation at point C, which is

$$\Delta_{Cz} = \frac{F_z L_{AB}}{A_b E} + \frac{F_x L_{BC}\left(L_{AB}^2 - 2L_{CD}L_{AB}\right)}{2EI_{by}} + \frac{F_z L_{BC}^2 L_{AB}}{EI_{by}} -$$
$$\frac{F_x L_{CD} L_{BC}^2}{2EI_{cy}} + \frac{F_z L_{BC}^3}{3EI_{cy}} + \frac{6F_z L_{BC}}{5GA_c} \qquad . \qquad \text{(A.105)}$$

A.4. Deformations at point *D*

The final step is to derive the equation for deformations at point *D*, where the force is applied. In order to do this the forces, moments and torques acting along and through section *CD* have to be derived, as presented in Section A.4.1.

A.4.1. Internal reaction forces and moments for section *CD*

The forces, moments, and torques acting through section *CD* were derived using the free body diagram for a part of the section of an arbitrary length along the *z*-axis, Fig. A.6.
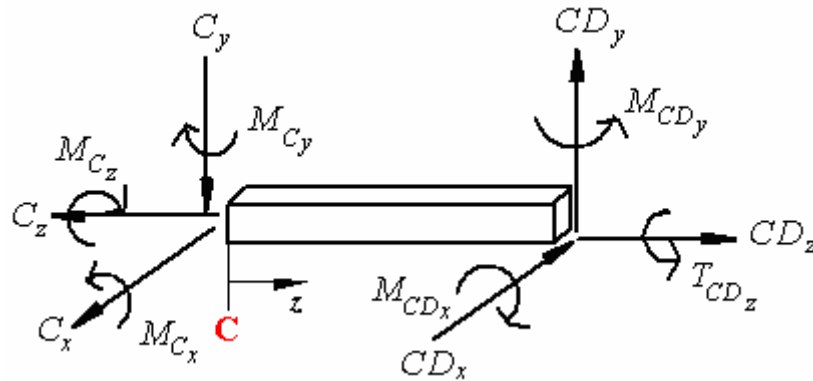
Fig. A.6. Free body diagram for a part of section *CD*.

Based on the free body diagram in Fig. A.6, the shear forces acting through section *CD* are

$$\sum F_X = 0 = CD_X - C_X \quad , \tag{A.106}$$

$$CD_X = C_X = F_X \quad , \tag{A.107}$$

$$\sum F_y = 0 = CD_y - C_y \quad , \tag{A.108}$$

$$CD_y = C_y = F_y \quad , \tag{A.109}$$

$$\sum F_z = 0 = CD_z - C_z \quad , \tag{A.110}$$

$$CD_z = C_z = F_z \quad , \tag{A.111}$$

and the moments acting thru section *CD* are

$$\sum M_{xCD} = 0 = -M_{Cx} + T_{CDx} - C_y z + C_z 0 \quad , \tag{A.112}$$

$$M_{CDx} = M_{Cx} + C_y z = F_y \left(z - L_{CD} \right) \quad , \tag{A.113}$$

$$\sum M_{yCD} = 0 = -M_{Cy} + M_{CDy} + C_x z - C_z 0 \quad , \tag{A.114}$$

$$M_{CDy} = M_{Cy} - C_x z = F_x \left(L_{CD} - z \right) \quad , \tag{A.115}$$

and

$$\sum M_{zCD} = 0 = -M_{Cz} + T_{CDz} + C_y 0 + C_x 0 \quad , \tag{A.116}$$

$$T_{CDz} = M_{Cz} = 0 \quad . \tag{A.117}$$

A.4.2. Derivation of the deformations at point *D*

Using the forces, moments, and torques defined by Eqs A.106 to A.117,

deformations at point *D*, where the forces are being applied, will be derived. To do this

partial derivative of the internal energy of the entire beam *AD*, not just that of the section

CD, will be taken with respect to the force, F_x, acting in the direction, *x*, of the desired

displacement. This means that partial derivative must be taken of the internal energy of

section *CD* and added to the deformation determined in Section A.3.3 for point *C*, i.e.,

$$\frac{\partial}{\partial F_x} U_{AD} = \frac{\partial}{\partial F_x}(U_{AB} + U_{BC} + U_{CD}) = \Delta_{Cx} + \frac{\partial}{\partial F_x} U_{CD} = \Delta_{Dx} \quad . \tag{A.118}$$

According to Eq. A.118,

$$\Delta_{Dx} = \Delta_{Cx} + \int_0^{L_{CD}} \frac{F_z}{A_b E}\left(\frac{\partial}{\partial F_x} CD_z\right) dz + \int_0^{L_{CD}} \frac{M_{CDx}}{EI_{by}}\left(\frac{\partial}{\partial F_x} M_{CDx}\right) dz +$$
$$\int_0^{L_{CD}} \frac{M_{CDy}}{EI_{by}}\left(\frac{\partial}{\partial F_x} M_{CDy}\right) dz + \int_0^{L_{CD}} \frac{6F_x}{5GA_b}\left(\frac{\partial}{\partial F_x} CD_x\right) dz + \quad . \tag{A.119}$$
$$\int_0^{L_{CD}} \frac{6F_y}{5GA_b}\left(\frac{\partial}{\partial F_x} CD_y\right) dz + \int_0^{L_{CD}} \frac{T_{CDz}}{GJ_b}\left(\frac{\partial}{\partial F_x} T_{CDz}\right) dz$$

After the derivatives are taken, Eq A.119 becomes

$$\Delta_{Dx} = \Delta_{Cx} + \int_0^{L_{CD}} \frac{F_z}{A_b E}(0) dz + \int_0^{L_{CD}} \frac{M_{CDx}}{EI_{by}}(0) dz +$$
$$\int_0^{L_{CD}} \frac{F_x(L_{CD}-z)}{EI_{by}}(L_{CD}-z) dz + \int_0^{L_{CD}} \frac{6F_x}{5GA_b}(1) dz + \quad , \tag{A.120}$$
$$\int_0^{L_{CD}} \frac{6CD_y}{5GA_b}(0) dz + \int_0^{L_{CD}} \frac{T_{CDz}}{GJ_b}(0) dz$$

which simplifies to

$$\Delta_{Dx} = \Delta_{Cx} + \int_0^{L_{CD}} \frac{F_x(L_{CD}-z)^2}{EI_{by}} dz + \int_0^{L_{CD}} \frac{6F_x}{5GA_b} dz \quad . \tag{A.121}$$

After integration, Eq. A.121 becomes

$$\Delta_{Dx} = \Delta_{Cx} + \frac{F_x L_{CD}^3}{3EI_{by}} + \frac{6F_x L_{CD}}{5GA_b} \quad , \tag{A.122}$$

and simplifies to the equation for the *x*-component of deformation at point *D*

$$\Delta_{Dx} = \frac{F_x}{3EI_{by}}\left(L_{AB}^3 - 3L_{AB}^2 L_{CD} + 3L_{AB}L_{CD}^2\right) + \frac{6F_x L_{AB}}{5GA_b} +$$
$$\frac{F_z L_{BC}}{2EI_{by}}\left(L_{AB}^2 - 2L_{AB}L_{CD}\right) + \frac{F_x L_{BC}}{A_c E} + \frac{F_x L_{CD}^2 L_{BC}}{EI_{cy}} - \frac{F_z L_{CD} L_{BC}^2}{2EI_{cy}} + \quad . \tag{A.123}$$
$$\frac{F_x L_{CD}^3}{3EI_{by}} + \frac{6F_x L_{CD}}{5GA_b}$$

To find the deformation in the y-direction at point D, partial derivative of the internal energy of the entire beam, section AD, was taken with respect to F_y, to obtain

$$\frac{\partial}{\partial F_y} U_{AD} = \frac{\partial}{\partial F_y}\left(U_{AB} + U_{BC} + U_{CD}\right) = \Delta_{Cy} + \frac{\partial}{\partial F_y} U_{CD} = \Delta_{Dy} \quad . \tag{A.124}$$

which yields

$$\Delta_{Dy} = \Delta_{Cy} + \int_0^{L_{CD}} \frac{CD_z}{A_b E}\left(\frac{\partial}{\partial F_y} CD_z\right)dz + \int_0^{L_{CD}} \frac{M_{CDx}}{EI_{bx}}\left(\frac{\partial}{\partial F_y} M_{CDx}\right)dz +$$
$$\int_0^{L_{CD}} \frac{M_{CDy}}{EI_{bx}}\left(\frac{\partial}{\partial F_y} M_{CDy}\right)dz + \int_0^{L_{CD}} \frac{6CD_x}{5GA_b}\left(\frac{\partial}{\partial F_y} CD_x\right)dz + \tag{A.125}$$
$$\int_0^{L_{CD}} \frac{6CD_y}{5GA_b}\left(\frac{\partial}{\partial F_y} CD_y\right)dz + \int_0^{L_{CD}} \frac{T_{CDz}}{GJ_b}\left(\frac{\partial}{\partial F_y} T_{CDz}\right)dz$$

After the derivatives are taken, Eq A.125 becomes

$$\Delta_{Dy} = \Delta_{Cy} + \int_0^{L_{CD}} \frac{CD_z}{A_b E}(0)dz + \int_0^{L_{CD}} \frac{F_y(z - L_{CD})}{EI_{bx}}(z - L_{CD})dz +$$
$$\int_0^{L_{CD}} \frac{M_{CDy}}{EI_{bx}}(0)dz + \int_0^{L_{CD}} \frac{6F_x}{5GA_b}(0)dz + \tag{A.126}$$
$$\int_0^{L_{CD}} \frac{6F_y}{5GA_b}(1)dz + \int_0^{L_{CD}} \frac{T_{CDz}}{GJ_b}(0)dz$$

which simplifies to

$$\Delta_{Dy} = \Delta_{Cy} + \int_0^{L_{CD}} \frac{F_y(z - L_{CD})^2}{EI_{bx}}dz + \int_0^{L_{CD}} \frac{6F_y}{5GA_b}dz \quad . \tag{A.127}$$

After integration, Eq. 127 becomes

$$\Delta_{Dy} = \Delta_{Cy} + \frac{F_y L_{CD}^3}{3EI_{bx}} + \frac{6F_y L_{CD}}{5GA_b} \quad , \tag{A.128}$$

and simplifies to the equation for the y-component of deformation at point D

$$\Delta_{Dy} = \frac{F_y}{3EI_{bx}}\left(L_{AB}{}^3 - 3L_{AB}{}^2 L_{CD} + 3L_{AB}L_{CD}{}^2\right) + \frac{6F_y L_{AB}}{5GA_b} + \frac{F_y L_{BC}{}^2 L_{AB}}{GJ_b} +$$
$$\frac{F_y L_{BC}{}^3}{EI_{cz}} + \frac{6F_y L_{BC}}{5GA_c} + \frac{F_y L_{BC}{}^2 L_{BC}}{GJ_c} + \frac{F_y L_{CD}{}^3}{3EI_{bx}} + \frac{6F_y L_{CD}}{5GA_b}$$
. (A.129)

Finally, to find the deformation in the *z*-direction at point *D*, partial derivative of the internal energy of section *AD* was taken with respect to F_z, i.e.,

$$\frac{\partial}{\partial F_z}U_{AD} = \frac{\partial}{\partial F_z}\left(U_{AB} + U_{BC} + U_{CD}\right) = \Delta_{Cz} + \frac{\partial}{\partial F_z}U_{CD} = \Delta_{Dz} \quad .$$
(A.130)

Equation A.130 can be expanded to

$$\Delta_{Dz} = \Delta_{Cz} + \int\limits_0^{L_{CD}} \frac{CD_z}{A_b E}\left(\frac{\partial}{\partial F_z}CD_z\right)dz + \int\limits_0^{L_{CD}} \frac{M_{CDx}}{EI_{by}}\left(\frac{\partial}{\partial F_z}M_{CDx}\right)dz +$$
$$\int\limits_0^{L_{CD}} \frac{M_{CDy}}{EI_{by}}\left(\frac{\partial}{\partial F_z}M_{CDy}\right)dz + \int\limits_0^{L_{CD}} \frac{6CD_x}{5GA_b}\left(\frac{\partial}{\partial F_z}CD_x\right)dz +$$
$$\int\limits_0^{L_{CD}} \frac{6CD_y}{5GA_b}\left(\frac{\partial}{\partial F_z}CD_y\right)dz + \int\limits_0^{L_{CD}} \frac{T_{CDz}}{GJ_b}\left(\frac{\partial}{\partial F_z}T_{CDz}\right)dz$$
. (A.131)

After the derivatives are taken, Eq A.131 becomes

$$\Delta_{Dz} = \Delta_{Cz} + \int\limits_0^{L_{CD}} \frac{F_z}{A_b E}(1)dz + \int\limits_0^{L_{CD}} \frac{M_{CDx}}{EI_{by}}(0)dz + \int\limits_0^{L_{CD}} \frac{M_{CDy}}{EI_{by}}(0)dz +$$
$$\int\limits_0^{L_{CD}} \frac{6F_x}{5GA_b}(0)dz + \int\limits_0^{L_{CD}} \frac{6F_y}{5GA_b}(0)dz + \int\limits_0^{L_{CD}} \frac{T_{CDz}}{GJ_b}(0)dz$$
, (A.132)

which simplifies to

$$\Delta_{Dz} = \Delta_{Cz} + \int\limits_0^{L_{CD}} \frac{F_z}{A_b E}dz \quad .$$
(A.133)

After integration, Eq. A.133 becomes

$$\Delta_{Dz} = \Delta_{Cz} + \frac{F_z L_{CD}}{A_b E} \quad ,$$
(A.134)

and simplifies to the equation for the *z*-component deformation at point *D*

$$\Delta_{Dz} = \frac{F_z L_{AB}}{A_b E} + \frac{F_x L_{BC}\left(L_{AB}{}^2 - 2L_{CD}L_{AB}\right)}{2EI_{by}} + \frac{F_z L_{BC}{}^2 L_{AB}}{EI_{by}} -$$
$$\frac{F_x L_{CD} L_{BC}{}^2}{2EI_{cy}} + \frac{F_z L_{BC}{}^3}{3EI_{cy}} + \frac{6F_z L_{BC}}{5GA_c} + \frac{F_z L_{CD}}{A_b E} \qquad . \qquad \text{(A.135)}$$

A.5. Determination of deformations at point *D*

Using Eqs A.123, A.129, and A.135 deformations at point *D* will be determined utilizing forces calculated in Appendix B and polysilicon as the material.

Equations A.136 to A.139 define the material properties of the polysilicon used in the modeling of the folded spring,

$$E = 160 \text{ GPa} \quad , \qquad\qquad\qquad\qquad\qquad\qquad\qquad\qquad \text{(A.136)}$$

$$v = 0.23 \quad , \qquad\qquad\qquad\qquad\qquad\qquad\qquad\qquad\qquad \text{(A.137)}$$

$$\rho = 2.33 \text{ g/cm}^3 \quad , \qquad\qquad\qquad\qquad\qquad\qquad\qquad \text{(A.138)}$$

$$G = \frac{E}{2(1+v)} \qquad\qquad\qquad G = 65 \text{ GPa} \quad . \qquad\qquad \text{(A.139)}$$

Equations A.140 to A.145 define dimensions of the folded spring used in this analysis,

$$L_{AB} = 98 \ \mu m \quad , \qquad\qquad\qquad\qquad\qquad\qquad\qquad\qquad \text{(A.140)}$$

$$L_{BC} = 17 \ \mu m \quad , \qquad\qquad\qquad\qquad\qquad\qquad\qquad\qquad \text{(A.141)}$$

$$L_{CD} = 111 \ \mu m \quad , \qquad\qquad\qquad\qquad\qquad\qquad\qquad \text{(A.142)}$$

$$b = 3 \ \mu m \quad , \qquad\qquad\qquad\qquad\qquad\qquad\qquad\qquad\qquad \text{(A.143)}$$

$$b_{BC} = 10 \ \mu m \quad , \qquad\qquad\qquad\qquad\qquad\qquad\qquad\qquad \text{(A.144)}$$

$$h = 2.5 \ \mu m \quad . \qquad\qquad\qquad\qquad\qquad\qquad\qquad\qquad\quad \text{(A.145)}$$

Equations A.146 to A.148 define the forces derived in Appendix B that were applied to the folded spring

$$F_x = 21.0572 \ \mu N \quad , \tag{A.146}$$

$$F_y = 0.000744747 \ \mu N \quad , \tag{A.147}$$

$$F_z = 0 \ \mu N \quad . \tag{A.148}$$

The cross sectional areas of sections *AB* and *CD* are defined as

$$A_b = bh \quad , \tag{A.149}$$

the cross sectional area of section *BC* is defined as

$$A_c = b_{BC}h \quad , \tag{A.150}$$

the polar moments of inertia of sections *AB* and *CD* are defined as

$$J_b = 0.219 \cdot bh^3 \quad , \tag{A.151}$$

the polar moment of inertia of section *BC* is defined as

$$J_c = 0.282 \cdot b_{BC}h^3 \quad , \tag{A.152}$$

the moments of inertia of sections *AB* and *CD* are defined as

$$I_{bx} = \frac{bh^3}{12} \quad , \tag{A.153}$$

$$I_{by} = \frac{hb^3}{12} \quad , \tag{A.154}$$

and the moments of inertia of section *BC* are defined as

$$I_{cz} = \frac{b_{BC}h^3}{12} \quad , \tag{A.155}$$

$$I_{cy} = \frac{hb_{BC}^3}{12} \quad . \tag{A.156}$$

Using, Eqs A.136 to A.156 and A.123, A.129, and A.135, the deformations at point D are calculated to be

$$\Delta_{Dx} = \frac{F_x}{3EI_{by}}\left(L_{AB}{}^3 - 3L_{AB}{}^2 L_{CD} + 3L_{AB}L_{CD}{}^2\right) + \frac{6F_x L_{AB}}{5GA_b} +$$

$$\frac{F_z L_{BC}}{2EI_{by}}\left(L_{AB}{}^2 - 2L_{AB}L_{CD}\right) + \frac{F_x L_{BC}}{A_c E} + \frac{F_x L_{CD}{}^2 L_{BC}}{EI_{cy}} - \frac{F_z L_{CD}L_{BC}{}^2}{2EI_{cy}} +$$

$$\frac{F_x L_{CD}{}^3}{3EI_{by}} + \frac{6F_x L_{CD}}{5GA_b}$$

or

$$\Delta_{Dx} \cdot 10^6 = 21.4583 \ \mu m \quad , \tag{A.157}$$

$$\Delta_{Dy} = \frac{F_y}{3EI_{bx}}\left(L_{AB}{}^3 - 3L_{AB}{}^2 L_{CD} + 3L_{AB}L_{CD}{}^2\right) + \frac{6F_y L_{AB}}{5GA_b} + \frac{F_y L_{BC}{}^2 L_{AB}}{GJ_b} +$$

$$\frac{F_y L_{BC}{}^3}{EI_{cz}} + \frac{6F_y L_{BC}}{5GA_c} + \frac{F_y L_{BC}{}^2 L_{BC}}{GJ_c} + \frac{F_y L_{CD}{}^3}{3EI_{bx}} + \frac{6F_y L_{CD}}{5GA_b}$$

or

$$\Delta_{Dy} \cdot 10^9 = 1.17257 \ nm \quad , \tag{A.158}$$

and

$$\Delta_{Dz} = \frac{F_z L_{AB}}{A_b E} + \frac{F_x L_{BC}\left(L_{AB}{}^2 - 2L_{CD}L_{AB}\right)}{2EI_{by}} + \frac{F_z L_{BC}{}^2 L_{AB}}{EI_{by}} -$$

$$\frac{F_x L_{CD}L_{BC}{}^2}{2EI_{cy}} + \frac{F_z L_{BC}{}^3}{3EI_{cy}} + \frac{6F_z L_{BC}}{5GA_c} + \frac{F_z L_{CD}}{A_b E}$$

or

$$\Delta_{Dz} \cdot 10^6 = -2.4268 \ \mu m \quad . \tag{A.159}$$

The time dependent in-plane force, defined by Eq. B.22, will be applied to Eqs. A.123 and A.135, defining deformations in the *x*-direction and *z*-direction, respectively. The range of time used for these calculations is

$$t = 0, 0.001...0.5 \text{ ms} \quad , \tag{A.160}$$

which represents five cycles of vibration of the proof mass resonating at 10 kHz. The other values necessary to solve for the time dependent force are the frequency of the motion of the proof mass

$$f = 10 \cdot 10^3 \text{ Hz} \quad , \tag{A.161}$$

the length of the combdrive fingers

$$L_f = 40 \text{ μm} \quad , \tag{A.162}$$

the amplitude of the motion of the proof mass

$$B = \frac{L_f}{2} - 3 \qquad\qquad B = 17 \text{ μm} \quad , \tag{A.163}$$

the angular speed of the motion of the proof mass

$$\omega = 2\pi \cdot f \qquad\qquad \omega = 6.2832 \times 10^4 \text{ rad}\!\Big/\!\text{sec} \quad , \tag{A.164}$$

the mass of the proof mass

$$m = 1.25502 \text{ μg} \quad , \tag{A.165}$$

the sinusoidal time-dependent acceleration of the proof mass

$$a(t) = -\left(B \cdot 10^{-6}\right) \cdot \omega^2 \cdot \sin\!\left[\omega \cdot \left(t \cdot 10^{-3}\right)\right] \quad , \tag{A.166}$$

the sinusoidal time-dependent force acting on the folded spring

$$F_x(t) = \frac{m a(t)}{4} \quad , \tag{A.167}$$

the sinusoidal time-dependent displacement, in the *x*-direction, of the folded spring at

point *D*

$$\Delta_{Dx}(t) = \frac{F_x(t)}{3EI_{by}}\left(L_{AB}^3 - 3L_{AB}^2L_{CD} + 3L_{AB}L_{CD}^2\right) + \frac{6F_x(t)L_{AB}}{5GA_b} +$$

$$\frac{F_zL_{BC}}{2EI_{by}}\left(L_{AB}^2 - 2L_{AB}L_{CD}\right) + \frac{F_x(t)L_{BC}}{A_cE} + \frac{F_x(t)L_{CD}^2L_{BC}}{EI_{cy}} - \frac{F_zL_{CD}L_{BC}^2}{2EI_{cy}} +$$

$$\frac{F_x(t)L_{CD}^3}{3EI_{by}} + \frac{6F_xL_{CD}}{5GA_b}$$

or

$$\Delta_{Dx\mu m}(t) = \Delta_{Dx}(t)\cdot 10^6 \quad , \tag{A.168}$$

and the sinusoidal time-dependent displacement, in the *z*-direction, of the folded spring at

point *D*

$$\Delta_{Dz}(t) = \frac{F_zL_{AB}}{A_bE} + \frac{F_x(t)L_{BC}\left(L_{AB}^2 - 2L_{CD}L_{AB}\right)}{2EI_{by}} + \frac{F_zL_{BC}^2L_{AB}}{EI_{by}} -$$

$$\frac{F_x(t)L_{CD}L_{BC}^2}{2EI_{cy}} + \frac{F_zL_{BC}^3}{3EI_{cy}} + \frac{6F_zL_{BC}}{5GA_c} + \frac{F_zL_{CD}}{A_bE}$$

or

$$\Delta_{Dz\mu m}(t) = \Delta_{Dz}(t)\cdot 10^6 \quad . \tag{A.169}$$

Equation A.168 is represented graphically in Fig. A.7 for five periods of oscillation, and

Eq. A.169 is represented in Fig. A.8.

DISPLACEMENT IN THE x-DIRECTION, μm

$^{\Delta}$Dxμm(t)

t
TIME, ms
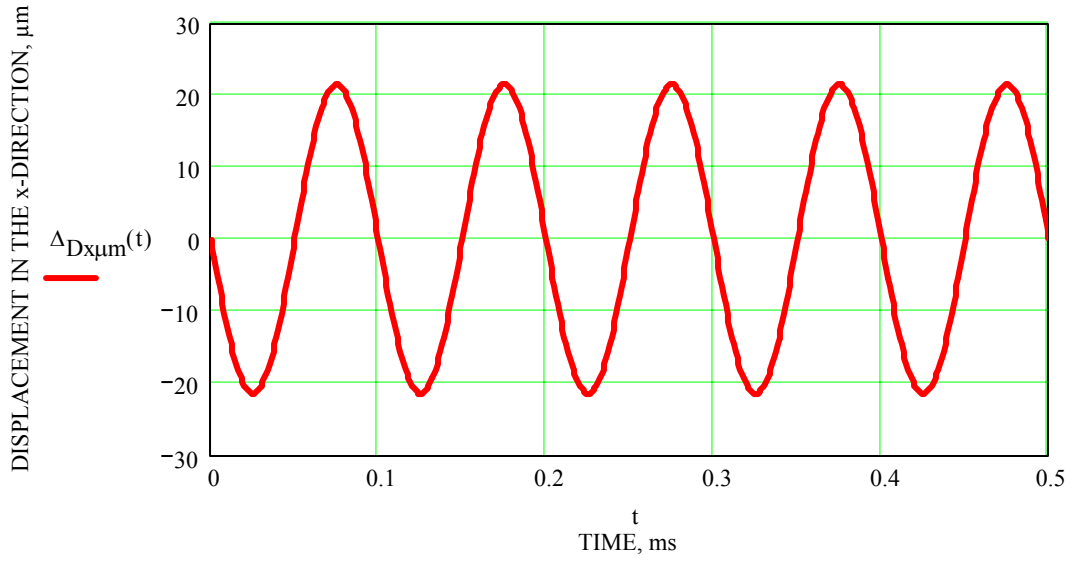
Fig. A.7. Sinusoidal motion of the spring in the x-direction.

DISPLACEMENT IN THE z-DIRECTION, μm

$^{\Delta}$Dzμm(t)

t
TIME, ms
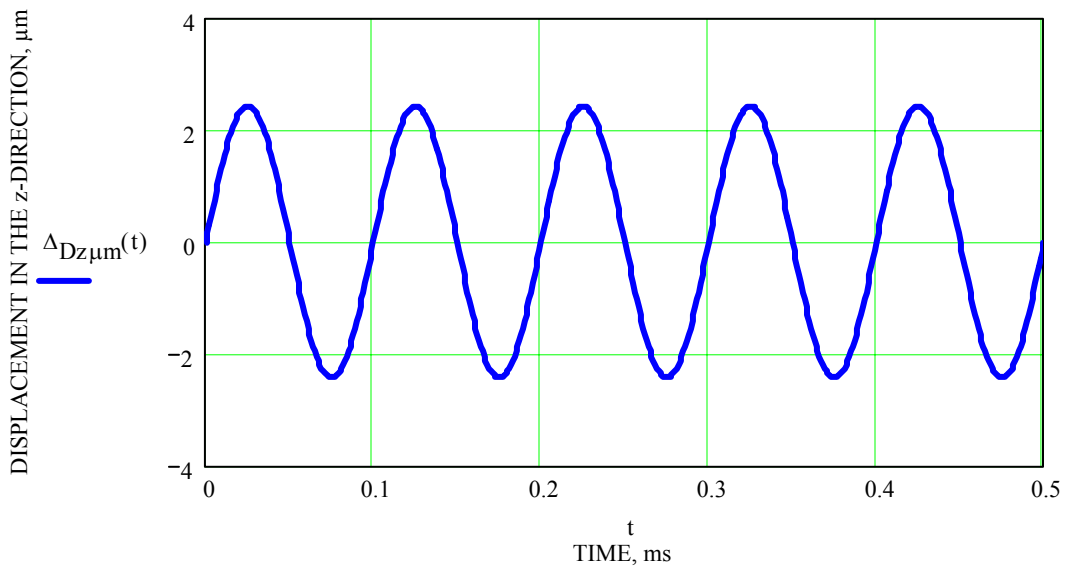
Fig. A.8. Sinusoidal motion of the spring in the z-direction.

215

APPENDIX B. DETERMINATION OF FORCES ACTING ON THE FOLDED SPRING OF THE MICROGYRO

In order to obtain deformations at point D, where the force is applied, Eqs A.85, A.91, and A.97 should be used. Forces used in these equations had to be determined. Because of the nature of the functional operation of the microgyroscopes studied in this thesis, forces acting in the x, i.e., in-plane, and y, i.e., out-of-plane, directions were calculated, while the force in the z-direction was assumed to be zero.

B.1. Derivation of the in-plane force acting on the folded springs

The first step in determining the force acting at point D in the x-direction was to find the area of the proof mass, including the fingers of the combdrives attached to the proof mass, where the length of the combdrive fingers is

$$L_f = 40\,\mu m \qquad . \tag{B.1}$$

Using this length and other measured dimensions the area for the proof mass was calculated to be

$$A_{shuttle} = (500)^2 \qquad\qquad A_{shuttle} = 2.5 \times 10^5\,\mu m^2 \quad , \tag{B.2}$$

$$A_{holes} = 62^2\,\frac{\pi(4)^2}{4} \qquad\qquad A_{hole} = 4.831 \times 10^4\,\mu m^2 \quad , \tag{B.3}$$

$$A_{combs} = 27\cdot 2\cdot L_f\,(4) \qquad\qquad A_{combs} = 8.64 \times 10^3\,\mu m^2 \quad , \tag{B.4}$$

$$A_{extra} = 4\cdot(20)\cdot(10) + 4\cdot(135)\cdot(8) \qquad\qquad A_{extra} = 5.12 \times 10^3\,\mu m^2 \quad , \tag{B.5}$$

$$A_{proof} = A_{shuttle} - A_{holes} + A_{combs} + A_{extra} \qquad\qquad A_{proof} = 2.155 \times 10^5\,\mu m^2 \quad . \tag{B.6}$$

216

The area calculated in Eq. B.6 was then multiplied by the thickness, Eq. B.7, in order to obtain the volume

$$h = 2.5\,\mu m \quad , \tag{B.7}$$

$$V_{proof} = A_{proof}\,h \qquad\qquad V_{proof} = 5.386\times10^5\,\mu m^3 \quad . \tag{B.8}$$

Using the volume of the proof mass and the density of the polysilicon, Eq. B.9, the mass of the proof mass was calculated as,

$$\rho = 2.33\,g/cm^3 \quad , \tag{B.9}$$

$$m = V_{proof}\left(10^{-6}\right)^3\rho \qquad\qquad m\cdot10^9 = 1.25502\,\mu g \quad . \tag{B.10}$$

The in-plane force, F_x, was calculated using the mass of the proof mass, Eq. B.10. This was done starting with the sinusoidal motion of the proof mass. In order to determine sinusoidal motion, time period was defined as

$$t = 0,\,0.001\ldots0.5\,ms \quad . \tag{B.11}$$

The other parameters necessary to solve for the time dependent force are the resonance frequency of the proof mass

$$f = 10\cdot10^3\,Hz \quad , \tag{B.12}$$

the amplitude of the motion of the proof mass, B, defined as half the length of the comb drives minus 3 μm to insure that there will be no bottoming out

$$B = \frac{L_f}{2} - 3 \qquad\qquad B = 17\,\mu m \quad , \tag{B.13}$$

the angular speed of the motion of the proof mass

$$\omega = 2\pi\cdot f \qquad\qquad \omega = 6.2832\times10^4\,rad/sec \quad , \tag{B.14}$$

and the period of the oscillations of the proof mass determined to be

217

$$\tau = \frac{1}{f} \qquad\qquad\qquad \tau = 1 \times 10^{-4} \text{ sec} \quad . \qquad (\text{B}.15)$$

Using Eqs B.11, B.13, and B.14, the displacement of the proof mass as a function of time can be determined to be

$$x(t) = B \sin\left[\omega\left(t \cdot 10^{-3}\right)\right] \quad . \qquad (\text{B}.16)$$

Equation B.16 is represented in Fig. B.1 for five periods of oscillation. Velocity of the proof mass was calculated by taking a time derivative of the Eq. B.16, i.e.,

$$v(t) = \left(B \cdot 10^{-6}\right) \cdot \omega \cdot \cos\left[\omega\left(t \cdot 10^{-3}\right)\right] \quad . \qquad (\text{B}.17)$$

The velocity determined from Eq. B.17 is represented in Fig. B.2 for five periods of oscillation. Acceleration of the proof mass can be calculated by taking a time derivative of Eq. B.17, or the second time derivative of Eq. B.16, with the result given by

$$a(t) = -\left(B \cdot 10^{-6}\right) \cdot \omega^2 \cdot \sin\left[\omega\left(t \cdot 10^{-3}\right)\right] \quad , \qquad (\text{B}.18)$$

which is displayed in Fig. B.3. Accelerations can also be represented in terms of g's by

$$a_g(t) = \frac{a(t)}{9.81} \quad , \qquad (\text{B}.19)$$

which gives the results in multiples of gravitational acceleration, Fig. B.4. The maximum acceleration will be obtained when *sin(ωt)* becomes equal to one; therefore the maximum acceleration felt by the proof mass of the gyroscope will be

$$a_{max} = B\omega^2 \qquad\qquad a_{max} = 6.711 \times 10^4 \text{ m}\!\!\Big/\!\!{}_{s^2} \quad , \qquad (\text{B}.20)$$

or in g's

$$a_{gs} = \frac{a_{max}}{9.81} \qquad\qquad a_{gs} = 6.841 \times 10^3 \text{ g} \quad . \qquad (\text{B}.21)$$

Using the maximum acceleration defined by Eqs B.20 and B.21, the maximum force

acting on the spring will be one quarter of the maximum force acting on the proof mass.

This is the case because it was assumed that each of the four springs, that support the

proof mass in each of the four corners, will evenly carry the load. Therefore, the

maximum force is calculated as

$$F_{xmax} = \frac{ma_{max}}{4} \qquad\qquad F_x \cdot 10^6 = 21.0572\ \mu N \quad , \qquad (B.22)$$

while the time dependent equation for the force is

$$F_x(t) = \frac{ma(t)}{4} \qquad\qquad F_{x\mu N}(t) = F_x(t) \cdot 10^6 \quad ; \qquad (B.23)$$

the behavior of the force calculated in Eq. B.23 is illustrated in Fig. B.5.
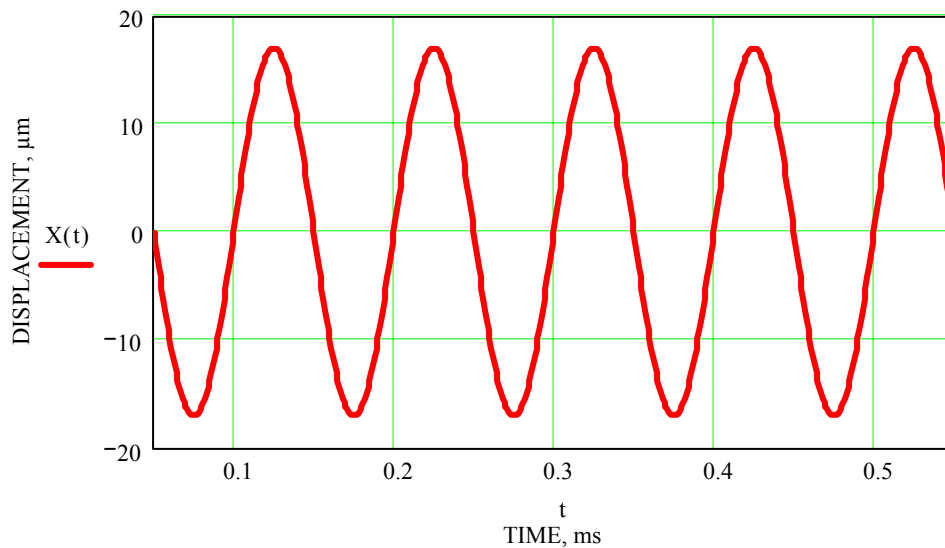
Fig. B.1. Sinusoidal displacement of the proof mass in the *x*-direction.
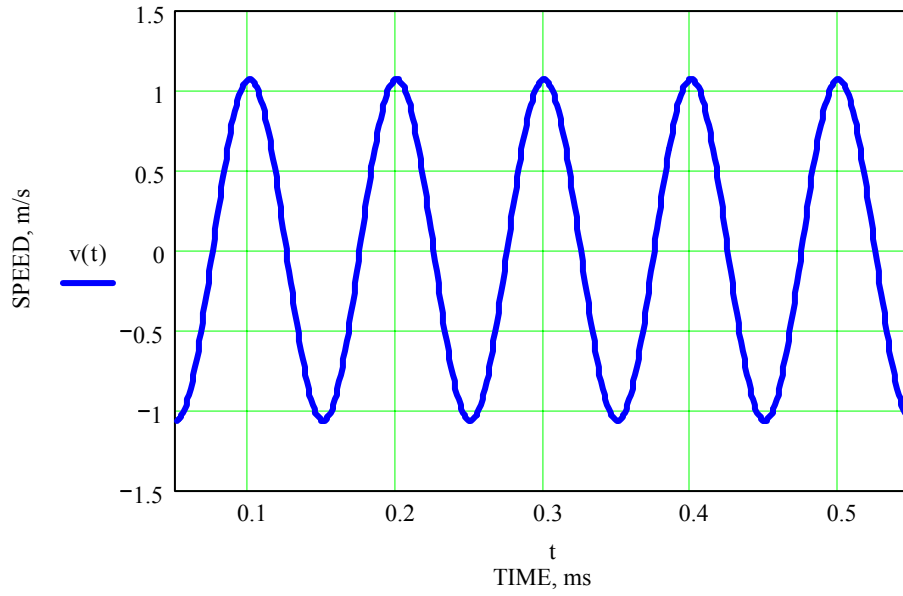
Fig. B.2. Sinusoidal speed of the proof mass in the *x*-direction.
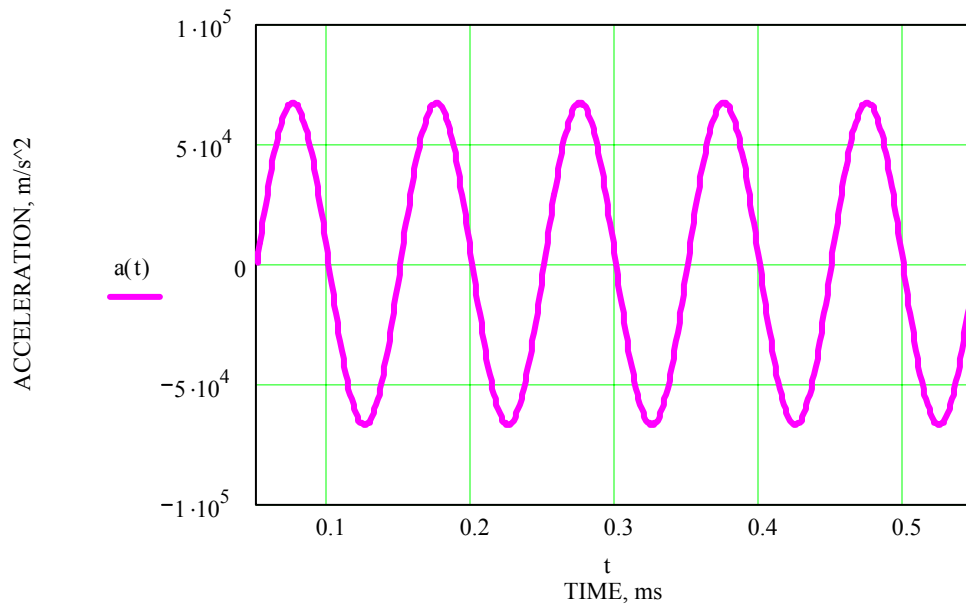
Fig. B.3. Sinusoidal acceleration of the proof mass in the *x*-direction.
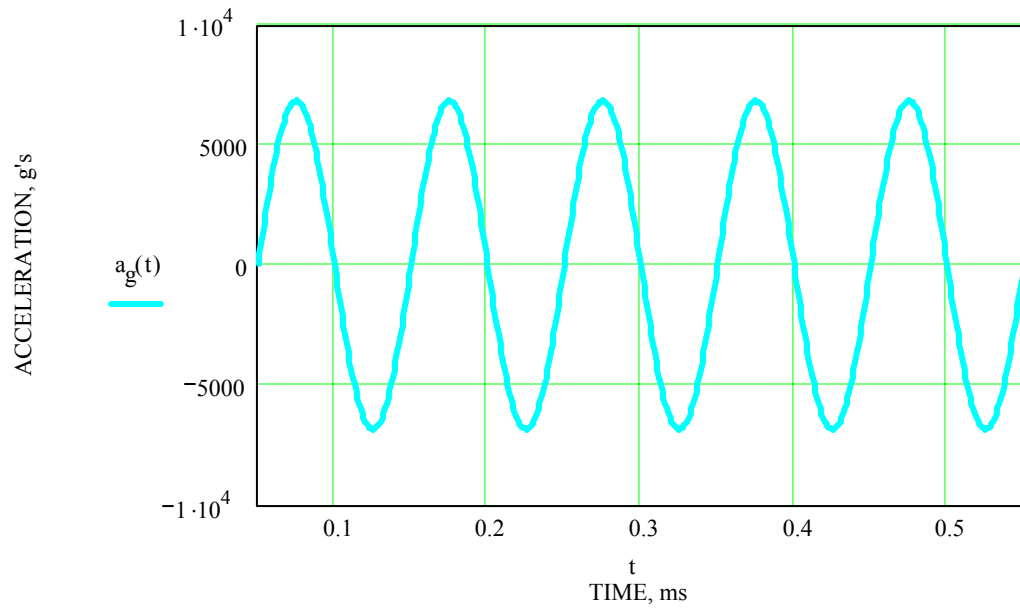
Fig. B.4. Sinusoidal acceleration, in g's, of the proof mass in the *x*-direction.
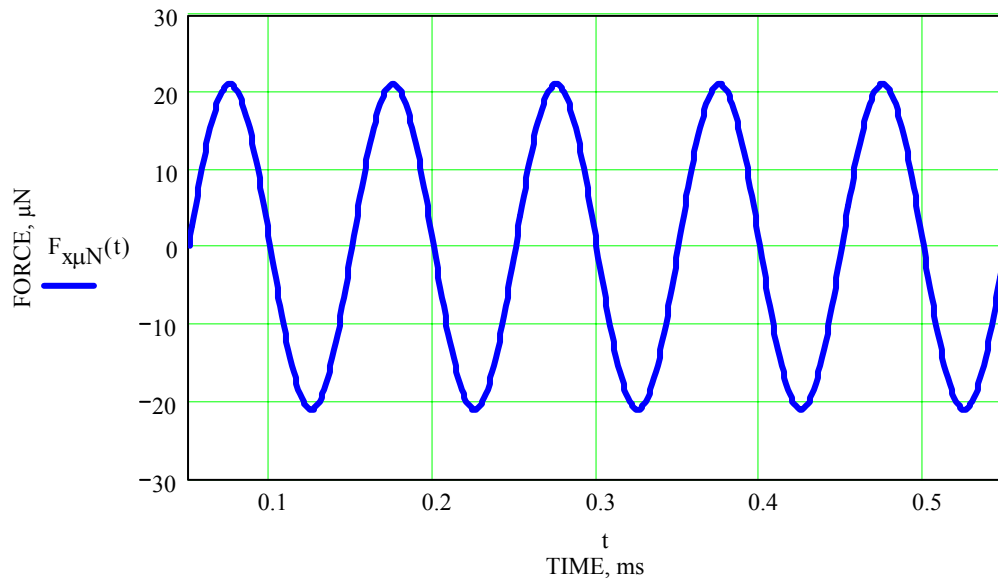
Fig. B.5. Sinusoidal force acting on the folded spring in the *x*-direction.

B.2. Derivation of the out-of-plane force, Coriolis force, acting on the folded springs

The first step in determining the Coriolis force is to calculate the in-plane velocity acting on the proof mass, i.e.,

$$v = \frac{4B}{\tau} \qquad\qquad v = 0.68 \text{ m}/_{\text{s}} \quad . \qquad\qquad (B.24)$$

The angular speed that the microgyro is subjected to for the purpose of these calculations is 100 deg/sec,

$$\Omega = 100 \frac{2\pi}{360} \qquad\qquad \Omega = 1.74533 \text{ rad}/_{\text{sec}} \quad . \qquad\qquad (B.25)$$

Using Eqs B.10, B.24, and B.25, the out-of-plane Coriolis force acting on the folded spring can be calculated from Eq. 2.7 to be

$$F_c = 2m \cdot v \times \Omega \quad , \qquad\qquad\qquad (B.26)$$

$$F_c = 2m \cdot v \cdot \Omega \qquad\qquad F_c \cdot 10^9 = 2.978986 \text{ nN} \quad . \qquad (B.27)$$

Therefore, the Coriolis force acting on a single folded spring is

$$F_y = \frac{F_c}{4} \qquad\qquad F_y \cdot 10^9 = 0.7447 \text{ nN} \quad . \qquad\qquad (B.28)$$

APPENDIX C. DETERMINATION OF UNCERTAINTIES IN THE DEFORMATION OF THE FOLDED SPRING

A RSS (root-sum-square) type uncertainty analysis was done on the deformations that were determined in Appendix A for the folded springs that support the proof masses of the Sandia microgyro. This was done to determine how good the results are.

C.1. Uncertainty analysis of deformation in the *x*-direction

The first step was to obtain the values and uncertainties of all of the parameters that are included in the equation for the displacement in the *x*-direction. Equations C.1 to C.6 define the dimensions of the model of the folded spring used in this analysis

$$L_{AB} = 98 \ \mu m \quad , \tag{C.1}$$

$$L_{BC} = 17 \ \mu m \quad , \tag{C.2}$$

$$L_{CD} = 111 \ \mu m \quad , \tag{C.3}$$

$$b = 3 \ \mu m \quad , \tag{C.4}$$

$$b_{BC} = 10 \ \mu m \quad , \tag{C.5}$$

and

$$h = 2.5 \ \mu m \quad . \tag{C.6}$$

Equations C.7 to C.9 define the material properties of the polysilicon used in the modeling of the folded spring

$$E = 160 \ GPa \quad , \tag{C.7}$$

$$v = 0.23 \quad , \tag{C.8}$$

and

$$\rho = 2.33 \text{ g/cm}^3 \quad . \tag{C.9}$$

Equations C.10 to C.18 define in the parameters nominal values of which are defined in Eqs C.1 to C.9, respectively,

$$\delta L_{AB} = 0.25 \text{ μm} \quad , \tag{C.10}$$

$$\delta L_{BC} = 0.25 \text{ μm} \quad , \tag{C.11}$$

$$\delta L_{CD} = 0.25 \text{ μm} \quad , \tag{C.12}$$

$$\delta b = 0.25 \text{ μm} \quad , \tag{C.13}$$

$$\delta b_{BC} = 0.25 \text{ μm} \quad , \tag{C.14}$$

$$\delta h = 0.01h \text{ μm} \qquad\qquad \delta h = 0.025 \text{ μm} \quad , \tag{C.15}$$

$$\delta E = 5 \text{ GPa} \quad , \tag{C.16}$$

$$\delta v = 0.005 \quad , \tag{C.17}$$

and

$$\delta \rho = 0.5 \text{ g/cm}^3 \quad . \tag{C.18}$$

The values and uncertainties defined in Eqs C.1 to C.18 were used to calculate the overall uncertainties in deformations at point D. The first uncertainty to be calculated was for the deformation in the x-direction. This was done by starting with the equation for the deformation in the x-direction, i.e.,

$$\Delta_{Dx} = \frac{F_x}{3EI_{by}}\left(L_{AB}^3 - 3L_{AB}^2 L_{CD} + 3L_{AB}L_{CD}^2\right) + \frac{6F_x L_{AB}}{5GA_b} +$$

$$\frac{F_z L_{BC}}{2EI_{by}}\left(L_{AB}^2 - 2L_{AB}L_{CD}\right) + \frac{F_x L_{BC}}{A_c E} + \frac{F_x L_{CD}^2 L_{BC}}{EI_{cy}} - \frac{F_z L_{CD}L_{BC}^2}{2EI_{cy}} + \quad . \tag{C.19}$$

$$\frac{F_x L_{CD}^3}{3EI_{by}} + \frac{6F_x L_{CD}}{5GA_b}$$

Using Eq. C.19, the phenomenological relationship for the deformation in the *x*-direction was derived to be

$$\Delta_{Dx} = \Delta_{Dx}\left(F_x, F_z, L_{AB}, L_{BC}, L_{CD}, A_b, A_c, I_{by}, I_{cy}, E, G\right) \quad, \tag{C.20}$$

where each of the parameters that define Δ_{Dx} are written as the following functions in terms of their own independent parameters that define them:

$$F_x = F_x(m, a) \quad, \tag{C.21}$$

$$m = m\left(V_{proof}, \rho\right) \quad, \tag{C.22}$$

$$V_{proof} = V_{proof}\left(A_{proof}, h\right) \quad, \tag{C.23}$$

$$a = a(B, \omega) \quad, \tag{C.24}$$

$$\omega = \omega(f) \quad, \tag{C.25}$$

$$B = B(L_f) \quad, \tag{C.26}$$

$$A_b = A_b(b, h) \quad, \tag{C.27}$$

$$A_c = A_c(b_{BC}, h) \quad, \tag{C.28}$$

$$I_{by} = I_{by}(b, h) \quad, \tag{C.29}$$

$$I_{cy} = I_{cy}(b_{BC}, h) \quad, \tag{C.30}$$

$$G = G(E, v) \quad. \tag{C.31}$$

Parameters appearing in Eqs C.21 to C.31, and their uncertainties, are defined in Eqs C.32 to C.49

$$f = 10 \times 10^3 \text{ Hz} \quad, \tag{C.32}$$

$$\delta f = 0.5 \times 10^3 \text{ Hz} \quad, \tag{C.33}$$

$$L_f = 40 \ \mu m \quad , \tag{C.34}$$

$$\delta L_f = 0.25 \ \mu m \quad , \tag{C.35}$$

$$L_{shuttle} = 500 \ \mu m \quad , \tag{C.36}$$

$$\delta L_{shuttle} = 0.25 \ \mu m \quad , \tag{C.37}$$

$$d_{holes} = 4 \ \mu m \quad , \tag{C.38}$$

$$\delta d_{holes} = 0.25 \ \mu m \quad , \tag{C.39}$$

$$b_{fingers} = 4 \ \mu m \quad , \tag{C.40}$$

$$\delta b_{fingers} = 0.25 \ \mu m \quad , \tag{C.41}$$

$$extra_1 = 20 \ \mu m \quad , \tag{C.42}$$

$$\delta extra_1 = 0.25 \ \mu m \quad , \tag{C.43}$$

$$extra_2 = 10 \ \mu m \quad , \tag{C.44}$$

$$\delta extra_2 = 0.25 \ \mu m \quad , \tag{C.45}$$

$$extra_3 = 135 \ \mu m \quad , \tag{C.46}$$

$$\delta extra_3 = 0.25 \ \mu m \quad , \tag{C.47}$$

$$extra_4 = 8 \ \mu m \quad , \tag{C.48}$$

$$\delta extra_4 = 0.25 \ \mu m \quad . \tag{C.49}$$

Using the parameters and their uncertainties, defined by Eqs C.21 to C.31 and Eqs C.32 to C.49, overall uncertainty in the deformation in the *x*-direction was determined as described in the following discussion.

The area of the proof mass and the uncertainty in the area were determined as

$$A_{shuttle} = L_{shuttle}^2 \qquad\qquad A_{shuttle} = 2.5 \times 10^{-7} \ m^2 \quad , \tag{C.50}$$

$$\delta A_{shuttle} = 2L_{shuttle} \cdot \delta L_{shuttle} \qquad\qquad \delta A_{shuttle} = 2.5 \times 10^{-10} \ m^2 \quad , \tag{C.51}$$

$$A_{holes} = 64^2 \frac{\pi d_{holes}^2}{4} \qquad\qquad A_{holes} = 4.8305 \times 10^{-8} \text{ m}^2 \quad , \tag{C.52}$$

$$\delta A_{holes} = 2 \cdot 64^2 \frac{\pi d_{holes}}{4} \delta d_{holes} \qquad\qquad \delta A_{holes} = 6.0381 \times 10^{-9} \text{ m}^2 \quad , \tag{C.53}$$

$$\delta A_{combs} = \left(27 \cdot 2 L_f b_{fingers}\right)^2 \qquad\qquad \delta A_{combs} = 8.64 \times 10^{-9} \text{ m}^2 \quad , \tag{C.54}$$

$$\delta Acombs\delta Lf = \left(27 \cdot 2 b_{fingers} \cdot \delta L_f\right)^2 \quad , \tag{C.55}$$

$$\delta Acombs\delta bfingers = \left(27 \cdot 2 L_f \cdot \delta b_{fingers}\right)^2 \quad , \tag{C.56}$$

$$\delta A_{combs} = \sqrt{\delta Acombs\delta Lf + \delta Acombs\delta bfingers}$$

or

$$\delta A_{combs} = 5.4269 \times 10^{-10} \text{ m}^2 , \tag{C.57}$$

$$A_{extra} = 4\left(extra_1 \cdot \delta extra_2\right) + 4\left(extra_3 \cdot \delta extra_4\right) \qquad A_{extra} = 5.12 \times 10^{-9} \text{ m}^2 \quad , \tag{C.58}$$

$$\delta Aextra\delta extra1 = \left(4 extra_2 \cdot \delta extra_1\right)^2 \quad , \tag{C.59}$$

$$\delta Aextra\delta extra2 = \left(4 extra_1 \cdot \delta extra_2\right)^2 \quad , \tag{C.60}$$

$$\delta Aextra\delta extra3 = \left(4 extra_4 \cdot \delta extra_3\right)^2 \quad , \tag{C.61}$$

$$\delta Aextra\delta extra4 = \left(4 extra_3 \cdot \delta extra_4\right)^2 \quad , \tag{C.62}$$

$$\delta A_{extra} = \sqrt{\delta Aextra\delta extra1 + \delta Aextra\delta extra2 + \delta Aextra\delta extra3 + \delta Aextra\delta extra4}$$

or

$$\delta A_{extra} = 1.3707 \times 10^{-10} \text{ m}^2 , \tag{C.63}$$

$$A_{proof} = A_{shuttle} - A_{holes} + A_{combs} + A_{extra}$$

or

$$A_{proof} = 2.1545 \times 10^{-7} \text{ m}^2 , \tag{C.64}$$

and

$$\delta A_{proof} = \sqrt{\delta A_{shuttle}{}^2 - \delta A_{holes}{}^2 + \delta A_{combs}{}^2 + \delta A_{extra}{}^2}$$

or

$$\delta A_{proof} = 6.0692 \times 10^{-9} \text{ m}^2 \quad . \tag{C.65}$$

The angular speed and the amplitude of the motion of the proof mass and their uncertainties were determined as

$$\omega = 2\pi \cdot f \qquad\qquad \omega = 6.2832 \times 10^4 \text{ rad}/_{sec} , \tag{C.66}$$

$$\delta\omega = \sqrt{(2\pi \cdot \delta f)^2} \qquad\qquad \delta\omega = 3.1416 \times 10^3 \text{ rad}/_{sec} , \tag{C.67}$$

$$B = \frac{L_f}{2} - \left(3 \times 10^{-6}\right) \qquad\qquad B = 1.7 \times 10^{-5} \text{ m} , \tag{C.68}$$

$$\delta B = \sqrt{\left(\frac{1}{2}\delta L_f\right)^2} \qquad\qquad \delta B = 1.25 \times 10^{-7} \text{ m} \quad . \tag{C.69}$$

Using Eqs C.66 to C.69, the maximum acceleration of the proof mass and the uncertainty in the acceleration were determined to be

$$a = B\omega^2 \qquad\qquad a = 6.7113 \times 10^4 \text{ m}/_s , \tag{C.70}$$

$$\delta a \delta B = \left(\omega^2 \cdot \delta B\right)^2 , \tag{C.71}$$

$$\delta a \delta\omega = \left(2\omega \cdot B \cdot \delta\omega\right)^2 , \tag{C.72}$$

$$\delta a = \sqrt{\delta a \delta B + \delta a \delta\omega} \qquad\qquad \delta a = 6.7294 \times 10^3 \text{ m}/_s \quad . \tag{C.73}$$

The mass of the proof mass and the uncertainty in the mass were determined by finding the nominal value and uncertainty in the volume, i.e.,

$$V_{proof} = A_{proof}\, h \qquad\qquad V_{proof} = 5.386 \times 10^5 \text{ } \mu m^3 , \tag{C.74}$$

$$\delta V proof \delta A proof = \left(h \cdot \delta A_{proof}\right)^2 \quad, \tag{C.75}$$

$$\delta V proof \delta h = \left(A_{proof} \cdot \delta h\right)^2 \quad, \tag{C.76}$$

$$\delta V_{proof} = \sqrt{\delta V proof \delta A proof + \delta V proof \delta h} \tag{}$$

or

$$\delta V_{proof} = 1.6101 \times 10^{-14} \text{ m}^3, \tag{C.77}$$

which yielded

$$m = V_{proof}\,\rho \qquad\qquad m = 1.255 \times 10^{-9} \text{ kg} \quad, \tag{C.78}$$

$$\delta m \delta V proof = \left(\rho \cdot \delta V_{proof}\right)^2 \quad, \tag{C.79}$$

$$\delta m \delta \rho = \left(V_{proof} \cdot \delta \rho\right)^2 \quad, \tag{C.80}$$

$$\delta m = \sqrt{\delta m \delta V proof + \delta m \delta \rho} \qquad\qquad \delta m = 3.7516 \times 10^{-11} \text{ kg} \quad. \tag{C.81}$$

The values for the cross sectional area of sections *AB* and *CD* were calculated as

$$A_b = hb \qquad\qquad A_b = 7.5 \times 10^{-12} \text{ m}^2 \quad, \tag{C.82}$$

$$\delta A b \delta b = \left(h \cdot \delta b\right)^2 \quad, \tag{C.83}$$

$$\delta A b \delta h = \left(b \delta \delta\right)^2 \quad, \tag{C.84}$$

$$\delta A_b = \sqrt{\delta A b \delta b + \delta A b \delta h} \qquad\qquad \delta A_b = 6.2948 \times 10^{-13} \text{ m}^2 \quad. \tag{C.85}$$

The values for the cross sectional are of section *BC* were calculated as

$$A_c = hb_{BC} \qquad\qquad A_c = 2.5 \times 10^{-11} \text{ m}^2 \quad, \tag{C.86}$$

$$\delta A c \delta b BC = \left(h \cdot \delta b_{BC}\right)^2 \quad, \tag{C.87}$$

$$\delta A c \delta h = \left(b_{BC} \delta h\right)^2 \quad, \tag{C.88}$$

$$\delta A_c = \sqrt{\delta Ac\delta bBC + \delta Ac\delta h} \qquad\qquad \delta A_c = 6.7315 \times 10^{-13} \text{ m}^2 \quad, \qquad (C.89)$$

The moment of inertia for bending in the in-plane direction for sections *AB* and *CD*, and the corresponding uncertainty were calculated as

$$I_{by} = \frac{hb^3}{12} \quad, \qquad\qquad\qquad (C.90)$$

$$\delta Iby\delta b = \left(\frac{hb^2}{4}\delta b\right)^2 \quad, \qquad\qquad\qquad (C.91)$$

$$\delta Iby\delta h = \left(\frac{b^3}{12}\delta h\right)^2 \quad, \qquad\qquad\qquad (C.92)$$

$$\delta I_{by} = \sqrt{\delta Iby\delta b + \delta Iby\delta h} \quad . \qquad\qquad\qquad (C.93)$$

The moment of inertia for bending in the in-plane direction for section *BC* and its uncertainty were calculated as

$$I_{cy} = \frac{hb_{BC}^{~3}}{12} \quad, \qquad\qquad\qquad (C.94)$$

$$\delta Icy\delta bBC = \left(\frac{hb_{BC}^{~2}}{4}\delta b_{BC}\right)^2 \quad, \qquad\qquad\qquad (C.95)$$

$$\delta Icy\delta h = \left(\frac{b_{BC}^{~3}}{12}\delta h\right)^2 \quad, \qquad\qquad\qquad (C.96)$$

$$\delta I_{cy} = \sqrt{\delta Icy\delta bBC + \delta Icy\delta h} \quad . \qquad\qquad\qquad (C.97)$$

The shear modulus and the uncertainty were calculated as

$$G = \frac{E}{2(1+v)} \qquad\qquad G = 65 \text{ GPa} \quad, \qquad\qquad (C.98)$$

$$\delta G \delta E = \left[\frac{1}{2(1+v)} \delta E \right]^2 \quad, \tag{C.99}$$

$$\delta G \delta v = \left[-\frac{E}{2(1+v)^2} \delta v \right]^2 \quad, \tag{C.100}$$

$$\delta G = \sqrt{\delta G \delta E + \delta G \delta v} \qquad\qquad \delta G = 0.335 \text{ GPa} \quad. \tag{C.101}$$

Finally the force in the *x*-direction and its uncertainty were determined to be

$$F_x = \frac{ma}{4} \qquad\qquad F_x \cdot 10^6 = 21.0572 \text{ } \mu N \quad, \tag{C.102}$$

$$\delta Fx \delta a = \left(\frac{m}{4} \delta a \right)^2 \quad, \tag{C.103}$$

$$\delta Fx \delta m = \left(\frac{a}{4} \delta m \right)^2 \quad, \tag{C.104}$$

$$\delta F_x = \sqrt{\delta Fx \delta a + \delta Fx \delta m} \qquad\qquad \delta F_x \cdot 10^6 = 2.2032 \text{ } \mu N \quad. \tag{C.105}$$

The uncertainty for the force in the *z*-direction was set to zero, i.e.,

$$F_z = 0 \text{ N} \quad, \tag{C.106}$$

$$\delta F_z = 0 \text{ N} \quad. \tag{C.107}$$

Using all of the independent parameters and their uncertainties, defined in Eqs C.32 to C.107, overall uncertainty in deformation in the *x*-direction was determined. This was done by first calculating components of the overall uncertainty due to each of the parameters in the phenomenological relationship, given by C.20, for the deformation in the *x*-direction, i.e.,

$$\delta\Delta Dx \delta Fx = \left\{ \left[\frac{1}{3EI_{by}} \left(L_{AB}{}^3 - 3L_{AB}{}^2 L_{CD} + 3L_{AB}L_{CD}{}^2 \right) + \right. \right.$$

$$\left. \left. \frac{6L_{AB}}{5GA_b} + \frac{L_{BC}}{A_c E} + \frac{L_{CD}{}^2 L_{BC}}{EI_{cy}} + \frac{L_{CD}{}^3}{3EI_{by}} + \frac{6L_{CD}}{5GA_b} \right] \delta F_x \right\}^2 \quad , \tag{C.108}$$

$$\delta\Delta Dx \delta Fz = \left\{ \left[\frac{L_{BC}}{2EI_{by}} \left(L_{AB}{}^2 - 2L_{AB}L_{CD} \right) - \frac{L_{CD}L_{BC}{}^2}{2EI_{cy}} \right] \delta F_z \right\}^2 \quad , \tag{C.109}$$

$$\delta\Delta Dx \delta LAB = \left\{ \left[\frac{F_x}{3EI_{by}} \left(3L_{AB}{}^2 - 6L_{AB}L_{CD} + 3L_{CD}{}^2 \right) + \right. \right.$$

$$\left. \left. \frac{6F_x}{5GA_b} + \frac{F_z L_{BC}}{2EI_{by}} \left(2L_{AB} - 2L_{CD} \right) \right] \delta L_{AB} \right\}^2 \quad , \tag{C.110}$$

$$\delta\Delta Dx \delta LBC = \left\{ \left[\frac{F_z}{2EI_{by}} \left(L_{AB}{}^2 - 2L_{AB}L_{CD} \right) + \frac{F_x}{A_c E} + \right. \right.$$

$$\left. \left. \frac{F_x L_{CD}{}^2}{EI_{cy}} - \frac{F_z L_{CD}L_{BC}}{EI_{cy}} \right] \delta L_{BC} \right\}^2 \quad , \tag{C.111}$$

$$\delta\Delta Dx \delta LCD = \left\{ \left[\frac{F_x}{3EI_{by}} \left(-3L_{AB}{}^2 + 6L_{AB}L_{CD} \right) - \frac{F_z L_{AB}L_{BC}}{EI_{by}} + \right. \right.$$

$$\left. \left. \frac{F_x L_{CD}L_{BC}}{EI_{cy}} - \frac{F_z L_{BC}{}^2}{2EI_{cy}} + \frac{F_x L_{CD}{}^2}{EI_{by}} + \frac{6F_x}{5GA_b} \right] \delta L_{CD} \right\}^2 \quad , \tag{C.112}$$

$$\delta\Delta Dx \delta Ab = \left[\left(\frac{-6F_x L_{AB}}{5GA_b{}^2} - \frac{6F_x L_{CD}}{5GA_b{}^2} \right) \delta A_b \right]^2 \quad , \tag{C.113}$$

$$\delta\Delta Dx \delta Ac = \left[\left(-\frac{F_x L_{BC}}{EA_c{}^2} \right) \delta A_c \right]^2 \quad , \tag{C.114}$$

$$\delta\Delta Dx\delta Iby = \left\{ \left[-\frac{F_x}{3EI_{by}{}^2}\left(L_{AB}{}^3 - 3L_{AB}{}^2 L_{CD} + 3L_{AB}L_{CD}{}^2\right) - \right.\right.$$
$$\left.\left. \frac{F_z L_{BC}}{2EI_{by}{}^2}\left(L_{AB}{}^2 - 2L_{AB}L_{CD}\right) - \frac{F_x L_{CD}{}^3}{3EI_{by}{}^2}\right]\delta I_{by}\right\}^2 , \qquad (C.115)$$

$$\delta\Delta Dx\delta Icy = \left[\left(\frac{F_x L_{CD}{}^2 L_{BC}}{EI_{cy}{}^2} + \frac{F_z L_{CD}L_{BC}{}^2}{2EI_{cy}{}^2}\right)\delta I_{cy}\right]^2 , \qquad (C.116)$$

$$\delta\Delta Dx\delta E = \left\{ \left[\frac{-F_x}{3E^2 I_{by}}\left(L_{AB}{}^3 - 3L_{AB}{}^2 L_{CD} + 3L_{AB}L_{CD}{}^2\right) - \right.\right.$$
$$\frac{F_z L_{BC}}{2E^2 I_{by}}\left(L_{AB}{}^2 - 2L_{AB}L_{CD}\right) - \frac{F_x L_{BC}}{A_c E^2} -$$
$$\left.\left. \frac{F_x L_{CD}{}^2 L_{BC}}{E^2 I_{cy}} + \frac{F_z L_{CD}L_{BC}{}^2}{E^2 I_{cy}} - \frac{F_x L_{CD}{}^3}{3E^2 I_{by}}\right]\delta E\right\}^2 , \qquad (C.117)$$

$$\delta\Delta Dx\delta G = \left[\left(\frac{-6F_x L_{AB}}{5G^2 A_b} - \frac{6F_x L_{CD}}{5G^2 A_b}\right)\delta G\right]^2 . \qquad (C.118)$$

Equations C.108 to C.118 were combined to determine the overall uncertainty in deformation in the *x*-direction, i.e.,

$$\delta\Delta_{Dx} = \left(\delta\Delta Dx\delta Fx + \delta\Delta Dx\delta Fz + \delta\Delta Dx\delta LAB + \delta\Delta Dx\delta LBC + \delta\Delta Dx\delta LCD + \right.$$
$$\left. \delta\Delta Dx\delta Ab + \delta\Delta Dx\delta Ac + \delta\Delta Dx\delta Iby + \delta\Delta Dx\delta Icy + \delta\Delta Dx\delta E + \delta\Delta Dx\delta G\right)^{1/2}$$

or

$$\delta\Delta_{Dx} \cdot 10^6 = 5.78856\,\mu m \quad . \qquad (C.119)$$

Using the value of overall uncertainty in Δ_{Dx} determined in Eq. C.119 and the value of the deformation based on Eq. A.122. i.e.,

$$\Delta_{Dx} \cdot 10^6 = 21.4583\,\mu m \quad , \qquad (C.120)$$

the percent overall uncertainty in the *x*-component of the deformation at point *D* was

calculated as

$$\%\text{Uncertainty}\Delta_{Dx} = \left| \frac{\delta\Delta_{Dx}}{\Delta_{Dx}} \right| \cdot 100 \qquad\qquad \%\text{Uncertainty}\Delta_{Dx} = 26.9758\% \quad . \qquad \text{(C.121)}$$

The result shown in Eq. C.121 means that the uncertainty calculated in Eq. C.119 for the

deformation in the *x*-direction is 28% of the nominal value of the deformation. In order

to see which of the independent parameters contributed most to the overall uncertainty,

percent contributions to the uncertainty of each of the individual uncertainties were

calculated as

$$\%\delta\Delta Dx\delta Fx = \frac{\delta\Delta Dx\delta Fx}{\delta\Delta_{Dx}{}^2} \cdot 100 \qquad\qquad \%\delta\Delta Dx\delta Fx = 15.0442\% \quad , \qquad \text{(C.122)}$$

$$\%\delta\Delta Dx\delta Fz = \frac{\delta\Delta Dx\delta Fz}{\delta\Delta_{Dx}{}^2} \cdot 100 \qquad\qquad \%\delta\Delta Dx\delta Fz = 0\% \quad , \qquad \text{(C.123)}$$

$$\%\delta\Delta Dx\delta LAB = \frac{\delta\Delta Dx\delta LAB}{\delta\Delta_{Dx}{}^2} \cdot 100 \qquad\qquad \%\delta\Delta Dx\delta LAB = 2.9932 \times 10^{-6}\% \quad , \qquad \text{(C.124)}$$

$$\%\delta\Delta Dx\delta LBC = \frac{\delta\Delta Dx\delta LBC}{\delta\Delta_{Dx}{}^2} \cdot 100 \qquad\qquad \%\delta\Delta Dx\delta LBC = 1.1315 \times 10^{-5}\% \quad , \qquad \text{(C.125)}$$

$$\%\delta\Delta Dx\delta LCD = \frac{\delta\Delta Dx\delta LCD}{\delta\Delta_{Dx}{}^2} \cdot 100 \qquad\qquad \%\delta\Delta Dx\delta LCD = 0.0617\% \quad , \qquad \text{(C.126)}$$

$$\%\delta\Delta Dx\delta Ab = \frac{\delta\Delta Dx\delta Ab}{\delta\Delta_{Dx}{}^2} \cdot 100 \qquad\qquad \%\delta\Delta Dx\delta Ab = 2.4642 \times 10^{-6}\% \quad , \qquad \text{(C.127)}$$

$$\%\delta\Delta Dx\delta Ac = \frac{\delta\Delta Dx\delta Ac}{\delta\Delta_{Dx}{}^2} \cdot 100 \qquad\qquad \%\delta\Delta Dx\delta Ac = 1.7329 \times 10^{-11}\% \quad , \qquad \text{(C.128)}$$

$$\%\delta\Delta Dx\delta Iby = \frac{\delta\Delta Dx\delta Iby}{\delta\Delta_{Dx}{}^2} \cdot 100 \qquad\qquad \%\delta\Delta Dx\delta Iby = 84.8804\% \quad , \qquad \text{(C.129)}$$

$$\%\delta\Delta Dx\delta Icy = \frac{\delta\Delta Dx\delta Icy}{\delta\Delta_{Dx}{}^2}\cdot 100 \qquad\qquad \%\delta\Delta Dx\delta Icy = 2.9914\times 10^{-4}\,\% \quad , \qquad (C.130)$$

$$\%\delta\Delta Dx\delta E = \frac{\delta\Delta Dx\delta E}{\delta\Delta_{Dx}{}^2}\cdot 100 \qquad\qquad \%\delta\Delta Dx\delta E = 0.0134\,\% \quad , \qquad (C.131)$$

$$\%\delta\Delta Dx\delta G = \frac{\delta\Delta Dx\delta G}{\delta\Delta_{Dx}{}^2}\cdot 100 \qquad\qquad \%\delta\Delta Dx\delta G = 9.1964\times 10^{-9}\,\% \quad . \qquad (C.132)$$

In order to ensure that the percent uncertainties were calculated properly, the values calculated in Eqs C.122 to C.132 were added together to make sure that they yield 100%, i.e.,

$$\%\delta\Delta_{Dx} = \%\delta\Delta Dx\delta Fx + \%\delta\Delta Dx\delta Fz + \%\delta\Delta Dx\delta LAB + \%\delta\Delta Dx\delta LBC + \%\delta\Delta Dx\delta LCD +$$
$$\%\delta\Delta Dx\delta Ab + \%\delta\Delta Dx\delta Ac + \%\delta\Delta Dx\delta Iby + \%\delta\Delta Dx\delta Icy + \%\delta\Delta Dx\delta E + \%\delta\Delta Dx\delta G$$

or

$$\%\delta\Delta_{Dx} = 100\,\% \quad . \qquad\qquad\qquad\qquad (C.133)$$

Based on the results of Eqs C.122 to C.133, the uncertainty in I_{by}, given by Eq. C.129, produces the largest contribution to the overall uncertainty in the deformation in the x-direction, amounting to 85%. The next step was to check the overall uncertainty in I_{by} to see which one of the independent parameters contributes most to its value,

$$\%\delta Iby\delta b = \frac{\delta Iby\delta b}{\delta I_{by}{}^2}\cdot 100 \qquad\qquad \%\delta Iby\delta b = 99.8403\,\% \quad , \qquad (C.134)$$

$$\%\delta Iby\delta h = \frac{\delta Iby\delta h}{\delta I_{by}{}^2}\cdot 100 \qquad\qquad \%\delta Iby\delta h = 0.1597\,\% \quad . \qquad (C.135)$$

The results of Eqs C.134 and C.135 were added together to check that they added up to 100%,

$$\%\delta I_{by} = \%\delta Iby\delta b + \%\delta Iby\delta h \qquad\qquad \%\delta I_{by} = 100\,\% \quad . \qquad (C.136)$$

Equations C.134 to C.136 show that the uncertainty in the width contributes over 99.8%, Eq. C.134, to the overall uncertainty of I_{by}. Since I_{by} is the largest contributor to the overall uncertainty in the deformation in the *x*-direction, the width contributes the most to the overall uncertainty in the deformation. Therefore, in order to reduce overall uncertainty in Δ_{Dx}, contributions due to the uncertainty in width must be reduced, i.e., δb must be lowered.

C.2. Uncertainty analysis of deformation in the *y*-direction

Since all of the independent parameters were defined in Section C.1, the first step was to obtain the phenomenological equation for the deformation in the *y*-direction, i.e.,

$$\Delta_{Dy} = \Delta_{Dy}\left(F_y, L_{AB}, L_{BC}, L_{CD}, A_b, A_c, I_{bx}, I_{cz}, J_b, J_c, E, G\right) \quad , \tag{C.137}$$

where each of the parameters that define Δ_{Dy} are written with respect to their own independent parameters that define them:

$$F_y = F_y(m, v, \Omega) \quad , \tag{C.138}$$

$$m = m\left(V_{proof}, \rho\right) \quad , \tag{C.139}$$

$$v = v(B, \tau) \quad , \tag{C.140}$$

$$B = B(L_f) \quad , \tag{C.141}$$

$$\tau = \tau(f) \quad , \tag{C.142}$$

$$A_b = A_b(b, h) \quad , \tag{C.143}$$

$$A_c = A_c(b_{BC}, h) \quad , \tag{C.144}$$

$$I_{bx} = I_{bx}(b, h) \quad , \tag{C.145}$$

$$I_{cz} = I_{cz}(b_{BC}, h) \quad , \tag{C.146}$$

$$J_b = J_b(b, h) \quad , \tag{C.147}$$

$$J_c = J_c(b_{BC}, h) \quad , \tag{C.148}$$

and

$$G = G(E, v) \quad . \tag{C.149}$$

Out of Eqs C.138 to C.149, m, B, A_b, A_c, and G are defined in the derivation of the overall uncertainty in the deformation in the x-direction and given by Eqs C.22, C.26 to C.28, and C.31, respectively, while other parameters will be defined in the discussion that follows.

The angular velocity that the microgyroscope was subjected to is defined as

$$\Omega = 100 \frac{2\pi}{360} \qquad \Omega = 1.74533 \; \text{rad}\big/\text{sec} \quad , \tag{C.150}$$

with an uncertainty of

$$\delta\Omega = 0 \quad . \tag{C.151}$$

The period of the oscillation of the proof mass and the uncertainty in the period are calculated as

$$\tau = \frac{1}{f} \qquad \tau = 1 \times 10^{-4} \; \text{sec} \quad , \tag{C.152}$$

$$\delta\tau = \sqrt{\left(\frac{-1}{f^2}\delta f\right)^2} \qquad \delta\tau = 5 \times 10^{-6} \; \text{s} \quad . \tag{C.153}$$

The velocity of the in plane oscillation of the proof mass and the uncertainty are defined as

$$v = \frac{4B}{\tau} \qquad\qquad v = 0.68 \, ^{m}\!/_{s} \quad, \qquad\qquad\qquad \text{(C.154)}$$

$$\delta v \delta B = \left(\frac{4}{\tau} \delta B \right)^{2} \quad, \qquad\qquad\qquad\qquad\qquad \text{(C.155)}$$

$$\delta v \delta \tau = \left(\frac{-4B}{\tau^{2}} \delta \tau \right)^{2} \quad, \qquad\qquad\qquad\qquad\qquad \text{(C.156)}$$

$$\delta v = \sqrt{\delta v \delta B + \delta v \delta \tau} \qquad\qquad \delta v = 0.0344 \, ^{m}\!/_{s} \quad . \qquad\qquad \text{(C.157)}$$

The moment of inertia for bending in the out-of-plane, y, direction for sections AB and CD were calculated as

$$I_{bx} = \frac{bh^{3}}{12} \quad, \qquad\qquad\qquad\qquad\qquad\qquad \text{(C.158)}$$

$$\delta Ibx \delta b = \left(\frac{h^{3}}{12} \delta b \right)^{2} \quad, \qquad\qquad\qquad\qquad\qquad \text{(C.159)}$$

$$\delta Ibx \delta h = \left(\frac{bh^{2}}{4} \delta h \right)^{2} \quad, \qquad\qquad\qquad\qquad\qquad \text{(C.160)}$$

$$\delta I_{bx} = \sqrt{\delta Ibx \delta b + \delta Ibx \delta h} \quad . \qquad\qquad\qquad\qquad \text{(C.161)}$$

The moment of inertia for bending in the y-direction for section BC was calculated as

$$I_{cz} = \frac{b_{BC} h^{3}}{12} \quad, \qquad\qquad\qquad\qquad\qquad\qquad \text{(C.162)}$$

$$\delta Icz \delta bBC = \left(\frac{h^{3}}{12} \delta b_{BC} \right)^{2} \quad, \qquad\qquad\qquad\qquad\qquad \text{(C.163)}$$

$$\delta Icz \delta h = \left(\frac{b_{BC} h^{2}}{4} \delta h \right)^{2} \quad, \qquad\qquad\qquad\qquad\qquad \text{(C.164)}$$

$$\delta I_{cz} = \sqrt{\delta Icz \delta bBC + \delta Icz \delta h} \quad . \qquad\qquad\qquad\qquad \text{(C.165)}$$

The polar moment of inertia and its uncertainty for sections *AB* and *CD* were calculated as

$$J_b = 0.219 \cdot bh^3 \quad , \tag{C.166}$$

$$\delta Jb\delta b = \left(0.219 \cdot h^3 \delta b\right)^2 \quad , \tag{C.167}$$

$$\delta Jb\delta h = \left(3 \cdot 0.219 \cdot bh^2 \delta h\right)^2 \quad , \tag{C.168}$$

$$\delta J_b = \sqrt{\delta Jb\delta b + \delta Jb\delta h} \quad . \tag{C.169}$$

The polar moment of inertia and the corresponding uncertainty for section *BC* was calculated as

$$J_c = 0.282 \cdot b_{BC} h^3 \quad , \tag{C.170}$$

$$\delta Jc\delta bBC = \left(0.282 \cdot h^3 \delta b_{BC}\right)^2 \quad , \tag{C.171}$$

$$\delta Jc\delta h = \left(3 \cdot 0.282 \cdot b_{BC} h^2 \delta h\right)^2 \quad , \tag{C.172}$$

$$\delta J_c = \sqrt{\delta Jc\delta bBC + \delta Jc\delta h} \quad . \tag{C.173}$$

Finally, the Coriolis force in the *y*-direction and the uncertainty in the force were determined as

$$F_y = \frac{m \cdot v \cdot \Omega}{2} \qquad\qquad Fy \cdot 10^9 = 0.7447 \text{ nN} \quad , \tag{C.174}$$

$$\delta Fy\delta m = \left(\frac{v \cdot \Omega}{2} \delta m\right)^2 \quad , \tag{C.175}$$

$$\delta Fy\delta v = \left(\frac{m \cdot \Omega}{2} \delta v\right)^2 \quad , \tag{C.176}$$

$$\delta Fy\delta\Omega = \left(\frac{m \cdot v}{2} \delta\Omega\right)^2 \quad , \tag{C.177}$$

$$\delta Fy = \sqrt{\delta Fy\delta m + \delta Fy\delta v + \delta Fy\delta\Omega} \qquad\qquad \delta Fy\cdot 10^9 = 0.057 \text{ nN} \quad . \qquad\qquad \text{(C.178)}$$

Using the independent parameters and uncertainties defined by Eqs C.32 to C.101 and C. 151 to C.179, overall uncertainty in deformation in the *y*-direction was calculated. This was done by calculating components of the overall uncertainty due to each of the parameters in the phenomenological relationship, given by C.137, for deformation in the *y*-direction, i.e.,

$$\delta\Delta Dy\delta Fy = \left\{ \left[\frac{1}{3EI_{bx}}\left(L_{AB}{}^3 - 3L_{AB}{}^2 L_{CD} + 3L_{AB}L_{CD}{}^2\right) + \right.\right.$$
$$\frac{6L_{AB}}{5GA_b} + \frac{L_{BC}{}^2 L_{AB}}{GJ_b} + \frac{L_{BC}{}^3}{3EI_{cz}} + \frac{6L_{BC}}{5GA_c} + \qquad , \qquad\qquad \text{(C.179)}$$
$$\left. \left. \frac{L_{CD}{}^2 L_{BC}}{GJ_c} + \frac{L_{CD}{}^3}{3EI_{bx}} + \frac{6L_{CD}}{5GA_b}\right] \delta F_y \right\}^2 \right\}$$

$$\delta\Delta Dy\delta LAB = \left\{ \left[\frac{F_y}{3EI_{bx}}\left(3L_{AB}{}^2 - 6L_{AB}L_{CD} + 3L_{CD}{}^2\right) + \right.\right.$$
$$\left. \left. \frac{6F_y}{5GA_b} + \frac{F_y L_{BC}{}^2}{GJ_b}\right] \delta L_{AB} \right\}^2 \qquad , \qquad\qquad \text{(C.180)}$$

$$\delta\Delta Dy\delta LBC = \left[\left(\frac{2F_y L_{BC}L_{AB}}{GJ_b} + \frac{F_y L_{BC}{}^2}{EI_{cz}} + \frac{6F_y}{5GA_c} + \frac{F_y L_{CD}{}^2}{GJ_c}\right) \delta L_{BC}\right]^2 \quad , \qquad \text{(C.181)}$$

$$\delta\Delta Dy\delta LCD = \left\{ \left[\frac{F_y}{3EI_{bx}}\left(-3L_{AB}{}^2 + 6L_{AB}L_{CD}\right) + \frac{2F_y L_{CD}L_{BC}}{GJ_c} + \right.\right.$$
$$\left. \left. \frac{F_y L_{CD}{}^2}{EI_{bx}} + \frac{6F_y}{5GA_b}\right] \delta L_{CD} \right\}^2 \qquad , \qquad\qquad \text{(C.182)}$$

$$\delta\Delta Dy\delta Ab = \left[\left(\frac{-6F_y L_{AB}}{5GA_b{}^2} - \frac{6F_y L_{CD}}{5GA_b{}^2}\right) \delta A_b \right]^2 \qquad , \qquad\qquad \text{(C.183)}$$

$$\delta \Delta Dy \delta Ac = \left[\left(-\frac{6F_y L_{BC}}{5GA_c^2} \right) \delta A_c \right]^2 \quad , \tag{C.184}$$

$$\delta \Delta Dy \delta Ibx = \left\{ \left[\frac{-F_y}{3EI_{bx}^2} \left(L_{AB}^3 - 3L_{AB}^2 L_{CD} + 3L_{AB} L_{CD}^2 \right) + \right. \right.$$
$$\left. \left. \frac{-F_y L_{CD}^3}{3EI_{bx}^2} \right] \delta I_{bx} \right\}^2 \quad , \tag{C.185}$$

$$\delta \Delta Dy \delta Icz = \left[\left(\frac{-F_y L_{BC}^3}{3EI_{cz}^2} \right) \delta I_{cz} \right]^2 \quad , \tag{C.186}$$

$$\delta \Delta Dy \delta Jb = \left[\left(\frac{-F_y L_{BC}^2 L_{AB}}{GJ_b^2} \right) \delta J_b \right]^2 \quad , \tag{C.187}$$

$$\delta \Delta Dy \delta Jc = \left[\left(\frac{-F_y L_{CD} L_{BC}}{GJ_c^2} \right) \delta J_c^2 \right]^2 \quad , \tag{C.188}$$

$$\delta \Delta Dy \delta E = \left\{ \left[\frac{-F_y}{3E^2 I_{bx}} \left(L_{AB}^3 - 3L_{AB}^2 L_{CD} + 3L_{AB} L_{CD}^2 \right) - \right. \right.$$
$$\left. \left. \frac{F_y L_{BC}^3}{3E^2 I_{cz}} - \frac{F_y L_{CD}^3}{3E^2 I_{bx}} \right] \delta E \right\}^2 \quad , \tag{C.189}$$

and

$$\delta \Delta Dy \delta G = \left[\left(\frac{-6L_{AB}}{5G^2 A_b} - \frac{F_y L_{BC}^2 L_{AB}}{G^2 J_b} - \frac{6F_y L_{BC}}{5G^2 A_c} - \right. \right.$$
$$\left. \left. \frac{F_y L_{CD}^2 L_{BC}}{G^2 J_c} - \frac{6F_y L_{CD}}{5G^2 A_b} \right) \delta G \right]^2 \quad . \tag{C.190}$$

Equations C.179 to C.190 were combined to calculate the overall uncertainty in deformation in the *y*-direction, i.e.,

$$\delta\Delta_{Dy} = (\delta\Delta Dy\delta Fy + \delta\Delta Dy\delta LAB + \delta\Delta Dy\delta LBC + \delta\Delta Dy\delta LCD + \Delta Dy\delta Ab +$$

$$\delta\Delta Dy\delta Ac + \delta\Delta Dy\delta Ibx + \delta\Delta Dy\delta Icz + \delta\Delta Dy\delta Jb + \delta\Delta Dy\delta Jc + \delta\Delta Dy\delta E + \delta\Delta Dy\delta G)^{1/2}$$

or

$$\delta\Delta_{Dy} \cdot 10^9 = 0.1186 \text{ nm} \quad . \tag{C.191}$$

Using the value of overall uncertainty in Δ_{Dy} determined in Eq. C.191 and the value of the deformation based on Eq. A.128, i.e.,

$$\Delta_{Dy} \cdot 10^9 = 1.17257 \text{ nm} \quad , \tag{C.192}$$

the percent overall uncertainty in the *y*-component of the deformation at point *D* was calculated as

$$\%\text{Uncertainty}\Delta_{Dy} = \left| \frac{\delta\Delta_{Dy}}{\Delta_{Dy}} \right| \cdot 100 \qquad \%\text{Uncertainty}\Delta_{Dy} = 10.1155\% \quad . \tag{C.193}$$

The results calculated by Eq. C.193 show that the percent overall uncertainty in deformation in the *y*-direction is 10.1% of the nominal value of the deformation. In order to see which independent parameter contributed most to the overall uncertainty, percent contributions to the uncertainty of each of the individual uncertainties were calculated as

$$\%\delta\Delta Dy\delta Fy = \frac{\delta\Delta Dy\delta Fy}{\delta\Delta_{Dy}^2} \cdot 100 \qquad \%\delta\Delta Dy\delta Fy = 33.6936\% \quad , \tag{C.194}$$

$$\%\delta\Delta Dy\delta LAB = \frac{\delta\Delta Dy\delta LAB}{\delta\Delta_{Dy}^2} \cdot 100 \qquad \%\delta\Delta Dy\delta LAB = 1.2271\times10^{-4}\% \quad , \tag{C.195}$$

$$\%\delta\Delta Dy\delta LBC = \frac{\delta\Delta Dy\delta LBC}{\delta\Delta_{Dy}^2} \cdot 100 \qquad \%\delta\Delta Dy\delta LBC = 0.0219\% \quad , \tag{C.196}$$

$$\%\delta\Delta Dy\delta LCD = \frac{\delta\Delta Dy\delta LCD}{\delta\Delta_{Dy}^2} \cdot 100 \qquad \%\delta\Delta Dy\delta LCD = 0.4037\% \quad , \tag{C.197}$$

$$\%\delta\Delta Dy\delta Ab = \frac{\delta\Delta Dy\delta Ab}{\delta\Delta_{Dy}^{2}} \cdot 100 \qquad \%\delta\Delta Dy\delta Ab = 7.3414\times10^{-6}\,\% \quad , \qquad (C.198)$$

$$\%\delta\Delta Dy\delta Ac = \frac{\delta\Delta Dy\delta Ac}{\delta\Delta_{Dy}^{2}} \cdot 100 \qquad \%\delta\Delta Dy\delta Ac = 4.499\times10^{-10}\,\% \quad , \qquad (C.199)$$

$$\%\delta\Delta Dy\delta Ibx = \frac{\delta\Delta Dy\delta Ibx}{\delta\Delta_{Dy}^{2}} \cdot 100 \qquad \%\delta\Delta Dy\delta Ibx = 65.7096\,\% \quad , \qquad (C.200)$$

$$\%\delta\Delta Dy\delta Icz = \frac{\delta\Delta Dy\delta Icz}{\delta\Delta_{Dy}^{2}} \cdot 100 \qquad \%\delta\Delta Dy\delta Icz = 3.7151\times10^{-6}\,\% \quad , \qquad (C.201)$$

$$\%\delta\Delta Dy\delta Jb = \frac{\delta\Delta Dy\delta Jb}{\delta\Delta_{Dy}^{2}} \cdot 100 \qquad \%\delta\Delta Dy\delta Jb = 0.0556\,\% \quad , \qquad (C.202)$$

$$\%\delta\Delta Dy\delta Jc = \frac{\delta\Delta Dy\delta Jc}{\delta\Delta_{Dy}^{2}} \cdot 100 \qquad \%\delta\Delta Dy\delta Jc = 0.0321\,\% \quad , \qquad (C.203)$$

$$\%\delta\Delta Dy\delta E = \frac{\delta\Delta Dy\delta E}{\delta\Delta_{Dy}^{2}} \cdot 100 \qquad \%\delta\Delta Dy\delta E = 0.0819\,\% \quad , \qquad (C.204)$$

$$\%\delta\Delta Dy\delta G = \frac{\delta\Delta Dy\delta G}{\delta\Delta_{Dy}^{2}} \cdot 100 \qquad \%\delta\Delta Dy\delta G = 1.3955\times10^{-3}\,\% \quad . \qquad (C.205)$$

In order to ensure that the percent uncertainties were calculated properly the values determined in Eqs C.194 to C.205 were added together to make sure that the sum yields 100%, i.e.,

$$\begin{aligned}\%\delta\Delta_{Dy} = {}& \%\delta\Delta Dy\delta Fy + \%\delta\Delta Dy\delta LAB + \%\delta\Delta Dy\delta LBC + \%\delta\Delta Dy\delta LCD + \%\Delta Dy\delta Ab + \\ & \%\delta\Delta Dy\delta Ac + \%\delta\Delta Dy\delta Ibx + \%\delta\Delta Dy\delta Icz + \%\delta\Delta Dy\delta Jb + \%\delta\Delta Dy\delta Jc + \\ & \%\delta\Delta Dy\delta E + \%\delta\Delta Dy\delta G\end{aligned}$$

or

$$\%\delta\Delta_{Dy} = 100\,\% \quad . \qquad (C.206)$$

243

Based on the results of Eqs C.194 to C.206, the uncertainty in I_{bx} produces the largest contribution to the overall uncertainty in deformation in the y-direction, amounting to 66%. The next step was to check the overall uncertainty in I_{bx} to see which one of the independent parameters contributes most to δI_{bx},

$$\%\delta Ibx\delta b = \frac{\delta Ibx\delta b}{\delta I_{bx}{}^2}\cdot 100 \qquad\qquad \%\delta Ibx\delta b = 88.5269\% \quad , \qquad\qquad \text{(C.207)}$$

$$\%\delta Ibx\delta h = \frac{\delta Ibx\delta h}{\delta I_{bx}{}^2}\cdot 100 \qquad\qquad \%\delta Ibx\delta h = 11.4731\% \quad . \qquad\qquad \text{(C.208)}$$

Sum of the results given by Eqs C.208 and C.209,

$$\%\delta I_{by} = \%\delta Ibx\delta b + \%\delta Ibx\delta h \qquad\qquad \%\delta I_{by} = 100\% \quad , \qquad\qquad \text{(C.209)}$$

is 100% indicating that the percentage uncertainties contributing to $\%\delta I_{bx}$ were determined properly. Furthermore, Eqs C.207 to C.209 show that the uncertainty in the width contributes over 88% to the overall uncertainty in I_{bx}. Since I_{bx} is the largest contributor to the overall uncertainty in Δ_{Dy}, the width contributes the most to the overall uncertainty in the deformation. Therefore, in order to reduce $\delta\Delta_{Dy}$, δb should be reduced subject to the limitations of the fabrication process used.

C.3. Uncertainty analysis of the deformation in the z-direction

All of the independent parameters needed for determination of overall uncertainty in deformation in the z-direction were defined in Section C.1; therefore, the first step was to obtain the phenomenological relationship for the deformation in the z-direction, i.e.,

$$\Delta_{Dz} = \Delta_{Dz}\left(F_x, F_z, L_{AB}, L_{BC}, L_{CD}, A_b, A_c, I_{by}, I_{cy}, E, G\right) \tag{C.210}$$

where each of the parameters that define Δ_{Dz} are written with respect to the independent

parameters that define them as

$$F_x = F_x(m, a) \quad , \tag{C.211}$$

$$m = m\left(V_{proof}, \rho\right) \quad , \tag{C.212}$$

$$V_{proof} = V_{proof}\left(A_{proof}, h\right) \quad , \tag{C.213}$$

$$a = a(B, \omega) \quad , \tag{C.214}$$

$$\omega = \omega(f) \quad , \tag{C.215}$$

$$B = B(L_f) \quad , \tag{C.216}$$

$$A_b = A_b(b, h) \quad , \tag{C.217}$$

$$A_c = A_c(b_{BC}, h) \quad , \tag{C.218}$$

$$I_{by} = I_{by}(b, h) \quad , \tag{C.219}$$

$$I_{cy} = I_{cy}(b_{BC}, h) \quad , \tag{C.220}$$

and

$$G = G(E, \nu) \quad . \tag{C.221}$$

The independent parameters defined by Eqs C.211 to C.221 and the corresponding

uncertainties were defined in the derivation of the uncertainty for the displacement in the

x-direction, Eqs C.32 to C.107. Using the independent parameters and uncertainties from

Eqs C.32 to C.107, overall uncertainty in deformation in the z-direction was calculated.

This was done by calculating components of the overall uncertainty due to each of the

parameters in the phenomenological equation, given by Eq. C.210, for the deformation in the *z*-direction, i.e.,

$$\delta\Delta Dz\delta Fx = \left\{\left[\frac{L_{BC}\left(L_{AB}{}^2 - 2L_{AB}L_{CD}\right)}{2EI_{by}} - \frac{L_{CD}L_{BC}{}^2}{2EI_{cy}}\right]\delta F_x\right\}^2 \quad , \tag{C.222}$$

$$\delta\Delta Dz\delta Fz = \left[\left(\frac{L_{AB}}{A_b E} + \frac{L_{BC}{}^2 L_{AB}}{EI_{by}} + \frac{L_{BC}{}^3}{3EI_{cy}} + \frac{6L_{BC}}{5GA_c} + \frac{L_{CD}}{A_b E}\right)\delta F_z\right]^2 \quad , \tag{C.223}$$

$$\delta\Delta Dz\delta LAB = \left\{\left[\frac{F_z}{A_b E} + \frac{F_x L_{BC}\left(L_{AB} - L_{CD}\right)}{3EI_{by}} + \frac{F_z L_{BC}{}^2}{EI_{by}}\right]\delta L_{AB}\right\}^2 \quad , \tag{C.224}$$

$$\delta\Delta Dz\delta LBC = \left\{\left[\frac{F_x\left(L_{AB}{}^2 - 2L_{AB}L_{CD}\right)}{2EI_{by}} + \frac{2F_z L_{BC}L_{AB}}{EIb_{cy}} - \right.\right.$$
$$\left.\left.\frac{F_x L_{BC}L_{CD}}{EI_{cy}} + \frac{F_z L_{BC}{}^2}{EI_{cy}} + \frac{6F_z}{5GA_c}\right]\delta L_{BC}\right\}^2 \quad , \tag{C.225}$$

$$\delta\Delta Dz\delta LCD = \left[\left(\frac{-F_x L_{AB}L_{BC}}{EI_{by}} - \frac{F_x L_{BC}{}^2}{2EI_{cy}} + \frac{F_z}{EA_b}\right)\delta L_{CD}\right]^2 \quad , \tag{C.226}$$

$$\delta\Delta Dz\delta Ab = \left[\left(\frac{-F_z L_{AB}}{A_b{}^2 E} - \frac{F_z L_{CD}}{EA_b{}^2}\right)\delta A_b\right]^2 \quad , \tag{C.227}$$

$$\delta\Delta Dz\delta Ac = \left[\left(\frac{-6F_z L_{BC}}{5GA_c{}^2}\right)\delta A_c\right]^2 \quad , \tag{C.228}$$

$$\delta\Delta Dz\delta Iby = \left\{\left[\frac{-F_x L_{BC}\left(L_{AB}{}^2 - 2L_{AB}L_{CD}\right)}{2EI_{by}{}^2} - \frac{F_z L_{BC}{}^2 L_{AB}}{EI_{by}{}^2}\right]\delta I_{by}\right\}^2 \quad , \tag{C.229}$$

$$\delta\Delta Dz\delta Icy = \left[\left(\frac{-F_x L_{CD}{}^2 L_{BC}}{EI_{cy}{}^2} + \frac{F_z L_{BC}{}^2 L_{CD}}{2EI_{cy}{}^2}\right)\delta I_{cy}\right]^2 \quad , \tag{C.230}$$

$$\delta \Delta Dz \delta E = \left\{ \left[\frac{-F_z L_{AB}}{E^2 A_b} - \frac{F_x (L_{AB} - 2L_{CD} L_{AB})}{2E^2 I_{by}} - \right. \right.$$

$$\left. \left. \frac{F_z L_{BC}{}^2 L_{AB}}{E^2 I_{by}} + \frac{F_x L_{CD}{}^2 L_{BC}}{2E^2 I_{cy}} - \frac{F_z L_{BC}}{3E^2 I_{cy}} - \frac{F_z L_{CD}}{E^2 I_b} \right] \delta E \right\}^2 \quad , \qquad \text{(C.231)}$$

and

$$\delta \Delta Dz \delta G = \left[\left(\frac{-6F_z L_{BC}}{5G^2 A_c} \right) \delta G \right]^2 \quad , \qquad \text{(C.232)}$$

Equations C.222 to C.232 were combined to calculate the overall uncertainty in deformation in the *z*-direction

$$\delta \Delta_{Dz} = (\delta \Delta Dz \delta Fx + \delta \Delta Dz \delta Fz + \delta \Delta Dz \delta LAB + \delta \Delta Dz \delta LBC + \delta \Delta Dz \delta LCD +$$

$$\delta \Delta Dz \delta Ab + \delta \Delta Dz \delta Ac + \delta \Delta Dz \delta Iby + \delta \Delta Dz \delta Icy + \delta \Delta Dz \delta E + \delta \Delta Dz \delta G)^{1/2}$$

or

$$\delta \Delta_{Dz} \cdot 10^6 = 0.678104 \, \mu m \quad . \qquad \text{(C.233)}$$

Using the value of overall uncertainty in Δ_{Dz} determined in Eq. C.233 and the value of the deformation based on Eq. A.134, i.e.,

$$\Delta_{Dz} \cdot 10^6 = -2.4268 \, \mu m \quad , \qquad \text{(C.234)}$$

the percent overall uncertainty in the *z*-component of the displacement at point *D* was calculated as

$$\% \text{Uncertainty} \Delta_{Dz} = \left| \frac{\delta \Delta_{Dz}}{\Delta_{Dz}} \right| \cdot 100 \qquad \% \text{Uncertainty} \Delta_{Dz} = 27.0716\% \quad . \qquad \text{(C.235)}$$

The result given by Eq C.235 show that the percent overall uncertainty in deformation in the *z*-direction is about 27% of the nominal value of the deformation. In order to see

which independent parameter contributed most to the overall uncertainty, percent

contributions to the uncertainty of each of the individual parameters were calculated as

$$\%\delta\Delta Dz\delta Fx = \frac{\delta\Delta Dz\delta Fx}{\delta\Delta_{Dz}{}^2}\cdot 100 \qquad\qquad \%\delta\Delta Dz\delta Fx = 14.9379\,\% \quad , \qquad (\text{C.236})$$

$$\%\delta\Delta Dz\delta Fz = \frac{\delta\Delta Dz\delta Fz}{\delta\Delta_{Dz}{}^2}\cdot 100 \qquad\qquad \%\delta\Delta Dz\delta Fz = 0\,\% \quad , \qquad (\text{C.237})$$

$$\%\delta\Delta Dz\delta LAB = \frac{\delta\Delta Dz\delta LAB}{\delta\Delta_{Dz}{}^2}\cdot 100 \qquad\qquad \%\delta\Delta Dz\delta LAB = 3.8714\times 10^{-4}\,\% \quad , \qquad (\text{C.238})$$

$$\%\delta\Delta Dz\delta LBC = \frac{\delta\Delta Dz\delta LBC}{\delta\Delta_{Dz}{}^2}\cdot 100 \qquad\qquad \%\delta\Delta Dz\delta LBC = 0.2976\,\% \quad , \qquad (\text{C.239})$$

$$\%\delta\Delta Dz\delta LCD = \frac{\delta\Delta Dz\delta LCD}{\delta\Delta_{Dz}{}^2}\cdot 100 \qquad\qquad \%\delta\Delta Dz\delta LCD = 0.0221\,\% \quad , \qquad (\text{C.240})$$

$$\%\delta\Delta Dz\delta Ab = \frac{\delta\Delta Dz\delta Ab}{\delta\Delta_{Dz}{}^2}\cdot 100 \qquad\qquad \%\delta\Delta Dz\delta Ab = 0\,\% \quad , \qquad (\text{C.241})$$

$$\%\delta\Delta Dz\delta Ac = \frac{\delta\Delta Dz\delta Ac}{\delta\Delta_{Dz}{}^2}\cdot 100 \qquad\qquad \%\delta\Delta Dz\delta Ac = 0\,\% \quad , \qquad (\text{C.242})$$

$$\%\delta\Delta Dz\delta Iby = \frac{\delta\Delta Dz\delta Iby}{\delta\Delta_{Dz}{}^2}\cdot 100 \qquad\qquad \%\delta\Delta Dz\delta Iby = 84.7055\,\% \quad , \qquad (\text{C.243})$$

$$\%\delta\Delta Dz\delta Icy = \frac{\delta\Delta Dz\delta Icy}{\delta\Delta_{Dz}{}^2}\cdot 100 \qquad\qquad \%\delta\Delta Dz\delta Icy = 0.0232\,\% \quad , \qquad (\text{C.244})$$

$$\%\delta\Delta Dz\delta E = \frac{\delta\Delta Dz\delta E}{\delta\Delta_{Dz}{}^2}\cdot 100 \qquad\qquad \%\delta\Delta Dz\delta E = 0.0133\,\% \quad , \qquad (\text{C.245})$$

$$\%\delta\Delta Dz\delta G = \frac{\delta\Delta Dz\delta G}{\delta\Delta_{Dz}{}^2}\cdot 100 \qquad\qquad \%\delta\Delta Dz\delta G = 0\,\% \quad . \qquad (\text{C.246})$$

In order to ensure that the percent uncertainties were calculated properly the values

calculated in Eqs C.236 to C.246 were added together to make sure that the sum yields

100%, i.e.,

$$\%\delta\Delta_{Dz} = \%\delta\Delta Dz\delta Fx + \%\delta\Delta Dz\delta Fz + \%\delta\Delta Dz\delta LAB + \%\delta\Delta Dz\delta LBC + \%\delta\Delta Dz\delta LCD + $$
$$\%\Delta Dz\delta Ab + \%\delta\Delta Dz\delta Ac + \%\delta\Delta Dz\delta Iby + \%\delta\Delta Dz\delta Icy + $$
$$\%\delta\Delta Dz\delta E + \%\delta\Delta Dz\delta G$$

or

$$\%\delta\Delta_{Dz} = 100\% \quad . \tag{C.247}$$

Based on the results of Eqs C.236 to C.247 the uncertainty in I_{by} produces the largest

contribution to the overall uncertainty in deformation in the z-direction, amounting to

85%. The next step was to check the overall uncertainty in I_{by} to see which one of

independent parameters contributes most to δI_{by},

$$\%\delta Iby\delta b = \frac{\delta Iby\delta b}{\delta I_{by}{}^2} \cdot 100 \qquad\qquad \%\delta Iby\delta b = 99.8403\% \quad , \tag{C.248}$$

$$\%\delta Iby\delta h = \frac{\delta Iby\delta h}{\delta I_{by}{}^2} \cdot 100 \qquad\qquad \%\delta Iby\delta h = 0.1597\% \quad . \tag{C.249}$$

Results of Eqs C.248 and C.249 were added together to check that they add up to 100%,

$$\%\delta I_{by} = \%\delta Iby\delta b + \%\delta Iby\delta h \qquad\qquad \%\delta I_{by} = 100\% \quad . \tag{C.251}$$

Equations C.249 to C.251 show that the uncertainty in the width contributes over 99% to

the overall uncertainty of I_{by}. Since I_{by} is the largest contributor to the overall uncertainty

in the deformation in the z-direction, δb contributes most to the overall uncertainty in the

deformation. One way to reduce the magnitude of this contribution is to use better means

for measuring the width, resulting in dimensions characterized by the least count lower than 0.5 μm.

APPENDIX D. EXPERIMENTAL RESULTS

D.1. OELIM determination of deformations of the right proof mass of the microgyro

Following the procedure used to obtain results presented in Section 5.4.2.2,

deformations of the right proof mass were determined, Figs D.1 to D.12.
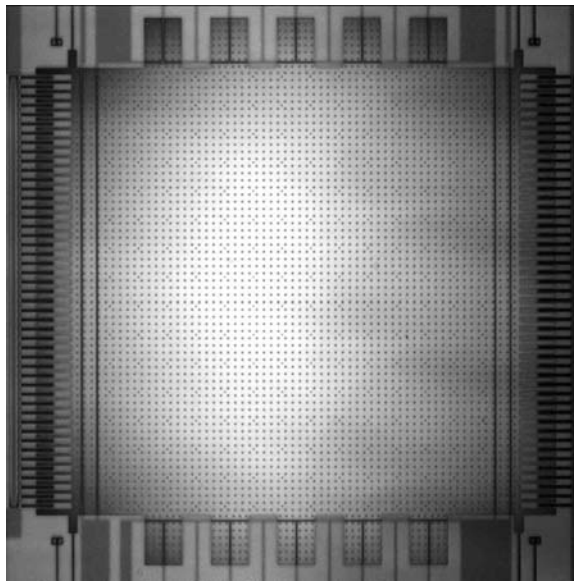
Fig. D.1. Representative OELIM interferogram
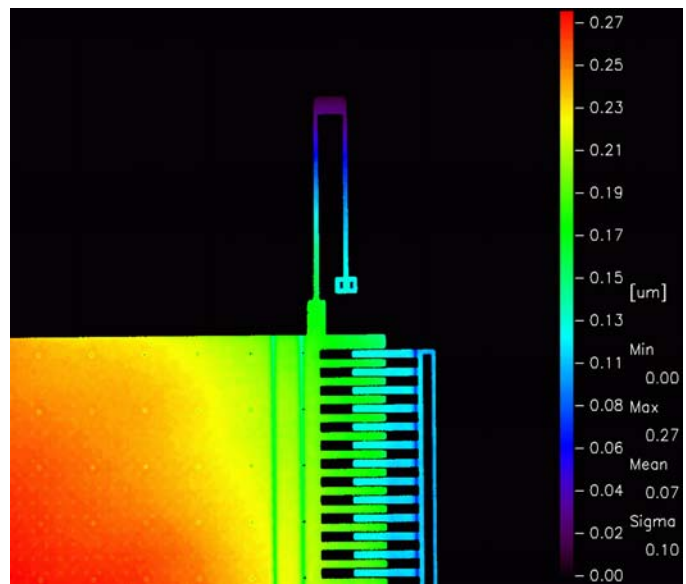of the right proof mass of the microgyro.
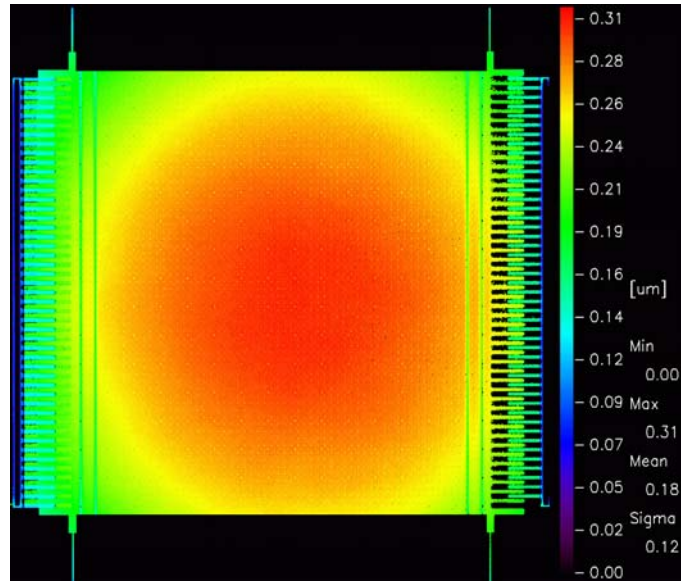
Fig. D.2. Two-dimensional color representation of
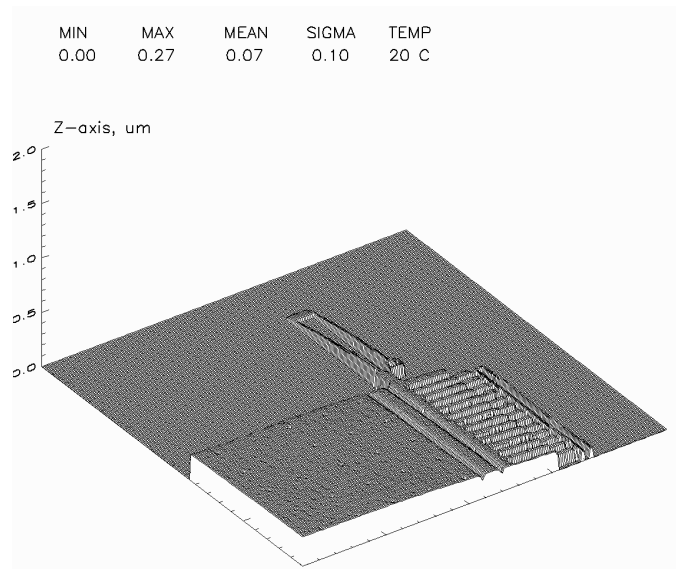deformations of the right proof mass.
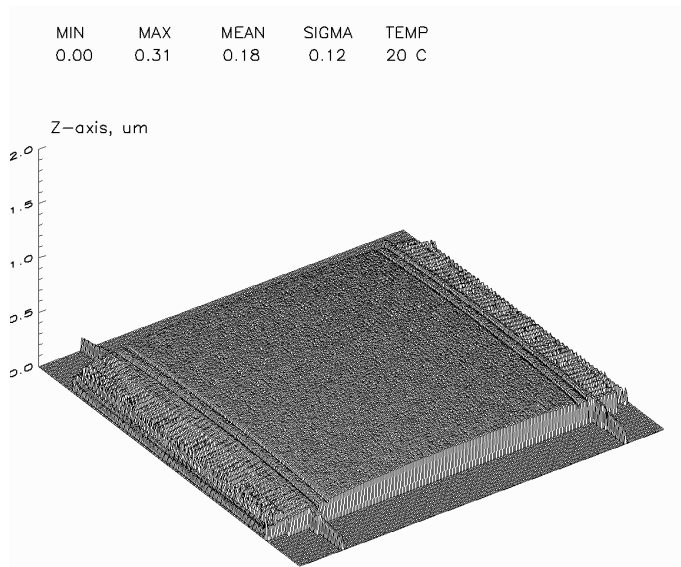
Fig. D.3. Three-dimensional wireframe representation
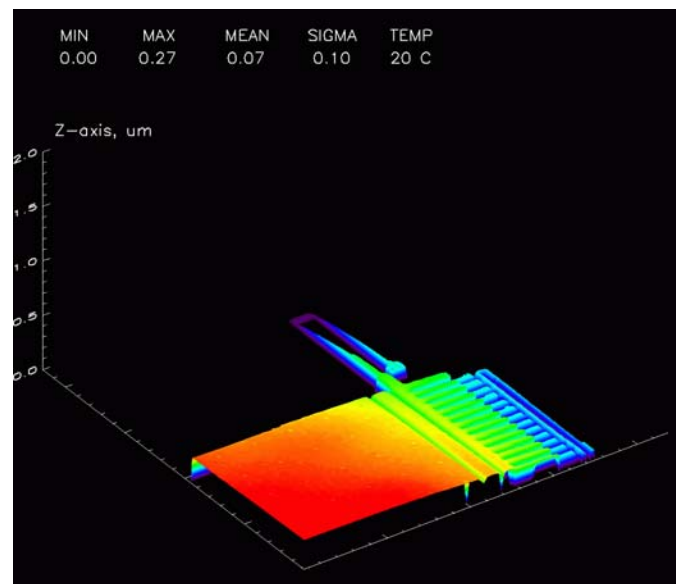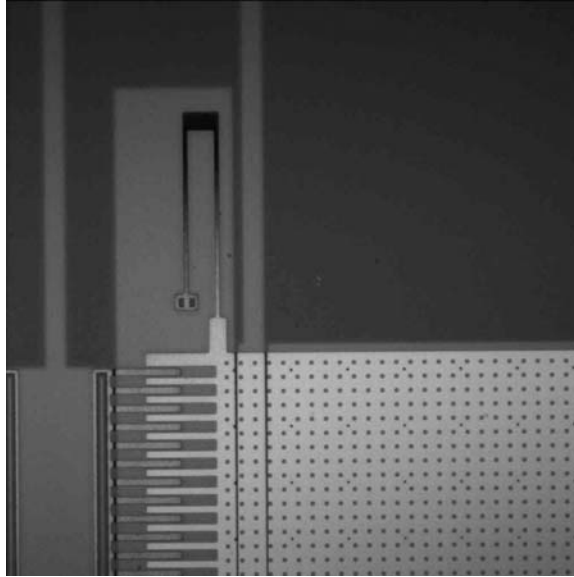of deformations of the right proof mass.
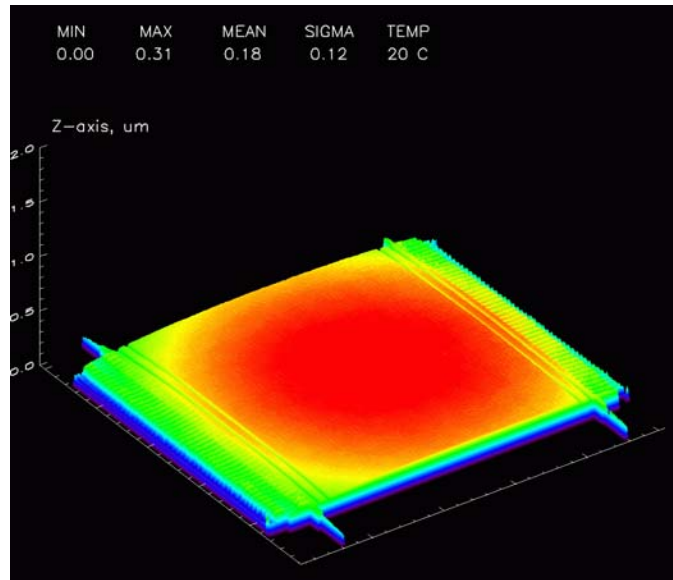
Fig. D.4. Three-dimensional color representation of deformations of the right proof mass.
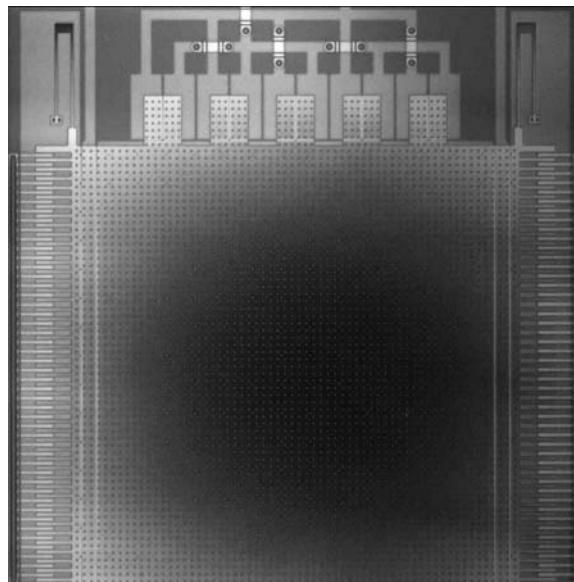
Fig. D.5. Representative OELIM interferogram of the upper part of the right proof mass of the microgyro.
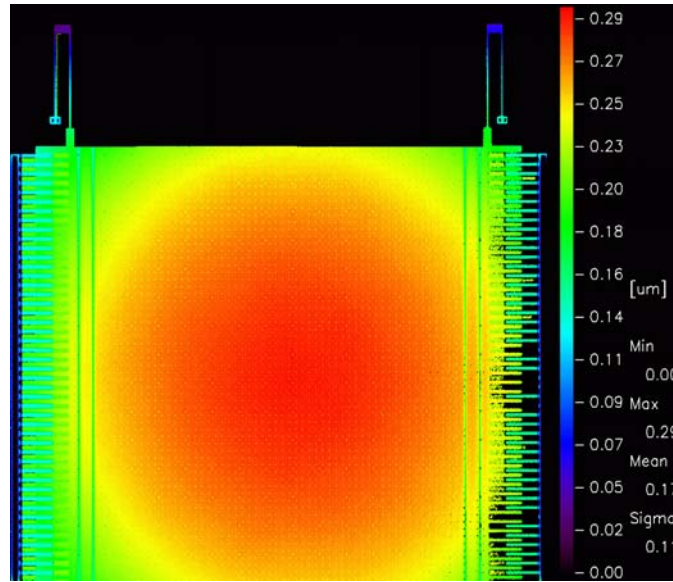
Fig. D.6. Two-dimensional color representation of
deformations of the upper part of the right proof mass.
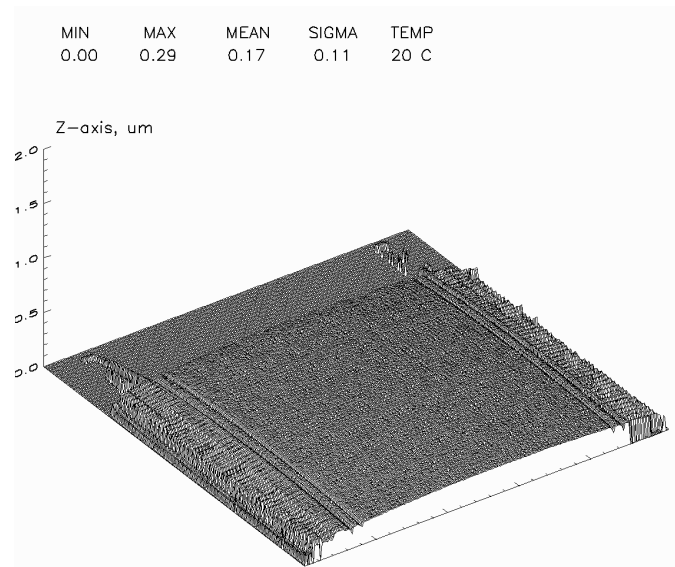
Fig. D.7. Three-dimensional wireframe representation of
deformations of the upper part of the right proof mass.
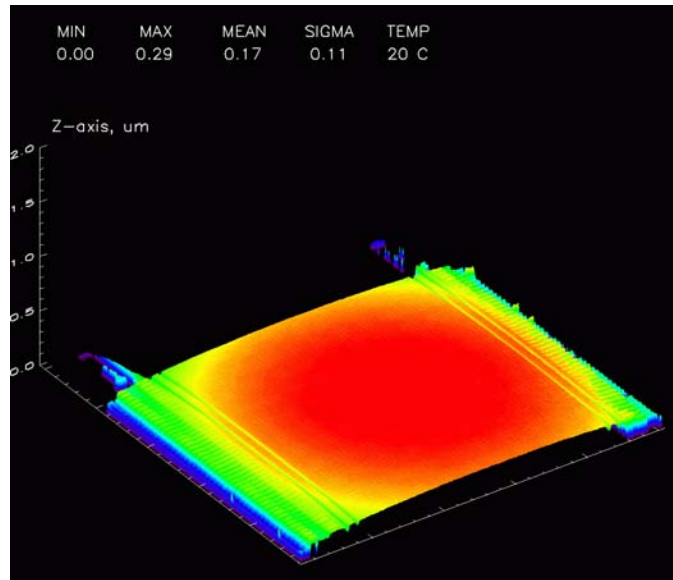
Fig. D.8. Three-dimensional color representation of deformations of the upper part of the right proof mass.
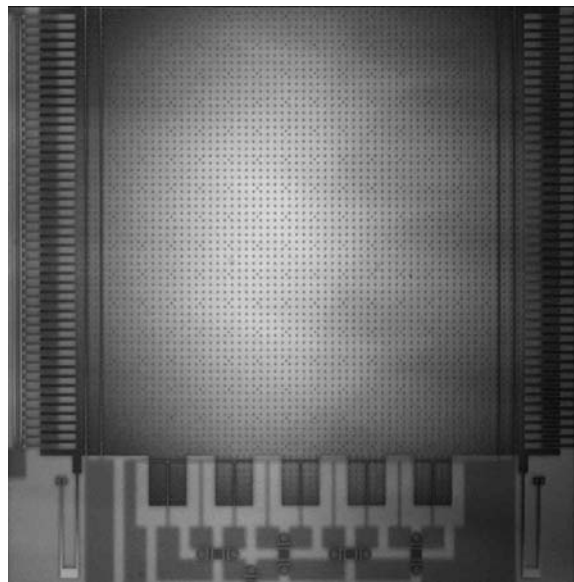
Fig. D.9. Representative OELIM interferogram of the lower part of the right proof mass of the microgyro.
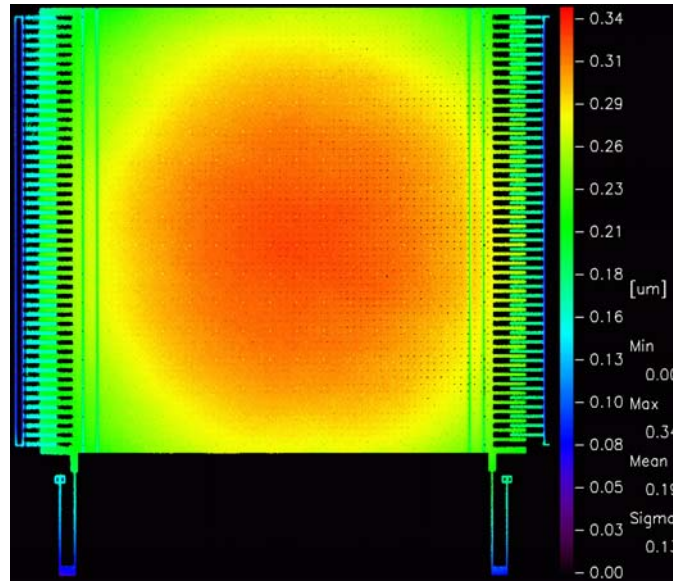
Fig. D.10. Two-dimensional color representation of deformations of the lower part of the right proof mass.
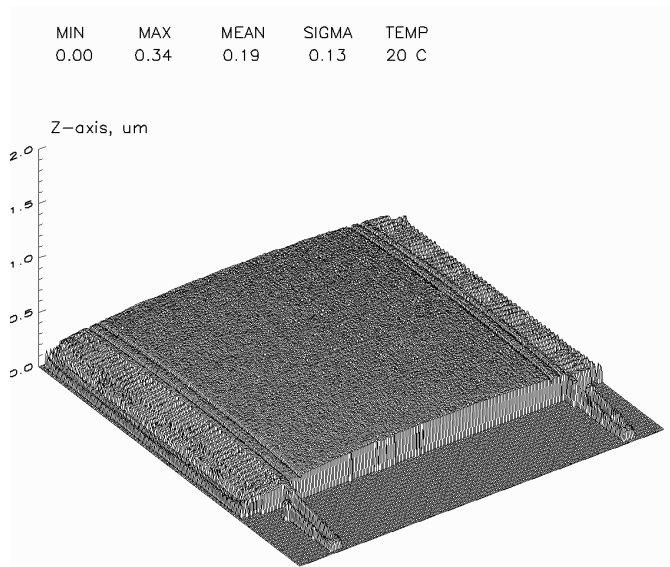
Fig. D.11. Three-dimensional wireframe representation of deformations of the lower part of the right proof mass.
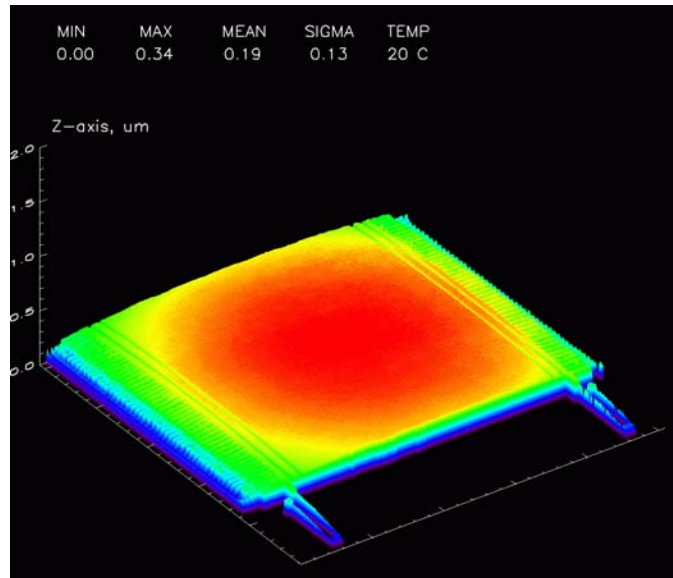
Fig. D.12. Three-dimensional color representation of deformations of the lower part of the right proof mass.

D.2. OELIM determination of deformations of the folded springs supporting the right proof mass of the microgyro

The folded springs that support the right proof mass, Springs 5 to 8, were also observed at an even higher magnification than that used to obtain the results presented in Sections 5.4.2.2 and D.1. The results obtained for these springs are illustrated in Figs D.13 to D.28.
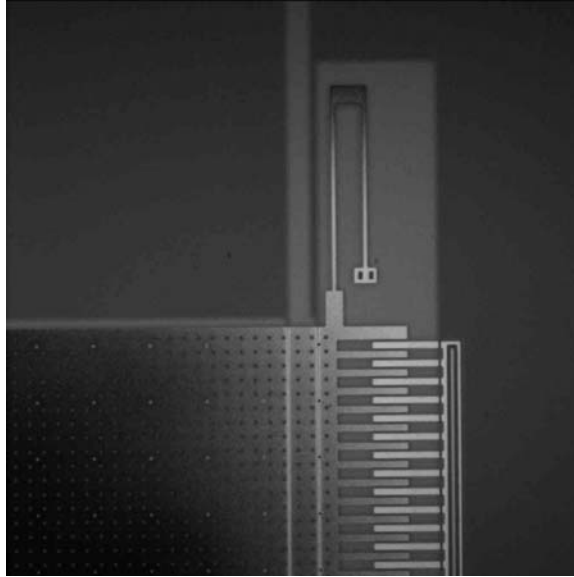
Fig. D.13. Representative OELIM interferogram of
Spring 5 of the microgyro.

Fig. D.14. Two-dimensional color representation of
deformations of Spring 5 of the microgyro.

Fig. D.15. Three-dimensional wireframe representation
of deformations of Spring 5 of the microgyro.

Fig. D.16. Three-dimensional color representation of
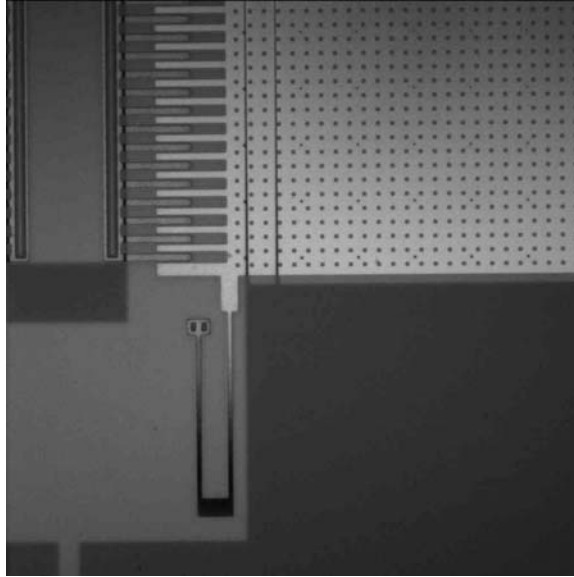deformations of Spring 5 of the microgyro.

Fig. D.17. Representative OELIM
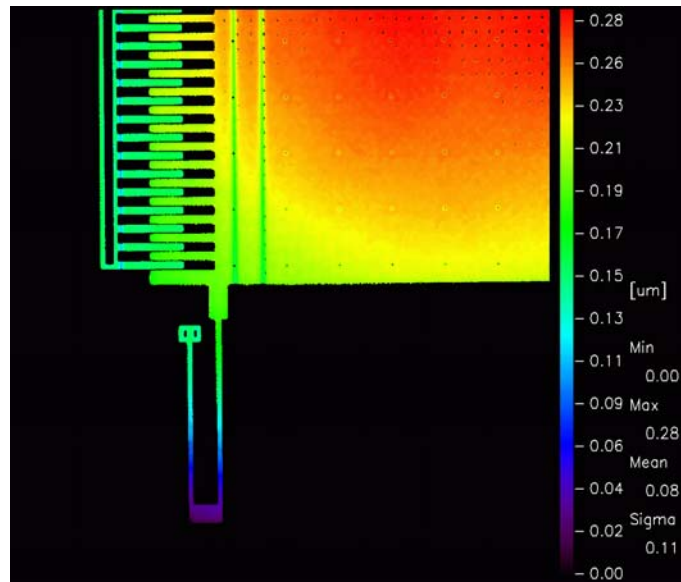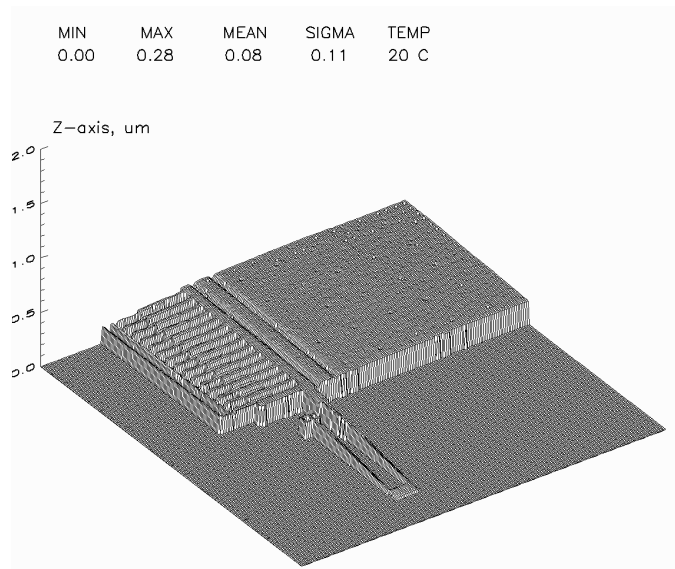interferogram of Spring 6 of the microgyro.
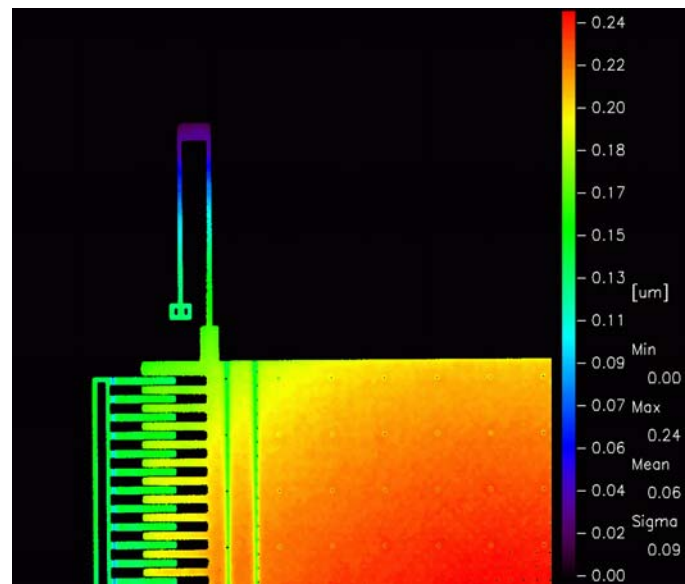
Fig. D.18. Two-dimensional color representation of
deformations of Spring 6 of the microgyro.
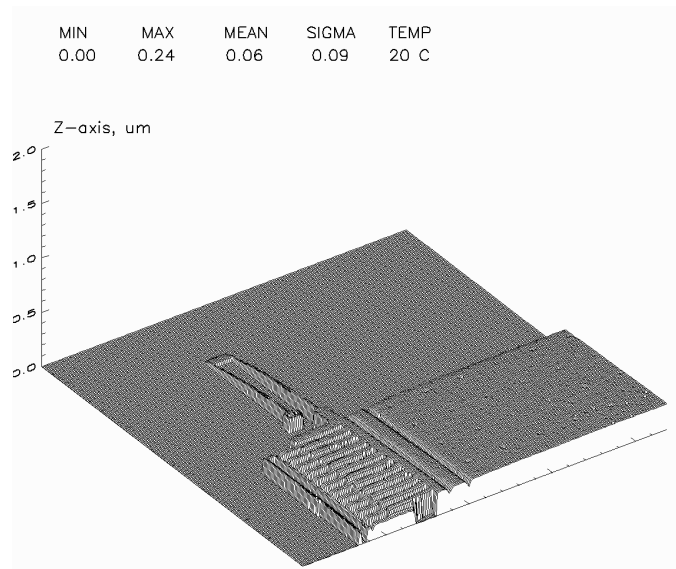
Fig. D.19. Three-dimensional wireframe representation
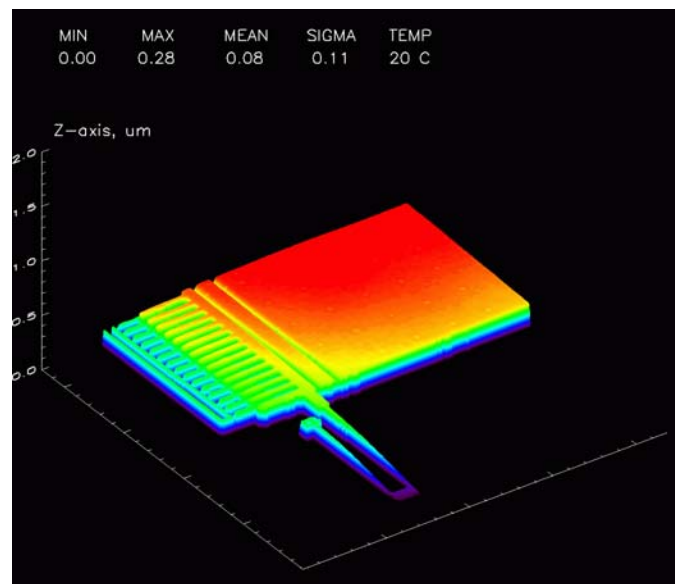of deformations of Spring 6 of the microgyro.
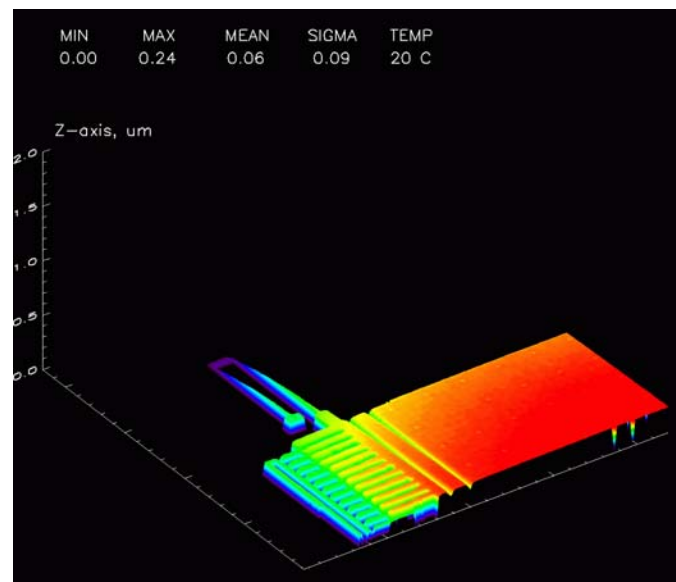
Fig. D.20. Three-dimensional color representation of
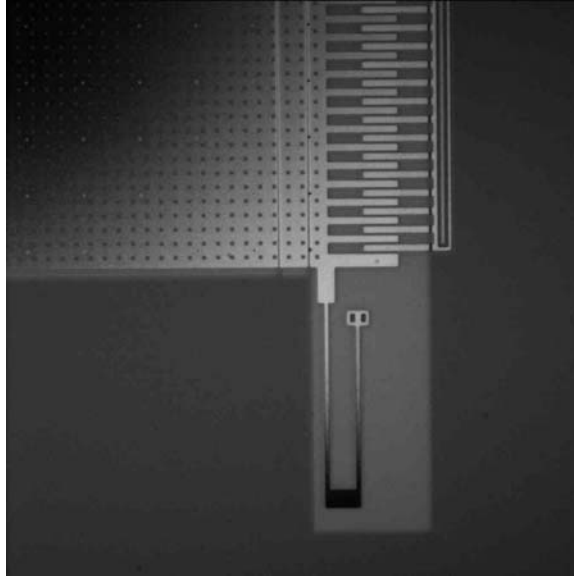deformations of Spring 6 of the microgyro.

261

Fig. D.21. Representative OELIM
interferogram of Spring 7 of the microgyro.

Fig. D.22. Two-dimensional color representation of
deformations of Spring 7 of the microgyro.

Fig. D.23. Three-dimensional wireframe representation
of deformations of Spring 7 of the microgyro.

Fig. D.24. Three-dimensional color representation of
deformations of Spring 7 of the microgyro.

Fig. D.25. Representative OELIM
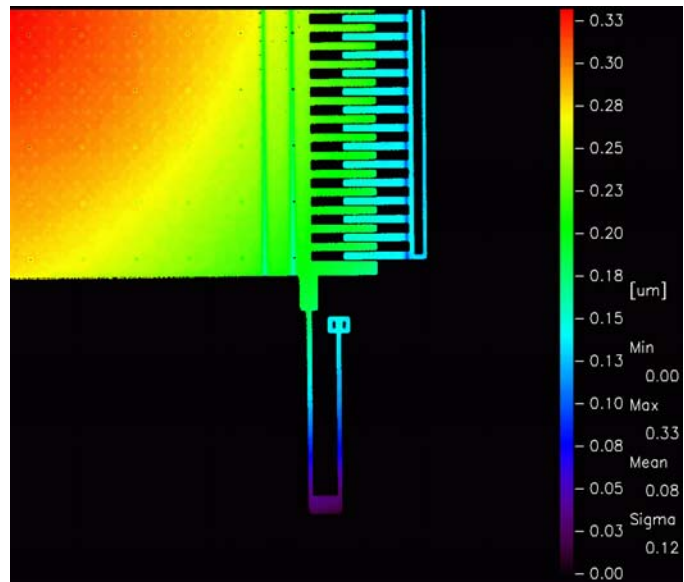interferogram of Spring 8 of the microgyro.

Fig. D.26. Two-dimensional color representation of
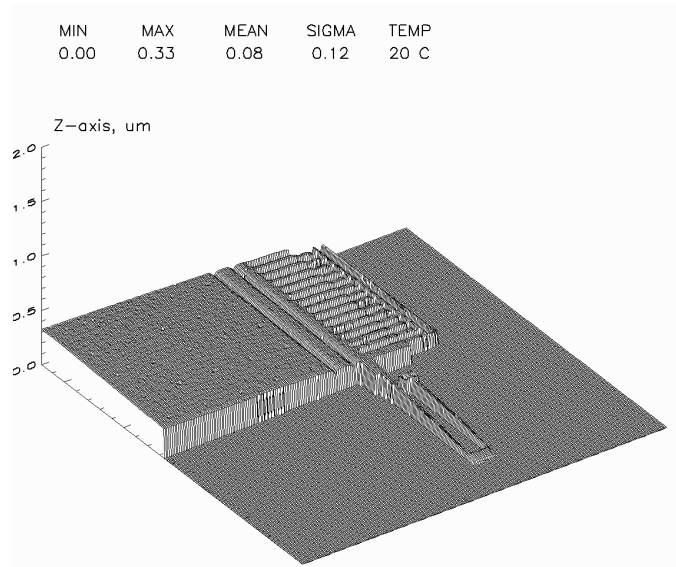deformations of Spring 8 of the microgyro.

Fig. D.27. Three-dimensional wireframe representation of deformations of Spring 8 of the microgyro.
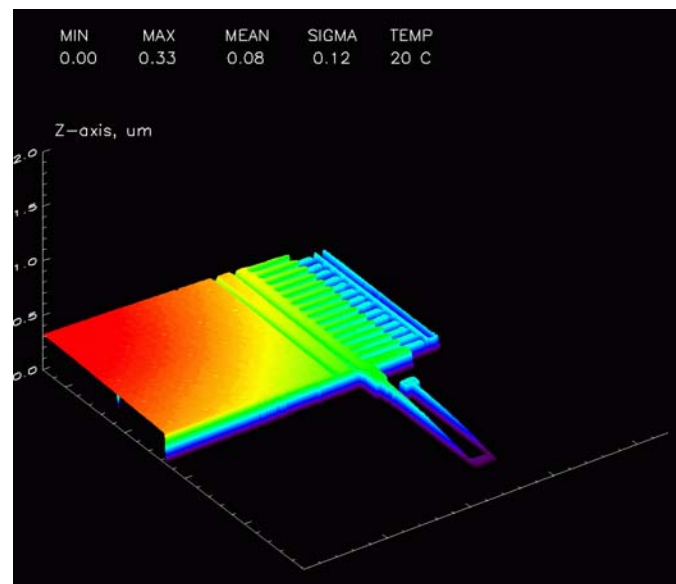

Fig. D.28. Three-dimensional color representation of deformations of Spring 8 of the microgyro.